Integrated Quality Control of Precision Assemblies using Computed Tomography

Stolfi, Alessandro

Publication date:
2017

Document Version
Publisher's PDF, also known as Version of record

Integrated Quality Control of Precision Assemblies using Computed Tomography

by

Alessandro Stolfi

For fulfilment of the degree Philosophiae Doctor

Department of Mechanical Engineering
Technical University of Denmark
January 2017

This Ph.D. thesis is dedicated to you

Preface and acknowledgements

This thesis has been prepared as one of the requirements of the Ph.D. degree at the Technical University of Denmark (DTU), Department of Mechanical Engineering.

The work has been carried out from November 2013 to November 2016 at the Department of Mechanical Engineering under the supervision of Prof. Leonardo De Chiffre and Dr. Lorenzo Carli. From March to May 2016, 5 weeks were spent at the Physikalisch-Technische Bundesanstalt (PTB), Braunschweig, Germany under the supervision of Dr. Markus Bartscher. From June to August 2016, 15 weeks were spent at Novo Nordisk A/S under the supervision of Dr. Lorenzo Carli.

I would like to thank my committee: Prof. Leonardo De Chiffre and Dr. Lorenzo Carli for their mentorship, encouragement, and discussion on all aspects of this project.

I would like to thank Lorenza, my family and my friends for their unconditional love and support. Nothing would have been started without them standing by me.

I would like to express my gratitude to the staff of department 5.34 Multisensor- Koordinatenmesstechnik at PTB, especially to Dr. Markus Bartscher, Mr. Fabricio Borges de Oliveira, Dr. Jens Illemann, Dr. Karin Kniel, Dr. Ulrich Neuschaefer-Rubeand, for their hospitality and trust. Special thanks go to Mr. Fabricio Borges de Oliveira and Dr. Jens Illemann who have contributed to this work with their suggestion. A part of this Ph.D. thesis with the title: “4.2 A Metrological Comparison of Surface Determination Methods used in CT for Metrology” has been carried out in collaboration with PTB.

I would like to thank the staff of the quality laboratory at Novo Nordisk A/S DMS Metrology & Calibration (DK) and the staff of testing laboratory at Novo Nordisk A/S Device R&D for their hospitality and trust. Special thanks go to Dr. Alessandro Godi, Ms. Charlotte Pia Haagensen, Ms. Maarja-Helena Kallasse, and Ms. Trine Sørensen, for their help during my secondment.

I would like to thank the participants of “InteraqCT comparison on assemblies”: The participation of the following organisations is acknowledged: 3D-CT A/S (DK), BAM Federal Institute for Materials Research and Testing (DE), Carl Zeiss IMT GmbH (DE), Danish Technological Institute (DK), Deggendorf Institute of Technology (DE), GRUNDFOS A/S (DK), Huddersfield University (UK), FMT Institute of Manufacturing Metrology Friedrich-Alexander-University Erlangen-Nuremberg (DE), Katholieke Universiteit Leuven (BE), NPL National Physical Laboratory (UK), Nikon Metrology (UK), Novo Nordisk A/S Device R&D (DK), Novo Nordisk A/S DMS (DK), Nuova Pignone (IT), Physikalisch-Technische Bundesanstalt (PTB), RWTH Aachen University (DK), SIMTech (SGP), University of Applied Science Upper Austria (AT), University of Nottingham (UK), University of Padova (IT), Werth Messtechnik GmbH (DE), YXLON International GmbH (DE). It would not have been possible without them.

I want to thank Mr. René Sobiecki and Mr. Erik Larsen for the pleasant time spent together at the Centre for Geometrical Metrology (CGM) at 20 ± 0.1 ºC.

I would like to thank Dr. Mary Kathryn Thompson for her valuable help with various aspects of this thesis and for introducing me to Axiomatic Design.

The work was funded by the Technical University of Denmark as an activity within the Marie Curie ESR Project INTERAQCT - International Network for the Training of Early Stage Researchers on Advanced Quality Control by Computed Tomography funded by the European Commission's 7th Framework Programme FP7-PEOPLE - under grant agreement No 607817. Detailed information is available at http://www.interaqct.eu/. Partners of the INTERAQCT project are acknowledged for very fruitful meetings, great collaboration, and pleasant dinners during these last 3 years of work together.

Lyngby, January 2017

Alessandro Stolfi

Abstract

Computed Tomography (CT) is bringing about a profound change in the way that tolerance verification is performed in industry. CT allows the inner and the outer geometry of a workpiece to be measured without the need for external access or destructive testing. These are significant advantages over coordinate measuring machines (CMMs) when working with complex and fragile parts. This Ph.D. project at DTU Mechanical Engineering concerns the applicability of CT for quality control of precision assemblies. Investigations to quantify the accuracy of CT measurements, reference artefacts to correct systematic errors in CT, and an international comparison on CT of Assemblies have been carried out during the project.

A series of investigations regarding the influence of the CT post-processing factors on the accuracy of CT measurements was carried out. Post-processing factors such as surface determination, data filtering and feature fitting were considered within the present investigations. The investigations were conducted on two CT systems, showing different metrological performances, and involved a variety of multi-material assemblies, having different shapes and materials. The investigation results have showed that CT measurements on assemblies can be successfully conducted and that the surface determination method appears to be able to segment multi-material workpieces without any loss of accuracy.

A novel type of artefact for calibration of the scale error in CT has been developed within the project. One kind of artefact comprises a carbon fibre tubular structure on which a number of reference ruby spheres are glued. Another kind comprises an invar disc on which several reference ruby spheres are positioned at different heights using carbon fibre rods. The artefact is positioned and scanned together with the workpiece inside the CT scanner producing a 3D reference system for the measurement. The two artefacts were calibrated on a tactile CMM and their applicability demonstrated using different calibrated workpieces. The use of the developed artefacts ensures a considerable reduction of time by compressing the full process of calibration, scanning, measurement, and re-calibration, into a single imaging. The use of the artefacts also allows a considerable reduction of the amount of data generated from CT scanning.

Interlaboratory comparison on Computed Tomography of assemblies was carried out as a part of the Ph.D. study. The comparison involved 22 research laboratories from 7 countries, and was based on the circulation of two assemblies. With respect to previous comparisons that only focused on physical items, the present comparison introduced a voxel item, which was an assembly scanned by the coordinator and distributed electronically to participants. The comparison results demonstrated that (*i*) length measurements are made without problems by most of the participants who corrected systematic errors effectively; (*ii*) CT post-processing has a sizable impact as the measurand complexity increases; (*iii*) the

majority of the participants stated measurement uncertainties although many of them provided poor statements.

Resume

Røntgen computer-tomografi (CT) bringer en grundlæggende ændring i den måde toleranceverifikation udføres i industrien. CT tillader måling af de indre og ydre geometrier af et emne, uden behov for ekstern tilgang eller destruktive forsøg. Dette er betydelige fordele i forhold til koordinatmålemaskiner (KMM), når der arbejdes med komplekse og skrøbelige emner. Dette ph.d. projekt ved DTU Mekanik omhandler anvendeligheden af CT for kvalitetskontrol af præcisionssamlinger. Herunder undersøgelser for at kvantificere nøjagtigheden af CT-målinger, referenceemner for at etablere måleteknisk sporbarhed af målinger og en international sammenligning af CT-systemer er blevet gennemført i løbet af projektet.

En række undersøgelser omhandlende influenceparametre ved CT-databehandling er udført for at undersøge deres indflydelse på nøjagtigheden af CT-målingerne. Influenceparametre som overfladebestemmelse, datafiltrering og element tilpasning er gennemgået i undersøgelserne. Undersøgelserne er udført med to CT-systemer med forskellige metrologisk karakteristika og med brug af multimaterialesamlinger med forskellige geometrier og materialer. Forsøgsresultaterne viste, at CT-målinger på samlinger med succes kan udføres, og overfladebestemmelsesmetoden kan segmentere multimaterielle emner uden tab af nøjagtighed.

Et nyt referenceobjekt for CT er udviklet i dette projekt. En type artefakt anvender en rørformet kulfiber struktur, hvorpå et antal rubinsfærer er limet på som referencer. En anden type omfatter plader af Invar, hvorpå rubinsfærer er positioneret ved forskellige højder med kulfiberstænger. Referenceobjektet er positioneret og scannet sammen med arbejdsemnet i CT-scanneren til at etablere et 3D-referencesystem til målingerne. Etablering af sporbarhed for alle objekter er udført ved hjælp af koordinatmålemaskiner med en kendt usikkerhed. De udviklede artefakter medfører en markant mindskning af tiden ved at komprimere processerne for kalibrering, scanning, måling samt re-kalibrering til et enkelt trin. Disse objekter reducerer også mængden af data genereret ved en CT-scanning.

En industriel audit af CT-systemer blev udført i løbet af dette projekt. Sammenligningen involverede 22 laboratorier fra 7 lande, hvor to samlinger er blevet brugt. I forhold til tidligere sammenligninger, hvor der kun er blevet fokuseret på fysiske emner, er der i den nuværende sammenligning introduceret et voxel-emne, som er en samling scannet af koordinatoren og distribueret til deltagerne. Sammenligningen har vist, at (i) længdemålinger foretages uden problemer af de fleste af deltagerne; (ii) CT-databehandling har en nævneværdig indflydelse ved komplekse måleopgaver; (iii) størstedelen af deltagerne angav måleusikkerhed selv om mange af dem leverede ringe usikkerhedsestimater.

List of contents

Chapter 1

Background and Objectives

1.1 Introduction

Manufacturing industry has moved into an extremely high competitive market, with tightening margins and competitive pressures from factors e.g. assembly quality which were not previously taken into account. Assembly quality has a direct and sizeable impact on the value perceived by the customer, so manufacturing industry has been struggling with a constantly increasing pressure on tolerances. As a consequence, optimization of the manufacturing process has risen in importance. Dimensional metrology is today a central part of manufacturing process because its implementation has decreased product recalls and increased profitability. Dimensional metrology when effectively used across a business, it can support all the fundamental decision-making processes in manufacturing environments.

Frost & Sullivan showed that the global dimensional metrology market in the automotive industry generated revenue of $940 million in 2013, and predicts the market will grow at an annual growth rate (CAGR) of 5.2% to approximately $1.22 billion in 2018 [1]. The report also states that investment in metrology prevents major issues appearing downstream.

The miniaturization of parts in the electronics and medical industries and the increasing need of verifying assemblies in assembled state or unreachable features pose new challenges for dimensional metrology which cannot be solved using traditional CMMs.

1.2 Computed Tomography

During the last 10 years, Computed tomography, CT, has stepped in the world of dimensional metrology, finding increasingly uses in research and development (R&D) and in quality control [1]. CT provides a new tool for coping with the product complexity, establishing a holistic dimensional metrology on a workpiece. By irradiating an object with X-rays, CT produces a 3D representation of an object including internal and external features. CT enables metrology on fragile or small parts due to its contactless measurement principle. CT can deliver relevant dimensions of parts regardless of complexity,

shape, colour of object being imaged. 3D representations of an object can then be compared with CAD by using Part-to-CAD comparison.

CT is extremely interesting for quality control of assemblies in assembled states. In fact, when force is established between two mating parts, it can frequently happen that the two parts, which initially complied with product specifications, do not match at the assembly. As a result, the functionality of the final product is compromised. CT provides a unique non-destructive way to 3D-visualize the assembly surface and to quantify deviations. As a result, assembly inspection based on CT measurements ensures more reliable information than any other destructive testing method, which irremediably deforms the assembly, biasing the results. Figure 1.1 shows an example of CT inspection conducted on an insulin pen produced by Novo Nordisk A/S [2] showing the deformation of one of its components after having been assembled. Frost & Sullivan reported that the global market for CT for metrology earned revenues of $85.2 million in 2014 with a positive outlook for next years.

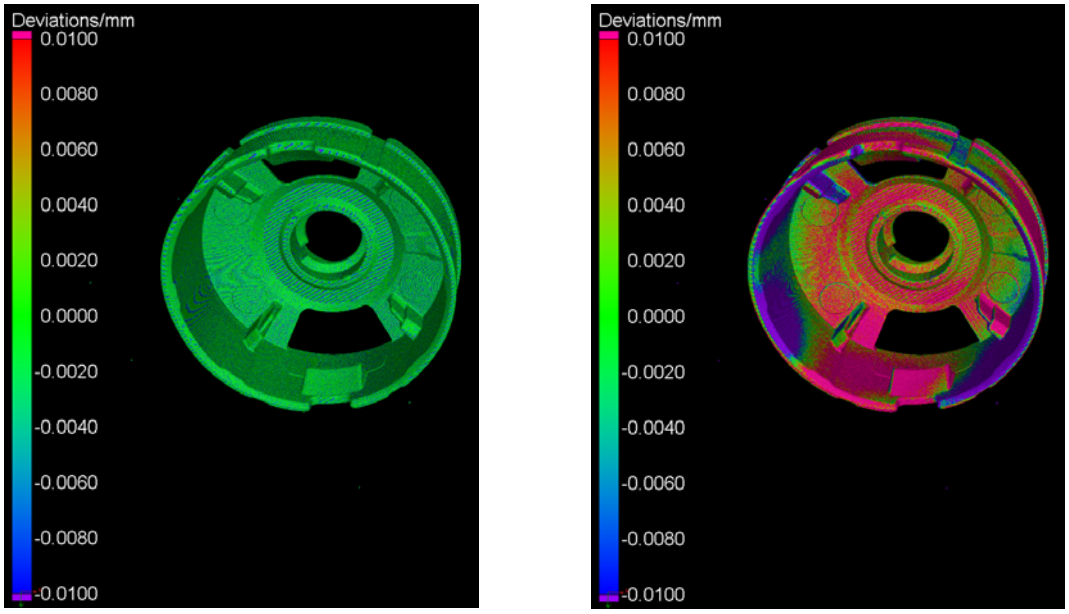

(a) (b)

Figure 1.1. 2 Part-to-CAD comparisons showing a component (a) before and (b) after having been assembled. It can be seen that the shape of the component has been dramatically modified

1.3 Project statement

CT has all the potential features to become a game-changing technology, especially for its unique feature for tolerance verification of assemblies. Its adoption in manufacturing industry will, however, depend on technology and normative developments. CT currently shows a performance gap compared to traditional equipment used in industrial metrology. Generally speaking, CT delivers measurement results with measurement uncertainties up to 10 times greater than CMMs. CT is still characterized by

a throughput that does not very well fit production environments. CT also shows a normative development gap, compared to other measuring techniques used in production environments, due to two main factors. Firstly, CT is multi-purpose measuring device and therefore measurement traceability cannot be easily achieved. Secondly, CT is a relatively new technology, the first example of CT for metrology was presented in 2005. The aim of this project is to test the applicability of CT for quality control of precision assemblies using Computed Tomography. The project was divided in the following phases:

1. State-of-the-art study on Computed Tomography and assembly verification.
2. Development of reference artefacts and calibration procedures;
3. Optimization of scanning parameters;
4. Tolerance verification of assemblies;
5. Development of artefacts for an international comparison in CT.

1.4 International Network for the Training of Early stage Researchers on Advanced Quality control by Computed Tomography (InteraqCT project)

This Ph.D. project at Department of Mechanical Engineering, Technical University of Denmark (DTU MEK) was as an activity within the Marie Curie ESR Project INTERAQCT - International Network for the Training of Early Stage Researchers on Advanced Quality Control by Computed Tomography funded by the European Commission's 7th Framework Programme FP7-PEOPLE - under grant agreement No 607817. Detailed information is available at http://www.interaqct.eu/. The INTERAQCT project has been conceived as a pan-European industrial-academic initiative providing the unique and encompassing training environment required, by bringing together expertise from industry and academia.

1.5 Project structure

The structure of the Ph.D. thesis involves seven chapters covering the project statement. A description on each chapter is given as follows:

Chapter 2 introduces CT for metrology and its fundamental elements such as source, detector, positioning system and informatics infrastructure. An identification and classification of influence factors in CT metrology is also presented. The chapter moreover provides a description of image artefacts commonly encountered in CT together with methods for their correction.

Chapter 3 gives a description of key concepts associated with tolerance verifications. The chapter commences with an introduction to part variation, followed by a presentation of Geometrical Product Specifications (ISO-GPS). The rule for proving conformity or nonconformity with specifications and

methods for the estimation of uncertainty in CT are also presented in this chapter. The chapter also presents how tolerances are typically inspected within the quality laboratories of the production environments.

Chapter 4 comprises a series of investigations that has aimed to quantify the impact of CT post-processing variables on the accuracy of measurements. The investigations have taken into account post processing influence factors such as data filtering, surface determination, datum system, and feature fitting. Industrial and reference assemblies having different sizes and materials have been used throughout the investigations.

Chapter 5 introduces two reference objects, the CT tube, and CT crown, for concurrent correction of the scale error in industrial CT. The two reference objects are presented in terms of manufacture and calibration. A series of experimental investigations showing the applicability of the two reference artefacts are also presented in this chapter

Chapter 6 presents the results of an international comparison on Computed Tomography of assemblies, which has involved 22 participants from 7 different countries. Two assemblies including different materials, dimensions have been circulated in parallel. In contrast to earlier comparisons that only focused on physical workpieces, this comparison has involved a voxel assembly, which was an assembly scanned by the coordinator and distributed electronically to participants.

Chapter 7 summarizes the most important findings and achievements of this work. Suggestions for future work in the field of CT based on this Ph.D. project are provided.

Chapter 2

Computed Tomography for Metrology

2.1 Computed Tomography and its main components

Computed Tomography, CT, is a well-established tool for clinical diagnostics, which now is becoming more and more used for industry applications such as materials characterization, non-destructive testing and metrology application. While the basic principles are common for both fields, some major differences can be observed between medical and industrial CT. In medical CT the entire equipment moves around the patient who is kept in a stable position in order to collect projections. In an industrial CT, the object being imaged is rotated while the entire equipment is fixed. The different kinematics leads to higher accuracy in industrial CT than medical CT. In medical CT, the imaging process should reduce the interaction between human tissues and X-rays for safety reasons. In industrial CT, the dosage does not pose any problem for the majority of objects being imaged. The different nature of materials being imaged leads to longer and stronger X-ray exposure in industrial CT than medical ones.

The basic hardware configuration of an industrial CT scanner consists of four hardware components (see Figure 2.1): (i) an X-ray source, (ii) a positioning system, (iii) an X-ray detector, and (iv) an informatics infrastructure for collecting the data generated by CT imaging.

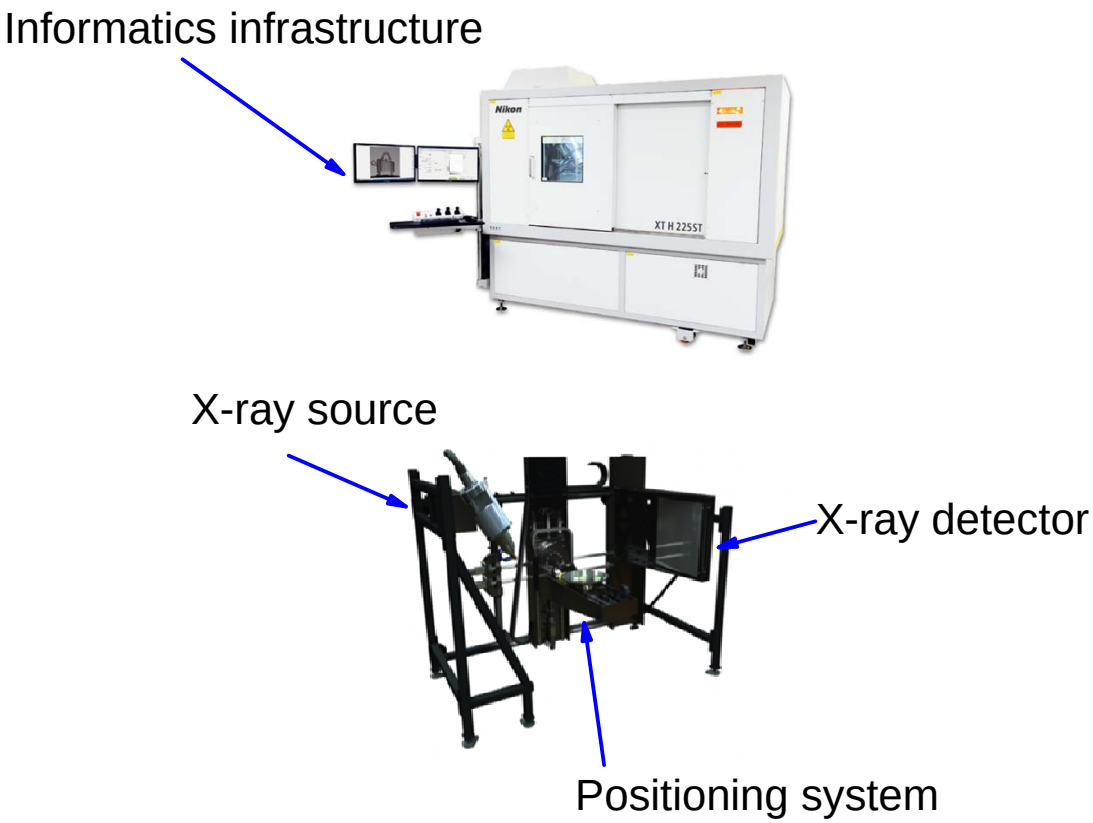

Figure 2.1. An example of industrial CT and its main four hardware elements. As an example, Nikon XT H 225 cone beam CT scanner available at DTU is shown

2.1.1 X-ray source

The X-ray source is a vacuum tube that converts electrical input power into X-rays. Any X-ray source consists of a cathode hairpin filament emitting electrons, a cylinder cap enclosing the cathode, a magnetic lens focusing electrons and a target producing X-rays.

The hairpin filaments are manufactured from high grade tungsten and annealed in vacuum in order to remove all manufacturing stress [4]. The filaments are manufactured with tolerance in the order of a few microns. The filament represents a consumable part of the X-ray source as the process of heating the filament to produce electrons leads the filament to evaporate.

The cylinder cap, also known as the Wehnelt cap[5][6], surrounds the filament and has a more negative charge than the filament. The Wehnelt establishes a repulsive electrostatic force condensing the generated electrons. The Wehnelt cap presents a through hole on its bottom part from which the generated electrons move towards the target.

Magnetic lens is a device for maintaining a constant radius of the electron flow over the scanning time by using the magnetic Lorentz force. The latter is established by passing currents through coils external to the tube. The stability of the current coils over time represents one of the most important factors affecting the imaging process. The size of the electron flow is commonly known as focal spot size.

Target represents the component of the X-ray source in which the X-radiation is produced. The target is made from solid metals having high atomic number, *Z*, a high melting point, and good thermal conductivity. The thermal properties of the target materials are extremely important as the targets are subjected to a large amount of heat. Generally speaking, 99% of the energy supplied to electrons is converted into heat (over 99%) and just 1% results in producing X-rays. More recently, a new kind of target, called liquid targets, has begun to emerge on the market. Liquid targets remove thermal limitations of solid targets by using a molten material which is regenerated over scanning time [7]. Gallium, *Ga*, and Indium, *In*, alloys are used as materials. As a consequence of the physical state of the target, an increase in the brightness and in the stability of the X-ray flow can be obtained.

Industrial X-ray sources can be grouped into two categories: open sources and closed sources. The open sources allow the filament to be replaced by end-users, so they require a pump ensuring the vacuum. The closed sources are completely sealed during manufacture, so that they do not require a pump.

Once electrons bombarded the target, electromagnetic radiations classified as X-rays are produced. The produced X-rays are created by two different atomic processes: (a) Bremsstrahlung radiation and (b) characteristic radiation. Bremsstrahlung is the dominant X-ray production process and takes place when an electron coming from the filament is decelerated at the target. As a consequence of the deceleration, all its kinetic energy is transformed into a single x-ray photon. Bremsstrahlung radiation produces a continuous X-ray spectrum. The maximum energy of the produced X-ray spectrum is limited by the kinetic energy of the incident electrons energy of the incident electron. Characteristic radiation occurs when high-energy particles, which can be photons and electrons, impact electrons of K-shell, which is the closest shell to the nucleus [8]. As a consequence, the electrons in the K-shell are ejected, leaving a series of vacancies. When those vacancies are filled by outer-shell electrons, X-rays are produced to re-establish energy equilibrium. The characteristic radiation is visible as a series of discrete peaks superimposed on the continuous X-ray spectrum. The generation of characteristic radiation requires that electrons have energies larger than the electron binding energy of K-shell electron, representing the minimum energy required for ejecting the electron from its shell. The energy of the peaks depends on the material target and its nuclear binding energies.

The voltage and current, applied to the X-ray source, govern the extension and intensity of the generated X-ray spectrum. The X-ray source voltage along with the electron charge controls the extension of the X-ray spectrum. For example, a tube energized at 100 kV will generate X-rays ranging from 0 to 100 kV. The X-ray source current governs the amount of energy characterising the X-ray spectrum. By increasing the current flowing through the filament, the number of electrons emitted increases until a given point referred to as saturation.

2.1.2 X-ray detector

Detectors are devices by which the X-rays are converted into digital information. The output of a detector is a series of two-dimensional grey images, known as projections. Most industrial CT scanners use scintillation-based X-ray detectors consisting of either an array of detector elements or a matrix of detector elements. The former are called linear detector arrays, *LDA*, while the latter are called flat panel detectors.

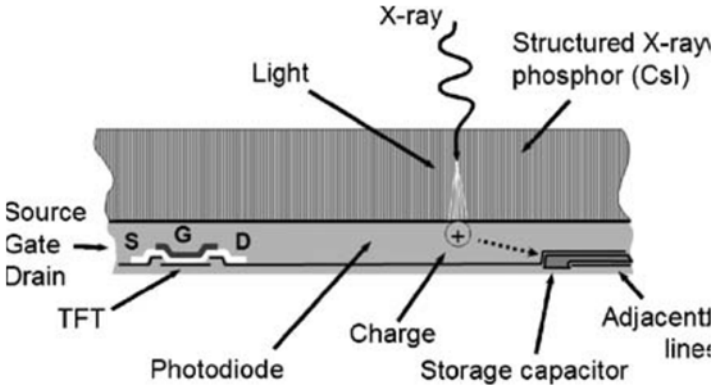

Figure 2.2. A cross-section of a detector showing a schematic representation of design principle of a detector element used in industrial CT. The first conversion takes place in the scintillator substrate where X-rays are converted into light. The second conversion takes place in the photodiode substrate where light is converted into current. The current is stored within thin film transistors, TFTs, during exposure time and then transferred to amplifiers for conversion into a digital signal [9]

Figure 2.2 shows a schematic representation of design principle of a detector element used in industrial CT scanners. A scintillator substrate converts the received X-rays into visible light. The latter travels through a series photodiodes that convert the coming light into current. The current is generated when photons are absorbed in the photodiodes. Some current is also produced when no light is present which is known as dark current. The current charge is stored into the thin film transistor, *TFT*. Once exposure is terminated, *TFTs* transfer the stored charge to an amplifier for analogue to digital conversion. The exposure time is the interval during which the detector elements are exposed to incident X-rays. The Analog-to-digital conversion is based on either 14 bit or 16 bit.

The majority of X-ray detectors use Cesium Iodide crystals doped with Thallium, *CsI(Tl),* Thallium doped Sodium Iodide, *NaI(Tl),* Cesium Iodide doped with Sodium, *CsI(Na),* and Gadolinium sulfoxylate, *GOS,* as scintillator materials [10]. The photodiode can be made from different materials, with the silicon-based photodiodes as the most adopted one.

Two production approaches, such as indirect deposition and direct deposition, are used for coupling scintillator and photodiode substrate. The indirect deposition uses a glass plate on which the scintillator layer is deposited. The scintillator layer attached on the plate is subsequently attached in close contact with the photodiode substrate [11][12]. In the direct deposition method, the scintillator is directly arranged on the photodiode substrate. The direct deposition process leads to a more sensitive detector than flipped scintillator because the direct deposition avoids scatter [12].

State-of-the-art 2D detectors have a maximum resolution of 4096 x 4096 pixels and a pixel size of 100 µm. State-of-the-art 2D detectors withstand powers up to about 450 kVe. 2D detectors have square or

rectangular shape. State-of-the-art 1D detectors can include up to 7422 pixels distributed along a sensor length of about 700 mm. State-of-the-art 1D detectors present a pixel size ranging smaller than 200 µm. An overview on the latest developed detector for industrial and metrology CT is given in Table 2.1.

Table 2.1. State-of-the-art detector for industrial and metrology CT

Detectors	Type	# Bits	Active pixels	Pixel Size	Max. frame rate
Varian 1313	Matrix	14-bit	1000 x 1000	127 µm	10 fps
Varian 2520		14-bit	1900 x 1516	127 µm	7.5 fps
Varian 4030		14-bit	2300 x 3200	127 µm	3 fps
Yxlon 2530		16-bit	1792 x 2176	139 µm	15 fps
Perkin Elmer 0820		16-bit	1000 x 1000	200 µm	7.5 fps
Perkin Elmer 1611 xP		16-bit	4096 x 4096	100 µm	3.75
SPS 80	Array	12-bit	Up to 7400	200 µm	/

2.1.3 Positioning system

The positioning system is constituted by a series of kinematic elements by which the object being inspected is moved within the CT cabinet. The positioning system of industrial CT consists of a motorized rotational stage and three motorized translational stages as shown in Figure 2.3.

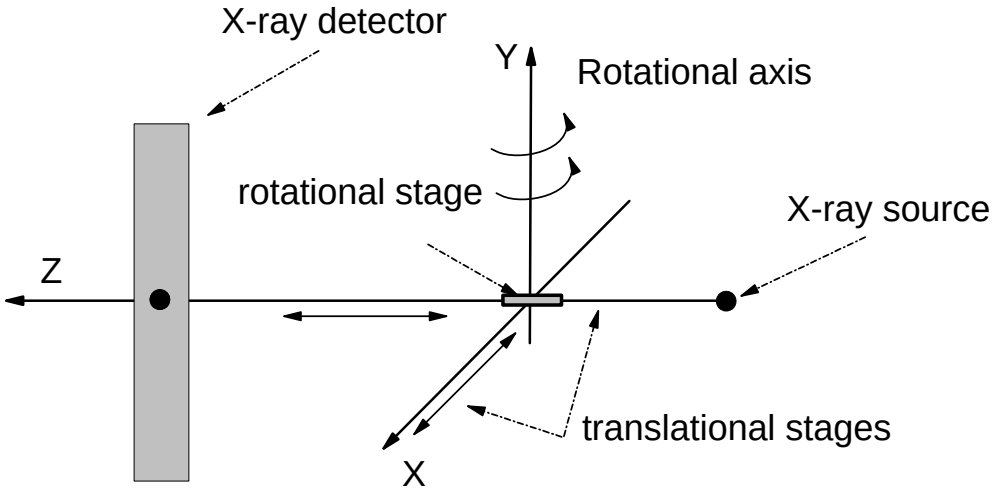

Figure 2.3. A schematic representation of a positioning system of an industrial CT. The represented positioning system includes a rotational stage on which the object being inspected is mounted and three translational stages providing movements of the rotary table along (a) x-axis, (b) y-axis, and (c) z-axis

The motorised rotational stage allows the object to be rotated while images are acquired at set increments depending on the desired number of projections. For example, an imaging process based on 2000 projections requires that the rotational stage turns at an increment of 0.18º. The rotation can be continuous or stepwise depending on the required accuracy. Stepwise rotations yield higher accuracy than the continuous ones that however reduce the scanning time. Rotary stages achieve rotating speeds up to 40° s^{-1} and have load capacities ranging from 50 to 1000 N. Load Capacity is the maximum force that can be applied to a rotary stage without modifying its ideal specifications. Rotary stages should have small geometrical errors such as eccentricity or radial run out, so that the rotation axis of the rotary device is parallel to the central plane of the detector during imaging.

The motorized translational stages provide the necessary degrees of freedom to move the workpiece within the permitted volume of measuring. Referring to the figure, the *x* and *y* -axes move the workpiece within the detector plane, while the *z*-axis changes the distance between the X-ray source and workpiece. The *z*-axis is also referred to as the magnification axis. The accuracy of the translational stages is imposed by both the minimum encoder resolution (measurement resolution) and by the minimum achievable mechanical motion possible (mechanical resolution). The mechanical resolution depends on the elements used for creating the linear movement. Leadscrew and ball screw represent the elements used for establishing linear motions. Leadscrews are mainly used in industrial CT for general applications. Ball screws are used in industrial CT designed for metrology due to their better repeatability.

The rotational and translational stages are assembled in different ways as shown in Figure 2.4. Figure 2.4a shows an example of cantilever configuration supported by a perimeter frame. Figure 2.4b shows

an example of modular configuration mounted on a granite basement, ensuring uncoupling kinematics. A modular configuration ensures higher stiffness, thermal stability, and vibration damping effect than any cantilever configuration. The modular configurations are used in most industrial CT designed for metrology. The cantilever configurations are adopted in industrial CT for general applications.

(a)

(b)

Figure 2.4. Examples of assembly configurations in industrial CT: (a) cantilever configuration supported by a perimeter frame, (b) modular configuration mounted on a granite base [3]

2.1.4 Computer for collecting and post-processing of data generated by CT measurement

The informatics infrastructure governs the acquisition of the projections and the reconstruction of the projection. The acquisition process takes place concurrently with the imaging process and enables the collection of all images produced as the workpiece is being turned. The infrastructure should, therefore, have sufficient bandwidth to follow the stream of projections coming from the detector. State-of-the-art detectors can deliver up to 10 projections per second.

Reconstruction is a process that generates a volumetric representation of the object out of a set of acquired X-ray projections. The Radon transform and its inverse function represent the mathematical basis for the reconstruction of tomographic information [13]. In fact, the acquired projections can be seen as the Radon transform of the cross-sectional absorption densities forming an image. As a consequence, the inverse of the Radon transform can be used to reconstruct the shape of the imaged object. The identification of the inverse of Radon transform can be done using analytic and iterative methods.

Filtered back-projection, *FBP*, represents the most popular analytic reconstruction method in CT thanks to its low computational cost [14][15]. A reconstruction based on *FBP* requires that the projections are first filtered and then reconstructed using a back-projection algorithm [15]. The filtering of projections is based on low pass filters, such as ramp filters [16], Hanning filters [17][18], Shepp-Logan filters [19] , and aims to reduce image distortions. The major limitation of *FBP* is that the reconstruction result will depart from the measured workpiece irrespective of scanning parameters. The most efficient implementation of *FBP* was developed by Feldkamp [20].

Iterative reconstruction algorithms are more versatile but less time-efficient [21]. All iterative reconstruction methods consist of three steps which are repeated iteratively. First, a forward projection of the volumetric object creates an artificial raw data. The second step is to compare the artificial raw data with the real measured raw data in order to find a correction function [22]. The latter is finally back projected onto the volumetric object estimate. Iterative methods also allow inclusion of some specific knowledge as to the system geometry and detector response in order to improve the reconstruction results. Iterative algorithms are rarely implemented and adopted to date.

The duration of the reconstruction process is in the range of 1-20 minutes depending on the number of collected projections and the computation power of the informatics infrastructure. In most industrial CT the reconstruction is automatically conducted so the operator is not involved.

2.2 CT workflow for dimensional metrology

The typical workflow of CT measurement for dimensional metrology requires a series of hardware and software steps. Some of the steps are typically found in any imaging process based on X-rays, other ones are specifically required for dimensional metrology [6]. An example of CT workflow is reported in Figure 2.5.

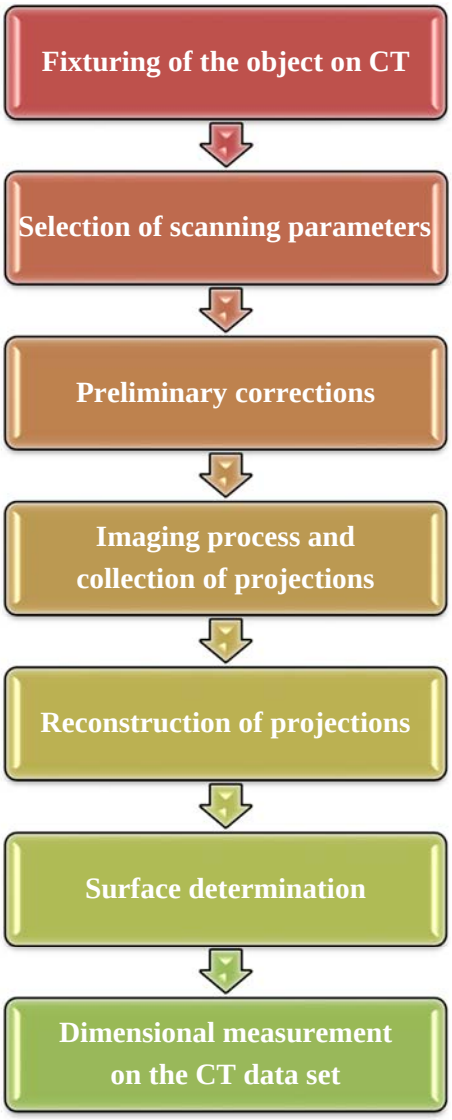

Figure 2.5. A flow chart of a typical dimensional CT measurement process

The first step to conduct is to identify a proper fixture holding the parts during scanning. The selection of the fixture should be based on the workpiece materials and size as well as the thermal condition within the cabinet.

The second step is to select the scanning parameters and to conduct preliminary corrections. A proper set of scanning parameters should allow imaging of a workpiece at any angular positions. Current, voltage, number of projections, magnification, integration time, and detector gain are the principal scanning

parameters. Scanning parameters are not independently connected to each other. For example, the selection of current and voltage defines the focal spot size which in turn constrains the size of the voxel. Preliminary corrections describe a class of activities that are conducted to minimise the impact of CT and environment on the imaging process. The main corrections are: detector correction, axis correction, and scale error correction. The detector correction is conducted with aim of reducing the variations in the pixel-to-pixel sensitivity of the detector [23][24][25]. Depending on the correction approach, the detector correction is conducted either on a scanning basis or on a monthly basis. The axis correction is used to take into account any changes in the kinematics of the CT occurring over time. This correction is conducted on a weekly basis in metrology CT. The scale error correction enables to establish a relation between voxel size and the metre [26]. This correction is conducted on a scanning basis. The presented corrections are conducted in any industrial CT but with speciation attention in cases where CT is used for metrology applications.

After having conducted all preliminary steps, the CT imaging can be conducted and the all projections are subsequently reconstructed as explained in Section 3.2.1. The reconstructed 3D object is composed of voxels where each single voxel represents a local attenuation of the object. The reconstruction software packages may also provide further tools for correcting residual imaging errors which could not be removed using preliminary corrections.

Once the reconstruction is done, the identification of the surface of the objected represents the next stage. The determination of the surface can be based on different approaches which are termed thresholding [27][28][29], edge-based [27] [30], and region-based [27] methods. Thresholding methods, which represent the most used and implemented methods, define a surface by comparing the grey level values of the reconstructed volume to one or more threshold values. As a consequence, grey values below the thresholds are assumed to belong to the background, while grey values above the thresholds are assumed to belong to the foreground. The threshold values are estimated from the histogram of grey values using methods, namely shape-based [31][32][33] and function-based [34]. Shape-based techniques quantify the thresholds based on the shape of the histogram. Function-based methods find the thresholds because of optimization of a mathematical function being fitted to the grey values. Thresholding algorithms represent the most popular way of segmenting. Thresholding algorithms based on a single threshold ensure fast segmentation but rather inaccurate. The thresholding algorithms based on a multiple thresholds deliver high accuracy at cost of long computation time. The thresholding algorithms based on a single threshold are usually used for materials characterisation, while those ones based on multiple thresholds are used for metrology. Region-growing methods segment a reconstructed volume by connecting voxels having similar image brightness across the reconstructed volume. Edge detection methods define a surface by identifying the most different voxels in the volume which are assumed to coincide with the boundaries of the object. Edge and Region-growing methods approach the determination of surface from two opposite directions. Region-growing methods and Edge detection methods are less adopted in CT for metrology than thresholding methods.

The CT workflow for metrology concludes with the inspection that can be conducted using either part-to-CAD comparison or substitute features. Part-to-CAD comparison is based on overlying the segmented volume with the CAD model. The alignment between the segmented volume and the CAD model is based on best fit. A colour-coded indicates the deviations with respect to the CAD. Part-to-CAD comparison can also be used as rough alignment and substitute features are used for the final evaluations. An example of inspection based on Part-to-CAD comparison is shown in Figure 2.6a. The figure shows all the dimensional differences between the actual CT surface and the CAD model by using colours. Green represents the areas where the CT measurements are in agreement with the original CAD model, with tolerances ranging from - 0.001 mm to + 0.001 mm. Yellow denotes the areas where the CT measurements are larger than the original CAD model. Blue indicates the areas where the CT measurements are instead smaller. Substitute features represent elements created by fitting the measured points. The most popular fitting approaches are: Least square, *LS*, Maximum inscribed fitting, *MI*, and minimum circumscribed fitting, *MC*. *LS* gives a substitute feature minimizing the sum of the squares of the offsets of the measured points. *MI* produces a substitute feature that has no measured points lying inside it. *MC* gives a substitute feature that has no measured points lying outside it. An example of inspection based on substitute features is shown in Figure 2.6b. The figure shows two fitted planes together with their coloured views showing the distribution of the fitted points with respect to the respective fitted features. Green represents fitted point with small deviations from their substitute feature. Yellow denotes any fitted point showing positive and wide deviations from their substitute feature. Blue indicates fitted points showing negative and wide deviations from their substitute feature. In precision assemblies, *MCC* and *MIC* are widely used to ensure functionality of assemblies.

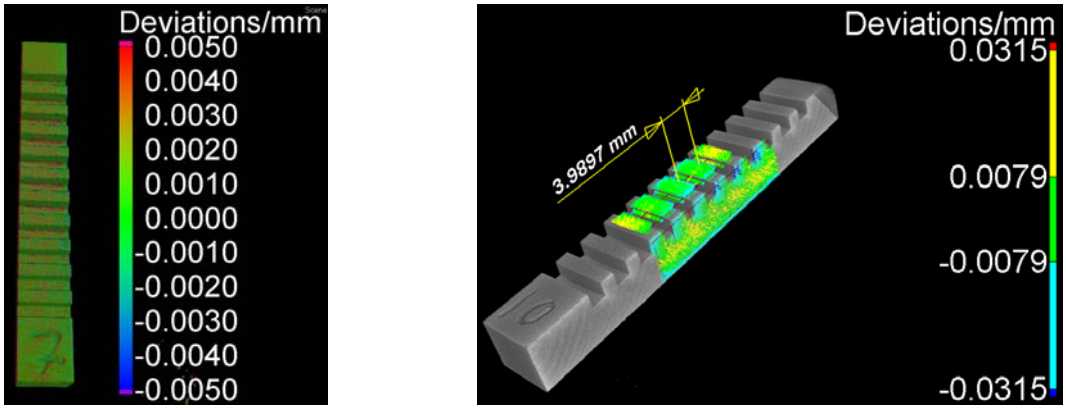

(a) (b)

Figure 2.6. (a) Part-to-CAD comparison inspection and (b) Substitute- based inspection showing two planes least square fitted on a miniature step gauge to measure a distance between flanks. The substitute features were based on 10000 equally distributed points. The imaged object is an aluminium step gauge

2.3 Influence factors in dimensional CT

There is a large variety of factors influencing the performance of CT. The German guideline VDI/VDE 2630-1.2 [35] provides a thorough overview of the factors impacting the measurement workflow. The influence factors can be split into five groupings of parameters: system, workpiece, data processing, environment and operator. Table 2.2 shows the influence factors that are responsible for influencing the performance of any CT. The presence of each influence factor can be significant or negligible depending on the type of measurement task.

Table 2.2. Influence factors in CT for metrology

Group	Influence factors
CT system	X-ray source X-ray detector Positioning system
Data processing	3D reconstruction Threshold determination and surface generation
Workpiece	Material composition Dimension and geometry Surface texture
Environment	Temperature Vibrations Humidity
Operator	Workpiece fixturing and orientation Magnification X-ray source settings Number of projections and image averaging Measurement strategy

2.3.1 CT system

An industrial system is composed of three main components: (i) an X-ray source, (ii) an X-ray detector, (iii) positioning system. The performance of each of those components impinges upon measurement. The accelerating voltage, filament current, focal spot size, target material and transmission window material all have significant effects on the final output of an X-ray source. The X-ray voltage determines the energy of the electrons. Changing the X-ray voltage modifies the spectrum, by increasing the average photon energy. The X-ray voltage influences the contrast between low density materials and the background noise level. The filament current controls the amount of electrons bombarding the target material. The more current flowing through the filament, the greater the emission of electrons

is. However, there exists a point at which the emission is at maximum. This is called saturation. Increasing the current through the filament after the saturation point would shorten the life of the filament or abruptly break it. Both current and voltage influence the focal spot size that represents the smallest diameter of the electron beam generated in the X-ray source. The spot size lies in the micrometre range and increases with increasing power to prevent the target from melting, evaporating and being subject to plastic deformation. In industrial CT, the focal spot is constant in the range of 6 W to 9 W and then increases at a rate of 1 µm W^{-1} [36]. Figure 2.7 shows a typical relationship between X-ray power and X-ray focal spot size of a microfocus X-ray source used for non-destructive inspection. X-ray power levels below 9 W result in a spot size of 8 µm, X-ray power levels ranging from 8 W to 16 W yield a spot size of 20 µm. A spot size of 40 µm characterizes the investigated X-ray source at power above 16 W.

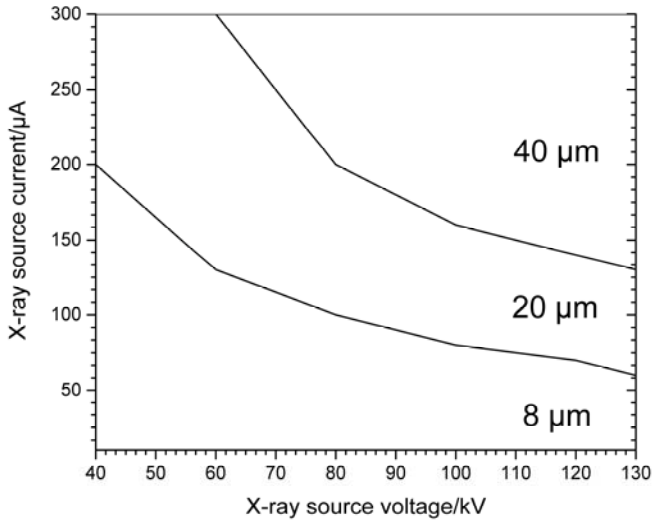

Figure 2.7. Relationship between X-ray power and X-ray focal spot size of a microfocus X-ray source used for non-destructive inspection. The operational range of the source is only represented. (Courtesy of Hamamatsu Photonics K.K).

The shape of the X-ray spectrum also depends upon the target material and its thickness. A tungsten target is the most widely used in industrial CT because it has a high atomic number, which increases the intensity of the X-rays, and because it has a very high melting point (3687 K), low rate of evaporation and mechanical proprieties that are almost independent of operating temperature. Targets made from low atomic number elements, such as copper and molybdenum, are well suited for imaging low absorption workpieces with high contrast. Tan [37] investigated the extent to which the target material influences dimensional measurements. The investigation was conducted using two different materials. Figure 2.8 shows that the choice of target material has a clear influence on the dimensions of a set of 2 mm diameter spheres, and yet that the tungsten target yields better imaging at powers used in industry.

In the case of transmission X-ray sources, the target thickness also influences the intensity of the generated X-rays. If the target thickness is smaller than the average penetration depth of electrons [38] electrons can pass through the target without interaction. Consequently, the X-ray emission will also be small. Increasing the target thickness, X-ray attenuation also increases during the penetration of X-rays

through the target. Ihsan et al. [39] stated that the X-ray intensity increases with the target thickness until a certain point at which the intensity abruptly decreases due to the increasing X-ray attenuation occurring during the penetration of X-rays through the target. The surface texture of the targets has also a consequence on the spectrum generated because it locally modifies the amount of material to be penetrated [40].

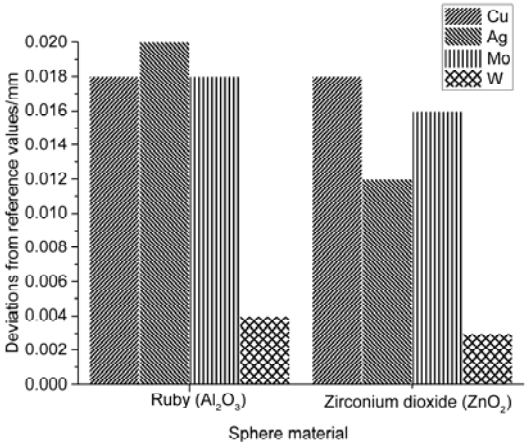

Figure 2.8. Comparison between contact coordinate measuring machine diameter measurements using two spheres of different materials: ruby sphere (Al_2O_3) and zirconium dioxide (ZnO_2) and four material targets: copper (Cu), molybdenum (Mo), silver (Ag) and tungsten (W). Each bar represents the average value of four CT measurements. A power (18 W) and voxel size (30 μm) were used throughout the course of the investigations [37]

There are many parameters affecting image quality in detectors. The important parameters include pixel pitch size, number of pixels, integration time, linear dynamic range, spectral response, and the detector quantum efficiency (DQE). The pixel pitch size has an impact on the spatial resolution and signal-to-noise ratio (SNR) [41]. Small pixel pitch sizes improve spatial resolution, making the detector unsharpness, which is of the order of two times the pixel size, negligible. Spatial resolution represents the ability of a CT to distinguish between intensities at closely spaced points. Large pixel pitch sizes result in better SNR as they present high fill factors, representing the fraction of the pixel area that is sensitive to light. For a fixed sensor frame size, decreasing the pixel size increases the number of pixel elements. This increase yields higher spatial sampling and a potential improvement in the system's modulation transfer function (MTF), provided that the resolution is not limited by other factors, such as the X-ray focus spot size and shape. Reducing the detector pixel size consequently reduces the amount of photons per reconstructed voxel. As a result, longer inspection times and, therefore, scanning times are necessary. A large number of active pixels generates a considerable amount of data, which are often not manageable in common workstations. A possible way around this data size issue is to adopt image binning, which combines adjacent detector pixels into a single effective pixel within the detector (hardware binning) or combines digital values from adjacent pixels in an acquired image (software binning). One major limitation of binning is saturation, which is the point at which a pixel cannot collect further information. Any charge beyond the saturation value will be truncated and the final pixel intensity will reflect the maximum pixel value rather than the actual value. Integration time is the lapse of time during which

the detector collects incoming X-rays. The integration time typically ranges from milliseconds to a few seconds. The linear range represents the range over which the sensitivity of the detector is almost constant. A constant sensitivity ensures the radiation intensity and the grey-scale values are linearly related. Flat panel detectors lose the linearity at pixel intensities of 75 % to 90 %, depending on noise, of the total dynamic range, representing the maximum extent of signal variation that can be quantified by the detector. At the extreme of the linear dynamic range, detectors may suffer from saturation causing distortion. The sensitivity of a detector depends on the sensitivity of the photodiode array near the peak emission wavelength. For detectors equipped with scintillators made from caesium iodide doped with thallium CsI(Tl), the photodiode should show a good sensitivity between 350 nm and 700 nm. The DQE describes how effectively a detector can transfer the energy of the incident X-ray beam out of the detector [42]. The DQE is generally expressed as the ratio of the variance of detector output to the variance of an estimate of the detector input. The DQE can be expressed as:

$$\mathrm{DQE} = \frac{\mathrm{SNR}_{\mathrm{out}}^2}{\mathrm{SNR}_{\mathrm{in}}^2}. \tag{1}$$

Here $\mathrm{SNR}_{\mathrm{in}}$ and $\mathrm{SNR}_{\mathrm{out}}$ are the input to the detector and the output from the detector respectively. $\mathrm{SNR}_{\mathrm{in}}$ and $\mathrm{SNR}_{\mathrm{out}}$ are both squared because they are assumed to be the standard deviation values of the detector input and output, respectively. The DQE is always smaller than unity. Compared to other performance metrics, the DQE allows the simultaneous measurement of the signal and noise performance of an imaging system at different spatial frequencies. The DQE values decrease as a function of energy, due to the decreased absorption of X-rays from the scintillator at higher energy levels. Geometry and atomic composition of the detector linearly influence the DQE as stated by Tan [37]. The resolution and sensitivity of flat panel detectors to X-rays also depend on the scintillator thickness. In 2003, the International Electrotechnical Commission (IEC) published a standard method for measurement of the DQE as a function of spatial frequency [43].

The geometry of industrial CT is defined by the relative position and orientation of the three components: the X-ray source, rotary table and X-ray detector. Figure 2.9 depicts the experimental geometry of a circular trajectory cone-beam CT set-up. In an ideal configuration, the X-ray focal spot, the axes of the rotary table and the centre of the detector should fall in a straight line [44]. Additionally the axis of the rotary table should be parallel to the detector and be projected onto the central column of the detector [44] which can lie on a pixel or on the edge between adjacent pixels. Whenever those conditions are not simultaneously satisfied, this will give measurement errors due to geometrical misalignments. In order to quantify these misalignments, nine parameters are necessary, which are the focal spot offsets along X and Y axis, (s_x, and s_y), the detector offsets along X, and Y axis (d_x and d_y), the perpendicular distance between the X-ray source and rotation axis, L_{SW}, the perpendicular distance from the X-ray source to detector, L_{SD}, and finally three orientations of the detector (ψ, φ and σ). The rotation ψ, also known as

skew, is an in-plane angle. The rotations, φ and σ, are two out-plane angles, known as tilt and slant, respectively. In this description, the misalignments of the rotary table are converted to those of the detector [45]. Moreover, this description assumes that all the components of CT are rigid bodies, thus their deformation is negligible.

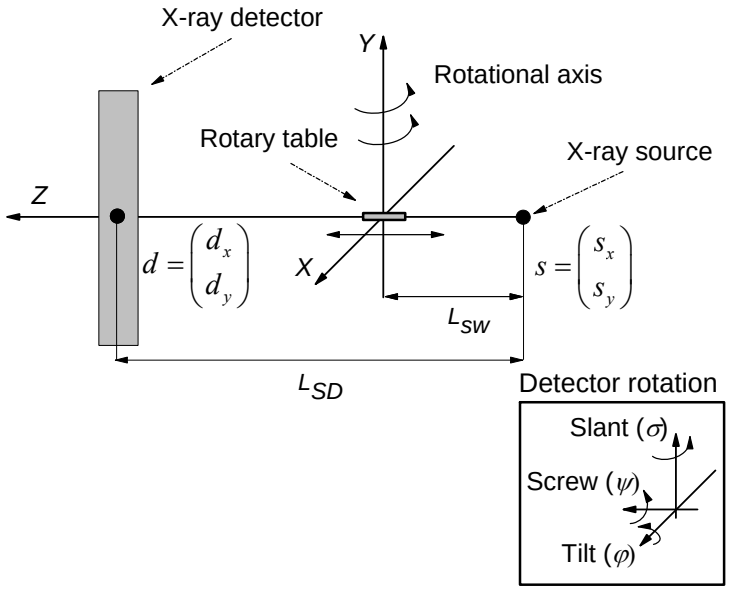

Figure 2.9. Illustration of CT geometry with the nine parameters

Misalignments associated with the X-ray source are usually due to difficulties in acquiring its centre coordinates from the projections of a calibration object, including fiducial markers, i.e. small metal balls. The position of the markers is subject to uncertainty whose magnitude depends on the CT, scanning parameters, environment conditions, etc. As a result, the centre coordinates of the source are subject to an uncertainty, which is at least as large as the calibration object according to the propagation of error. Kumar et al. [46] investigated the simulated effect of the source position on the accuracy of measurements by using two ball bars of different size. The results show that varying the position of source leads to either overestimating or underestimating distances, depending on the voxel size used for imaging. By increasing the voxel size, the impact of source position decreases, and vice versa. Source misalignment can also be caused by the X-ray filament that is not symmetrically bent into a V-shaped hairpin.

Positioning errors along the z-axis influence the measured dimensions, yielding maximum length measuring errors in the order of 0.15 - 0.20 % for size measurements (e.g. a nominal length of 10.00 mm will result in a measured length in the range of 9.98 to 10.02 mm). Tilting errors of the rotary table are known as wobble and eccentricity. Eccentricity describes the displacement of the geometric centre of a rotation stage from the rotation axis in the plane defined by bearings. Wobble represents the tilt of rotation axis during rotation and is quantified with respect to a reference surface. The error deviations appear to have similar trends for all three positions but different sign. The selected measurands are strongly underestimated when the workpiece is placed at position 1, while the measurands appear to be both underestimated and overestimated for the other positions. From the figure is can also be seen that measurements performed in the central X-ray beam (X-ray beam perpendicular to the detector, yield the

highest accuracy). Wobble and eccentricity similarly impair the structural resolution as they can be deemed fluctuations of the focus spot across the detector.

Kumar et al. [46] investigated the influence of detector misalignments by using simulations. The results showed that out-of-plane tilts are more important than the in-plane tilt ψ. The effect of the out-of-plane tilt φ is to magnify the projections in the vertical direction, while σ magnifies the projection in the horizontal direction. The out-of-plane tilts are somewhat difficult to remove, even after physical adjustments. Errors in the detector position are not a major problem regardless of the size of the workpiece. A detector can be misaligned by more than one rotation angle simultaneously. Geometrical errors of the detector can also be caused by manufacturing errors.

2.3.2 Workpiece

Any workpiece can be scanned, provided that it fits inside the detector and that X-rays are able to penetrate it with sufficient contrast. Table 2.3 reports the typical maximum penetrable thicknesses for CT at different voltages.

Table 2.3. Typical maximum penetrable material thicknesses for common industrial materials. All values in the above table ensure a minimum transmission of around 14 % [47]

X-ray voltage	130 kV	150 kV	225 kV
Steel	< 5 mm	< 8 mm	< 25 mm
Aluminium	< 30 mm	< 50 mm	< 90 mm
Plastic	< 90 mm	< 130 mm	< 200 mm

Higher penetration lengths are achievable by accepting lower transmission values. The overall size and mass of the workpiece also introduces some limitations in the use of CT. Industrial CT withstands workpiece masses of up to 100 kg. The part mass also has a role in the rotary table performance as it modifies the response of the rotary table with respect to the performance stated by manufacturers. The effect of workpiece mass on the rotary table performance is difficult to predict as it depends on several factors. In the cases in which CT is used for metrology, the workpiece weight should not exceed 5 kg (≈ 60 N) in order to maintain mechanical specifications while moving. A further workpiece feature influencing the CT performance, especially for metrology, is surface texture. Figure 2.10 shows the influence of surface texture on evaluations compared to that on a tactile coordinate measuring machine (CMM). The CMM is less affected by the workpiece surface due to the intrinsic filtering of the probing sphere. The bigger the probing sphere, the less the impact of surface texture. Aloisi et al. (2016) found that surface texture gives surface offsets of about *Rz/2* for additively manufactured parts. The *Rz* parameter is the mean maximum height of a measured profile (the mean of five sampling lengths). Bartscher et al. [10] also quantified the systematic error due to the surface texture as a percentage of *Rz*. Aloisi et al.

[48] reported that smaller surface offsets are expected for workpieces having surfaces with higher bearing area curves (i.e. the material is more distributed on the peaks) than workpieces having lower bearing curves (i.e the material is more distributed on the valleys). The bearing area curve, also known as the Abbott-Firestone curve, is the cumulative probability density function of the surface profile's height and can be quantified by integrating the profile trace [49]. In the literature, the effect of surface texture is considered either as a systematic error or as an uncertainty contribution.

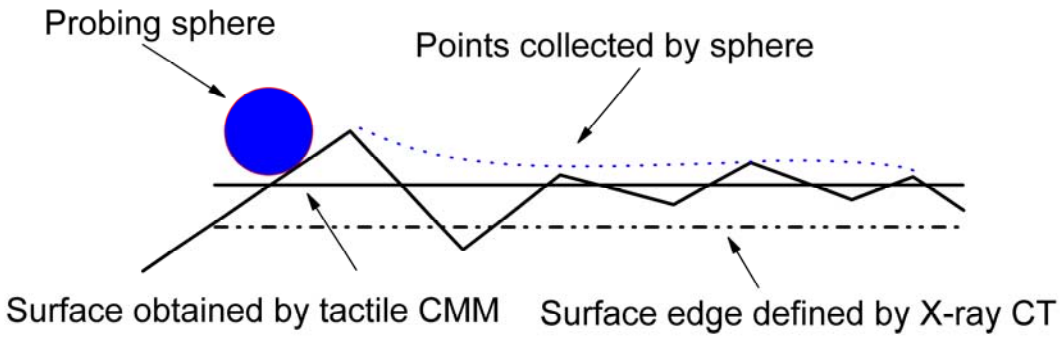

Figure 2.10. Illustration of the influence of surface roughness on the difference between CT and tactile CMM

2.3.3 Environment

Accurate dimensional metrology generally calls for measurements to be performed at 20 ºC with variations in the order of 1 ºC or less. Temperature variations cause dimensional changes in both the workpiece and the CT, depending on the material thermal proprieties. For example, a 1 m long bar of steel expands by approximately 0.012 mm K^{-1} in temperature, while one made of plastic by more than 0.05 mm K^{-1}. Temperature variations in CT modify the kinematics of all the components involved by further magnifying the geometrical errors. The temperature also influences the electronic components by generating thermal agitation inside an electrical conductor at equilibrium. The major effect of thermal agitation is to modify the detector response and to corrupt the detector calibration, usually at the expense of accuracy of geometrical measurements. If a CT measurement is started as soon as the workpiece is placed on the rotary table, temperature changes during measurement may produce significant measurement errors. A good solution is leave the workpiece and its fixture within the CT cabinet for some time (e.g. 1-2 hours). The usual humidity range requirement for metrology laboratories is 40 % to 60 % relative humidity without condensation. A stable humidity is important to prevent oxidation or rust on the measurement equipment, but also to avoid workpiece expansion. When polymer parts are exposed to moisture, water molecules will diffuse into the matrix, by passing through the open structure of the polymer. Moisture can decrease the surface free energy and simultaneously increase the volume of the polymer. Compared to other environmental considerations, humidity is a minor contribution. Shock and vibration have an impact on accuracy when they exceed the maximum levels of vibration a CT can withstand. Vibrations are often caused by heavy-duty machine tools, located in adjacent rooms. A sudden fracture of the filament can occur under the influence of shock or vibration. Vibration also modifies

the alignment between the X-ray focal spot, the axis of the rotary table, and the detector with a direct repercussion on the success of the measurements.

2.3.4 Post-processing of CT data

The efficiency of the reconstruction process based on filtered back-projection algorithms is influenced by the used filter. The simplest filter model is a ramp, also known as a Lak filter [50]. This filter compensates the unwanted blurring, provided the image quality is very high. The disadvantage of the Lak filter is that it boosts high frequencies, which bring unwanted information into the final reconstruction volume. Several other low-pass filters with high frequency cut-offs have been developed [50]. The Shepp-Logan and Butterworth filters yield the least smoothing at any frequency [51], whereas the Hamming filter induces the strongest smoothing. Despite the smoothing effect, high frequency cut-off values have an impact on the structural resolution. Hamming and cosine filters typically reduce the structural resolution by up to 20 % [52] compared to the Ram-Lak filter. In the presence of low noise levels, all filters yield similar reconstruction outcomes and thus measurement results.

Surface determination for dimensional metrology is usually based on thresholding methods. Global thresholding methods, based on ISO 50 %, are the straightforward way to segment a CT data set and lead to accuracy in the order of voxel used. Local thresholding methods are capable of reaching sub-voxel accuracy, even in the presence of low quality data sets [53]. Several comparisons between global and local thresholding method have been conducted and all state that local thresholding approaches lead to more repeatable measurements than global methods [6]. Figure 2.11 shows a comparison between global and local methods by using a step gauge made from aluminium. The results show that a global thresholding segmentation results in deviations up to 6 µm compared to a local approach. Tan et al. [37] stated that local thresholding segmentation reduces down to 50 % the standard deviation obtained with global thresholding approaches. Stolfi et al. [54] reported that local thresholding approaches are highly repeatable. Borges et al. [53] also confirmed the sub-voxel accuracy of local thresholding methods for multi-material segmentation. All thresholding methods are influenced by the starting point, which represents the grey value intensity from which the segmentation process starts. Changing the starting points, even of a few grey values, results in surface offsets because of the absence of a sharp transition between grey values of the workpiece and background. Depending on the homogeneity of the grey value distribution, a transition can vary from a tenth of a voxel to several voxels.

Global methods are, however, more sensitive to the starting points than local methods in which the starting point is refined locally. Other surface determination methods, based on region-based segmentation [53] and edge-based segmentation [55], exist. Unfortunately, these methods are still in a state of evolution and, therefore, the range of applications is somewhat restricted. The impact of surface determination on the measurement depends on the feature investigated. Features such as diameters and

lengths are more sensitive to the determined surface than the distance between the centres of two spheres.

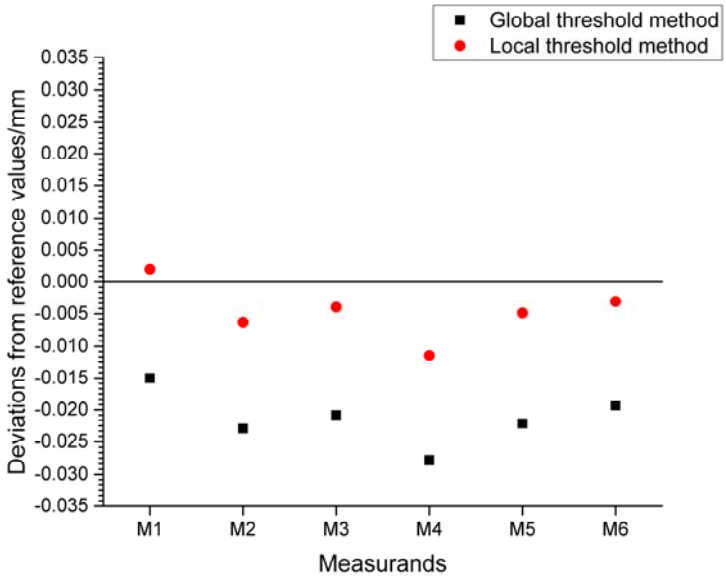

Figure 2.11. A comparison showing differences between Global (black squares) and Local (red circles) threshold method. Six calibrated lengths of a polymer step gauge were considered: M1 = 2 mm, M2 = 6 mm, M3 = 10 mm, M4 = 2 mm, M5 = 14 mm, M6 = 18 mm, and M6 = 21 mm. The lengths were based on plane-to-plane distances

CT volume data can be handled as either voxel models (volume models) or STL models (surface models). Voxel models are usually regarded as more robust than STL models that are more prone to meshing errors. The magnitude of the meshing errors depends on a series of factors such as the number of triangles used, linear and angular resolution, and the quality of data sets from which the STL model is generated. Linear resolution is expressed as a linear dimension and refers to the maximum distance that the surface of a STL model is allowed to deviate from the original voxel model. The angular resolution refers to the angular deviation allowed between adjacent triangles. Linear and angular resolution should be kept below the target measurement uncertainty. Image quality of data sets has an impact on the information accuracy of STL model. Inspections conducted on Voxel and STL models coming from high quality data sets generally result in similar measurement results. Inspections conducted on Voxel and STL models coming from low quality data sets result in very different measurement results, especially for geometrical measurands. The big advantage of STL models over voxel models is the relatively small size of the data to be handled due to the absence of volumetric information.

2.3.5 Operator

Workpiece fixturing and orientation, magnification, X-ray source, number of projections and image averaging, and measurement strategy are the key factors by which an operator may influence CT performance.

Workpiece fixturing and orientation

Figure 2.12 shows the influence of the two fixtures, a loose fixture and a tight fixture, on six length measurements. The results show an increase in measurement errors between 0.3 µm and 5 µm, depending on the position of measurand within the measured volume, can be obtained when a loose fixture is used. A good fixture should therefore be able to hold the workpiece, avoiding displacements and rotations during imaging. A good fixture should also have a very low absorption in order not to modify the spectrum. These two conditions are very difficult to achieve for very low absorption materials. Fixture materials such as polyurethane and polystyrene are mostly used for low absorption workpiece materials. A disadvantage of polymeric fixtures is the material relaxation and the thermal instability, both of which cause slippage. Epoxy resins are used for high abortion materials as well as for heavy parts.

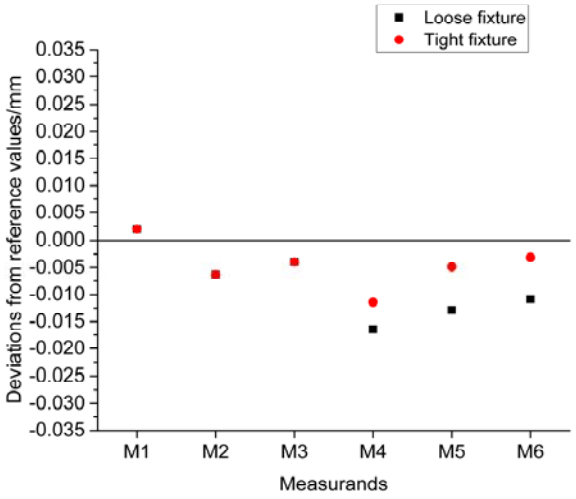

Figure 2.12. A comparison showing difference between a step gauge in a loose fixture (black squares) and in a tight fixture. Six calibrated lengths of a polymer step gauge were considered: M1 = 2 mm, M2 = 6 mm, M3 = 10 mm, M4 = 2 mm, M5 = 14 mm, M6 = 18 mm, and M6 = 21 mm. The lengths were based on plane-to-plane distances

The orientation of the workpiece has a considerable impact on the variation of the length of the way the X-rays pass through the object during scanning. In the presence of significant length variation and improper image reconstruction are experienced. Villarraga-Gómez et al. [56] investigated the link between orientation and measurement accuracy by using several workpieces and different materials. The authors stated that angles in the range of 10° to 40° lead to smaller measurement errors, including for

form measurement. Angular positions above 60° yield larger deviations. The impact of orientation becomes more and more evident for high absorption material such as steel. Angel et al. [57] reported that for steel step gauge measurement, errors at 90° are five times higher than those at 45°.

Magnification

The magnification can be expressed as follows:

$$M = \frac{L_{SD}}{L_{SW}}, \tag{2}$$

where L_{SD} is a distance between the source and the detector and L_{SW} is a distance between the source and the workpiece, as shown in Figure 2.13.

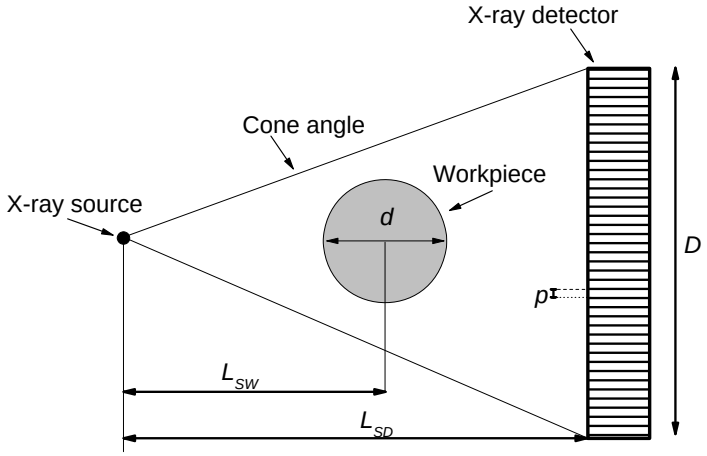

Figure 2.13. Geometrical magnification is determined by the source-workpiece distance L_{SW}, source-detector distance, L_{SD}, the detector width, D, the measuring volume, d, and the detector pixel size, p

Users obtain a small voxel size by selecting very low values for L_{SW} or high values for L_{SD} and thus a very large geometrical magnification. In order to make an accurate reconstruction of the volumetric data, the entire workpiece must remain within the field of view during the rotation. The maximum magnification, M_{max}, is limited by the ratio of the effective detector width D and the workpiece diameter d and can be expressed as:

$$M_{max} = \frac{D}{d}. \tag{3}$$

From magnification, the voxel size, V, can be derived, which is also related to the detector pixel size, p. The characteristic curve linking the three parameters is presented below:

$$V = \frac{M}{p}. \tag{4}$$

X-ray source settings

The choice of the proper voltage and current of the X-ray source for a specific measurement workpiece should satisfy two conditions. The first condition is that the X-rays are strong enough to penetrate the object at all rotation angles. The second condition is that the X-rays must not saturate at any rotation angle any part of the image to be used. Operators can easily satisfy these two conditions with simple workpieces, whereas they find it difficult to achieve the same aim in workpieces having large variations in the cross section. The voltage and current selected for a particular cross section may not fully penetrate the workpiece in directions in which the material being penetrated is larger and simultaneously to avoid detector saturation in the directions in which there is less material. As a result, some projections can be well-exposed and others badly-exposed. In order to have a uniform projection exposure, operators usually find a compromise, based on prior experience, between the X-ray penetrability and the detector saturation. Figure 2.14 shows how twenty operators selected X-ray source settings for two items used during an international comparison [58]. It can be seen that although the items are very different in X-ray absorption and size, very similar power levels were used for both parts.

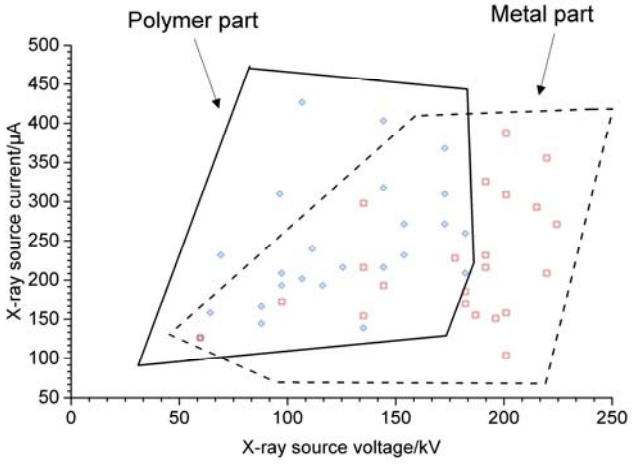

Figure 2.14. Current vs. voltage for polymer part (blue diamonds) and for a metal part (red squares) [58]

The situation described is even more complex for multi-material assemblies that simultaneously include low absorption and high abortion materials. Low energy X-rays are sufficient for lower absorption material. High energy X-ray beams are necessary for completely penetrating the denser parts. Multi-material assemblies having absorption coefficients close one another can more easily be imaged.

Measurement strategy

Dimensional measurements can be performed using actual-to-nominal com-parison or using substitute features. Actual-to-nominal comparison allows the highlighting of differences between a CT data set and its reference information by using a colour map. Each colour represents a different extent of variation between the scanned part and reference information, which can be obtained from a more accurate measuring instrument or from a nominal CAD model. Results of actual-to-nominal comparisons are directly influenced by the alignment process used to overlay the two data sets. Three families of alignment methods are available in in-spection software packages namely: best-fit alignment, iterative closest point alignment and non-iterative alignment. Best-fit alignment is a method that globally minimises the distance of every measured point to its reference, using an iterative least-squares fitting algorithm. All points are considered to be equally important in the alignment calculation. This simple equality condition may lead to errors in the presence of data sets with low quality. Iterative closest point alignment methods define an alignment based on selected features rather than points. Closed form alignment methods resolve the alignment by specific coordinates that the user sets. Changing alignment method affects mean values, even if the repeatability is similar. In many cases, alignment differences are also dependent on the coordinates of the CT data set relative to the reference data. Substitute features are mathematical geometries with no defect whose orientation and size are defined from the points measured on the surface of the workpiece.

Substitute features are affected by three parameters, namely the number of workpieced points, the distribution of points and the strategy of fitting. The number of points should be sufficient to have a sound representation of the geometric feature.

By increasing the number of points used for a given measurement, the resulting measurement will generally be more accurate, especially for complex shapes. In some cases, a large number of points is counterproductive as the probability of having outliers increases. The distribution of measured points should yield a uniform coverage of the feature being measured with a distance between points smaller than the expected defects. This condition will ensure that even small defects are measured. Regular or random distributions can be used depending on the nature of the object's surface texture. The fitting strategy also plays a role in the measurement accuracy, as many inspection software packages allow users to select a percentage of the measured points. Varying the percentage of points, will significantly change the resulting measurement. For example, form measurements on a ruby sphere can change on the order of several micrometres when increasing the percentage of points from 95 % to 98 %. Müller et al. [60] reported that the choice of a specific measuring strategy did not yield significant differences, provided that the data set presents a good image quality. Nevertheless, the authors noticed that the measurement strategy plays a role in the condition of low quality data sets. Similar results were reported by [54].

2.4 Image artefacts in dimensional CT

In CT, the term “artefact” is applied to any systematic discrepancy causing streaking, shading, rings and bands in a reconstructed volume that are not present in the original object. No reconstructed volume can be assumed to be free of discrepancies. However, different conditions can accentuate the impact of image artefacts on reconstructed volumes. This section presents the most significant image artefacts occurring in CT

2.4.1 Feldkamp artefacts

The Tuy-Smith sufficiency condition [61] states that exact reconstruction is possible, provided that all surfaces intersecting the object intersect the trajectory of the X-ray source at least once. CT based on circular trajectory can only satisfy this condition within a torus region, in 3D Radon space [50]. Outside the torus, shadow zones along the axis of rotation, z, exist, which make any reconstruction of the 3D object inaccurate, regardless of the detector resolution. Shadow zones can be seen as void regions in 3D Radon space for all images. Shadow zones generate rhombus-like artefacts in the reconstructed volume, commonly known as Feldkamp artefacts. Feldkamp artefacts are present at the top and bottom of reconstructed volumes. Asymmetrical distributions of those artefacts are also possible in a CT having local errors. The extent of Feldkamp artefacts varies with the cone angle, as shown in Figure 2.15. It can be seen that increasing the cone angle, increases the portion of volume corrupted. However, these errors are less significant when the cone angle is small, that is, when the distance from the X-ray source to the specimen is large in comparison with the object size. An investigation, conducted using a ball plate, showed that large cone angles may result in deviations from a CMM up to 30 μm. The presence of those artefacts leads to overestimating the sphericity of a sphere up to five times [62]. Sphericity is a measure of how spherical a workpiece is.

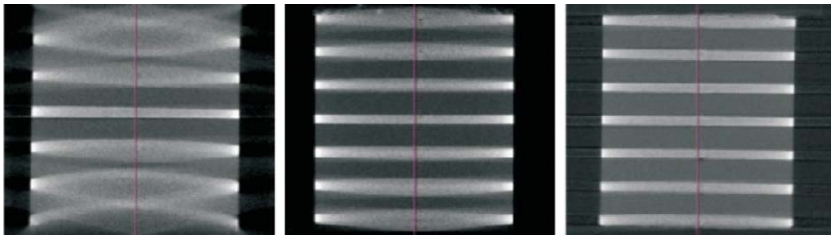

(b) (c) (d)

Figure 2.15. CT reconstruction slices acquired with a cone angle of (b) 30°, (c) 11°, and (d) 5°. The artefacts increases as cone angle increases [63]

Feldkamp artefacts are also caused by the longitudinal truncation owing to the limit of a cone beam in irradiating the whole measuring volume uniformly [64]. The non-uniform coverage means that the portion of the measuring volume lying closer to the detector is entirely sampled. The portion that is closer

to the X-ray source is scarcely irradiated. Because of the irradiation discrepancies, the reconstruction process cannot deliver correct results in the truncated region. The longitudinal truncation is only an issue for long workpieces. If the object is spherical, cone-beam projections can penetrate the object without significant data truncation.

2.4.2 Beam hardening artefacts

The assumption that the X-ray source emits photons having the same energy is rarely satisfied [65]. A real source provides an energy spectrum which has the general shape of a broad distribution between zero and a cut-off equal to the maximum energy applied to the electrons, known as peak energy. For example, a peak energy of 120 kVe produces X-rays varying between 10 kV and 120 kV with a mean energy of only one-third to one-half of the peak energy. Given that the mean energy is definitely below the peak energy, many of the photons comprising an X-ray beam will be characterised by energy levels far below the mean energy. Very low energy X-rays do not cause any problem because they are immediately absorbed within the target and X-ray window. Low energy X-rays are absorbed after the first few millimetres of material to be traversed, principally because of photoelectric absorption [66]. Consequently, the spectrum of the beam becomes richer in high-energy photons and harder to attenuate as it penetrates the workpiece. This nonlinear effect is referred to as beam hardening and shown in Figure 2.16.

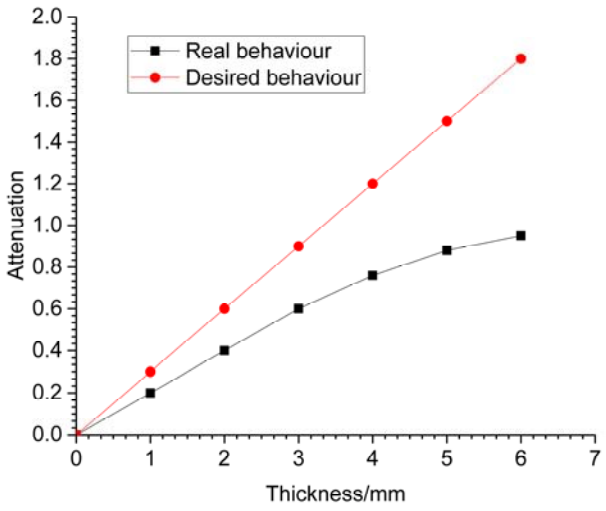

Figure 2.16. Relation between the X-ray attenuation and the penetrated material thickness with (line with red circles) and without (line with black squares) beam hardening effect

The result of beam hardening is an underestimation of the attenuation and a lowering of opacity values along the ray paths most suffering from this error. Examples of the typical artefacts in CT images arising from beam hardening are shown in Figure 2.17.

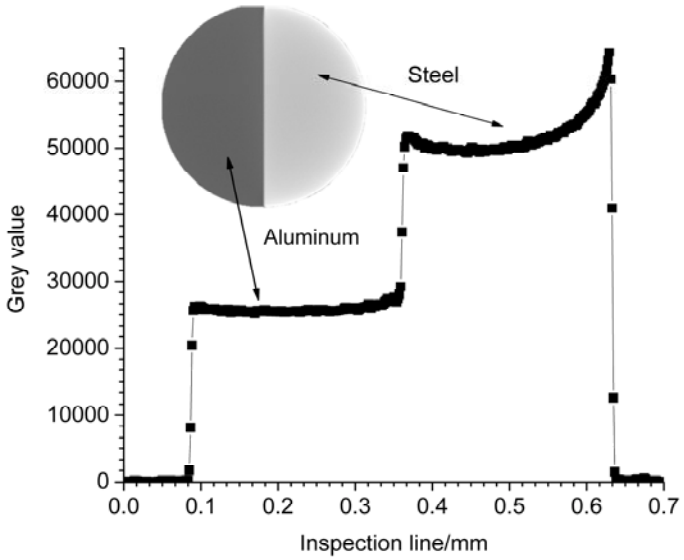

Figure 2.17. A grey value profile of a multi-material sphere with a diameter of 10 mm. The half-sphere made out of steel shows the cupping effect while the grey value profile of the half-sphere made out of aluminium showing no cupping effect. Grey values are mapped ranging from 0 to 65000 with background at 0. The data set was based on simulation

The cupping artefacts have the effect that the apparent material absorption decreases with the depth of material penetrated [67]. As a result, the X-ray intensity at the centre of a projection is smaller than the true values. Streak artefacts can be seen in scans including more workpieces in the measuring volume simultaneously. When an X-ray beam passes through two workpieces, it becomes harder than when it only passes through one material. The presence of beam hardening artefacts can also be seen within the grey value histogram of a CT data set as a severe distortion of the grey value peaks. Beam hardening occurs in any workpiece but its magnitude increases with the absorption and the thickness of the workpiece. Polymer workpieces do not suffer from beam hardening even in the presence of large wall thickness values. When beam hardening artefacts corrupt the datasets, a low frequency drop occurs on the MTF.

Beam hardening influences dimensional measurements by decreasing the inner dimensions and increasing outer dimensions [68]. This diametrically opposite effect may be explained by the fact that beam hardening modifies the inner and outer grey values of the background, influencing the contrast and surface determination. Beam hardening, however, induces larger measurement errors for outer dimensions than for inner dimensions due to the fact that the X-ray attenuation-thicknesses relationship is strongly non-linear for the first millimetres of material to be penetrated. Form and bidirectional length measurements are typically influenced by beam hardening, which spreads the distribution of fitted points by increasing the likelihood of having outliers. Unidirectional length measurements are not affected by beam hardening as they are not sensitive to the workpiece material [62].

The relevance of the problems caused by beam hardening resulted in a broad variety of artefact reduction methods. The latter can be grouped into three classes: hardware, linearization, and iterative. Hardware corrections use a physical filter on the X-ray source's output window. The presence of the filter

reduces the gap of intensity between the parts of the image formed by X-ray penetrating large path lengths and the parts formed by X-rays not passing through the object. Moreover, the filter removes low-energy photons, leaving Compton scattering as the dominant attenuation mechanism. In common CT, filter materials generally used are Aluminium, Copper, Silver, and Tin. The thickness of X-ray filters varies from 0.1 mm to several millimetres, depending on the material used. Since hardware correction reduces the overall amount of X-rays hitting the detector, an increase in noise may occur, unless the image exposure is increased to tackle the noise. Notice that the spatial resolution is also improved by beam hardening correction [69]. This is due to the fact that beam hardening enhances the edges, making two objects in an image easier to be discerned. The selection of a proper X-ray filter is still very difficult, especially in the presence of workpieces resembling a hollow cylinder. Several studies reported that any physical filter simultaneously reduces outward edge offsets and increases inward edge offsets.

Linearization methods aim to transform the measured polychromatic attenuation data into monochromatic attenuation data by means of a beam hardening curve [70]. Beam hardening curves can be identified either using a calibrated workpiece similar to the object being corrected or using preset beam hardening curves, based on polynomial functions of an order up to six, which are typically implemented within the reconstruction software packages.

Beam hardening curves based on a calibrated workpiece ensure higher efficiency than preset beam hardening curves, provided that the calibrated object and the workpiece to be corrected are made from same material and are both investigated under similar scanning and environmental conditions. In industry, preset beam hardening curves are more popular than beam hardening curves based on a calibrated workpieces. Preset beam hardening curves of second order polynomial curve are generally sufficient for low absorption materials such as polymer and thin aluminium parts. High absorption materials typically require polynomials of higher order. In multi-material workpieces, the selection of a well-suited linearization curve is even more difficult because it requires compensating the high absorption material without modifying the grey value distribution of the low absorption counterpart.

2.4.3 Positioning system artefacts

If there are misalignments in the X-ray CT, reconstructed images will suffer from artefacts. Geometrical artefacts vary from the doubling of edges to changes of magnification. The most popular approach for compensation of geometrical errors is based on reference artefacts having measurands independent of surface determination. Centre-to-centre distances represent the class of measurands used for scale error corrections because they are not biased by image artefacts such as beam hardening and noise. The reference artefact shall be imaged under similar scanning conditions as the workpiece to be subsequently inspected. It is of paramount importance that the positioning system is not moved between the two scans. In the following a description of the most used reference artefacts for scale error correction together with information regarding their materials, design, manufacture, and calibration is given.

1D reference artefacts

1D artefacts (see Figure 2.18) are characterized by having one or more lengths along one common axis. Ball bars and hole bars are the two types of 1D artefacts adopted for scale error correction. Ball bars are based on at least two reference elements mounted on a supporting frame. The frames of ball bars are usually based on materials having high thermal and mechanical stability as well as low absorption coefficients. Carbon fiber is the most used material for frames. Polymers and ceramics are also used as frames. MACOR® has been used due to its low density and low coefficient of thermal expansion. Polyoxymethylene, *POM*, polyphenylene sulfide reinforced using glass fibers, *PPS*, have been used for their low X-ray absorption coefficient. Ceramics should wherever possible be preferred to polymers due to their better thermal stability during calibration and application. The frames of ball bars are designed to withstand deformation coming from fixturing and handling.

Ruby (Al_2O_3Cr) represents the most used material for reference artefacts because it shows similar properties to aluminium, making them visible at different X-ray voltage levels. Silicon nitride (Si_3N_4) spheres are also adopted due to its high hardness, making the qualification process using tactile CMMs more independent of probing force. Silicon nitride spheres also show high transmission ratio of approximately 40%, making them visible at very low X-ray voltages. The thermal expansion coefficient of the silicon nitride spheres is smaller than ruby ones, which may represent an advantage in connection with the thermal stability of the reference artefacts. Other materials such as steel, titanium, and Zirconia Toughened Alumina are often used for spheres. Diameters ranging from 1 mm to 10 mm are typically used. The size of the spheres should always be selected taking into account their X-ray attenuation coefficient and the maximum power used available in CT.

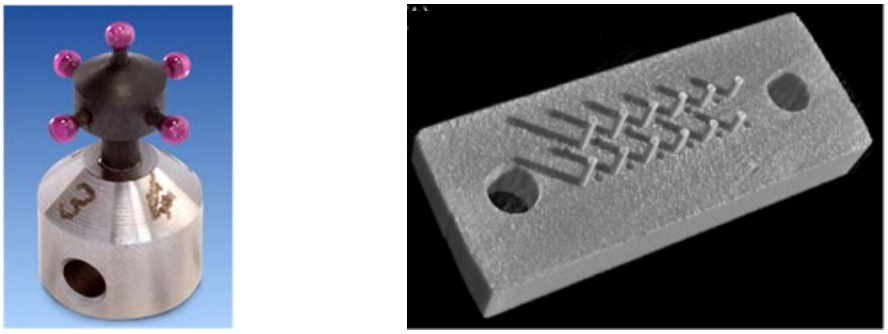

(a) (b)

Figure 2.18. 1D reference objects: (a) a multiple ball bar (Courtesy of PTB) and (b) a hole bar [72]

The connection between the frame and sphere is established using either adhesive joints or threaded joints. The adhesive joints can be external or internal. In external joints, the glue covers an external portion of the sphere. In internal joints, the glue is distributed on a surface of a blind hole. From X-ray prospective, both types of joints are quite equivalent. The use of adhesive connections may yield some concerns in connection with the effects of environmental factors on the stability of reference artefacts. Adhesive joints are susceptive to changes in humidity, leading to dimensional deformation in the order

of several micrometres. The extent of deformation depends on the amount of glue, the relative humidity level and the elapsed time. Nevertheless, it should also be kept in mind that reference artefacts are calibrated, used and stored under environmental conditions under which the humidity and temperature do not undermine the dimensional stability.

The threaded joints are used when ball plates are assembled using CMM probes. The threaded joints ensure high thermal and dimensional stability. The threaded joints also reduce the number of materials used for producing the reference artefacts. Threaded joints cannot be produced when carbon fibre is used as frame material. The reason is that the tensile strength in composite material comes from the continuity of the fibre reinforcement. As soon as the continuity is broken then the strength is highly compromised. Ball bars are multi-material workpieces (elements + frame), which may represent a problem for surface determination.

Hole bars are artefacts whose reference elements are machined within the frame. Aluminium, titanium, and steel are the most used raw materials for those artefacts. Aluminium is typically used for CT with an available energy below 150 kV while titanium and steel are used at higher power levels (> 225 kV). Attention should be paid to selecting aluminium alloys which do not contain alloying elements such as Lead and Bismuth, which yield local distortions of X-ray paths due to their extremely high absorption coefficient. Lead and Bismuth are commonly used to protect users from harmful X-rays. The dimensional and geometrical as well as surface accuracy of holes is generally lower than ball bars. Finishing is often a necessary step in order to improve microscale and macroscale accuracy.

The calibration of 1D artefacts is conducted using coordinate measuring machines. Tactile coordinate measuring machines are widely used as they ensure low calibration uncertainty. The number of points used for each sphere typically varies from a few points to thousand points. Although collecting a larger number of points using continuous probing paths is increasingly used, this may be counter-productive for flexible parts owing to sliding forces. The latter occurs during the sliding of the probing sphere on the surface of the workpiece during the scanning. Reversal method techniques are largely used during the calibration of 1D artefacts. In the absence of a complete symmetry of the hole and ball bars, partial reversal methods are used. Measurement uncertainties below 1 μm can be achieved for 2D artefacts when reversal method techniques are adopted. In cases of artefacts presenting adhesive joints, it is a good practice to correct the effect of the probing force on the measurement results. The typical procedure requires measurement of each element using at two increasing probing forces. Then assuming small displacements, the measurement results at a probing force of 0 N can be extracted by using a linear fitting method. The standard deviation values being associated with the slope and intercept of the found linear fit are considered within the uncertainty budgets.

1-D CT artefacts yield a limited amount of information per scan. As a consequence, a large number of scans are necessary to evaluate the cylindrical measuring volume of a CT.

2D reference artefacts

Hole plate, ball plate and calotte plates are the three types of 2D artefacts adopted for scale error correction. They include lengths distributed over two dimensions. An overview of 2 D-CT Artefacts is given in Figure 2.19.

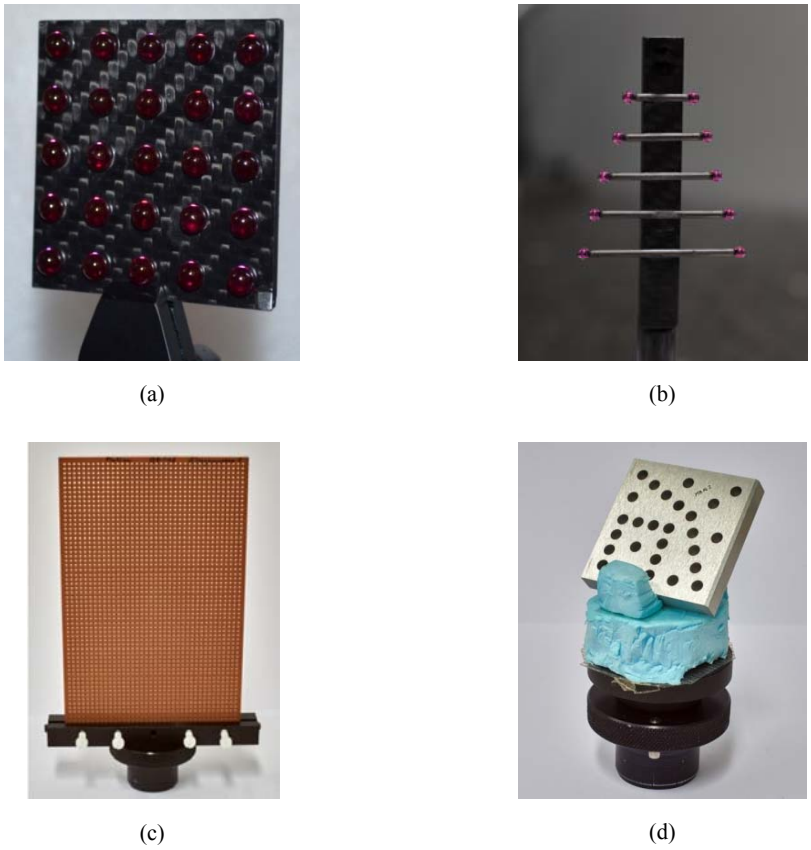

(a) (b)

(c) (d)

Figure 2.19. 2D reference objects: (a-b) two kinds of ball plates [26] [74], (c-d) two kinds of hole plates [62] [73]

2D artefacts result in larger number of individual element-to-element distances than 1D-artefacts. For example, a ball plate having 25 elements provides 300 independent element-to-element distances, whereas a ball bar with 5 elements just yields 10 independent distances. The mathematical relationship between elements and lengths is given by the binomial distribution. The distribution of elements can be either symmetric or asymmetric depending on the application. Symmetric patterns make the reference artefacts more stable because the weight is more uniform in connection with fixturing. Symmetric patterns make the X-ray absorption of the reference artefact constant as the absorption does not change between two angular positions, as shown in Figure. It can be seen that the grey value profiles are similar, including noise fluctuations. The visible systematic shifts of grey value profiles are due to the impossibility of exactly overlapping the two profiles. Symmetrical patterns allow fitting of different measuring volumes (different magnifications), making a single artefact suitable for a large variety of measuring tasks. A further advantage of symmetrical patterns is that they enable use of reversal methods.

Asymmetrical patterns provide variable penetration lengths at any angular direction. This may be an advantage when different penetration conditions need to be simultaneously obtained. The asymmetrical distribution of the elements provides seven spatial directions with five independent lengths each. This asymmetrical distribution represents a 2D artefact in agreement with the new ISO 10360-11 draft. The size of the hole plate is such that at least 5% of the X-ray radiation from the source can hit the detector in any projection direction. Manufacture and calibration procedures for 2D artefacts are very similar to those used for 1D artefacts.

3D reference artefacts

3D artefacts represent the highest source of information available in metrology. They are based on fiducial elements placed in such a way as to define patterns wrapping the measuring volume. A list of such artefacts is presented in Figure 2.20. The majority of 3D artefacts are based on spheres because they are invariant with rotation. Spheres can be probed even if they are tilted.

3D artefacts require thick frames to withstand the spatial distribution of elements, which may give problems in connection with the X-ray travel. Many 3D artefacts are manufactured using carbon fibre or ceramic rod mounted on a base. Bases are usually made from invar ensuring the thermal and mechanical stability of reference objects over a range of temperature. The thermal stability is very important in connection with the storage and use. Invar alloys have a coefficient of thermal expansion in the range of 0.6 - 1.2 $\times 10^{-6}$ K^{-1}, which up to 20 times smaller than ordinary steels. Some invar alloys can be blended to yield negative thermal expansion characteristics. Invar can be easily machined. Bases are also made from ZERODUR®, which is a zero expansion glass ceramic [75]. ZERODUR exhibits a constant coefficient of thermal expansion over the entire temperature range. The coefficient of thermal expansion is $\pm$ 0.01 $\times 10^{-6}$ K^{-1}, over the range of 0 - 50°C. Since, bases have high atomic numbers, leading to image inaccuracies, they are usually not imaged.

The calibration of 3D-CT artefacts is often time consuming because it may require multiple repositioning actions and complex probe configurations. Moreover, programming the 3D probe paths is also very difficult. The stability of the fixture becomes an important influence factor, especially when the rotary table is used. As a result, measurement uncertainties associated with 3D-CT artefacts are generally larger than the other artefacts. A well-established way to minimise the measurement uncertainty of 3D-CT artefacts is to distribute the elements in a symmetrical way.

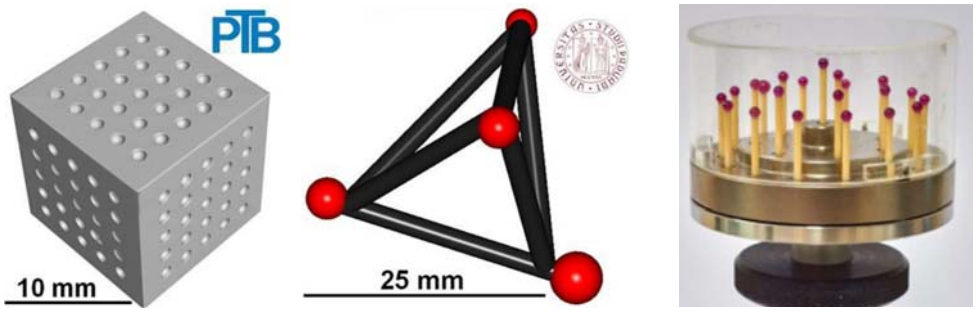

(a) (b) (c)

Figure 2.20. 3D reference objects: (a) Calotte cube [76], (b) CT tetrahedron [77], (c) multi-sphere standard Metrotom Check [73]

Although the use of reference artefacts efficiently minimises the extent of the scale errors, their use increases the scanning time, post-processing time and generated data. As a result, the CT throughput strongly decreases when the presented reference artefacts are adopted.

2.4.4 Noise artefacts

Image noise is unwanted variation of intensity across an X-ray projection. Five categories of image noise: random noise, quantum noise, electronics noise, round-off noise and reconstruction noise, can impair the CT measurement process. Random noise is due to fluctuations that have an approximately Gaussian amplitude distribution. Random noise can be neither predicted nor corrected. Thermal noise, also known as Johnson–Nyquist noise [80], is one example of random noise which charges carriers inside an electrical conductor, regardless of the applied voltage. Quantum noise is associated with the limited number of X-ray photons that are used for creating the voxel information. Mathematically, the number of photons, x, measured by a given sensor element over a time interval t is modelled by the Poisson distribution [81] as follows

$$P(x) = \frac{e^{-\lambda t}(\lambda t)^{x}}{x!}, \tag{5}$$

where λt is the shape parameter that indicates the average number of expected incident photons in the given time interval. Figure 2.21 shows what happens when the number of photons per voxel decreases with respect to the ideal condition. Reducing the amount of X-rays per voxel, the workpiece surface becomes noisy, thereby influencing the repeatability of surface determination and measurement inspections. For large numbers, the Poisson distribution tends to a normal distribution about its mean, and the elementary events (photons, electrons, etc.) are no longer individually observed, typically making quantum noise indistinguishable from Random noise. Electronic noise is due to the electronic circuits that inevitably add noise to signals. Analogue circuits are much more susceptible to noise than digital circuits, as a small change in the signal can represent a significant change in the information conveyed in

the signal. Round-off noise is a kind of error due to the limited number of bits used to represent a signal digitally. For example, the product of two numbers must be rounded up to the least significant bit available in the computer representation of the number. Additional noise comes from reconstruction and from geometrical errors of measurement equipment (see Section 5.1.1.3). In general, noise increases from the projection to the reconstructed image. An experiment conducted on a ruby sphere showed that noise present in a volume model is almost twice as much as the projection noise. Noise power spectrum (NPS) analysis is a useful image metric that provides a quantitative description of the amount and frequency of the noise fundamentally produced through CT imaging [82]. In metrology, noise influences both dimensional and geometrical measurements. In particular, geometrical measurements are greatly influenced by noise as even one outlier in the data set significantly influences the result [59]. Noise can be quantified conducting a probing error test assessing the diameter and form deviation of a calibrated sphere having negligible form and surface error. Probing error test should be conducted in condition reflecting the normal scanning condition. The results of the test may be used as an indication of systematic error caused by noise.

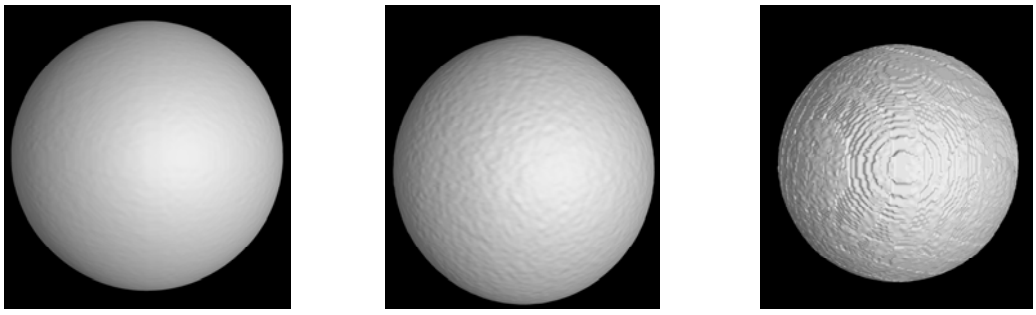

(a) (b) (c)

Figure 2.21. CT volumes simulated using (a) 3 10^9, (b) 3 10^5, and (c) 3 10^4 photons per voxel. Reducing the number of photons the extent of noise increases. The simulations conducted using a ruby sphere with a diameter of 10 mm

Two classes of methods, namely signal enhancement and image filtering can help in reducing the noise. Signal enhancement methods rely on the fact that quantum noise is signal-dependent (standard deviation varies with the square root of the signal). An increase in the X-ray voltage yields stronger X-rays passing right through the specimen to hit the detector, so that the signal becomes stronger. Increasing the X-ray voltage however reduces the contrast between low density materials and the background noise level. The X-ray current reduces the noise, by spreading the grey value histogram over the linear range of the detector. As a result, the grey values of the background and the workpiece appear to be well apart from each other, which leads to well-exposed projections at any angular position. If the voltage is high enough, then increasing the current is a better option than increasing the voltage further. It is however important to ensure that the selected voltage and current lead to grey values always within the linear range of the detector at any angular position. If they are close to the linearity limit or even in the non-linear range, the information value of the projections will be reduced. A good rule of thumb is to make sure all image pixels fall within the linear range of detector.

Image averaging is a further noise reduction technique working on the assumption that noise is random. By averaging more and more similar images random fluctuations will disappear with the square root of the number of images averaged. Image averaging requires that the frames to be averaged are sampled under similar conditions of temperature and X-ray source voltage in order to successfully scale down noise. Even small changes between projections can reduce the efficiency of this technique.

Image filtering tends to increase the SNR by reducing the extent of noise. The first method to reduce patter noise is the Flat field correction [83], which is a pre-processing method. The idea behind the method is to collect a number of projections, called reference projections, without workpiece in view at different power levels, including a dark level in which no X-rays are produced. The reference projections captured with the sensor in the dark aim to minimise a component of image noise which is the off-set from the average across the imaging array at a particular setting (temperature, integration time). The reference projections taken at increasing power levels aim to correct the variation of sensitivity between pixels for a uniform level of light intensity. The reference projections acquired are subsequently used as a mask to normalize the workpiece projections. The corrected projections can also be stored and used over a long period of time, provided that environmental conditions are stable over time. Attention should be paid to selecting an adequate number of projections in order to keep noise in the reference projections as small as possible. For example, if the reference projections and workpiece projections show a similar noise level, the corrected projections will have a higher noise due to the propagation of the error associated with the convolution. Although this procedure is well-suited for noise removal, it does not ensure against noise caused by variations in X-ray emission and temperature. Moreover, the flat field correction methods assume a strictly linear behaviour of the detector, which is not fully true when increasingly large regions of the detector are used. The flat field corrections are conducted before scanning and typically require between a few minutes and several hours depending on the scanning parameters.

2.5 Conclusions

This chapter has introduced CT for metrology and its fundamental elements such as source, detector, positioning system and informatics infrastructure. Information regarding the design and manufacture of any element of an industrial CT has also been presented.

A step-by-step description of the typical CT workflow for dimensional metrology has also been presented. Based on this, it can be observed that a CT measurement for dimensional metrology requires a large number of hardware and software steps. Some of the steps are typically found in any imaging process based on X-rays, others are specifically required for dimensional metrology. The description has also involved the preliminary corrections which have a large impact on the success of any CT measurement.

Influence factors affecting any element of a CT have been described and when possible quantified according to literature searches or own investigations. It has been seen that sizeable improvements in the accuracy of dimensional measurements can be obtained when the influence factors are reduced.

A description of image artefacts commonly encountered in CT has been given. The description has however been limited to image artefacts that will be considered in the following chapters of this thesis. In the next chapter, the concept of tolerance and its verification will be presented.

Chapter 3

Tolerances and their Verification

3.1 Part variation

All manufacturing processes are afflicted by variation, resulting in final products that will not look the same from time to time [84]. Several researchers have investigated into the reason of variation in manufacturing, leading to identifying five main causes, namely process, material, environment, operator, assembly [85].

Variations in the process are usually caused by the machinery repeatability, tool, and wear. The machinery repeatability describes how well a process replicates the same feature under unchanged conditions. Figure 3.1 shows two different manufacturing processes having different repeatability. The first process in the figure has a very high repeatability because the produced features lay in the centre of the target. The second process in the figure has low repeatability because the features do not lie in the centre of the target. Variations in manufacturing process caused by the tool arise from the impossibility of manufacturing tools exactly identical in terms of size geometry and surface. An example of tool variation is cavity-to-cavity variation in injection moulding, leading to significant differences between parts injected at the same time. Wear describes the degradation of the functionality of a manufacturing process over time. A well-known example of wear is the tool wear that can lead to loss of dimensional accuracy.

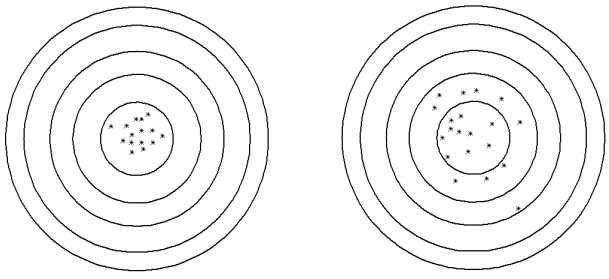

(a) (b)

Figure 3.1. Two targets describing two manufacturing processes (a) one showing high repeatability and (b) one showing low repeatability

If the materials used for producing components change, the final size and geometry of products will also change. The variation in the coefficient of thermal expansion (CTE) is an example of material

variation impairing the estimation of the thermal expansion of a component as the temperature increases. The variability of the CTE can be in the order of 20-30% of the nominal CTE value. Material variation becomes a relevant problem when more than one supplier is involved.

Environment variation includes any unpredictable changes in temperature, humidity, and vibration affecting the manufacture of a component. Changes in the temperature affect the geometry of parts while being manufactured because the material expands when heated. Changes in the temperature can also influence the performance of lubricants, accelerating the wear of cutting tools. Moisture is known to affect negatively numerous properties of polymers and their composites. Most hygroscopic materials under normal atmospheric conditions can absorb 0.1-0.2% water over an extended period.

Operator variations include improper handling and clamping of material, improper maintenance of the production equipment. The impact of the operator can vary depending on the level of automatization in manufacturing process.

Assembly variation results in that two mating parts, which individually meet the tolerance specifications, that not fitting together. The two key factors originating assembly variation are clamping force and assembly force. The clamping force represents the force that a gripper uses for holding an object during the assembly process. This force cannot be assumed to be constant due to errors in controlling the gripper, and in shape of a workpieces. As a consequence, the workpiece undergoes a deformation due to the variation of contact force at its interface, which cannot be quantified.

Two mating parts can be assembled in tight or loose ways. The extent of tightness or looseness is termed as fit. There exist three different classes of fits, namely clearance fits, transition fits, and interference fits. Clearance fits are used when two mating components need to be loosely held. Transition fits are used when two mating components need to be held precisely, yet not so tightly that it cannot be disassembled. Interference fits are used when two mating components need to be securely held together. Interference fits require some force for assembly because the two mating components have different sizes. The average pressure at the shrink-fit interface is usually calculated using FEM simulations [83] [84] [85]. The force of interference fits can, unfortunately, vary with the geometrical errors of the two mating objects to be assembled. In the case of perfect contact surfaces, the pressure at the interface of two mating parts is constant and consists of a radial compression and a hoop tension. When the contact surfaces present geometrical errors, there is a phase shift between the mentioned stresses. As a consequence, it is possible to have a mean pressure at the interface that is greater than in the case of perfect surfaces. To simulate interference fits in the presence of geometrical errors is not trivial because it requires having comprehensive information regarding the surface of two mating components.

Since the part variation cannot, in any case, be avoided, engineers have introduced the concept of tolerance. Tolerance defines the permitted amount of variation of a part which does not impair the functionality of the final product. By using the tolerances, a final product will perform as the designer intended, even though its components do not exactly reflect the drawing dimensions.

3.2 Geometrical Product Specifications (ISO-GPS)

Geometrical Product Specifications, ISO-GPS, defines an international language by which a designer can unequivocally express tolerances in the drawing. The ISO-GPS language is defined in a number of ISO standards developed by ISO Technical Committee 213 "Dimensional and geometrical product specifications and verification" [86]. With respect to traditional tolerancing methods, ISO-GPS avoids any specification ambiguities at inspection of a component by synergically linking dimensional and geometrical information of a component. Figure 3.2 shows an example of a drawing based on the traditional tolerancing method and the same drawing based on ISO-GPS. It can be seen that using ISO-GPS any tolerance is straightforward and does not show any ambiguities [87].

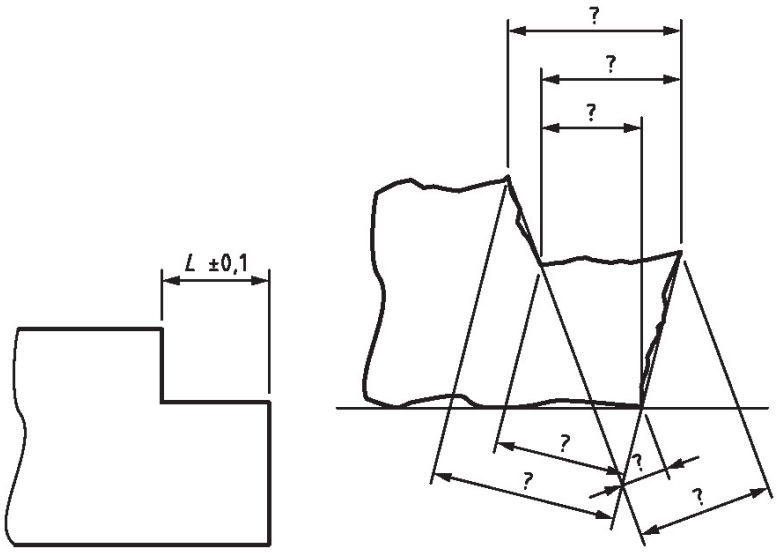

Figure 3.2. Example of a linear step dimension showing ambiguity due to the geometrical errors of two surfaces [88]

The major advantage of ISO-GPS is that it enables the locking of all the tolerances together in a coordinate system. This coordinate system is called datum system. A datum system of a workpiece consists of a series of features, known as datum features, that are defined on an object in such a way as to lock all six degrees of freedom of an object. Figure shows the most used datum features.

Depending on the number of degrees of freedom that a datum feature locks, the latter can be identified as primary, secondary and tertiary datum. The primary datum represents the datum locking as many degrees of freedom as possible. The secondary datum locks as many unconstrained degrees of freedom as possible. The tertiary datum locks the remaining degrees of freedom. Depending on the geometry of the part, two or three datum features are necessary to control its kinematics. Three datum features are requested for asymmetrical objects, while two datum features are sufficient for symmetrical objects. Figure 3.3 shows an example of well-designed datum system for a shaft that should be fit into a housing. The primary datum is defined as the straight line passing through the centre of two circles *F* and *R*. Those circles are defined on the surfaces of the shaft that will make contact with the housing at the

assembly. The secondary datum is defined on a surface of the shaft which will also make contact with the housing. The primary and secondary datum features do not produce any redundancy as they constrain different degrees of freedom of the shaft. Because of the axial symmetry of the shaft, two datum features are sufficient.

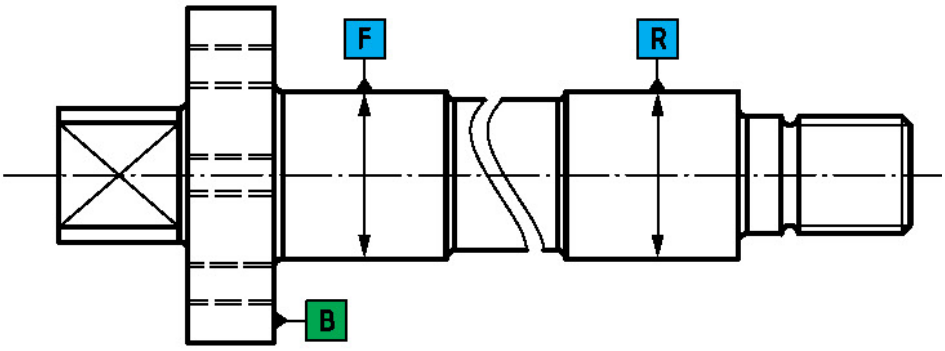

Figure 3.3. Global datum system for a shaft based on three different features [87]

In order to define a correct datum system, a designer should take into account how a component will interface with other components. The definition of datum systems should also consider how the part will be held at the inspection point.

ISO-GPS controls any geometrical characteristics of the component by using four types of tolerances describing any feature geometry, namely size, form, orientation, and location. Figure 3.4 shows the symbols coding all geometrical characteristics. Form tolerance prescribes that given a feature its shape must lay within two imaginary features apart. The distance between the two features is the defined tolerance. Examples of form tolerances are flatness, circularity, cylindricity and straightness. In cases of freeform features, their form is controlled using profile tolerance. Surface profile is a very flexible tolerance type because it can be used to create a form requirement for a surface that is neither plane nor cylindrical nor sphere. Position tolerances control the position of a feature with respect to the datum system frame. Concentricity and coaxiality are examples of position tolerances that are usually applied when the dynamical balance of a feature with respect to a rotation axis is of importance. Orientation tolerances control how much a feature may tilt relative to a datum system. Parallelism and perpendicularity are typical orientation tolerances. ISO-GPS specifications always refer to an inspection temperature of 20° C. This is important because any material expands with increasing temperature, and without a reference temperature size tolerance would cause ambiguity. ISO-GPS specifications apply to clean components, therefore chips, cutting fluids and other contaminants shall be removed before the component can be verified correctly.

Tolerances	Characteristics	Symbol	Datum needed
Form	Straightness	—	no
	Flatness	▱	no
	Roundness	○	no
	Cylindricity	⌭	no
	Profile any line	⌒	no
	Profile any surface	⌓	no
Orientation	Parallelism	//	yes
	Perpendicularity	⊥	yes
	Angularity	∠	yes
	Profile any line	⌒	yes
	Profile any surface	⌓	yes
Location	Position	⌖	yes or no
	Concentricity (for centre points)	◎	yes
	Coaxiality (for axes)	◎	yes
	Symmetry	⌯	yes
	Profile any line	⌒	yes
	Profile any surface	⌓	yes
Run-out	Circular run-out	↗	yes
	Total run-out	⌰	yes

Figure 3.4. Symbols for geometrical characteristics according to ISO-GPS [88]

3.3 Tolerance analysis

Since any component is characterized by its own tolerances, it is important to predict how the tolerances of different components accumulate and propagate through a final assembly. The accumulate variation is a key factor as it happens often that an assembly of components, which all met the tolerances specifications did not either fit together at assembly stage or ensure the required functionality. Tolerance analysis represents one of the most effective ways to quantify the cumulated variations affecting a final product. Simple methods of tolerance analysis include the worst case, WC, method and the root-square-sum, *RSS*, method. The *WC* method [89][90] does not consider the distribution of the individual variables, but only the maximum value of the tolerance of each component. By using WC method, a complete interchangeability of manufactured components constituting the final product can be achieved. The *WC* method avoids scrap and rework costs. The *WC* method is appropriate for parts that are not mass-produced and that have a very high unit cost. The *RSS* method [89] predict the variation in a final assembly by assuming the variation of each component as normally distributed. The variation of an assembly can then be quantified taking the square root of the sum of component variations. The *RSS* method is less strict because it guarantees only a partial interchangeability. Using The *RSS* method, 99.73% of all assemblies will meet the required assembly dimension. Although the use of normal distribution works

well, there are influence factors, e.g. tool wear, which cannot be represented using a normal distribution. The *RSS* method has therefore been amplified by taking into account non-normal distributions [91][92] [93]. In some cases, the *RSS* methods have also been amplified by taking into account the skewness and the kurtosis of the selected distribution [94] and by assuming non-centred process [95].

Other methods based on fuzzy logic [96], Jacobian-matrix [97] [99], T-maps [100] [101], and vector-loop [102] have also been developed for dealing with tolerance analysis. Fuzzy logic models describe the part variation using fuzzy numbers based on selected statistical distributions. Jacobian methods use kinematic chains to formulate the displacement matrices. Vector-loop-based model uses vectors to represent the dimensions in an assembly. The vectors are arranged in chains, representing those dimensions which are stacked together to determine the resulting assembly dimensions.

The tolerance analysis usually works well for solving many of the geometric problems encountered in the majority of assemblies, although they require several assumptions. One typical assumption is that all components present tolerances along only one direction. Another assumption is that the components expand in a linear fashion as the temperature increases. This assumption may yield problems in plane-like components. A further assumption is that components have a perfect form and do not change over time. The assembly process is therefore not fully reproduced, but extensively simplified.

3.4 Part verification using traditional coordinate measuring machines

Coordinate measuring machines, CMMs, represent the principal equipment used for verification of tolerances in industry. A typical CMM workflow for tolerance verification requires a series of steps. (see Figure 3.5). The first step is to select of the features to be inspect. This step is typically prescribed by the functionality requirements of the workpiece to be inspected. In some cases, a component could have some features that either cannot be measured on a CMM due to accessibility problems or could be more cost effectively measured using other equipment.

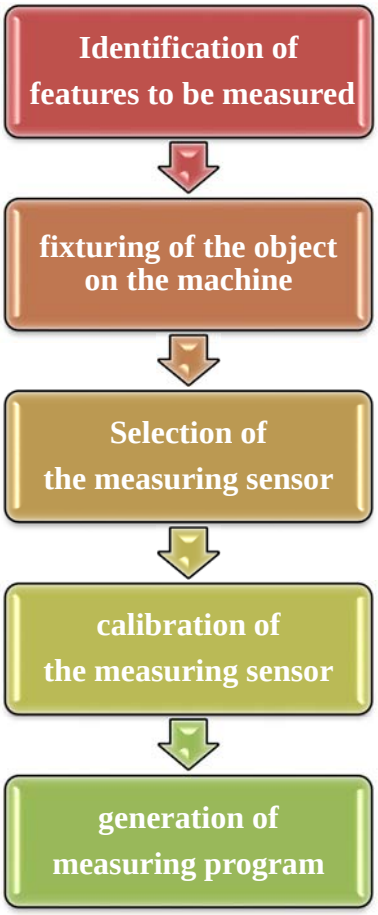

Figure 3.5. A flow chart of a typical CMM measurement process

The second step is the selection of measuring sensor and the fixture. Optical sensors guarantee no risk of damaging and contaminating the specimen because no contact is established during the measurements. Optical sensors ensure short inspection times as the latter is independent of the number of features to be inspected. The major disadvantage of those sensors is that they do not ensure accurate measurement when high aspect ratio features is being inspected. The aspect ratio represents the maximum depth for which a cylinder with a defined diameter can be assessed. A further disadvantage of optical sensors is that they are extremely sensitive to the surface finish of the component being measured. Tactile sensors physically characterise the feature using a sphere tip mounted on a stylus. The probing tip should be as small as possible to reach any features to be inspected. The probing tip should be as large as possible to reduce the impact of texture finish of the feature on the measurements. The stylus should be as small as possible to reduce any mechanical deflections. Each probe should be qualified before being used. The probe qualification improves the accuracy of some measurements, such as bidirectional lengths. By increasing the number of points used in the probe qualification, the resulting sphere diameter will be more accurate. The major drawback of tactile sensors is the probing force which may generate plastic deformation (see Figure 3.6). Although the contact probing force can be reduced down to 0.05 N, the effective moving mass of the entire probe is bigger. As a result, large contact force can be expected. Tactile and optical sensors can also be combined in order to combine their advantages. The fixturing of parts for

CMM measurement should be able to hold the part without reducing the accessibility to the part. In general, it is important to use a single set-up of the workpiece for the measurement of most of features to be inspected.

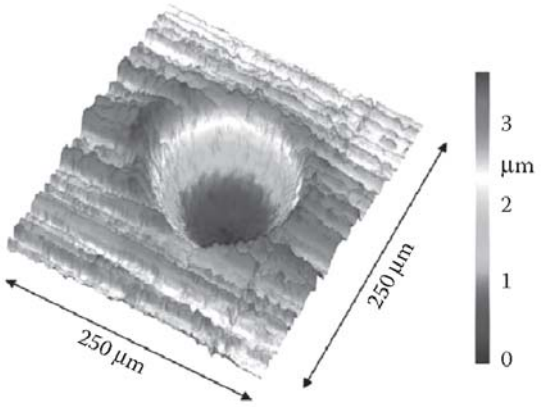

Figure 3.6. Plastic deformation of an aluminium surface due to probing force of 0.2 N [103]

The last step is the generation of measuring program. This step defines the datum system on the parts and how each selected feature should be measured in terms of number and distribution of the measuring points. By increasing the number of points used, features will make inspections more accurate. However, the larger the number of contact points used the longer the time needed to measure a feature.

The ISO 10360 series of standards [104][105] detail the acceptance, reverification, and interim check tests required to determine whether the tactile and optical CMM performs to the manufacturer‘s specifications. The tests only allow a statement to be made about the overall length-measurement capability of the CMM. As a consequence, the workpieced length-measurement uncertainty cannot be considered to be representative of all the possible measurement tasks that CMMs perform on a daily basis.

3.5 Tolerance verification using Computed Tomography

CT is now becoming an accepted inspection equipment for a large number of industrial applications. A typical CMM workflow for tolerance verification has been presented in Section 2.2 CT workflow for dimensional metrology. With respect to CMMs, which require a specific procedure for each object to be inspected, CT allows to use a single scanning procedure for a large variety of workpieces similar sizes and materials. As a consequence, CT presents higher flexibility than CMMs. Moreover, CT inspection can be conducted using same inspection software packages used for traditional CMMs. Figure 3.7 shows a comparison between traditional CMMs and metrology CT. It can be seen that increasing the number of features being inspected the measuring time increases for traditional CMMs compared to CT. The increase in measuring time is larger for tactile CMMs than optical CMMs for the reasons mentioned before.

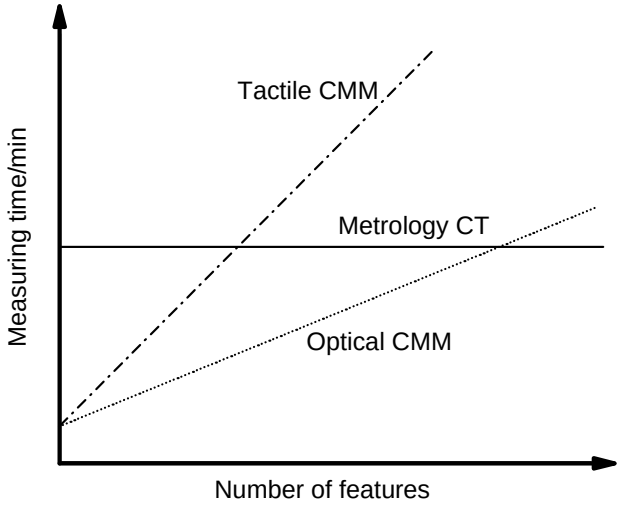

Figure 3.7. Measuring time versus number of features to be measured: schematic comparison of (a) tactile CMM, (b) optical CMM and (c) metrology CT [47]

Several workpieces can also be scanned at once compared to traditional CMMs where each part is individually measured. Note that the number of parts does not influence the CT workflow. The opportunity of scanning several parts at the same time reduces the scanning time per component to the same extent as traditional CMMs. Loading and unloading of the workpiece being scanned can also be integrated with robots, reducing the human errors as shown in Figure 3.8. With respect to traditional CMMs, the loading and unloading process does not affect the repeatability of CT measurements as CT does not rely on either an external reference system or a reference system based on the workpiece being imaged.

Figure 3.8. Automated loading and unloading of the workpiece being scanned [106]

Being CT a contactless measuring technique, the costs associated with design and manufacturing of CT fixtures for inspection can be reduced. The absence of measuring force also shortens the fixturing time compared to traditional CMMs. Generally speaking, the fixturing of a workpiece in CT is of 30-50% shorter that the same procedure for CMMs. Compared to traditional CMMs, no international standard CT for dimensional metrology has been published to date although the development of a possible

standard has been commenced. A task force of ISO/TC 213/WG 10 has been established to develop a new part of ISO 10360 specifically for CT [86]. The future standard will specify the acceptance tests for verifying that CT used for measuring linear dimensions complies with the manufacturer´s statement. The standard will also specify the interim checks which are required to determine whether the equipment complies with the manufacturer‘s specifications overt time. In the meantime, that an international standard will be produced, Germany and Japan have produced a series of their own national standards. In Germany, the development of national guidelines for CT used for dimensional metrology has started in 2004 in the VDI/VDE Technical Committee 3.33, which has led to six guidelines.

VDI/VDE 2630 part 1.3 [107] deals with the application of DIN EN ISO 10360 for coordinate measuring machines with CT sensors. The guideline is defined to be comparable to existing guidelines for traditional CMMs. VDI/VDE 2630 part 1.3 prescribes to measure five lengths, covering seven different directions of the measured volume, at two different magnifications. The guideline also prescribes that the test replicated three times. 210 measurement values are collected for a test. An example of the output of a test conducted according to VDI/VDE 2630 part 1.3 is shown in Figure 3.9. It can be seen that the measurement errors are all inside the specifications stated by the manufacturer. As already mentioned for CMMs, the tests only ensure compliance with specifications.

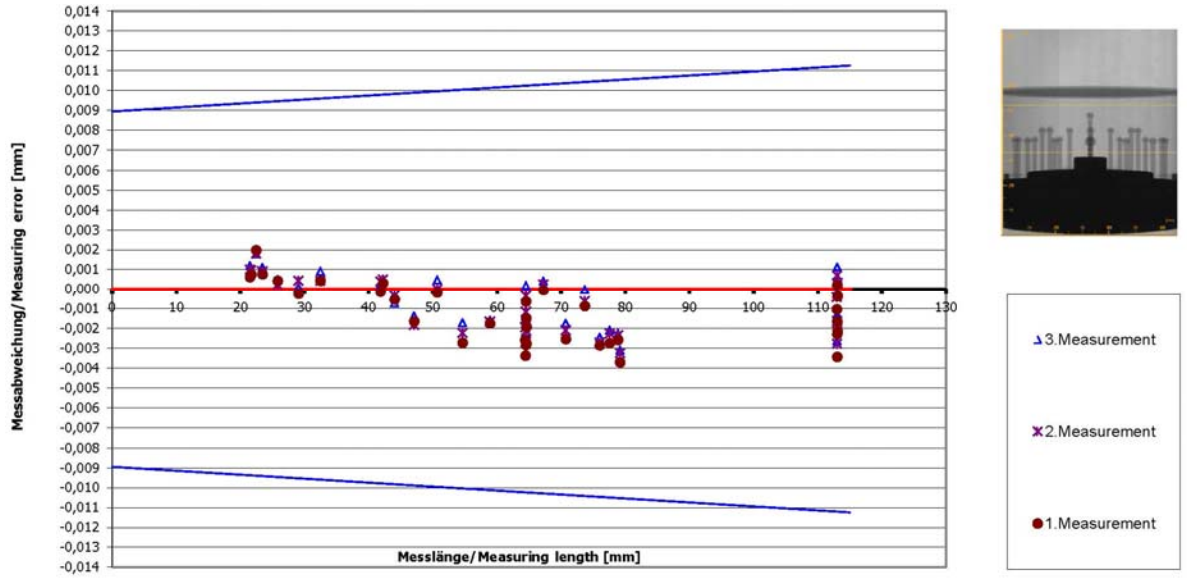

Figure 3.9. The results of a VDI/VDE 2630 part 1.2 test. The inspected CT was found to be within the specification stated by the manufacturer

3.6 Decision rules for proving conformity with specifications

GPS, through the ISO standard 14253-1 [108], sets a rule for determining when a feature of a specific workpiece complies with a given tolerance, taking into account the uncertainty of measurement. ISO 14253-1 stated that a feature is in conformance with its specification when the measurement result falls

within the tolerance zone reduced by the expanded uncertainty. On the contrary, a feature is not in conformance with its specification when the measurement result falls outside the tolerance zone increased on either side by the expanded uncertainty. The conformance and non-conformance zones are shown in Figure 3.10.

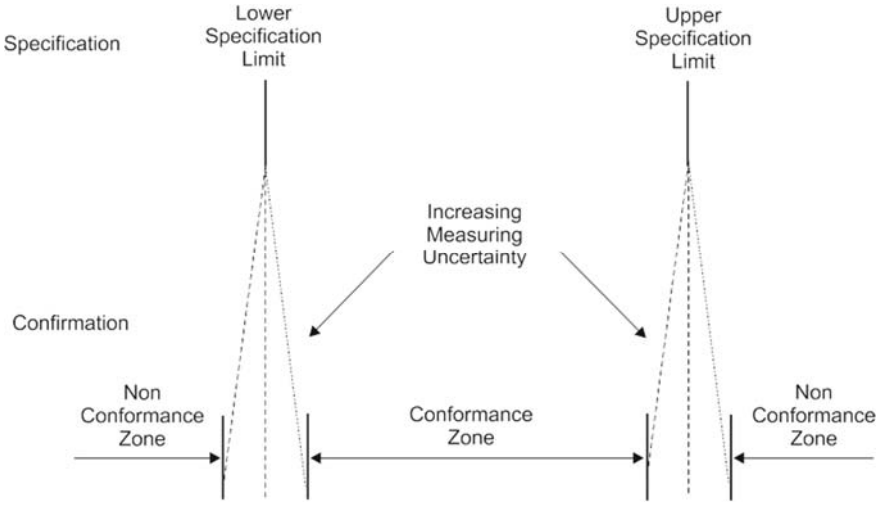

Figure 3.10. Conformance and nonconformance zones with the specification according to ISO 14253–1

ISO 14253-1 ensures a probability of false rejection, which is at most 2.3 %. The false rejection probability is the measure of the likelihood that the inspection process will incorrectly reject a workpiece, which complies with specifications.

When measurement results lie within the two guard-band zones, it results in an indeterminate decision of compliance. Consequently, workpieces can be neither accepted nor rejected. As shown in the figure, the larger the value of expanded measurement uncertainty the larger is the probability that a workpiece is going to be judged incorrectly. Historically, the reduction of the probability of indeterminate decisions was achieved by improving measurement process and equipment, according to the "golden rule" of metrology [109]. This rules states that a more “precise”, i.e. more capable, measuring instrument leading to a smaller measurement uncertainty is in general always less expensive than a more precise machine tool [110]. This approach has become much too expensive as a result of the demand for increasingly tight tolerances. More recently, the operating cost characteristic and optimised uncertainty [111] [112] represent the most adopted methodologies for economically quantifying the measurement uncertainty. By using those methods, the measurement uncertainty is fixed to a value ensuring an economically tolerable number of indeterminate decisions.

Besides refining the measurement uncertainty, the occurrence of indeterminate situations is also reduced by improving the stability of the manufacturing process.

3.7 Quantifying the measurement uncertainty in CT

As just presented, measurement uncertainty is a factor of importance in tolerance verification because it directly influences the extension of conformance zone and the probability of indeterminate situations. In metrology, measurement uncertainty represents an interval in which the true value of the measured quantity should statistically lie. The uncertainty of measurement comprises many components, known as standard uncertainties, which are subsequently summed resulting in a combined measurement uncertainty. The combined measurement uncertainty is finally multiplied by a coverage factor, suggested symbol *k*, in order to achieve a desired level of confidence. This new measurement uncertainty is termed expanded uncertainty and its evaluation of expanded uncertainty of measurement in CT can be based on either methods used in the traditional coordinate metrology such as GUM method [113], ISO 14253-2 [114], ISO 15530-3 [115] or a method specifically developed for CT such as VDI/VDE 2630 part 2.1 [116].

The GUM represents the most general method for estimating of measurement uncertainty. The GUM allows quantifying of measurement uncertainties using two approaches, namely *Type A* and *Type B*. *Type A* evaluations of standard uncertainty are based on any valid statistical method for treating data. A *Type A* evaluation is generally based on the standard deviation of repeated measurements. *Type B* evaluations of measurement uncertainty rely on scientific judgment using any relevant information, including previous measurement results, manufacturer´s specifications, and experience [117]. A *Type B* evaluation basically converts such relevant information into a standard uncertainty using a shape factor. A shape factors depends on the statistical distribution assumed to explain an influence factor. The most adopted probability distributions are: normal, rectangular, triangular, and U. The rectangular distribution is used when all values are equally probable. The rectangular distribution is usually used for specifications and reference book values. The triangular distribution is used when most probably outcomes are close to an expected value. The U-distribution is used when outcomes most probably lie close to the limits. The U-distribution is widely used for modelling standard uncertainty caused by the enhanced temperature. *Type B* evaluations are largely used when the amount of information is limited, at risk of having overestimated uncertainty estimations. The GUM is rarely used in practice because it requires estimation of all influence factors affecting the measurement process.

ISO 14253-2:2011 guidance as to the implementation of the concept of the GUM in industry introduces the Procedure for Uncertainty MAnagement (PUMA), which is a practical, iterative procedure based on an upper bound strategy. The PUMA method is extremely useful for industrial settings where the uncertainty of a workpiece is unlikely to be propagated into another measurement system [118]. As in the GUM, ISO 14253-2:2011 allows estimating measurement uncertainties using *Type A* and *Type B* evaluation approaches. ISO 14253-2 is used for estimating the measurement uncertainties of CT measurements when different workpieces are inspected on a daily basis.

The ISO 15530-3 and VDE/VDI 2630 part 2.1 describe two very similar procedures for evaluating the measurement uncertainty in CMM and CT, respectively, by using calibrated workpieces. The two methods prescribe measuring of a calibrated workpiece very similar to the workpiece to be subsequently inspected. The similarity condition includes size, geometry, and x-ray absorption, which is extremely important to achieve reliable uncertainty estimations. The similarity of material is a peculiarity of VDE/VDI 2630 part 2.1 as it has specifically been developed for CT.

Besides the similarity of the workpiece, it also important that calibrated workpiece and inspected workpiece are both post-processed in the same way. This means that CT workflow should not be modified in order not to lose information. By using those two methods, the expanded measurement uncertainty, U, of any measured parameter is always calculated using the following equation

$$U = k \times \sqrt{u_{cal}^2 + u_p^2 + u_b^2 + u_{wp}^2}. \tag{6}$$

Here, k, is the coverage factor and it is recommended to be chosen equal to 2 for a coverage probability of 95 %; u_{cal} is the standard uncertainty evaluated from the expanded measuring uncertainty, U_{cal}, and the coverage factor, k, given in the calibration certificate; u_p is the standard uncertainty of the 20 independent measurements conducted on the calibrated workpiece; u_b represents the standard uncertainty associated with the uncertainty in the CTE value for the calibrated workpiece; u_{wp} represents the standard deviations of the measurement conducted on the workpiece. This uncertainty contribution is necessary to take into account the variations of form errors and roughness between the calibrated workpiece and workpiece. In the presence of extremely critical measurement tasks, the uncertainty of measurement determination should be based on several calibrated workpieces in order to ensure that the influence of systematic errors is taken into account with sufficient reliability.

ISO 15530-3:2011 and VDE/VDI 2630 part 2.1 are largely adopted in manufacturing environments where similar workpieces are repetitively inspected. A major limitation of those methods is the long-time stability of calibrated workpieces, especially when calibrated workpieces made from polymers are used. The application of the substitution approach for uncertainty estimation for CT dimensional measurements was used in [119] [59].

In order to ensure that the size of a measurement uncertainty is correct, the concept of metrological compatibility of measurement results can be used. The criterion states that the absolute value of the difference between two sets of measurement results for a given measurand should be smaller than the square root of the sum of their squared expanded measurement uncertainties. The metrological compatibility can be adopted to verify either two sets of measurement results acquired using the same measuring equipment or two sets of measurement results acquired using two different measuring equipment. The former is used to check the stability of a measuring equipment over time, while the latter is used to compare two equipment. The concept of metrological compatibility is largely used in this thesis to compare CT measurement results with reference measurement results.

3.8 Conclusions

In this chapter, the main elements of tolerance and its verification have been discussed. It has been seen that there exists a standardized way of expressing the tolerances which is known as Geometrical Product Specifications, ISO-GPS. With respect to traditional tolerancing methods, ISO-GPS avoids any specification ambiguities at inspection of a component by linking dimensional and geometrical information of a component. ISO-GPS prescribes more than 15 tolerance symbols allowing full control of any geometrical feature of a workpiece. It has been shown that ISO-GPS, through the ISO 14253-1, provides a rule for determining when a feature of a specific workpiece complies with a given tolerance, by taking into account the measurement uncertainty. This method ensures that the probability of false rejection is smaller than 2.3 %.

The chapter has presented a typical workflow for inspecting a workpiece using CMMs and CT. It has been seen that traditional measuring equipment ensures lower measurement uncertainty than CT that conversely ensures higher flexibility and lower cost of programming. It has also recognized that CT suffers from the lack of international standards detailing the acceptance tests for verifying the performance of CT used for measuring linear dimensions compared to traditional measuring equipment. A partial solution is currently given by VDI/VDE 2630 part 1.3.

The estimation of measurement uncertainty in CT has also been presented in this chapter, as it is highly relevant to tolerance verification. It has been seen in the chapter that the measurement uncertainty in CT can be quantified using different approaches such as GUM, representing the most exhaustive method for estimation of uncertainty, PUMA which represents a simplification of GUM, and ultimately ISO 15530-3 and VDI/VDE 2630 part 2.1 which are two methods relying on calibrated workpieces. VDI/VDE 2630 part 2.1 is currently the only method specifically developed for CT. The concept of metrological compatibility has also been detailed.

The concept of tolerance analysis and its most popular methods have been presented. It has been seen that the Tolerance analysis methods can be grouped into two classes. There are methods based on full interchangeability among parts and there are methods based on partial interchangeability among parts.

Chapter 4

Experimental Investigations

The chapter comprises three experimental investigations concerning the optimization of CT measurements and the estimation of influence factors coming from the post-processing of CT measurements.

All the investigations were conducted using multi-material assemblies, and involved different measurands such as lengths, diameters, and roundness. The used assemblies were all calibrated and their calibration procedures are also presented in the chapter.

The first investigation, Section 4.1, reports the results of an investigation regarding the use of data filtering for improving the CT accuracy. Among digital filtering techniques, 3D medial filtering was selected due to its well-known ability to remove noise from images. Two variables were considered within this study, namely the kernel size of the medial filter and the stage in which the filtering is applied.

The second investigation, Section 4.2, concerns a comparison of surface determination methods commonly available in inspection software. Seven different surface determination methods ranging from a simple method such as thresholding to more complex methods based on the theory of sets were taken into account.

The third investigation, Section 4.3, has aimed to quantify the contribution of CT post-processing operations to the measurement uncertainty of CT measurements. Post-processing operations such as surface determination, data fitting, and the definition of the datum systems were considered. The evaluations were performed on an industrial assembly. Dimensional and geometrical measurands were selected to have different responses to the various post-processing settings.

4.1 Investigation of the Impact of 3D Data Filtering on the Accuracy of CT Measurements

4.1.1 Workpiece and its calibration

The workpiece is an assembly component from a commercial insulin injection device from Novo Nordisk A/S. The inner component is made of acrylonitrile butadiene styrene –polycarbonate (ABS-PC). The outer component is made of Polyoxymethylene (POM). Information on materials is reported in Table 4.1. Both components are produced via injection moulding. The workpiece was selected due to its complex shape, which makes available a large variety of measurands simultaneously. A total of six measurements were selected for the investigation. Three measurands were selected on the inner part, as shown in a section view in Figure 4.1a. *D1* represents the inner of the smallest cylindrical feature measured at z –3 mm from *Datum A*. *R1* is roundness of *D1*. *L2* represents the distance between *Datum A* and a plane on the bottom of the largest cylinder. Likewise, three measurands were selected on the outer part, as shown in a section view in Figure 4.1b. *D3* represents the inner diameter of the smallest cylindrical feature measured at z -5 mm above *Datum B*, while *R3* represents the roundness of *D3*. *L4* is the distance between *Datum B* and a plane on the bottom flange. Diameters were evaluated as minimum circumscribed circles. The measurands were all selected to be dependent on noise. Moreover, the similarity of measurands was chosen to adequately compare the effect of filtering on both components.

Table 4.1. Information on materials comprising the workpiece

Component	Density [g/cm³]	Thermal expansion coefficient [10^{-6} K $^{-1}$]
Inner	1.40	110 ± 20%
Outer	1.10	80 ± 20%

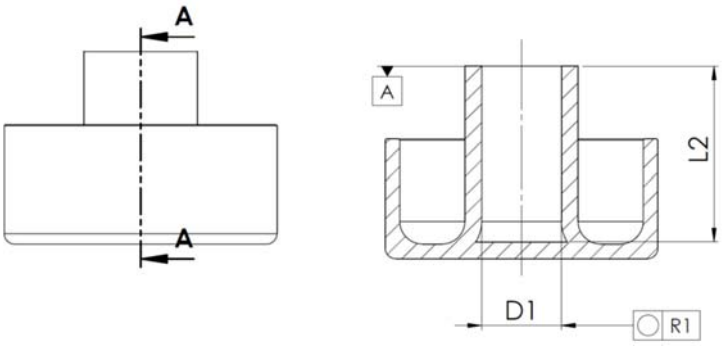

(a)

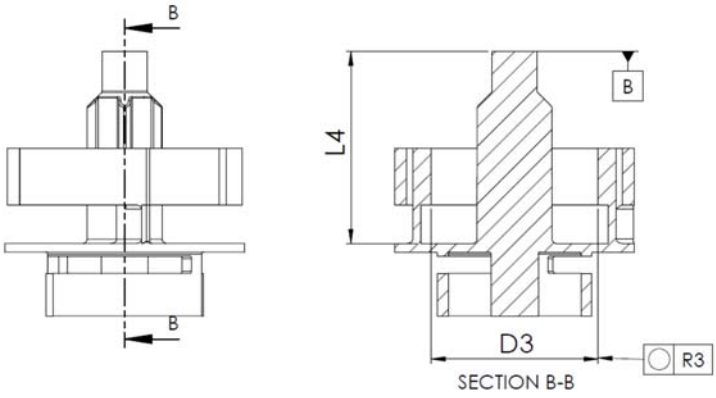

(b)

Figure 4.1. 2D definition of measurands for (a) inner and (b) outer component

The CMM measurements were performed using a Zeiss OMC 850 in a temperature-controlled laboratory (20 ± 1°C) with the temperature sampled constantly throughout the process. A 10 mm long probe equipped with a 0.8-mm-diameter probing sphere was used for all the measurements. All measurements were repeated five times. The CMM evaluations were made with Calypso 5.4 software from Zeiss. The measurement uncertainty statements were provided according to [114]. Unless differently stated, a Type B evaluation of uncertainty was assumed [12] (equation 8):

$$U_D^{cal} = k \times \sqrt{u_{cert}^2 + u_p^2 + u_T^2}, \tag{7}$$

where u_{cert} is the standard uncertainty associated with the material standard (a ring reference artefact and a gauge block); u_p is the Type A evaluation of standard uncertainty of the measurement procedure; u_T is the evaluation of standard uncertainty due to the temperature variability (± 0.5°C) assuming a U-distribution; k is the confidence level coverage factor (k=2 for a coverage probability of 95 %). The same quantification of uncertainties was adopted for geometrical measurands except for the temperature contribution, which was not considered. The uncertainty quantification resulted in the values below 4 µm.

Table 4.2 lists CMM reference values for all six measurands together with their measurement uncertainties at 95% confidence level. The CMM measurements on the two components were not replicated over time so no information regarding the short-time stability is available.

Table 4.2. CMM reference values for all six measurands together with their measurement uncertainties at 95% confidence level. All values were rounded to the nearest integer and are expressed in mm

Measurand	X [mm]	U (95%) [mm]
D1	3.289	0.003
R1	0.006	0.002
L2	6.924	0.003
D3	6.974	0.003
R3	0.022	0.002
L4	7.549	0.003

4.1.2 Experimental plan

The experimental test plan is schematically shown in Figure 4.2. After scanning and reconstructing the stack of X-ray projections, the CT volume model was elaborated using three different workflows: two 3D filtered workflows and one unfiltered workflow, which was only used as a reference throughout the elaborations. The filtered workflows were performed similarly, the only exception being the stage in which the filter was applied, namely before performing surface determination (hereafter "*B-SD*") or after the latter (hereafter "*A-SD*"). The filters considered in this investigation were 3D median filters that are a class of nonlinear digital filtering technique very useful for preparing CT data sets for subsequent processing. The main idea behind the median filtering is to run through all the image elementary entities (e.g. pixel or voxel), and then replacing each image element brightness with the median brightness of its neighbouring elements. The number of image elements used to quantify the median brightness for each image element defines the convolution kernel of the filter. Median filters are well-known for being edge preserving filters [120] under certain conditions (small kernel sizes) and for their high robustness because they rely on the median value which has the highest breakdown point (0.5). By using a median value, it is possible to minimise the effect of beam hardening leading to local fluctuations of grey values distribution biasing the surface determination. 3D filtering was only considered in this work for three main reasons. The first one is that the 3D filtering runs on data sets compared to 2D filtering needing the projections, which are often not provided to users. The second one is that the 3D filtering is easier to use than 2D ones requiring software and routines to be set. The last one is that the 3D median filtering affects the metrological structural resolution less than 2D filtering. The metrological structural

resolution is generally defined as the cut-off spatial wavelength (λc, in mm) for an amplitude transmission model value of 50% [121].

Two symmetrical kernels of 3 (hereafter "*Small kernel*") and 5 (hereafter "*Big kernel*") voxels were taken into account. Bigger kernel sizes were not considered because it is known that increasing the kernel size a median filter tends to a Gaussian filter, which does not preserve edge [122]. Larger kernels furthermore call for longer computations which negatively impact on the inspection throughput. The data sets were analysed using VG Studio Max 2.2.6. The surface determination was based on a local adaptive thresholding method (with a search distance of 7 voxels) in which the starting point was selected per data set independently of other ones. This choice was made to record any change in the histogram of grey values due to the noise imaging. CMM and CT alignment and evaluations were performed alike. All primitive features were fitted using 10000 points (step width of 0.020 mm, search distance of 0.010 mm, and maximum gradient of 15 degrees).

The number of points used for fitting the features corresponds to the maximum amount of points which can be fitted. The evaluations of geometrical measurands were conducted taking into account the whole distribution of fitted points in order not to introduce any further filtering. All the evaluations were conducted without rebooting the inspection software.

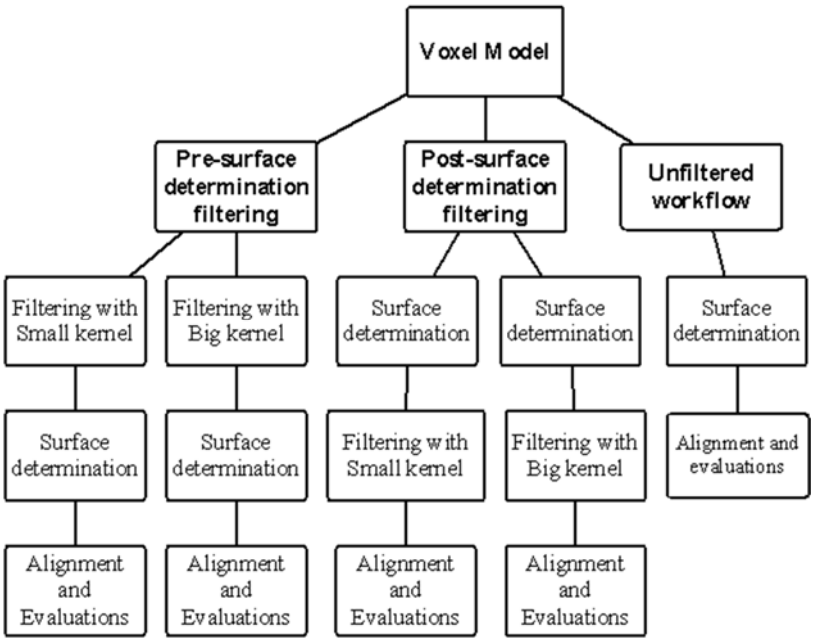

Figure 4.2. Schematic representation of the experimental test plan

4.1.3 CT measurements

A Nikon XT H 225 CT system was used for the investigation and set according to Table 4.3. The workpiece was scanned five times, placed within a low-absorption fixture. The workpiece was imaged using half of the detector area available in order to minimise the error effect caused by the tilt of rotary stage. This procedure was only possible because the workpiece is small and the selected measurands

laid in a part of the measured volume far from the lateral surfaces of the X-ray cone beam. A flat-panel correction based on 4 power levels and 64 projections per level was done before scanning. The four levels were selected at increasing levels of the selected power, namely 0%, 25%, 70%, and 100%. The correction reduced the original noise of about 84% and required 384s to be accomplished. The corrected projections resulted in a noise across the detector with a variance of about 280 grey values. The cabinet temperature was logged, found to be 24.5 ± 0.5 °C, and assumed to correspond to the workpiece temperature due to the acclimatisation of the workpiece within the cabinet for some hours. The detector temperature was also measured at the beginning and at the end of the scanning batch and found to be quite constant. The detector temperature was measured at the centre and at one side of the detector using a laser thermometer. The detector temperature was found to be increased by 3 °C at the end of the scanning period.

Table 4.3. Overview of the scanning parameters

Parameter	Unit	Value	Parameter	Unit	Value
X-ray source voltage	KV	100	Magnification		7
X-ray source current	µA	270	No. of projections		1500
Voxel size	µm	40	Integration time	ms	1500
Focal spot size	µm	22	Frames per projection		1

The X-ray source was warmed for 35 minutes at selected scanning power before proceeding with the scans in order to have a better repeatability of measurements, especially between the two first scans.

The reconstruction was performed on the CT Pro software package provided by Nikon Metrology, while the evaluations were conducted on the voxel-based data sets using VG Studio Max 2.2.6 inspection software. During the reconstruction no beam hardening correction was applied. The data sets were reconstructed as 32-bit floating point numbers rather than 16-bit integers to have their grey value distributions always comparable at a cost of larger data sets.

A scale error correction was conducted using a ball plate [4] that was scanned twice (at the beginning and the end of three CT scans) in order to consider the X-ray source drift. This scanning strategy for the ball plate was imposed by the fact that this investigation was one of the first investigations concerning metrology on this CT, so no a priori knowledge on the stability of the positioning system and the source was available. The correction was only based on 10 of 300 centre-to-centre distances available in the ball plate. The measurement results of two data sets of the ball plate showed a very good agreement, confirming the stability of the system and the environment during the entire scanning time. An average value based on two data sets was used for correcting the voxel size. An increase in noise was furthermore observed between two scans suggesting the detector lost its performance over the scanning time. The noise can be explained by the variation in the detector temperature.

The correction of systematic errors caused by the enhanced temperature was based on simulations. The components in the assembly were modelled assuming an isotropic behaviour of materials, meshed using 15000 elements, and finally processed using SolidWorks 2015. Figure 4.3 shows a 3D representation of the outer component of the workpiece before and after having been simulated. It can be seen from the figure that the inner component expanded, enhancing its tapered shape. The 3D results of simulations were converted into STL files and imported in VG Studio Max 2.2.6 in order to quantify the thermal expansion of each measurand. The simulation did not consider the variation in the thermal expansion coefficients as this effect is typically in the order of tenths of microns for workpieces of these sizes. The correction values are reported in Table 4.4. Based on the simulations, the enhanced temperature seemed not to influence the dimensional stability of workpiece, as negligible deformation in the contact zone between the components took place. The values reported in the table were then subtracted from the measurement results.

(a) (b)

Figure 4.3. 3D representation of the outer component of component (a) before and (b) after having been simulated

Table 4.4. Correction values to subtract from length and diameter measurements due to the increased temperature of 4.5°C above the reference temperature of 20°C. All values were rounded to the nearest integer and are expressed in mm

Measurand	D1	L2	D3	L4
Expansion	0.0014	0.0037	0.0025	0.0027

The magnification selected for this investigation did not cause missing frequencies in the vertical direction, as confirmed by the Fourier analysis conducted on a reconstructed slice along the central plane (see Figure 4.1.4).

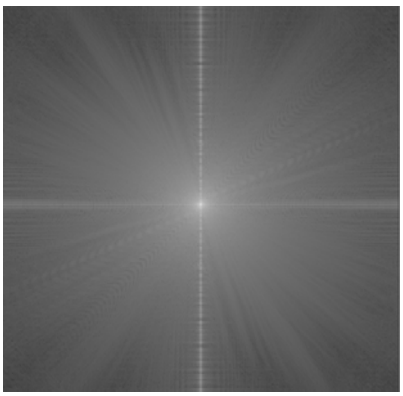

Figure 4.4. 2D FFT transform of a reconstructed slice in the central vertical plane. No missing frequencies can be observed along the vertical direction.

The uncertainty assessment was based on the PUMA method [114], as described in equation 9.

$$U = k \times \sqrt{u_r^2 + u_p^2 + u_T^2 + u_{noise}^2}, \tag{8}$$

where k is the coverage factor *(k = 2* in order to have a coverage interval of 95%), u_r is the standard uncertainty of the reference artefact used for scale error correction. This approach was used because the reference artefact and the workpiece are comparable from an X-ray point of view. The similarity was documented using simulations involving a multi-material reference artefact. The latter comprised a series of half-spheres made from ruby, resembling the spheres of the ball plate, and POM, which is the same material as the workpiece. Spheres with a diameter of 5 mm as the spheres of the ball plate were considered for both materials. The simulations were conducted using aRTist, a computer simulation program developed by BAM, set with X-ray source and detector characteristics as well as scanning parameters similar to the real CT. The simulations were carried out using polychromatic X-rays and scatter. The simulation results (see Figure 4.5) suggested that two materials appeared to be alike under the scanning conditions used in this work.

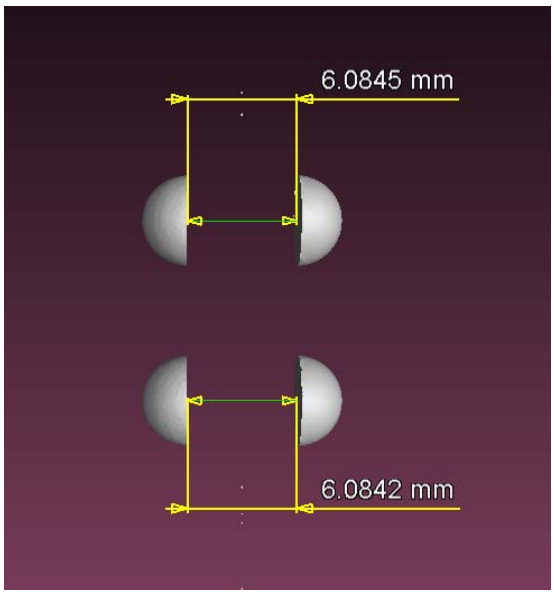

Figure 4.5. A 3D view showing the reconstructed volume model of a multi-material ball plate. The upper half spheres are made out of ruby while the lower ones are made out of POM. As indicated in the figure, the differences are negligible

The uncertainties of sphere-to-sphere distances were used for length and diameter measurements, while the uncertainties of form errors of spheres were used for roundness measurements; u_p is the standard uncertainty describing the measurement procedure for each measurand, based on the standard deviation from the reproduced measurements (five scans); u_T is the temperature-related standard uncertainty calculated for a deviation of ± 0.5 °C and using a coefficient of linear expansion for both components. This contribution was only considered for dimensional measurements. u_{noise} stands for the standard uncertainty due to noise. This contribution was assessed based on the probing error form conducted on a few spheres of the ball. The quantification was conducted on unfiltered data set. This contribution was considered for all measurands due to their dependence on noise.

Measurement uncertainties are reported per workflow, kernel size, and measurand in Table 4.5. It can be seen from the table that measurement uncertainties appear to be independent of the workflow and kernel size, leading to the assumption that filtering does not significantly affect the repeatability of the inspection process. The maximum difference between either two workflows or two kernel sizes was found to be below 0.4 µm.

Table 4.5. Expanded uncertainties at 95% confidence level for the measurands of the two parts. All values were rounded to the nearest integer and are expressed in mm

Component	Measurand	Unfiltered	A-SD Small Kernel	A-SD Big Kernel	B-SD Small Kernel	B-SD Big Kernel
Inner	D1	0.007	0.007	0.007	0.007	0.007
	R1	0.008	0.008	0.008	0.008	0.008
	L2	0.010	0.011	0.010	0.010	0.010
Outer	D3	0.008	0.008	0.008	0.008	0.008
	R3	0.008	0.008	0.008	0.008	0.008
	L4	0.010	0.011	0.010	0.010	0.010

Measurement uncertainties appear to be dependent upon the measurand. The measurements of two lengths of both components show larger measurement uncertainties due to the bad quality of surfaces used for defining those measurands. The surfaces were noted to be not completely flat, resulting in fitting errors. Measurement uncertainties of diameter and roundness measurements of both components are similar in size because of the absence of beam hardening, giving well-shaped distributions of grey values for both components. Similar uncertainty values were also achieved as both components were segmented using an automatic procedure reducing surface offsets associated with the initial threshold value. A repeatability of 1.2 µm was registered for measurements of *D1*, *R1*, *D3*, *R3*, and *L4*. A repeatability of 1.8 µm was obtained for length measurements of *L2*.

4.1.4 Results and discussions

Results are presented in Table 4.6 using the E_n criterion [123], which considers deviations from reference quantities, reported in Table 4.6, and measurement uncertainties simultaneously [4]. Since the measurement uncertainties are rather constant (see Table 4.5), the E_n values represent a suitable way to present the results. It can be observed from the table that all measurements are in agreement with the reference measurements (none of the measurement results exceeded the critical condition $E_n > 1$). It can also be seen that most measurands are however close to the critical condition. The table also shows that generally filtering decreases E_n values, resulting in smaller systematic errors for both components of the workpiece. A reduction in the E_n values of more than 30 can be calculated from the results. The reduction of E_n values does not appear to be constant but varies as workflow and kernel size changes.

Table 4.6. E_n values for the measurands of the two components. All values were rounded to the nearest integer

Component	Measurand	Unfiltered	A-SD Small Kernel	A-SD Big Kernel	B-SD Small Kernel	B-SD Big Kernel
Inner	D1	0.90	0.64	0.52	0.60	0.56
	R1	0.90	0.60	0.54	0.60	0.54
	L2	0.25	0.38	0.38	0.45	0.45
Outer	D3	0.89	0.69	0.66	0.80	0.72
	R3	0.83	0.64	0.52	0.60	0.52
	L4	0.24	0.30	0.33	0.47	0.47

Regardless of the kernel size, *A-SD* workflow yielded better E_n values in the order of 7-10% for all measurands. A possible explanation for the obtained results could be that in the *A-SD* workflow, filtering is applied to a segmented data set, so it just removes small structures on the surfaces similarly to a morphological operator such as closing and opening [124]. The *B-SD* workflow operates on a non-constrained data set, producing a stronger flattening at cost of expanding the data set, as shown in Figure 4.6. It can be seen from the figure that the *B-SD* workflow yielded surface expansions.

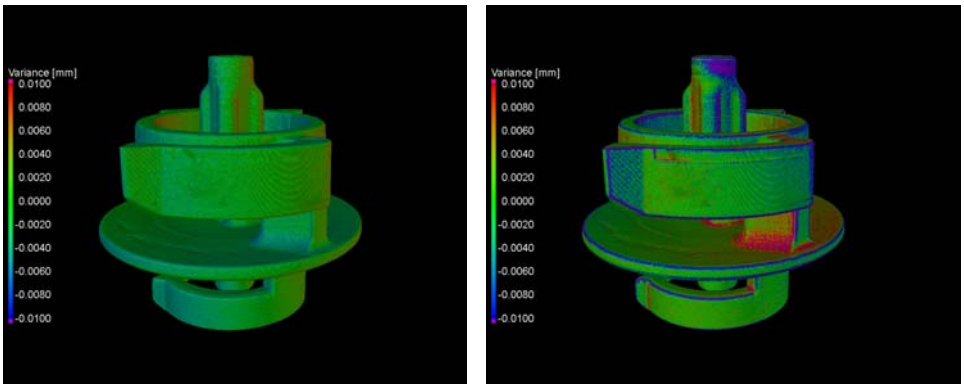

(a) (b)

Figure 4.6. Colour deviation maps of the inner component showing dimensional differences with respect to the unfiltered volume for (a) A-SD and (b) B-SD workflow

Image analysis showed that both workflows yielded a similar reduction of noise with respect to the unfiltered workflow. The amount of noise reduction was quantified using several X-ray slices taken in the XY plane of the CT coordinate system. The slices were processed using Fiji imaging analysis software package. As to the surface determination, no differences were recorded between two workflows both based on the same kernel. Negligible differences were also observed as to computation time between the workflows in processing the same kernel.

The two kernels of *A-SD* and *B-SD* improved the accuracy of the majority of the considered measurands compared to the unfiltered workflow. *Big Kernel* and *Small Kernel* reduced the E_n values of measurements of *R1* and *R3*, and of *D1* and *D3* by up to 54 % and 40 %, respectively. It is interesting to report that increasing the kernel size roundness measurements improved in terms of positive and negative deviations in exactly the same way. This reduction in the deviations suggests that noise affected the surface was symmetrically distributed and that the noise completely hides the form errors of the components. As a consequence, most of information used to estimate a geometrical measurand does not actually correspond to the workpiece.

The feature of the distribution of noise explains why the measurements of diameters, which were evaluated using a minimum circumscribed fitting method, improved less than roundness measurements, *R1* and *R3*. Although *Big Kernel* resulted in lower E_n values for roundness and diameter measurements of two components, it did not make a considerable improvement compared to *Small Kernel*, as shown in Figure 4.7. It can be seen from the figure that measurement results of roundness filtered using *Big Kernel* and *Small Kernel* are similar. The similarity of two kernels was also confirmed using a Two-sample test based on Student's t-distribution [125].

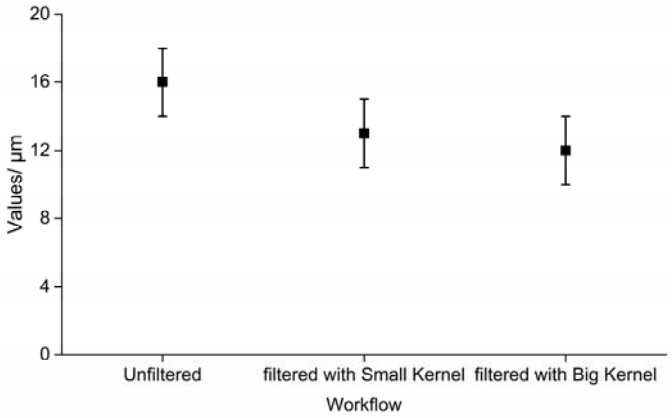

Figure 4.7. Comparison between *Small Kernel* and *Big Kernel* for measurement result of R1, roundness of outer component. Bars represent the standard deviations of five CT measurements

Big Kernel and *Small Kernel* increased the E_n values of the measurements of *L1* and *L2* by more than 20 %. The worsening of E_n values may have been caused by the smoothing of the asperities of component surfaces resulting in making the considered lengths longer. The smoothing effect is of the same order as the surface texture of the surfaces used for defining the measurands (see Figure 4.8). The worsening of E_n values of length measurements may also be due to a result of the expansion of the data set due to filtering, which would have added some background voxels to the workpiece. The extent of this effect was verified comparing the volume of the workpiece before and after having been filtered and was found that the volume shrank by up to 0.06% after having been filtered. Since the lengths were measured longer, this shrinkage does not represent a possible cause.

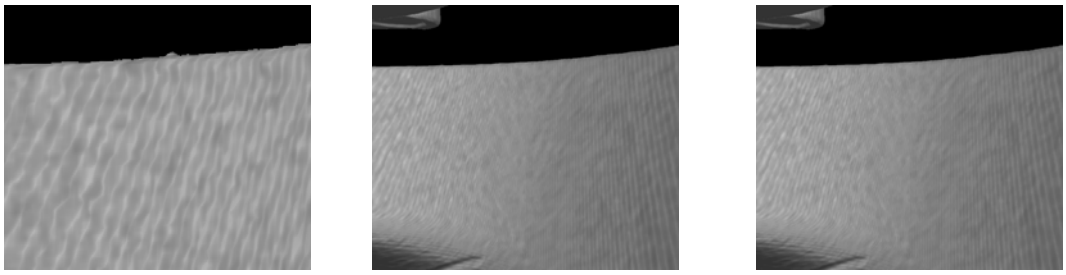

(a) (b) (c)

Figure 4.8. Three 3D views showing the same surface (a) unfiltered, (b) filtered using Small kernel and (c) filtered using *Small kernel*. It can be noticed that increasing the filtering, the surface improves in both peak and valley distributions

By investigating the transition from grey values of background to grey values of two components in the aligned X-ray slices, the impact of filtering on the shape of the surface edge was also investigated. Profile analysis did not highlight any change in the shape of the edge between the two kernel sizes with respect to unfiltered workflow as shown in Figure 4.9. The transient area between the background and material also did not change when median filtering was applied to the data sets. This result confirms that in the presence of normal noise levels, the median filters do not modify the surface edges and thereby the structural resolution. It is however believed that some changes in the shape of the edges [121] occurred but the used workpiece was quite rough to highlight those differences. Both kernel sizes reduced noise in the background with respect to the unfiltered workflow. The average reduction of fluctuation was quantified in 65% and 84% for *Small Kernel* and *Big Kernel* respectively compared to the unfiltered data set. These presented values were averaged over five different reconstructed projections, each of which was inspected in two equally sized areas (300 x 300 pixels).

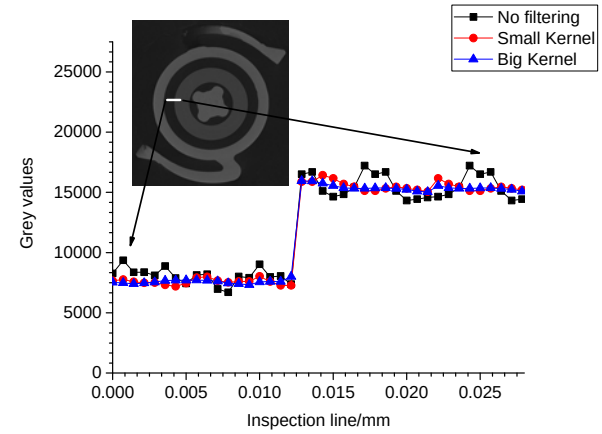

(a)

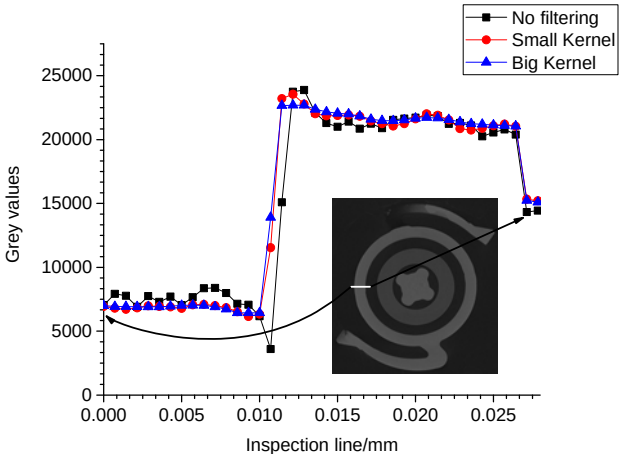

(b)

Figure 4.9. Grey value profiles across an (a) inner edge and (b) outer edge of the workpiece. The profile describes the three filtering conditions experimented in this work. Increasing filtering kernel reduces the oscillating signal in the background and in the material without affecting the shape of the edges

4.1.5 Conclusions

This study has evaluated the features of 3D median filtering with respect to two variables such as the application stage of filtering within the CT measurement workflow and the kernel size. The following conclusions can be provided.

- The measurement uncertainties for the CT measurements were found to vary between 8 and 11 µm depending on the measurands, and a repeatability better than 1.8 µm was quantified for all the measurands. Both components showed similar uncertainties as a result of the absence of beam hardening.
- Filtering decreases E_n values for both components and their measurands. The accuracy enhancement does not appear to be constant but varies as workflow and kernel size changes. Regardless of the kernel size, *A-SD* workflow yielded better E_n values in the order of 7-10% for all measurands. It was however concluded that two workflows led to similar results from a metrological point of view. *Big Kernel* and *Small Kernel* reduced the E_n values of measurements of *R1* and *R3*, and of *D1* and *D3* by up to 54 % and 40 %, respectively. On the contrary, *Big Kernel* and *Small Kernel* increased the E_n values associated with measurements of *L2* and *L4* by more than 20 %. The worsening of those E_n values is due to the smoothing of the asperities of component surfaces.
- Profile analysis did not highlight any change in the shape of the edge between the two kernel sizes with respect to unfiltered workflow. This result suggests that in the presence of normal noise levels, the median filters do not modify the surface edges and thereby the structural resolution.

4.2 A Metrological Comparison of Surface Determination Methods used in CT for Metrology

4.2.1 Workpieces and their calibration

Three step gauges made from aluminium, *Al*, polyphenylene sulphide, *PPS,* and polyetheretherketone, *PEEK* were used as workpieces in this work. The used step gauges have dimensions of 55 mm × 8 mm × 7 mm and have 11 grooves at 2 mm steps. Information on design and manufacture can be found in [10]. The step gauges were adopted for the following reasons. They provide a plurality of length measurands, reducing the number of investigations to be conducted. The step gauges are characterized by flank-to-flank distances which are strongly influenced by the surface determination strategy compared to other types of distances (e.g. sphere-to-sphere distances). Moreover, all flanks show a similar amount of material to be penetrated, meaning that image artefacts can be assumed to be uniformly distributed. The step gauges can be calibrated with low uncertainties, resulting in smaller test uncertainties. Ultimately, the step gauges are made from materials that are very popular in industry and that show a good stability against X-rays. Ten bidirectional lengths (nominally *B1* = 2 mm, *B2* = 6 mm, *B3* = 10 mm, *B4* = 14 mm, *B5* = 18 mm, *B6* = 22 mm, *B7* = 2 mm, *B8* = 6 mm, *B9* = 10 mm, and *B10* = 14 mm) were selected as measurands (see Figure 4.10). Measurands from *B1* to *B6* are inner bidirectional lengths. Measurands from *B7* to *B10* are outer bidirectional lengths.

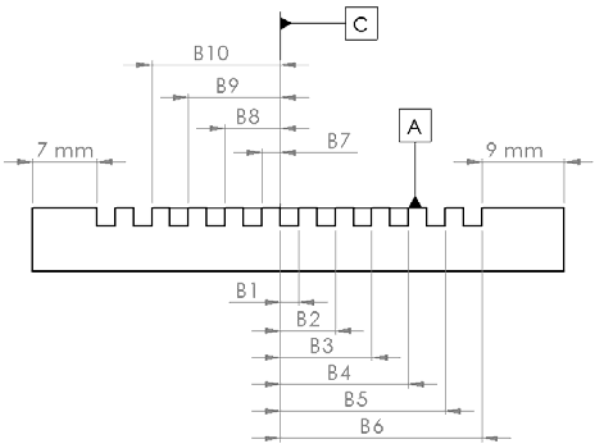

Figure 4.10. Definition of the measurands and datum system. Note that *Datum B* is not visible in this view

Reference measurements of the step gauges were performed at DTU in a controlled environment of (20±0.5) ºC. A Carl Zeiss UPMC 850 CARAT equipped with a probe of a diameter of 0.8 mm was used for all the measurements. The datum system for the step gauges (see Figure 4.11) was constructed using three datum features, namely *Datum A*, *Datum B*, and *Datum C*. *Datum A* was created as a common zone plane over four teeth areas positioned on the top of the step gauge teeth between groove 4 and 8. *Datum B* was constructed as the symmetry plane of the two parallel planes fitted along the step gauge

longitudinal length. *Datum C* was fitted on the left side of the sixth groove. A number of 15 points were used per datum feature.

With respect to the previous calibrations [57][126], the present calibration was based on point-to-point distances for all selected measurands. Each point represented the centre of mass of five points for each flank. The five points were distributed in a star pattern covering an area of 2 mm^2. By replacing planes with points, the impact of flatness of flanks and parallelism between two flanks on the measurements can be definitely reduced.

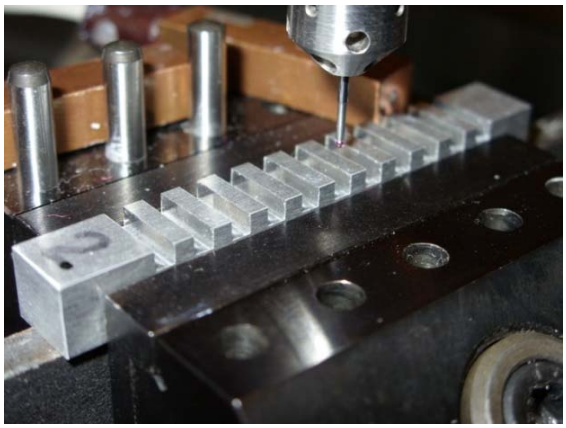

Figure 4.11. Measurement setup used for the calibration of the step gauges. The aluminium step gauge is shown in the figure

Traceability of measurement results was established using a reference artefact involving a series of 2-mm gauge blocks. The reference artefact was assembled for the calibration task. The artefact was placed in the same fixture and in the same orientation as the step gauges being calibrated. Ten repeated measurements were conducted on the artefact without modifying the alignment. Reference measurements were conducted over several days and then average values were used. This multi-day strategy should minimise the effect of influence factors such as temperature and probe hysteresis.

The calibrations were conducted without personnel close to the measuring equipment in order to achieve the better and more stable environment conditions. Measurement uncertainties were quantified using the PUMA approach [114]. The considered uncertainty contributors are given in Equation 10 and described in Table 4.7.

$$U = k \times \sqrt{u_r^2 + u_{rep}^2 + u_{drift}^2 + u_{T(1)}^2 + u_{T(2)}^2 + u_{T(3)}^2 + u_p^2}. \quad (9)$$

The components of Equation 10 are described in Table 4.7. It can be seen from the table that uncertainty components were evaluated using either *Type A* or *Type B* uncertainty evaluations. The latter were based on either the rectangular distribution or the U-distribution. Measurement uncertainties were found to be 1 µm for the *Al* step gauge, 1.3 for the *PPS* step gauge, and 1.5 µm for the *PEEK* step gauge. The latter shows the highest uncertainty most likely due to its worst surface texture. The use of points reduced the measurement uncertainty by more than 80% compared to previous calibrations.

Table 4.7. List of the uncertainty contributors for the measuring uncertainty budget of the reference measurements

Symbol	Involved uncertainty contributions	Type
u_r	Uncertainty component from the reference artefact	B (rectangular)
u_{rep}	Uncertainty component from repeatability on the reference artefact	A
u_{drift}	Uncertainty component due to CMM geometrical errors along the measuring axes	B (rectangular)
$u_{T(1)}$	Uncertainty component from temperature deviation from standard reference temperature for instrument	B (U-shape)
$u_{T(2)}$	Uncertainty component from temperature deviation from standard reference temperature for workpiece	B (U-shape)
$u_{T(3)}$	Uncertainty component from workpiece expansion coefficient uncertainty	B (U-shape)
u_p	Uncertainty component from measurement process	A

CMM measurements were replicated after one month in order to ensure the short-term stability of the step gauges. Measurement values of two calibration rounds were in close agreement with each other.

Once the calibration was concluded, the step gauges were assembled giving three assemblies, *Assembly 1*, *Assembly 2*, and *Assembly 3*, with different density and absorption ratios as reported in Table 4.8. The step gauge having lower absorption coefficient in each assembly is coded as *LAS* throughout the chapter. The step gauge having higher absorption coefficient in each assembly is coded as *HAS* throughout the chapter.

Table 4.8. Assemblies and their density and absorption coefficient ratios. HASs are marked in bold

	Assembly 1	Assembly 2	Assembly 3
Materials (id_2/id_1)	PEEK/**PPS**	PPS/**Al**	PEEK/**Al**
Density ratio (ρ_2/ρ_1)	0.8	0.6	0.5
Absorption coefficient ratio at 150 kV (μ_2/μ_1)	0.4	0.6	0.2

4.2.2 Experimental plan

The surface determination methods compared within this work are described in the following.

ISO method

ISO-50 method (hereafter "*ISO*") uses a global threshold value for segmenting a data set. The segmentation of *LAS* was carried out selecting grey values belonging to *LAS* and to the background. The grey values were all selected within small areas in order to reduce the impact of image artefacts, such as beam hardening and noise. As a result, a point halfway between the two peaks is calculated, which represents the thresholding condition. The segmentation of *HAS* was based on a similar procedure. The segmentation of *HAS* resulted in fully removing *LAS*. *ISO* is the fastest and simplest segmentation process applied in this study.

Advanced mode (Adv)

The advanced mode (hereafter "*Adv*") is based on the local behaviour of the grey values, using a starting contour of the object. *LASs* were automatically segmented using Adv. *HASs* were manually segmented according to the procedure described for ISO. *Adv* was implemented using the default software preferences e.g. a searching distance of 4 voxels, throughout the course of this work.

Cutting-out method

The cutting-out method (hereafter "*Cut*") is based on eliminating the unwanted grey values of the data set using ROIs. After having removed the unwanted material, a surface is defined using *Adv*.

Region growing method

This segmentation method (hereafter "*RGrow*") relies on the region growing process. The method requires a seed voxel representing the starting point from which the algorithm runs through the data set and connects voxels which are similar to the seed. The similarity between seed voxel and voxel is based on a tolerance value. In this study, two different seed and tolerance values were used depending on the material being segmented. The tolerance value for segmenting *LASs* was set to be twice as much as the standard deviations of *HASs*. The tolerance value for segmenting *HASs* was selected to be three times as much as the standard deviations of *HASs*. The seed voxel for *LASs* was smaller than those one used for *HASs*.

Histogram method

The histogram segmentation method (hereafter "*Hist*") aims to exclude the unwanted range of grey values from the histogram of grey values. Using *Hist*, mono-material histograms can be obtained. The range of unwanted grey values should be able to fully cover the peak of the material to be removed. In this study, the range was set twice as much as the standard deviation of the grey value distributions. As a result, a new volume was created from the active part of the histogram and segmented using Adv.

Complement method

This method (hereafter "*ROI*") is based on the concept of the complement of a set. The theory of sets demonstrates that given two sets, *A* and *B*, the complement set of *A* in *B* is the set is the set of elements in *B* but not in *A*. The complement set was obtained using two *ROIs*. The first *ROI* included the entire

distribution of grey values, namely both *HAS* and *LAS*. The second *ROI* was defined to only include grey values belonging to *HAS*. By subtracting the two defined *ROIs*, a new *ROI* that only comprise *LAS* was obtained.

Inverse method

This segmentation method (hereafter "*Inv*") is also based on the theory of sets and was used for segmenting *LASs* in this work. The first step was to define a *ROI* including *HAS*. The second step was to invert that *ROI*. The inverted volume was segmented using *Adv*.

In conclusion, seven surface determination methods were considered per assembly. All presented methods were applied to the *LASs*. Five of seven surface determination processes, all except Complement and Inverse methods, were applied to the *HASs*.

The evaluations of the different surface determination approaches were based on deviations from tactile CMM measurements. Similar alignment and measuring procedure were applied for CT and CMM measurements in order to have comparable data, the

4.2.3 CT measurements

The three assemblies were all positioned tilted at 45º and scanned using a Nikon MCT225 system at PTB, and the same uncorrected voxel size (37 μm). Three repeated scans were performed for each assembly without opening the CT cabinet. A scale error correction was performed before and after each batch to remove residual scaling errors. The scale error correction was based on the reference object showed in Figure 2.19c. The correction highlighted some residual systematic errors (≈ 0.001 %) even though the CT is equipped with laser corrected linear guideways. Such systematic errors can be due to either the system drift or the calibration uncertainty of the reference object used for the correction. Scanning parameters, which are reported in Table 4.9, were independently selected per assembly with aim of achieving comparable noise and beam hardening in all assemblies. The selection of scanning parameters was based on an iterative process that involved several preliminary scans. The iterative process was conducted with aim of spreading the histogram of grey values as much as possible. The same number of projections was used but not the same integration time that was increased for the scans comprising the aluminium gauge for enhancing the contrast at any angular position of the measured volume.

Table 4.9. CT scanning parameters used for each assembly

	Assembly 1	Assembly 2	Assembly 3
Voltage in kV	120	180	170
Current in µA	8037	113	120
Filter in mm and (material)	0.5 (Aluminium)	1.5 (Copper)	1.5 (Copper)
Number of projections	2000	2000	2000
Integration time in ms	1400	2829	2829

In order to minimise the impact of measurement uncertainty of the results of the investigation, it was opted to establish the traceability of CT measurements using the CMM measurements. The estimation of uncertainty of CT measurements was based on [114] according to the equation 11.

$$U = k \times \sqrt{u_r^2 + u_\alpha^2 + u_T^2 + u_p^2}, \tag{10}$$

here, k is coverage factor (k = 2, for a coverage interval of 95%); u_r is the measurement uncertainty of the reference measurements reported in Section 4.2.1; u_α is the uncertainty contribution due to the variation of the coefficients of linear thermal expansion (*CTE*), quantified to be 20% of the nominal value; u_T is the uncertainty due to the variation of the temperature during scanning. The quantification was based on a Type B uncertainty treated using a U-distribution; u_p is uncertainty component from measurement process based on three repeated scans. The quantification of this contribution was based was based on a Type B uncertainty treated using rectangular distribution. No uncertainty contribution due to the scale error correction conducted was taken into account in this investigation. The expanded uncertainties were quantified to be below 3 µm for all assemblies. An example of the distribution of uncertainty contributions is summarized in Figure 4.12 for the PEEK step gauge in *Assembly 1*. The graph shows that the uncertainties coming from the calibration and from the measuring process are the dominant factors.

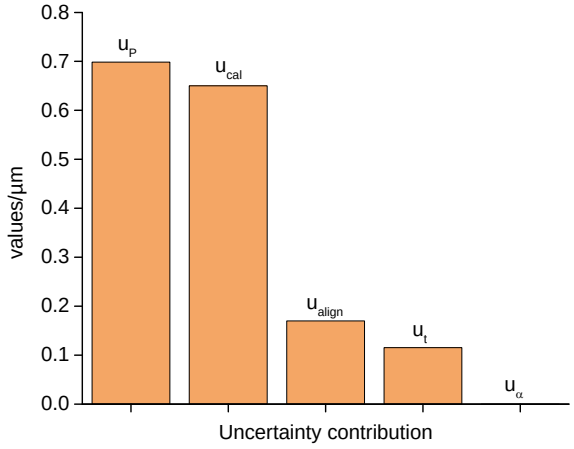

Figure 4.12. Distribution of uncertainty contributions for *PEEK* step gauge in Assembly 1

4.2.4 Results and discussions

The results are presented in Figure 4.13. Each graph reports the measurement results per step gauge.

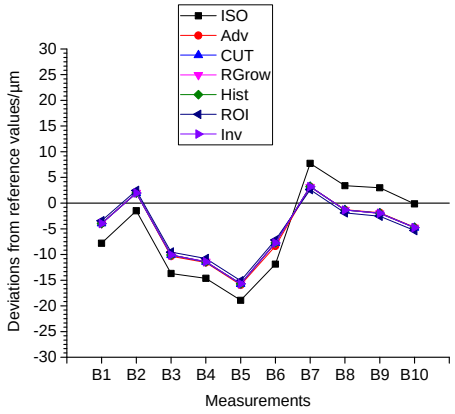

Assembly 1 **PEEK**/PPS

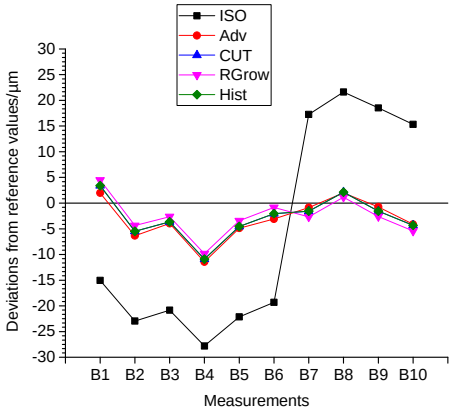

Assembly 1 PEEK/**PPS**

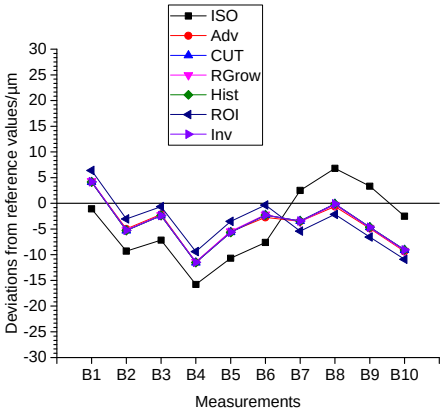

Assembly 2 **PPS**/Al

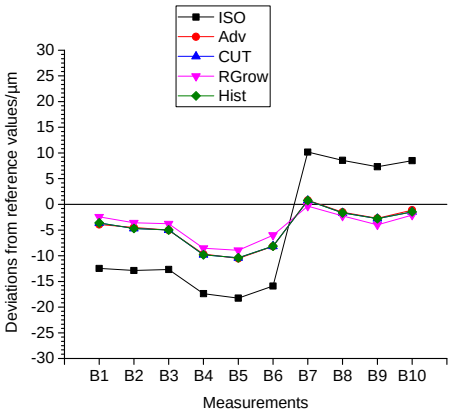

Assembly 2 PPS/**Al**

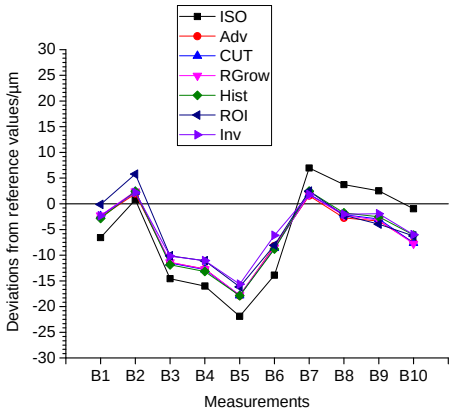

Assembly 3 **PEEK**/Al

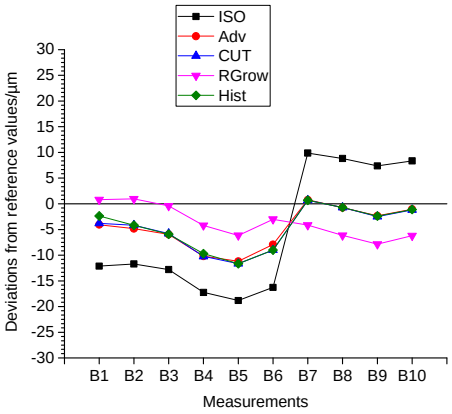

Assembly 3 PEEK/**Al**

Figure 4.13. Results of the multi-material scenarios. The measured step gauges are marked in bold

A maximum measurement error of 40% of the voxel size (≈15 µm) was recorded for all segmentation methods based on *Adv*. The extent of deviations confirms the sub-voxel accuracy of those methods in the presence of good quality data sets (high CNR). Smaller measurement errors in the order of 15% of voxel size were noticed for measurands imaged in the centre of the X-ray beam. Those measurement errors are in the order of the surface texture of the step gauges. *ISO* yielded a maximum measurement error in the order of the corrected voxel size (32 µm) for *HASs*. The measurement errors are typically negative for inner length measurements and positive for the outer length measurements. Negative errors are larger than positive ones. *ISO* yielded smaller measurement error for *LASs* than for *HASs*. The different size of measurement deviations can be explained by the fact that the segmentation of *HASs* is done manually, whereas the segmentation of *LASs* is done automatically.

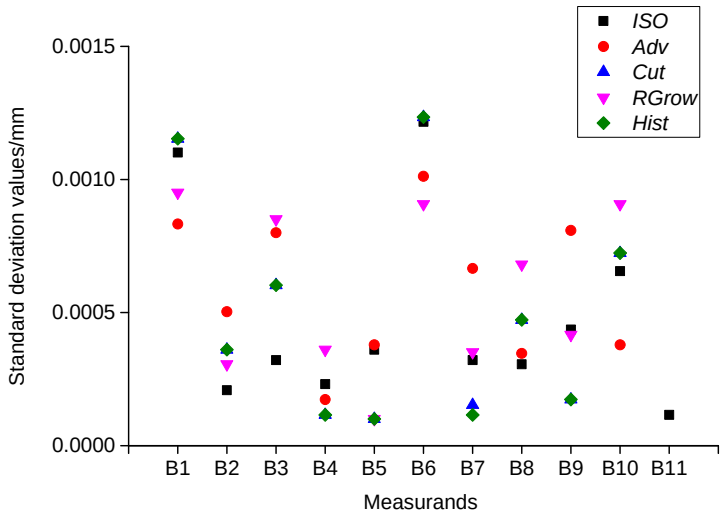

Figure 4.14. Scatter plot for all the measurands of PPS step gauge in Assembly 1. Five surface determination methods, *ISO, Adv, Cut, RGrow,* and *Hist* were used for the segmentation

Small differences among the standard deviations of the surface determination methods were observed for each single step gauge, as reported in Figure 4.14. On the contrary, large differences among the standard deviation values of the surface determination methods were observed for the same step gauge involved in two different assemblies. The *PEEK* step gauge in *Assembly 3* showed standard deviations being up to 119% greater than the same gauge in *Assembly 1*. Note that the *PEEK* gauge was *LAS* in both *Assembly 1* and *Assembly 3*. On the contrary, the *PPS* step gauge in *Assembly 1* presented standard deviation values being up to 45% smaller than the same gauge in *Assembly 3*. The *PPS* gauge was *HAS* in Assembly 1 and *LAS* in *Assembly 2*. The standard deviation values were found to be independent of the inspected length. In some cases, similar standard deviation values were recorded for measurands having different size, as shown in Figure 4.15.

Since the thresholding methods are all sensitive to the starting points (see Section 2.3.4 Post-processing of CT data), the effect of the latter was also investigated, leading to two main considerations. The first one is that better measurement results were achieved when the starting point is automatically defined for all surface determination methods investigated, including *ISO*. The second one is that the optimal

thresholding value did not necessarily represent the minimum grey value between air and material distribution. The optimal thresholding value can vary depending on how the software estimates the distribution parameters and what kind of statistical distribution the inspection software assumes for meshing the grey values. No information is disclosed by VG on this matter.

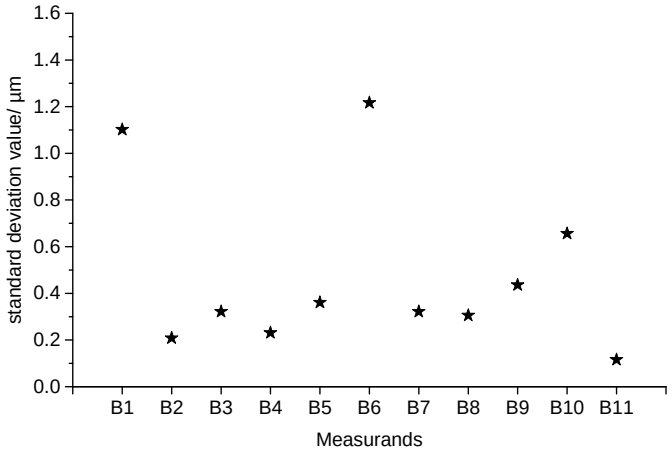

Figure 4.15. Scatter plot for all the measurands of PPS step gauge in Assembly 1. *Adv* was used as segmentation method

As to the multi-material influence on the measurements, it was noticed that the measurement error behaviour appeared to be positively influenced by *HASs*. It can be seen from the measurements of the *PPS* step gauge show smaller systematic errors in *Assembly 2* than in *Assembly 1*, with a reduction of up to 50% in systematic errors. A possible explanation for this result may be the fact that *HAS* acts as a further beam hardening filter. *HASs* did not appear to be influenced by *LASs*, even for the lowest absorption ratio. The measurements of the *Al* step gauge all show a similar error trend independently of the material of the second step gauge included in the assembly. The obtained measurement results were also compared to results of mono-material investigations involving the same step gauges [53]. No differences were observed in terms of measurement accuracy under similar scanning conditions. It can be concluded that multi-materials investigation can be done without any loss of accuracy provided that a suitable set of scanning parameters is found.

4.2.5 Conclusions

This study has concerned a comparison of surface determination methods commonly available in commercial software for dimensional inspection. The study was based on three multi-material assemblies, each of them involving two step gauges, and led to the following conclusions:

- Most segmentation methods yielded a maximum measurement error of 40% of the voxel size. Smaller measurement errors in the order of 15% of voxel size were noticed for measurands imaged in the centre of the X-ray beam. *ISO* yielded measurement errors in the order of 1 voxel size.
- All surface determination methods show similar repeatability as small differences among the standard deviations of the surface determination methods were observed for each single step gauge. The standard deviation values were found to be independent of the inspected length. In some cases, similar standard deviation values were recorded for measurands having different size.
- Concerning the multi-material influence on the measurements, it was noticed that the measurement error behaviour appeared to be positively dominated by *HASs*. Multi-materials investigation can be conducted without any loss of accuracy provided that the surface determination process is fine-tuned for each component in an assembly.
- The effect of the starting point was also investigated, leading to two main considerations. The first one is that better measurement results were achieved when the starting point was automatically defined for all surface determination methods. The second one is that the optimal thresholding value did not necessarily represent the minimum grey value between air and material distribution.

4.3 Quantification of the Contribution of Post-Processing to CT Measurement Uncertainty

4.3.1 Workpiece

The measured workpiece is the two-part component from a commercial insulin injection device from Novo Nordisk A/S already presented in Section 4.1.1. Six measurands were selected on assembly and shown in Figure 4.16.

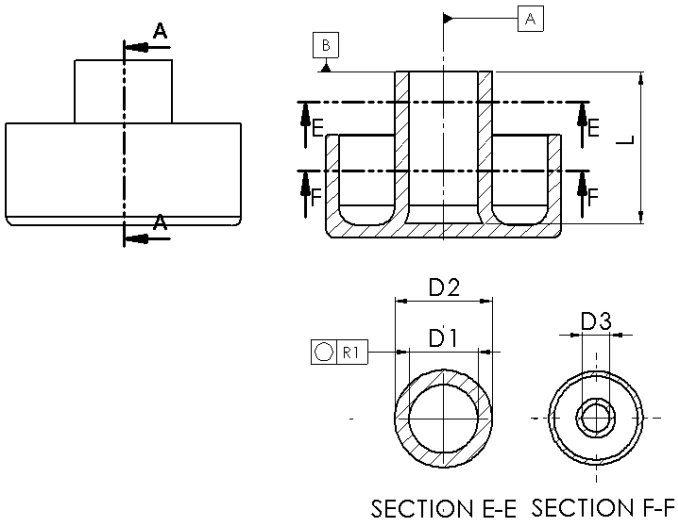

(a)

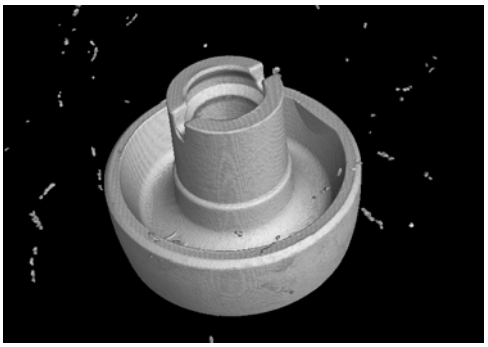

(b)

Figure 4.16. The workpiece and its (a) datum system and measurands and (b) CT representation

Six measurands (four dimensional and two geometrical measurands) were selected on the assembly in this work. *D1* and *D2* represent the inner and outer diameter of the smallest cylindrical feature measured at 2 mm below the *Datum B*. *D3* is the inner diameter of the smallest cylindrical feature measured at -5 mm from the *Datum B*. *R1* represents the roundness of *D1*, *F* stands for the flatness, measured at the bottom of the item (external surface). *L* corresponds to the distance between the top and the bottom of the inner component. These measurands were chosen in such a way as to provide a mix of datum-dependent (e.g. diameter, roundness) and datum-independent (e.g. flatness) results. The positions of the measurands were selected to generalize the results with respect to anisotropies in the measuring volume of CT that result from factors such as noise, the Feldkamp effect, the tilt of the rotary axis, and the

anisotropy of the detector performance. The workpiece was selected for its surface texture being representative of industrial parts produced using injection moulding.

The figure also reports the used datum system that was based on two features, namely *Datum A* and *Datum B*. *Datum A* is determined as the axis of a cylinder defined by means of two circles. This datum feature enables the locking of 4 degrees of freedom. *Datum B* is defined as a plane on a flat surface of the component. This datum feature enables the locking of the two missing degrees of freedom. The cylinder covers the whole volume of component including the selected measurands. The origin of the datum reference is defined in the intersection of two selected datum features. The datum features were least square fitted.

4.3.2 Experimental plan

The investigation was carried out according to the procedure outlined in Figure 4.17. After scanning and reconstructing the stack of X-ray projections, the CT volume model was loaded in the inspection software and then inspected. The inspection was conducted using a measurement template. The template included all measurands except alignment. Once the measurands were extracted, the software was shut down and restarted to ensure the same set of initial conditions for post-processing. The procedure was replicated 10 times distributed over two working days. The long data collection period was necessary in order to remove or at least minimise mnemonic behaviours of the operator. Surface determination was based on local thresholding approach available in VG Studio Max 2.2.6. The 3D evaluation was performed on the voxel model using VG Studio Max 2.2.6 inspection software, as it behaves in relation to the geometrical measurements. The evaluations were performed using primitive features available in the used inspection software. Diameter measurements were performed at the selected positions as shown in figure. The diameters were fitted using circles as elementary features rather than cylinders due to the tapered profile of the workpiece. The diameters were all based on a least-square fit at the 99 % confidence level. Roundness measurements were based on 95% of fitted points in order to filter some noise out. Flatness was measured within a rectangular area of 3.5 x 3.5 mm and its quantification based on a least-square method. Length measurements were evaluated as a distance between two planes, which were both least square fitted. All features were fitted using 2000 points, which guaranteed a fitting step below 30 μm for all features. Further parameters such as fitting gradient and edge avoidance were kept constant for all evaluations as it is usually done in industry.

All analyses were conducted on a singular CT volume model to minimise the influence of other influence factors (mainly related to CT stability over time) on the investigation, but also in order to avoid any correlated errors in the present investigation.

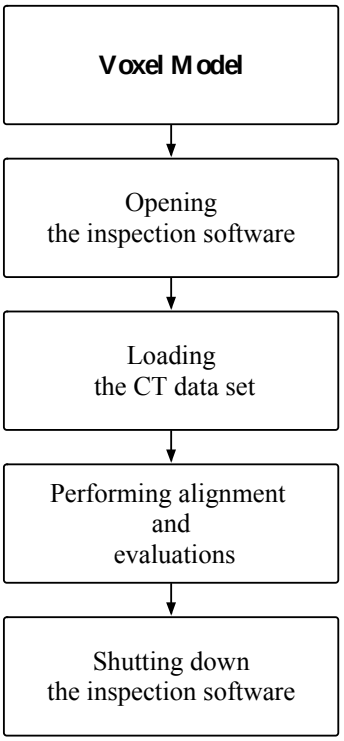

Figure 4.17. Measurement procedure used for the investigation. The procedure was replicated 10 times in order to collect sufficient statistics

4.3.3 CT measurements and measurement uncertainties

The CT measurements were carried out at Novo Nordisk using a Zeiss Metrotom 1500. The XCT system was located in an air-conditioned laboratory with the temperature controlled to 20 ± 1°C and a relative humidity of 50% ± 10%. A measuring device was placed on the rotation table to record the temperature during measuring. This information was used for the correction of systematic error and for the measurement uncertainty statements. Since the temperature was recorded only at one spatial point, temperature gradients inside the measuring volume including the workpiece were not considered. Nevertheless, it is reasonable to assume that the temperature is rather uniform within the limited measurement volume including the workpiece. The item was placed in a slightly tilted fixture to minimise the Feldkamp error [1]. The scanning parameters (see Table 4.10) were selected to stretch the available grey values in the histograms as much as possible, as a larger histogram produces better CT data.

Table 4.10. Scanning parameters used for the scan

Parameter	Unit	Value	Parameter	Unit	Value
X-ray source voltage	KV	100	Magnification		7
X-ray source current	µA	390	No. of projections		1000
Voxel size	µm	39	Integration time	ms	1500
Spot size	µm	36	No. of images for projection		1

The spot size was kept as small as possible to avoid influencing the image sharpness. The number of projections, and therefore the scanning time, was chosen to limit the X-ray beam drift due to heat generation. The limited power used makes spot-drift-blurring negligible with respect to other blurring contributions. The magnification was selected as a compromise to reduce the border artefacts (most likely caused by the Feldkamp effect) while limiting the uncertainty contribution from the voxel size. No physical systematic error corrections (e.g. scale error correction) were done because the CT is equipped with guides and drives that produce a negligible scale error with respect to other systematic errors affecting CT. The workpiece was gently cleaned in order to remove dust which can contribute to noise. Software corrections (e.g. shading correction and beam hardening correction) were automatically performed during the reconstruction by scanner. The shading correction was relatively quick (less than 6 min). A qualification of the rotary axes was also conducted because of the limited size of the workpiece. The qualification was based on a reference object having a sharp edge. Neither beam hardening nor Feldkamp artefacts were noted on any surfaces (see, Figure 4.18). The uniformity of grey values confirms the feasibility of scanning the two components in assembled state. The outer surfaces of workpiece, which are covered by the fixture, show an inferior quality compared to the fixture-free surfaces. In contrast, a large distribution of background noise was observed in the X-ray projections. Noise was measured as the standard deviation of the grey value in a region of 10 x 10 pixels each and was found to be approximately 350 grey values. High gain used to achieve a well-spread grey value histogram may represent the main contribution to noise.

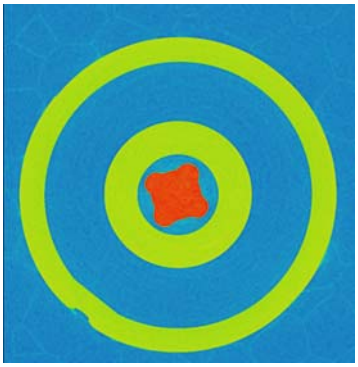

Figure 4.18. Reconstruction slice, modified in Fiji image processing software, of the two-part component showing the complete absence of image artefacts. Inner component shows a different colour because of its higher X-ray absorption

Expanded measurement uncertainties for CT measurements of the assembly were estimated according to the PUMA method (ISO 14253-2) [114], as described in equation 12.

$$U = 2 \times \sqrt{u_r^2 + u_p^2 + u_{res}^2 + u_T^2 + u_{noise}^2}, \tag{11}$$

where u_r is the standard uncertainty owing to traceability quantified using the MPE_{SD} (9 µm + L/50). The MPE_{SD} represents the maximum permissible error for sphere-to-sphere measurements. The MPE_{SD} value was transformed into an uncertainty contribution by using a Type B and a rectangular shape [12]. It is necessary to point out that the *MPE* was only used as an estimate of traceability measurement because the CT is periodically controlled without showing any departure from the specification stated by manufacturer; u_p is the standard uncertainty of the measurement procedure assumed to be 1.1 µm; u_{res} is the standard uncertainty due to the CT resolution, quantified as follows

$$u_{res} = \sqrt{u_f^2 + u_{rec}^2}, \tag{12}$$

where u_f and u_{rec} are the standard uncertainties associated with the focus spot size and the eccentricity of the rotary table [14]. The focus spot size was based on the manufacturer information reported in the manual, while the eccentricity of the rotary table was assumed to be 2 µm. Those uncertainties were both quantified using a *Type B* evaluation and using a rectangular distribution. Note that the voxel size was not considered as a source of influence for the resolution as the scan was conducted at high magnification at which resolution, or better structural resolution, is governed by focus spot size and the rotary table errors; u_T is the evaluation of standard uncertainty of the temperature deviation (± 1 °C). This uncertainty was quantified using a *Type B* and a *U-shape* distribution [12], u_{noise} is the evaluation of standard uncertainty due to the scanning noise. Such a contribution was based on the histograms of fitted points and modelled using a rectangular distribution. Such a contribution was only taken into account for form measurements as dimensional measurements are all Gaussian-based features, which are, by

definition, very robust against noise. The noise uncertainty was quantified to be 1 μm. The expanded measurement uncertainties at 95% confidence level were found to lie in the range of 11 to 13 μm. The CT measurement and their measurement uncertainties showed a good metrological compatibility with CMM measurements, as proved by the E_n values ranging from 0.29 to 0.75. By taking into account the E_n values, it is believed that an additional reduction of measurement uncertainties would be feasible. The E_n values quantified in this investigation were found to be in a very good agreement with the E_n values of CT measurements conducted on single components using the same operator and measuring equipment. As a result, an increase in the throughput of a CT measurement of approximately 50% can be achieved.

4.4.4 Results and discussions

Table 4.11 lists the standard deviation value per measurand and the average value of all standard deviations, σ_m. The latter was quantified assuming no correlation between the standard deviations, σ_i.

$$\sigma_m = \frac{1}{6} \times \sqrt{\sum_{i=1}^{N=6} \sigma_i^2}. \tag{13}$$

Table 4.11. Standard deviation value for each measurands (σ) along with the mean of all standard deviations (σm). The values are rounded and expressed in μm

Measurands	identification	σ_{10}
D1	Diameter (datum feature)	4.0
D2	Diameter	2.5
D3	Diameter (datum feature)	2.8
R1	Roundness	3.0
F	Flatness (datum feature)	1.5
L	Length	3.0
σ_m		2.8

Statistical tools such as the Anderson-Darling test [15] and Chauvenet's criterion [15] were used to ensure the absence of measurement errors such as outliers or mean drifts. No outliers were observed in the results, and none of the Anderson-Darling tests reported any departure from normality.

Diameter and roundness measurement generally showed the largest variation, ranging from 2 µm to 4 µm depending on the feature size. Inner and outer diameters yielded similar results, most probably due to the negligible beam hardening. Outer diameter *D2* yielded the greatest standard deviation, which is coherent with the fact that *D1* is biggest feature investigated. Those measurands are all influenced by all three parameters under investigation. The measurements of *F* showed the smallest variation because that measurand only depends on fitting and surface determination. As a consequence, it can be believed that fitting and surface determination are less important uncertainty contributions than the datum system.

Since the results obtained in this form did not enable an independent assessment of the three variables under investigation, two further tests were conducted. The first test was conducted fitting all selected features 10 times within the same evaluation (and thus same alignment and surface determination as well as starting points). The features were fitted using randomly distributed starting points. Since neither surface determination nor datum system was modified, the standard deviation values collected were assumed to be the fitting repeatability, which was found to be of about 0.3 µm. An example of results is reported in Figure 4.19 for diameter D2.

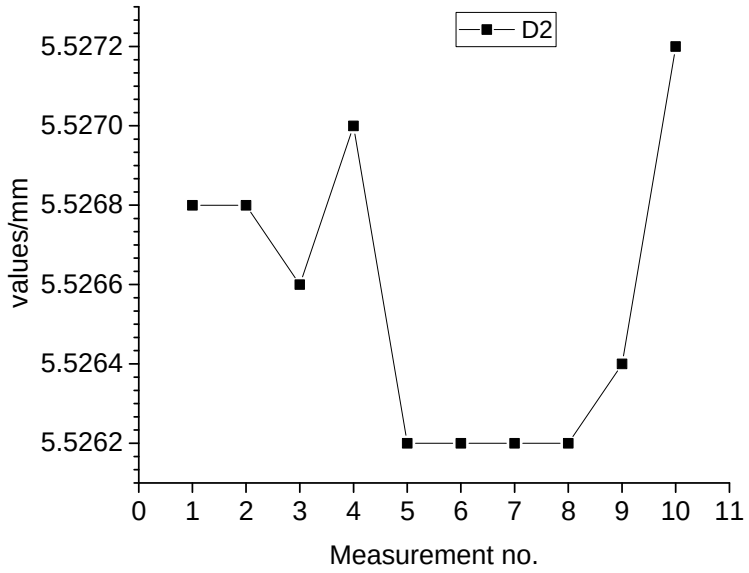

Figure 4.19. Results of diameter measurements, *D2*. The feature was measured 10 times without modifying datum system and surface determination. The registered variability is only due to the fitting variation

The second test dealt with the surface determination repeatability. The test was designed in such a way as to keep fitting and datum system unchanged. Surface determination was found to be repeatable with a maximum standard deviation of about 0.1 µm. This high repeatability was obtained in the presence of a fully automatic surface determination process and a rather uniform distribution of grey values. It is therefore reasonable to expect a worse repeatability when surface determination is manually defined by operators.

Taking into account the results of all three investigations, it was concluded that the datum system is the factor that mainly caused the observed measurement variation. The quantification of the datum system uncertainty was approached using two models. The first model is based on σ_m. The second model

quantifies the uncertainty contribution due to the datum system by weighting the various datums as shown in equation 15.

$$u_{datum} = \sqrt{\frac{4}{6}\sigma_A^2 + \frac{2}{6}\sigma_B^2}, \tag{15}$$

where σ_A and σ_B are the standard deviations for the *Datum A* and *Datum B*. Since *Datum A* was based on two datum features (*D1* and *D3*), the maximum standard deviation between the two datum features was assumed as σ_A. The weighting factors represent the number of degrees of freedom locked by each datum feature. The equation is based on the propagation of errors and assumes no correlation among features used for defining the datum system. Despite the modelling effort, the refined uncertainty provides a negligible difference ($u_{datum} = 2.60\ \mu m$) with respect to the first model. By adding the datum system uncertainty to equation 12, the new measurement uncertainties were found to be in the range of 12.9 to 14.0 µm, with an increment of up to 17 % compared to the first estimated measurement uncertainties.

Since the increase in the measurement uncertainties appeared to be important, it was thought useful to present solutions which may reduce the impact of the datum system. The first and simplest solution is to use a CAD file to roughly align the CT data sets and then using datum features for establishing a fine alignment. This procedure may be easily implemented in industry as CAD files of the inspected workpieces are available. Under specific conditions, the CAD file may be replaced with a CT data set involving the same component. A second solution could be to improve the imaging process by using e.g. more frames per projection. This strategy decreases the image noise at cost of increasing the scanning time. A further possibility would require defining datum systems based on features lying in the centre of the beam, in which the image noise has a small extent.

4.3.5 Conclusions

This third work has investigated the extent to which the CT post-processing operations contribute to the uncertainty of CT measurements. Post-processing operations such as surface determination, data fitting, and the definition of the datum systems has been taken into account. The evaluations were performed on an industrial assembly. Dimensional and geometrical measurands were selected to have different responses to the various post-processing settings. The following conclusions can be drawn:

- Surface determination was not found to be a source of influence because it was characterized by a very high repeatability. It was also believed that the repeatability may be larger for inspections involving more absorbing materials.
- Fitting algorithms were likewise found to have high repeatability. No impact of the distribution of the initial fitted points on the measurement results was noticed
- The datum system was found to be the most prominent source of uncertainty in the investigation. This was observed using two different approaches to the quantification (2.80 or 2.75 μm). Because of datum uncertainty, the expanded measurement uncertainties incremented by up to 17 % for measurands depending upon the datum system.
- The uncertainties of the CT measurements were found to vary between 11 and 13 μm. A good agreement between the CT and CMM measurements was found according to E_n values. The E_n values quantified in this investigation were furthermore found to be in a very good agreement with the E_n values of CT measurements conducted on single components using the same operator and measuring equipment. As a general result, an increase in the throughput of a CT measurement of approximately 50% can be achieved.

Chapter 5

Development of Reference Artefacts for Concurrent Scale Error Correction

Summary

A novel type of artefact for calibration of the scale in CT is presented. The artefact is positioned and scanned together with the workpiece inside the CT scanner producing a 3D reference system for the measurement. The artefact allows a considerable reduction of time by compressing the full process of calibration, scanning, measurement, and re-calibration, into a single process. Furthermore, the method allows a considerable reduction of the amount of data generated from CT scanning. Two prototypes, CT tube and CT crown, were calibrated on a tactile CMM and their applicability demonstrated using different calibrated workpieces.

5.1 CT tube: design, manufacture, and calibration

CT tube, shown in Figure 5.1, consists of a number of ruby spheres spatially placed on a carbon fibre tube. Ruby spheres were selected as reference elements for their X-ray attenuation properties enabling good detectability at acceleration voltages used in industrial CT, and their low predisposition to create imaging artefacts [3]. The spheres are distributed in such a way as to avoid any overlap between two spheres at any angular position. This selected pattern minimises the impact of spheres on the surface quality of the workpiece being imaged. The tube was selected because it gives a uniform amount of material to be penetrated at any angular position. The manufacture of the tube was based on a series modulus Toray T700, oriented at 0° and 90°, providing high penetrability to X-rays and good mechanical proprieties, and giving room to scaling down the wall thickness, which is 1.6 mm in the current prototype. X-rays will penetrate 3.2 mm at any angular position. The selected thickness value was based on a trade-off involving three critical factors, namely absorption value, mechanical stability and market availability.

Figure 5.1. CT tube surrounding a workpiece (Lego brick)

The fabrication of the artefact was based on adhesive joints, the only exception being a series of 1 mm centre holes drilled on the tube to trap the glue. The same amount of glue in each hole was injected, ensuring that all joins show similar thermal and dimensional behaviours. All spheres were visually inspected in order to detect potential scratches and residual glue. The tube is mounted on an Invar™ plug. The inner diameter of the invar plug was designed to provide an interference fit over the inner tube surface of approximately 15 mm. The thickness of plug was designed to withstand a workpiece without being itself deformed. This is a factor of importance in connection with the dimensional stability during the use of the CT tube. The design of the plug was carried out assuming that workpieces placed within the CT tube will have weights smaller than 0.1 kg. The weight was modelled as an equally distributed force on the surface of the plug. The outer diameter of the plug was chosen to give a large contact area simplifying the positioning of the CT tube on any rotary table. In order to unequivocally identify the spheres, three through holes were machined on the tube. Two of the three holes are placed at the same angular position but at different heights and define the zero position. The third hole is placed at a different angular position and defines the counting direction of the spheres.

The artefact can be considered as a 3D CT artefact with the main ability of correcting scale error. The CT tube can however be adopted for characterizing the measuring volumes.

Calibration was accomplished using a Zeiss CARAT tactile CMM, characterized by a maximum permissible error MPE = 0.4 + L/900 μm (L in mm). Figure 5.2 shows the measurement set up for calibration of CT tube. The CMM was equipped with an integrated rotary table and a 4 mm diameter probe, with the probe direction normal to the spheres on the CT tube. The use of the rotary table enabled the use of a single probe for all spheres, reducing measurement uncertainty. Generally speaking, the calibration of each probe yields an uncertainty in the range of 0.1 to 0.1 μm, depending on the performance of the used CMM. Measurements were performed at a temperature of 20 ± 0.5°C with automatic temperature compensation by the CMM software. A constant probing force of 0.05 N was used throughout

the calibration. The calibration was performed after the artefact acclimatisation. The calibration concerned sphere-to-sphere distances as well as sphere diameters and form errors. Traceability was transferred using a Zerodur hole plate for the sphere-to-sphere distances, and a 8 mm reference sphere for the diameter and form of spheres. Table 5.1 reports information regarding the two material standards used for achieving traceability of the features being calibrated. Due to its high thermal stability, the hole plate was also used for correcting the systematic errors of the CMM.

Although the hole plate did not fully resemble the CT tube´s shape, its source of traceability was assumed to be reliable for the following reasons. Firstly, the single probe only moved along one axis due to the use of the rotary table as an angular indexing feature. As a consequence, the CT tube can be seen as a ball bar. Secondly, both spheres and holes are probed by CMM inspection software in the same way. The CT tube was aligned using the typical alignment procedure commonly used for artefacts resembling a tetrahedron. A plane was defined using three spheres. A line was constructed using two other spheres. Ultimately, the intersection between plane and line was selected as zero point of the alignment system.

Table 5.1. Information regarding calibration artefacts used for establishing traceability of calibration equipment

Object	Certificate
Calibration sphere, Ø8 mm	Carl Zeiss Certificate 2715 Dated: 10th August 2012
Zerodur hole plate, 50 mm between Hole 1 and Hole 2	PTB Certificate 4758 PTB 05 Dated: 16th September 2005

Figure 5.2. Measurement set up for calibration of CT tube

The artefact was measured in one position comprising two measurement sequence patterns (clockwise and anti-clockwise). Such patterns offer a way to isolate and minimise drift and rotary table effects by averaging the results [5]. The position of the artefact was kept under control by probing the first sphere

at the beginning and end of each sequence, and subsequently calculating the *X*, *Y*, and *Z* distances between the spheres. The deviations were for both patterns found to lie within the *MPE* of the CMM. Assuming a rectangular distribution for this influence factor, the uncertainty contribution coming from the positioning error was found to be 0.18 µm. Such magnitude confirmed the good stability of the rotary table and of the fixturing strategy during the calibration process. No additional error separation techniques (e.g. swing around [6]) were used due to the lack of a fully symmetrical distribution of reference elements.

Spheres were probed using 25 points evenly distributed over 5 lines equally spaced at 0.3 mm steps, and their diameters quantified using a least square fitting. The sphere surfaces being close to the carbon fibre frame were not probed to avoid glue. This procedure is typically used in any artefacts involving sphere, including those ones used for probe qualification in tactile CMMs. A series of calibration cycles were performed over different days and their results taken into account for quantifying the repeatability of the calibration process. The different calibrations were also conducted to investigate the stability of the joints and fixture, and the repeatability of the rotary table. The calibration equipment was not used for other measuring tasks throughout the course of the artefact calibration. The environmental conditions were found to be in agreement with the laboratory specifications. Ultimately, the inspection was not rebooted in order not to modify the zero point to which the datum system had been defined. Measurement uncertainties, *U*, based on the short-term repeatability according to [114] are quantified as follows:

$$U = k \times \sqrt{u_{cer}^2 + u_{tran}^2 + u_{rot}^2 + u_p^2}, \tag{15}$$

where k is coverage factor ($k = 2$ for a confidence level of 95%), u_{cert} is the standard uncertainty from the calibration certificate of the material standard, calculated as $u_{cert}=U_{cert}/k$, u_{tran} is the standard uncertainty during the traceability transfer u_{tran} quantified by the standard deviation s of $n = 5$ repeated measurements on the hole plate, u_{rot} is the standard uncertainty coming from the indexing error of the rotary table, and u_p the standard uncertainty from measurement repeatability in two sequence patterns calculated according to equation 17:

$$U_p = \sqrt{\sum_{i=1}^{m} \frac{(S_i^c)^2}{n} + \sum_{i=1}^{m} \frac{(S_i^{ac})^2}{n}}. \tag{16}$$

In equation 17, s^c and s^{ac} are the standard deviation of repeated measurements in the clockwise and anticlockwise pattern, respectively, and n is number of measurements performed ($n = 20$, i.e. 5 measurements in 4 calibration cycles).

Additional uncertainty contributions such as temperature deviation, workpiece expansion coefficient variation, and rotary table errors were taken into account and found to be negligible. Details as to the procedure used for measurement uncertainties are reported in Table 5.2. The results document general calibration uncertainties for the sphere-to-sphere distances below 3.2 µm. The uncertainties for the sphere-to-sphere distances were quantified propagating the error of X-, Y-, and Z-coordinates of the two spheres used for defining each sphere-to-sphere distance.

Table 5.2. Expanded calibration uncertainties (K=2) for all features of the CT tube. *S*, *F*, *X*, *Y,* and *Z* correspond to diameter, sphericity, and X-, Y- and Z-coordinates respectively. All values were rounded to the nearest integer and are expressed in mm

Uncertainty contribution	Symbol	Modelling	Measurand				
			D [µm]	*S* [µm]	*X* [µm]	*Y* [µm]	*Z* [µm]
Traceability	u_{cert}	Type B	0.3	0.3	0.3	0.3	0.3
Transfer	u_{tran}	Type A	0.2	0.2	0.5	0.5	0.5
Rotary table	u_{rot}	Type A	0.1	0.1	0.1	0.1	0.1
Repeatability	u_p	Type A	0.4	0.4	0.4	0.4	0.9
Expanded uncertainty	U (k = 2)		1.10	1.10	1.42	1.43	2.22

5.2 CT crown: design, manufacture, and calibration

The CT crown, shown in Figure 5.3, comprises a rigid base on which a number of spheres are positioned on stems. The spheres are made of ruby providing high contrast and low predisposition to create imaging artefacts. The stems are made from carbon fibre which is a low X-ray absorption material, and have the same diameter (8 mm) but different lengths ranging from 20 mm to 60 mm, giving spatially distributed sphere-to-sphere distances. The stems were drilled for positioning the spheres. The base was fabricated via turning, from an invar bar, with a series of though holes to accommodate the stems. Interference fit was used for fixing the stems within the holes. The artefact was assembled using adhesive joints. Some glue was also distributed at the interfaces between stems and invar base.

Figure 5.3. CT crown positioned with a Lego brick placed inside

The calibration of the CT crown was accomplished using the same tactile CMM used for the calibration of the CT tube. The measurements were performed using a 20 mm long probe with a 3 mm spherical probe. A force of 0.05 N was set and its systematic contribution to measurements corrected interpolating the deflection of two additional probing forces, such as 0.10 N and 0.15 N. Such procedure was not used for the CT tube due to its higher stiffness along the probing direction. Figure 5.4 shows the measurement set up used for the calibration of CT crown. The calibration concerned sphere-to-sphere distances as well as sphere diameters and form errors.

Traceability was established using a Zerodur™ hole plate for the sphere-to-sphere distances, and a 8 mm reference sphere for the diameter and form of spheres. Table 5.1 reports information regarding the two material standards used for the calibration. Systematic errors in the order of 0.15µm were quantified for the CMM used for the calibration task. Each sphere of the CT crown was probed at 21 positions, distributed over three equally spaced sections. From the measurement results, a Gaussian least squares sphere is calculated. No filtering method was applied for form measurements. The fitting strategy used was based on a macro program available in the CMM software.

Measurements were performed at a temperature of 20 ± 0.5 °C with automatic temperature compensation by the CMM software. 2 calibration cycles of 10 measurements each were performed on the artefact. The calibration was conducted on two different days in order to take into account the stability of the measurement set-up. Different fixturing strategies were also involved. No correlation was observed between fixturing strategies and measurement repeatability. Expanded measurement uncertainties, *U*, based on the short term repeatability according to [114] are quantified as follows:

$$U = k \times \sqrt{u_{cert}^2 + u_{tran}^2 + u_{force}^2 + u_p^2}, \tag{17}$$

where k is coverage factor (k = 2 for a confidence level of 95%), u_{cert} is the standard uncertainty from the calibration certificate of the material standard, calculated as $u_{cert} = U_{cert}/k$, u_{tran} is the standard uncertainty during the traceability transfer u_{tran} quantified by the standard deviation s of n = 10 repeated measurements on the hole plate, u_{force} is the standard uncertainty coming from the correction of probing force. This last contribution was not taken into account for sphericity measurements; u_p the standard uncertainty from measurement repeatability in two measuring patterns, one clockwise and one anti-clockwise. Details as to the measurement uncertainty contributions are reported in Table 5.3. The results document general calibration uncertainties for the sphere-to-sphere distances, and for the diameter and form of the spheres below 2.3 µm. The repeatability was found to be similar for all measured features including the *Z*-coordinate whose repeatability is typically low due to the adhesive joints. The results document general calibration uncertainties for the sphere-to-sphere distances below 3 µm. This value was based on the propagation of the error [127].

Figure 5.4. Measurement set up used for the calibration of CT crown

Table 5.3. Expanded calibration uncertainties (K=2) for all features of the CT crown. *S*, *F*, *X*, *Y,* and *Z* correspond to diameter, sphericity, and X-, Y- and Z-coordinates respectively. All values were rounded to the nearest integer and are expressed in mm

Uncertainty contribution	Symbol	Modelling	Measurand				
			D [µm]	*S* [µm]	*X* [µm]	*Y* [µm]	*Z* [µm]
Traceability	u_{cert}	Type B	0.3	0.3	0.3	0.3	0.3
Transfer	u_{tran}	Type A	0.2	0.2	0.5	0.5	0.5
Force	u_{force}	Type A	0.3	-	0.2	0.2	0.2
Repeatability	u_p	Type A	0.7	0.7	0.7	0.7	0.9
Expanded uncertainty	U (k = 2)		1.70	1.59	1.62	1.62	1.98

5.3 CT workflow using the developed reference artefacts

The first step is to physically place the workpiece being inspected inside the artefact as shown in Figure 5.3. Any contact between the artefact and the workpiece should be avoided in order not to modify the geometry of the artefact and of the workpiece during scanning. The workpiece can be placed inside the tube by using low absorption fixtures which can also be glued on the invar base for better grip.

The selection of scanning parameters in the presence of the reference artefact should be done by seeking to have a good contrast in both workpiece and spheres. It is advisable to have the total distribution of grey values covering a range of values from 12000 to 59000. The magnification factor should be large enough to image at least two spheres at any angular position, otherwise some image frequencies will be missing.

The reconstruction of the data sets including the reference artefact did not present any difference with respect to the typical process used for a single workpiece. The projections can be cropped during reconstruction in order to reduce the file size.

The determination of the surface for all investigations should also be conducted in two separate processes. The first process defines the surface of the artefact while the second one of the workpiece. Two separate surface determination processes are required due to the different absorption coefficients between the artefacts and workpieces. The determination of the surface of the reference artefacts is conducted by manually selecting the spheres and the frame on the reconstruction images by means of region of interests (*ROIs*). As a result, two representative grey values (one for spheres, one for frames) are defined. From those two grey values, a thresholding condition which is improved using a local surface method can be computed. The local surface method is conducted using a search distance ranging from 6 voxels to 10 voxels depending on the physical distance between the workpiece and the artefact. Surface determination methods other than thresholding can also be used to define the surface. The determination of the surface of the workpiece follows the presented procedure, the only exception being the considered grey value. In cases where the workpiece materials are similar to the artefact ones, a single surface determination process could be sufficient. Figure 5.5 reports a reconstructed volume model of the CT tube before and after having been segmented.

As for the determination of the surface, the inspection of a data set including a reference artefact requires two steps. The first step is to inspect the workpiece according to the specific requirements. The second step is to measure the sphere-to-sphere distances of the artefact. Each sphere should be least square fitted using a large number of equally distributed points on its upper hemispherical part. Note that area of spheres which are close to the frame should not be fitted due to some residual glue. Depending on the features implemented in the inspection software packages, the upper hemispherical portion of each sphere can be obtained either using a *ROI* or using fitting ad-hoc patterns. The use of ROIs requires a preliminary alignment system. Sphere-to-sphere distances can be finally used for correction

according to any method developed for scale error correction. In this thesis the quantification of the scale error correction, S_{vox}, was based on Equation 19.

$$S_{vox} = \frac{1}{n}\sum_{i=1}^{n}\frac{L_i^{CMM}}{L_i^{CT}}, \tag{18}$$

where, L_i^{CMM} and L_i^{CT} are *i*-sphere-to-sphere distances measured by CMM and CT, respectively; *n* stands for the number of lengths used for correction. The developed prototypes provide up to 15 independent lengths. The corrected voxel size is given by multiplying the S_{vox} value by the original voxel. When the S_{vox}, which is an average value, presents a large standard deviation value due to e.g. noise, the S_{vox} value is replaced by the median value, S_{vox}^{median}. The median is a robust measure of central tendency. The median has a breakdown point of 50%, while the mean has a breakdown point of 0% [128].

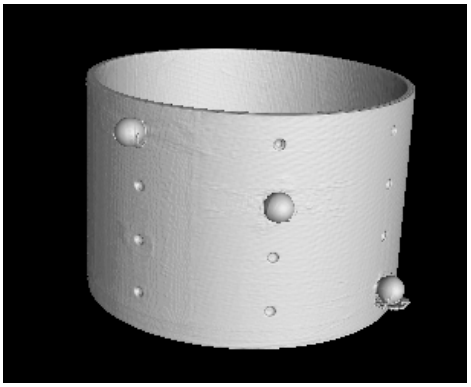

(a)

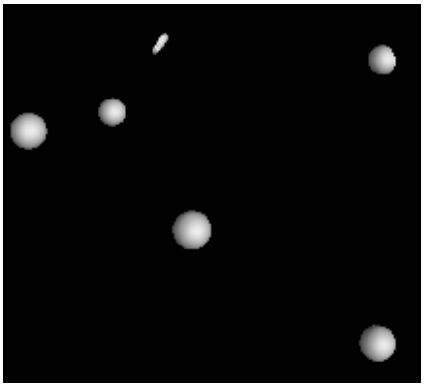

(b)

Figure 5.5. Reconstructed volume model of the CT tube (a) before and (b) after having been segmented

5.4 Application on industrial CT scanner using calibrated workpieces

Four different experiments were conducted to evaluate the applicability of the online reference artefacts. The investigations included different workpieces, materials, and measurands. The applicability of the online reference artefacts was based on comparisons with an off-line reference artefact and two tactile CMMs. Measurement uncertainties were also stated for all investigations involving online reference artefacts.

Experiment 1: Testing of the CT tube using a mono-material workpiece

The CT tube was used as an online reference artefact, while a miniature PPS step gauge with a calibration uncertainty ranging from 1.5 to 2 µm depending on the measurand was used as a workpiece (see Figure 5.6). The test procedure consisted of two series of scans on a Nikon XT H 225 CT: three repeated scans of the step gauge alone, after scanner calibration, and three repeated scans of the step gauge placed inside the CT tube. The scanning parameters listed in Table 5.4, with the step gauge tilted at 45°, were-used in both cases. From the table it can be seen that an X-ray source power of 37 W was used in order to give good contrast without extending scanning time (integration time = 1 s).

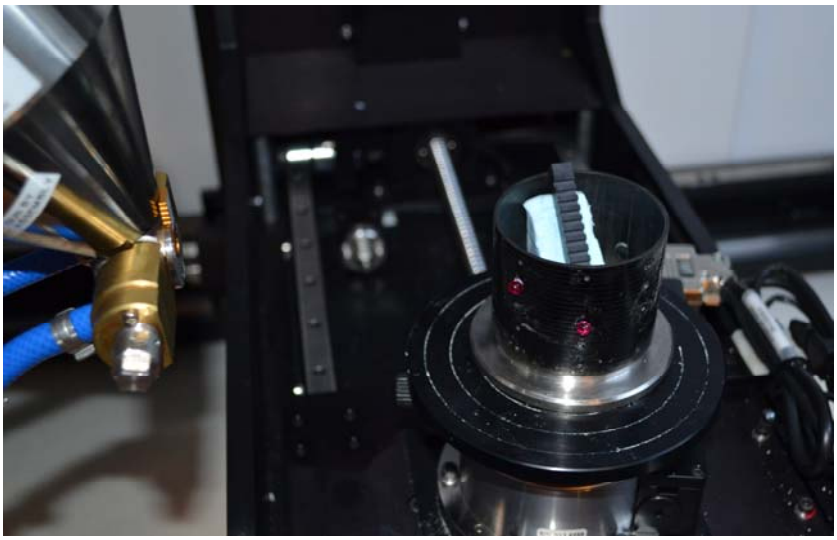

Figure 5.6. CT tube positioned on a CT rotary table with the PPS step gauge

No averaging was used in order not to smooth the noise effect. Spot size was kept below the voxel size leading to negligible geometrical unsharpness on the detector. The X-ray source was set with a tungsten target having an emission spectrum with the predominance of high energy frequencies at the power required. The temperature in the cabinet during scanning was 23°C ± 1.5°C. Step gauge, CT tube and CT ball plate were all acclimatised for 2 hours. Before scanning the detector was inspected in order to exclude the presence of some structures due to previous scans. Some residual structures were observed in the detector but their effect was neglected in connection with the size of the workpiece being imaged.

Physical as well as numerical beam hardening correction, 0.25 mm thick copper sheet and 2nd order software correction, respectively, as well as noise correction based on a Hanning filter, were adopted for all scans. Note that copper filter was added to improve the surface quality of spheres. The correction led to a uniform grey value profile across the step gauge. The data sets were saved as 16-bit files after having been reconstructed. A scale error correction of the CT scanner was carried out using the CT ball plate for the batch comprising the step gauge alone while directly using the CT tube for scale correction of the second series of scans. Both correction methods were based on the approach presented in Section 5.3. A number of 5 sphere-to-sphere distances were used for the CT tube, while 20 distances were used for the CT ball plate. Note that CT tube and CT ball plate have spheres of similar size and material. A detector correction (shading correction) was also performed and kept unchanged during each batch. A correction of systematic error due to the enhanced temperature was done by using a linear model of thermal expansion. No correction was considered for the CT tube as it was assumed to be stable against the temperature. Image analysis was undertaken on the X-ray images considering the grey value profiles at the centre of the step gauge, where the signal-to-noise ratio reaches the lowest values. Fiji open source image processing package was used for this analysis.

Table 5.4. CT scanning parameters used for all conducted CT measurements

Parameter	Unit	Value	Parameter	Unit	Value
X-ray source voltage	kV	150	Magnification		3.5
X-ray source current	µA	250	No. of projections		1600
Voxel size	µm	40	Integration time	ms	1000
Spot size	µm	21	No. of images		1

Measurement accuracy analysis was based on the deviations from CMM measurements for 11 measurands (see Figure 5.7) including 3 unidirectional (*U1* = 4 mm, *U2* = 8 mm, and *U3* = 12 mm) and 5 bidirectional lengths (*B1* = 2 mm, *B2* = 6 mm, *B3* = 10 mm, *B4* = 14 mm, and *B5* = 17 mm), as well as flatness of 3 flanks (*F1* at top, *F2* at centre, and *F3* at bottom of gauge). Such typologies of measurements were believed to be appropriate for examining whether the CT tube has a negative role in the measurement accuracy because of their well-known sensitivity to material [62] and beam hardening, noise, and surface determination thresholding value.

Additionally, the flatness measurements were selected to evaluate whether noise and scattering change while moving closer to the invar base. VG Studio Max 2.2.6 was used for performing surface determination and evaluations. The latter involve a series of length measurements, evaluated as plane-to-plane distances, and flatness evaluations. Almost the entire flank was used for defining planes. All the primitive features were evaluated using least square fit. The evaluations were automatically performed using

a measurement template allowing better replicating of the evaluations. The datum system for the step gauge is performed according to the procedure used during calibration. The primary datum is created through least square fitting of four teeth areas positioned on the top of the teeth of the step gauge. The secondary datum is defined as a symmetry plane of the two most extreme areas along the step gauge longitudinal length. The origin of the datum system is constructed on the left side of the sixth groove. All datum features were based on 1000 equally distributed points and then filtered with a cut-off at 95 %. This means that 950 out of 1000 fitted points were used for constructing each datum feature. In order to replicate betterthe alignment and inspections, each data set was aligned against a CAD file. Subsequently, the datum features were used for fine alignment. No morphological nor image filtering was applied on data sets, whereas point cloud filtering was conducted removing 5% of the biggest deviations of the fitted points, followed by a refitting of the considered feature [62].

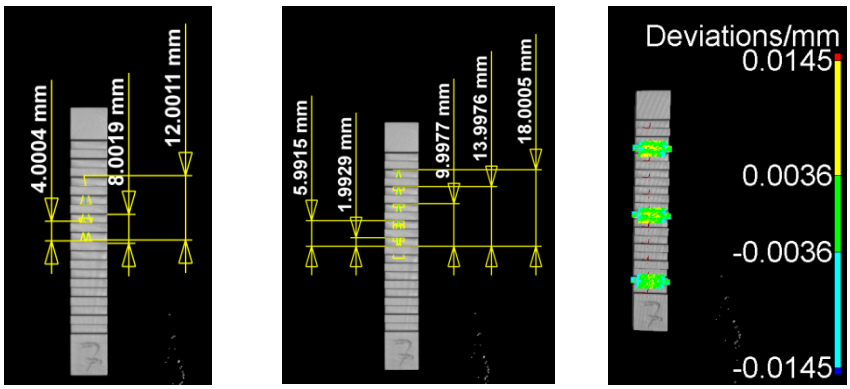

(a) (b) (c)

Figure 5.7. 11 Measurands used for the investigation: (a) 3 unidirectional lengths, (b) 5 bidirectional lengths, and (c) 3 flatness at the top of three teeth. The lengths range from 1.99 mm to 18 mm

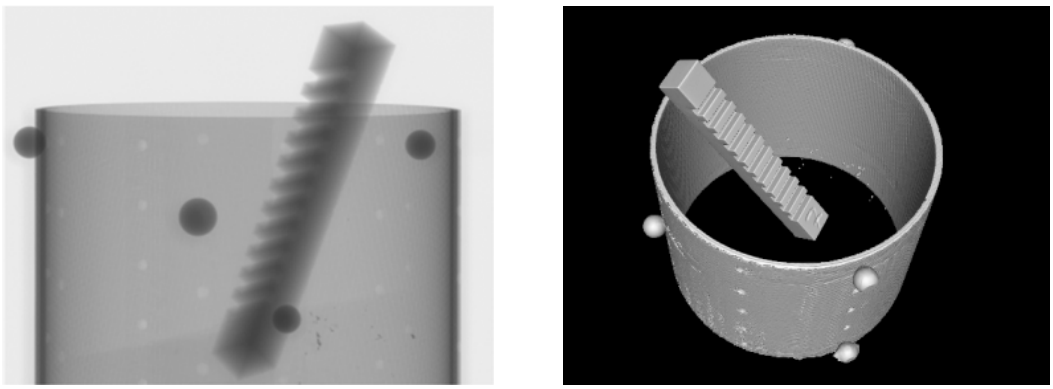

(a) (b)

Figure 5.8. (a) X-ray and (b) 3D reconstruction depicting spheres, carbon tube, and step gauge in 2D and 3D view

Image quality analysis, carried out on the uncorrected X-ray projections for both configurations at the same angular position, see Figure 5.8a, provided evidence that the artefact seems to produce some changes in the distribution of grey values, see Figure 5.9, especially at angular positions at which the gauge was partially hidden by a sphere. This effect does not crucially affect the applicability of the CT tube due to the moderate surface covered by the spheres. The spheres cover approximately 2.4 % of the entire surface of the CT tube. The negligible impact of the spheres on image quality was proved using a two-sample t-test [129]. This test is used to determine if two population means are equal. The test resulted in a *t-value* of - 0.43 and *p-value* of 0.671. Since the obtained *p-value* is bigger that the limit *p-value* of 0.05, it can be concluded that the presence of the CT tube did not yield difference in the distribution of grey values.

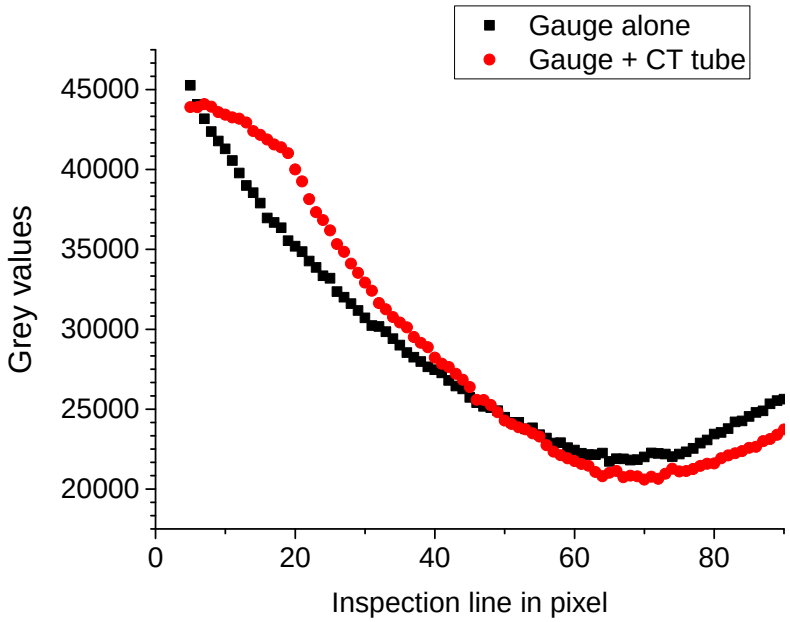

Figure 5.9. Intensity profile comparison between Step gauge alone (blue diamonds) and Step gauge inside CT Tube (red dots). The profile was extracted from two X-ray projections taken at the same angular position. The projections were analysed using Fiji as image processing package

No additional scattering due to the invar fixture was noted on the projections, as it was observed from the grey value gradient profiles at three different heights, at 5, 7, and 9 mm from the bottom of the tube. The determination of the surface, see Figure 5.8b, which is necessary before performing evaluations on a data set, was conducted without problems. This is due to the fact that most of the grey value distributions of the artefact materials and workpiece material occupy different portions within the histogram of the grey values.

Measurement uncertainties for scanning after scanner calibration using the CT ball plate and for scanning using the CT tube together with the workpiece are given by equations 20 and 21, respectively.

$$U_{CTplate} = k \times \sqrt{u_{cal}^2 + u_p^2 + u_T^2 + u_{cor}^2}. \tag{19}$$

$$U_{CTtube} = k \times \sqrt{u_{cal}^2 + u_p^2 + u_T^2 + u_{cor}^2}. \tag{20}$$

Here, k is the coverage facto set equal to 2, u_{cal} is the standard uncertainty from the calibration certificate of the CT tube and of the CT ball plate, respectively, calculated as $u_{cal}=U_{cal}/k$; u_p is the standard uncertainty due to the repeated CT measurements (n=3); u_T is the standard uncertainty due to the temperature (ΔT = ± 1°C), and u_{cor} is the standard uncertainty associated with the reliability over time of the scale error correction. The experimental standard deviations were found to be approximately 1.3 µm for all measurands. The only difference between the two equations is that u_{cor} = 0 in the case of concurrent calibration using the CT tube. This contribution can become extremely relevant in case of a long delay time between scanner calibration and workpiece scanning. In this investigation, the time between scanner calibration and workpiece measurement during the first series was limited and u_{cor} is therefore small

also in the case of off-line calibration using the CT ball plate. Expanded uncertainties $U = 3.4$ µm were estimated for all measurands and for both series of CT measurements. Measurements on the step gauge carried out in the two different ways were found to be in agreement, as shown in Figure 5.10 and confirmed by E_n values [15] all less than 0.6. Table 5.5 reports all the E_n values. The above figure also shows that the stated measurement uncertainties are not sufficient to cope with the systematic errors affecting the CT measurements.

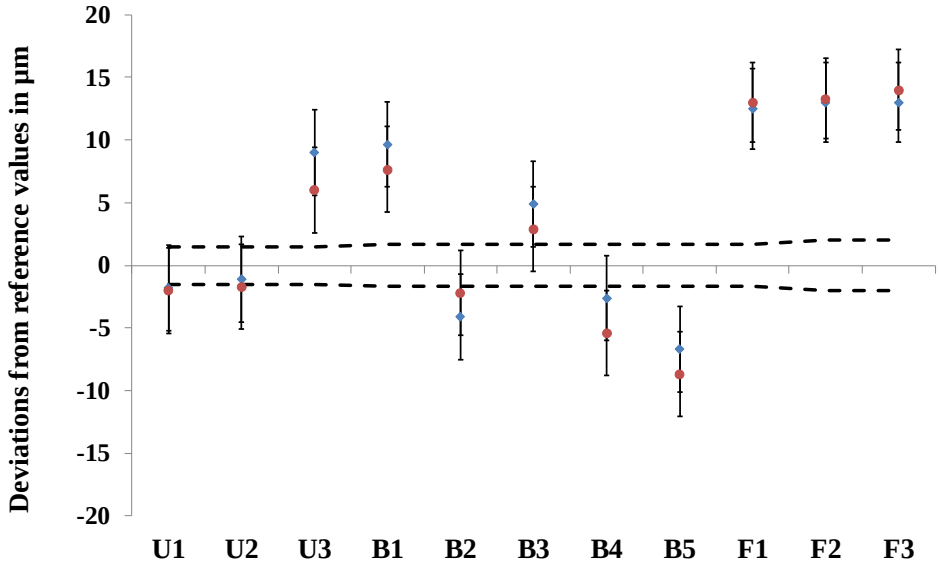

Figure 5.10. Deviations from CMM with step gauge alone (blue diamonds) and step gauge inside the CT Tube (red dots). Codes: see in the text. Error bars indicate the expanded uncertainties of CT measurements. Dotted lines show expanded uncertainty of CMM measurements. Values in µm

Table 5.5. E_n values for both correction approaches.

Measurand	U1	U2	U3	B1	B2	B3	B4	B5	F1	F2	F3
Step gauge + CT plate	-1.8o	-1.1	8.7	9.7	-4.1	4.9	-2.6	-6.7	12.5	13.0	13.0
Step gauge + CT tube	-2.0	-1.7	6.0	7.7	-2.2	2.9	-5.4	-8.7	13.0	13.3	14.0
$U_{CT\ plate}$	3.4	3.4	3.4	3.4	3.4	3.4	3.4	3.4	3.4	3.4	3.4
$U_{CT\ tube}$	3.4	3.4	3.4	3.4	3.4	3.4	3.4	3.4	3.4	3.4	3.4
E_n	0.1	0.1	0.6	0.4	0.4	0.4	0.6	0.4	0.1	0.1	0.2

Experiment 2: Testing of the CT crown using a mono-material workpiece

The CT crown was used as an online reference artefact, while the miniature PPS step gauge was used as the workpiece (see Figure 5.11). The test procedure fully replicated the one used in the previous investigation. The scanning parameters listed in Table 5.6, were used for all the scans conducted. Since all the scans were conducted over one day, the source was pre-conditioned at a maximum voltage of 225 kV, as prescribed by the equipment manufacturer, and then stabilized for more than 30 minutes.

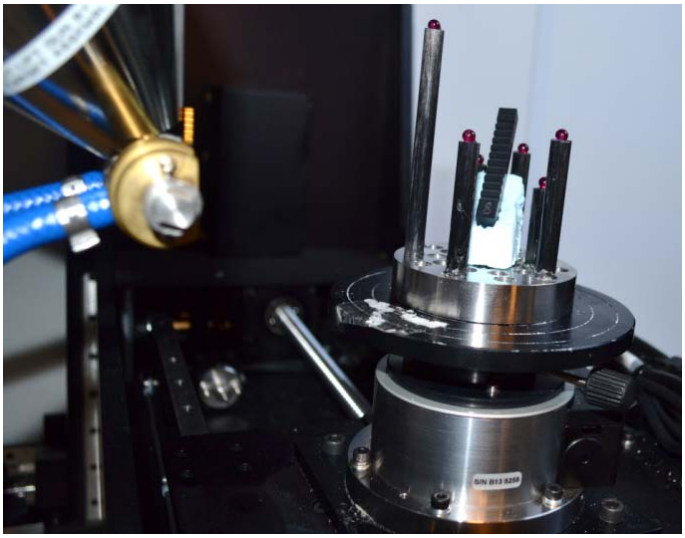

Figure 5.11. CT crown positioned on a CT rotary table with the PPS step gauge

Table 5.6. CT scanning parameters.

Parameter	Unit	Value	Parameter	Unit	Value
X-ray source voltage	kV	150	Magnification		3.5
X-ray source current	µA	250	No. of projections		1600
Voxel size	µm	40	Integration time	ms	1000
Spot size	µm	40	No. of images		2

Image quality analysis, carried out on the uncorrected X-ray projections for both configurations at the same angular position provided that the CT crown does not modify the X-ray spectrum. No local impact of the stems, having a thickness value larger than the frame of the CT tube, was observed on the surfaces of the workpiece.

No scattering due to the invar base was registered when analysing the grey value profiles. Measurement accuracy analysis involved 11 measurands including 8 bidirectional lengths (*B1* = 2 mm, *B2* = 6 mm, *B3* = 10 mm, *B4* = 14 mm, *B5* = 17 mm, *B6* = 22 mm, *B7* = 2 mm, and *B8* = 6 mm), and flatness of 3 flanks (*F1* at top, *F2* at centre, and *F3* at bottom of gauge). The measured values together with their measuring uncertainties, U_{BP} = 3.5 µm and U_{CR} = 3.0 µm for the measurements corrected using CT ball

plate and CT crown, respectively, are reported in Figure 5.12. The measurement uncertainties were quantified for both configurations by taking into account the calibration uncertainty, the CT repeatability, and the temperature variation. Measurements on the gauge carried out in the two different ways were found to be in agreement with E_n values [15] below 0.45. The E_n concept was used as the measurement uncertainties are very similar for the two methods.

With both methods, some systematic errors can be still observed in the Figure 5.12. The maximum extent of the residual errors amounts to 4 µm (11.2 % of the corrected voxel size). These errors can be due to the surface texture of the used flanks, which was measured using a profiler and found to be (Rz ≈ 6 µm). The surface texture of the flanks was estimated using a stylus profilometer and subsequently filtered using a λc cut-off wavelength of 0.8 mm, according to the ISO 4287 standard [130]. Repeatability of datum system and residual temperature effects may also have contributed to the residual deviations. Form measurements were found to be at the same level of accuracy for both correction methods, confirming that the CT crown did not yield additional noise.

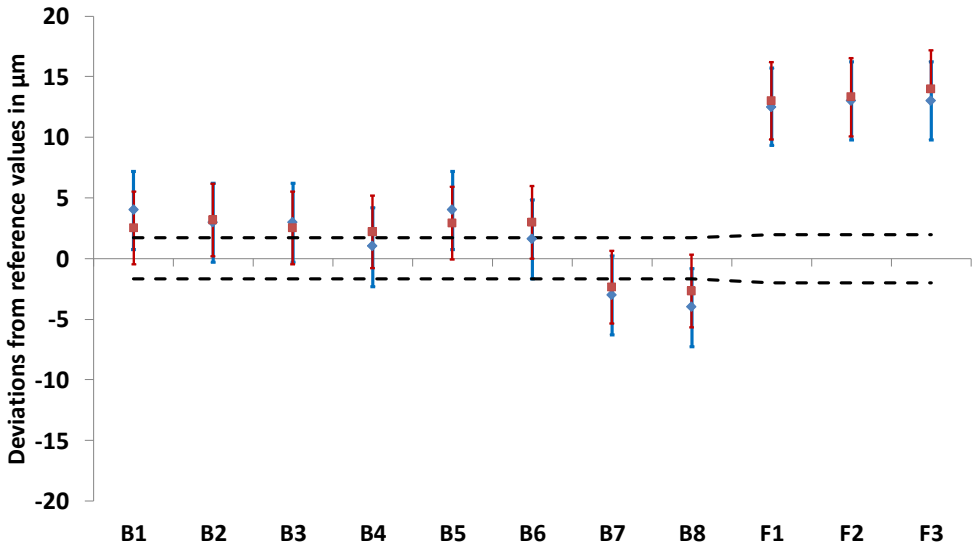

Figure 5.12. Deviations from CMM with step gauge alone (blue diamonds) and step gauge inside the CT crown (red dots). Codes: see in the text. Error bars indicate the expanded uncertainties of CT measurements. Dotted lines show expanded uncertainty of CMM measurements. Values in µm

In addition to what stated above, the investigation also showed that the geometrical errors originated by the rotary table are small as no trend can be seen from the results. Finally, it can be seen that measurements of B1 and B7 show a similar extent of systematic errors but a different sign. The difference between the means of the measurements of B1 and B7 can be used as an estimation of image noise affecting the measurements. A similar consideration can be drawn for the measurements of B2 and B8.

Experiment 3: Testing of the CT crown using an industrial assembly

The applicability of the CT crown was tested using an assembly produced by a Danish hearing aid manufacturer as a workpiece (see Figure 5.13). The assembly comprises three parts: shell, battery holder and pin joint. The assembly was selected to prove that the CT crown could also be used for inspection of small and highly penetrable objects.

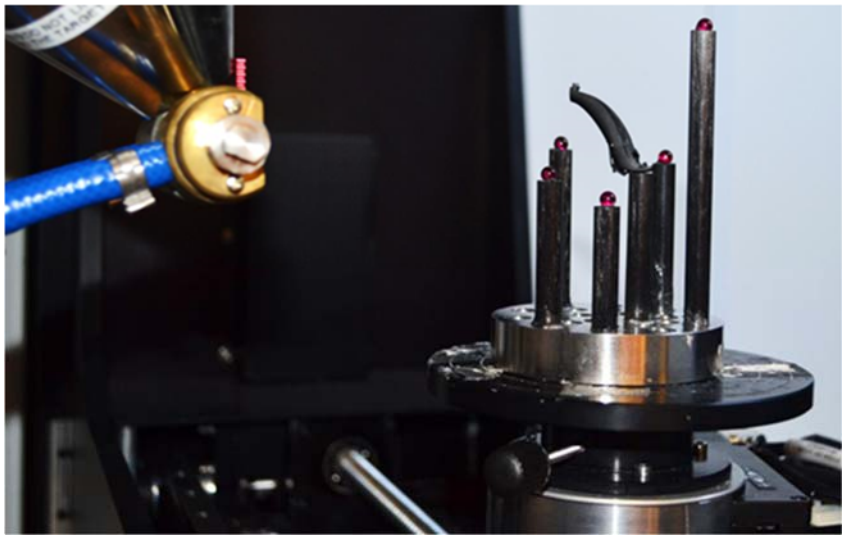

Figure 5.13. CT crown positioned on a CT scanner rotary table with the industrial assembly

Five measurands (four dimensional and one geometrical) were selected for this investigation. These are: external length (*E*), internal length (*I*), thickness of left wall (*T1*), thickness of right wall (*T2*), flatness of bottom surface of the holder (*F*). Measurands *E*, *I*, *T1*, and *T2* were selected on shell. Measurand F was selected on the battery holder. The considered dimensional measurands are all bidirectional lengths. Nominal dimensions of measurands and their tolerances are reported as follows: $E = 7.40 \pm 0.050$ mm, $I = 6.40 \pm 0.050$ mm, $T1 = 0.55 \pm 0.050$ mm, $T2 = 0.55 \pm 0.050$ mm, and F = 0.050 mm.

CMM measurements were performed using a Zeiss OMC 850 in a temperature-controlled laboratory (20 ± 1°C). A 10mm long probe equipped with a probing sphere of 0.8 mm was used for all the measurements. Measurements were all conducted using 0.10 N as probing force. The CMM evaluations were made with Calypso 5.4 software from Zeiss using a least square fit. The part was glued on a flat support and cured for more than 24 hours. CMM measurement together with their measurement uncertainties are reported in Table 5.7.

Table 5.7. CMM reference values for all five measurands together with their measurement uncertainties at 95% confidence level. All values were rounded to the nearest integer and are expressed in mm

Measurand	X [mm]	U (95%) [mm]
E	7.413	0.004
I	6.321	0.004
T1	0.557	0.004
T2	0.554	0.004
F	0.028	0.002

The scanning parameters are reported in Table 5.8. It can be seen in the table that the magnification was low compared to the size of the workpiece. The used magnification would not cause any problem because the selected features are far bigger than the used voxel size. The workpiece was scanned five times. A copper target was set for this investigation, instead of the tungsten target normally used, because of its advantages in ensuring better contrast at low powers. Physical beam hardening correction was conducted putting a 2-mm thick aluminium on the X-ray source.

Table 5.8. CT scanning parameters used for imaging the industrial assembly

Parameter	Unit	Value	Parameter	Unit	Value
X-ray source voltage	kV	120	Magnification		5
X-ray source current	µA	100	No. of projections		1200
Voxel size	µm	40	Integration time	ms	500
Spot size	µm	21	No. of images per projection		4

The evaluations were performed using VG Studio Max 2.2.6 on the voxel model. The measurands were least square fitted as follows: External length (*E*) was defined as a distance between two parallel planes created on the flat surfaces by fitting approximately 1000 points. Internal length (*I*) was measured as a distance between two small parallel planes created by fitting approximately 1000 points. 2 wall thicknesses (*T1*, *T2*) were defined as a distance between two parallel planes created on the inner and outer surface of the shell. A number of 1000 points were used for those planes. Each thickness is quantified as the distance of the two representative points on two fitted planes. Flatness (*F*) is measured fitting approximately 1000 points. The points were all taken away from the edges of the holder. Flatness is calculated using 95% of fitted points. The evaluation time was estimated to be 40 min, including the time for producing the measuring program in VG Studio Max.

Measurement uncertainties for CT measurements, U, were estimated following ISO 14253-2 [114]. The formula for uncertainty estimation for CT measurements is given by equation 22

$$U = k \times \sqrt{u_r^2 + u_{tran}^2 + u_p^2 + u_T^2 + u_{noise}^2 + u_{datum}^2}. \quad (21)$$

Here, k is the coverage factor (k = 2, for a coverage interval of 95%), u_r is the standard uncertainty of the CT crown, u_{tran} is the standard uncertainty during the traceability transfer quantified as the standard deviation of *5* CT measurements of the CT crown, u_p is the standard uncertainty from measuring process based on the three measurements of the industrial assembly. Note that transfer and repeatability uncertainty were quantified using the same three data sets; u_T is the evaluation of standard uncertainty due to the temperature variability (± 1°C) by assuming a U-distribution [8], u_{noise} is the standard uncertainty due to the noise based on the sphericity of two spheres of the CT crown. The two most distant spheres in vertical direction were used to quantify the noise. This choice allowed more comprehensive accounting of the image noise coming from the geometrical errors. The measurement deviations with respect to the reference values were assumed as the noise contribution; u_{datum} is the uncertainty contribution due to the repeatability of the datum system, based upon experience [9]. This result confirms the robustness of centre-to-centre spheres compared to other measurands.

Expanded uncertainty values ranging from 10 to 11 µm were obtained. Although measurement uncertainties were calculated in a range that is acceptable for CT measurements, they reduce the stated tolerances by up to 30 %, increasing the risk of indeterminate situations. As a consequence, a refinement of measurement uncertainty was attempted, according to Procedure for Uncertainty MAnagement" (PUMA). The refinement of uncertainty measurements was conducted by improving the estimation of the largest measurement uncertainty, namely noise. The new estimate of the noise uncertainty was conducted by using 95% of the fitted points on the two spheres. As a result of the process, the refined measurement uncertainties were reduced by 14 % with respect to the first iteration. The uncertainty values were all estimated to be less than 10 µm, as shown in Table 5.9. A further reduction of the measurements uncertainties was not possible due to the large noise affecting the data sets.

Based on the quantified uncertainties, it was also investigated whether those measurement uncertainties well suit the economics of a hypothetical enterprise. It is well known that the inspection process reduces the true capability of a manufacturing process due to the increase in the number of erroneously rejected parts. [110]. Assuming that the manufacturing process used for producing the inspected assembly has a capability index of c_p = 1.5, the mathematical relationship linking the measurement uncertainty, tolerance, and true capability of the manufacturing process is shown in Figure 5.14. Note that measurement uncertainty and tolerance are expressed in terms of uncertainty-to-tolerance ratio, *U/T*.

Table 5.9. Uncertainty budget for CT measurements. All values are in µm

Uncertainty contribution	Symbol	Modelling	Measurand				
			E [µm]	I [µm]	T1 [µm]	T2 [µm]	F [µm]
Traceability	u_r	Type B	1.5	1.5	1.5	1.5	1.5
Transfer	u_{tran}	Type A	0.5	0.5	0.5	0.5	0.5
Repeatability	u_p	Type A	1.5	1.5	1.5	1.5	1.5
Temperature	u_T	Type B	0.2	0.2	0.2	-	-
Noise	u_{noise}	Type B	2.7	2.7	2.7	2.7	4.4
Datum	u_{datum}	Type A	2.3	2.3	2.3	2.3	-
Expanded uncertainty	U		7	7	7	7	10

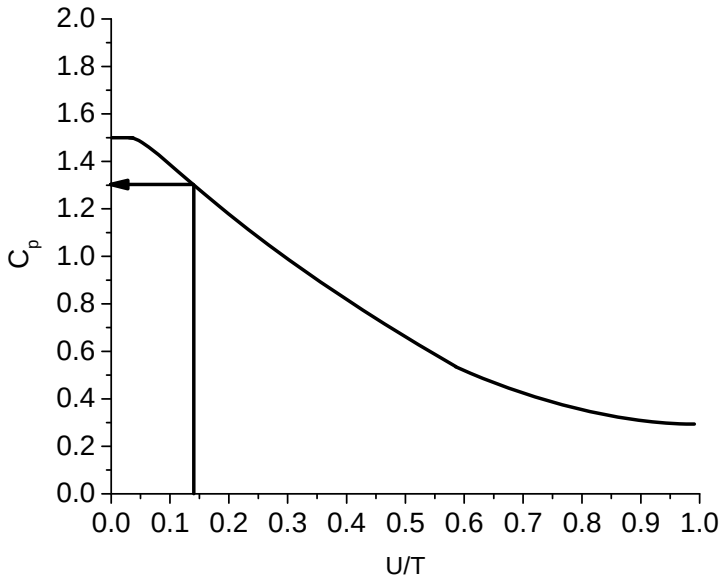

Figure 5.14. Impact of CT measurement uncertainty on the capability of the manufacturing process used for producing the inspected components. $U/T = 0.14$ for all dimensional measurands

It can be observed that the inspection process resulted in a real c_p being equal to 1.20. As a consequence, the defects rate, expressed in part per millions PPM, increases from 7 PPM for a $c_p = 1.50$, to 380 PPM for a $c_p = 1.20$, 379 of which are erroneously rejected parts. The inspection process can be considered to be still capable to deal with the specified tolerances. The obtained defect ratio should now be compared with the unit cost of each part in order to draw a meaningful conclusion regarding a real application of CT equipped with the CT crown.

The results of geometrical and dimensional measurements of the workpiece are reported in Table 5.10. Mean values, uncertainty values, nominal values and tolerance values are reported in the table per measurand. All measurement results presented in the table were corrected for scale error and temperature. It can be seen from the table that the CT measurements are in close agreement with CMM measurements for all considered measurands, despite some residual errors are present.

Table 5.10. Average value, X, expanded uncertainty, U95%, nominal value, N, and tolerance limit, T, for each measurand. All values are rounded and expressed in mm

Measurand	X	$U_{95\%}$	N	T
E	7.419	0.007	7.415	±0.050
I	6.315	0.007	6.322	±0.050
T1	0.557	0.007	0.550	±0.050
T2	0.548	0.007	0.550	±0.050
F	0.035	0.010	0	0.050

As listed in the table, that CT measurements of *E* are bigger than CMM measurements, while CT measurements of *I* are smaller than CMM measurements. This can be due to two reasons: noise and the probing force. Noise generally affects the bidirectional measurements, yielding that inner bidirectional measurements, e.g. *I*, are smaller while outer bidirectional measurements, e.g. *E*, are measured larger in CT. The probing force deforms the workpiece, resulting in larger inner bidirectional measurements and smaller outer bidirectional measurements. In this study, the probing force seemed to be the most dominant factor explaining the measurement deviations. A very good agreement between CT and CMM was registered for measurements of *T1* and *T2*, most probably due to the absence of the beam hardening effect. The results of measurements of *F* showed that the CT overestimated the measurand by more than 30 % with respect to the CMM. The distribution of fitted points of the flatness measurements appeared to follow a Gaussian distribution closely, giving evidence that flatness measurement is largely biased by the image noise.

A question which may now be posed is whether the CT crown contributed to the image noise biasing the flatness measurements. In order to give an answer, three additional scans were conducted with the workpiece without CT crown. Since the new scans were not carried out just after the five scans with the CT crown, a particular care was taken to restore similarity conditions. The scans were conducted without changing any scanning parameters, including the fixture and reconstruction and inspection settings. The measurements of flatness without the CT crown resulted in smaller systematic errors. The reduction of the systematic errors was of just 1.7 µm. This difference is in the order of the repeatability of the used CT measurements. It was therefore concluded that the CT crown did not amplify the image noise in this investigation.

Experiment 4: Testing of the CT crown using a multi-feature workpiece

The CT crown was used as an online reference artefact, while the miniature a multi-feature workpiece was used as a workpiece. Information on design and manufacture can be found in [10]. This investigation was set to prove the applicability of the CT crown when a workpiece with a large X-ray absorption coefficient has to be scanned. Nine measurands (8 dimensional and 1 geometrical) were selected for this investigation and shown in Figure 5.15.

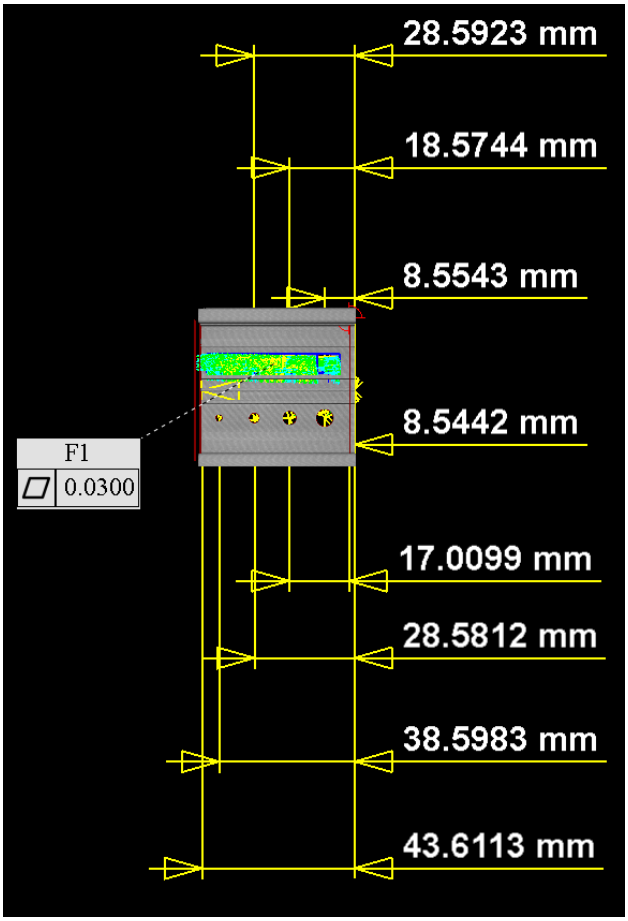

Figure 5.15. 9 Measurands used for the investigation: 8 lengths ranging from 8.5 to 43.6 mm and 1 flatness at the bottom surface of the multi-feature workpiece

The measurands were all calibrated using a Werth Video Check HA 400 in temperature controlled laboratories (20 ± 1°C). Calibration values together with their measurement uncertainties at 95% confidence level are listed in Table 5.11.

Table 5.11. CMM reference values for all five measurands together with their measurement uncertainties at 95% confidence level. All values were rounded to the nearest integer and are expressed in mm

	Measurands								
	F1	L1	L2	L3	L4	L5	L6	L7	L8
Description	Flatness	Length							
X [mm]	0.027	8.482	8.482	18.481	18.482	28.487	28.480	38.478	43.995
U (95%) [mm]	0.004	0.006	0.006	0.006	0.006	0.006	0.006	0.005	0.005

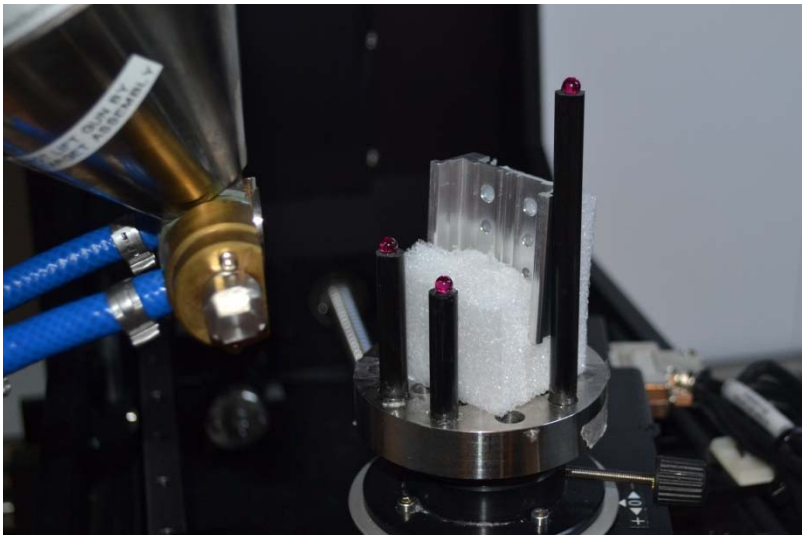

Figure 5.16. CT crown positioned on a CT scanner rotary table with the multi-feature workpiece

The workpiece was scanned using a Nikon XT H 225 CT available at DTU (see Figure 5.16). The scanning parameters are reported in Table 5.12. In order to fully penetrate the workpiece at any angular position, high energy was used.

Table 5.12. CT scanning parameters used for scanning the multi-feature workpiece

Parameter	Unit	Value	Parameter	Unit	Value
X-ray source voltage	kV	200	Magnification		4.8
X-ray source current	µA	200	No. of projections		1000
Voxel size	µm	75	Integration time	ms	500
Spot size	µm	42	No. of images per projection		4

Physical beam hardening correction was based on a multi-material filter. The filter was constituted of 0.2 mm of Tin, followed by 1 mm of Copper. Tin removed low and medium energy X-rays causing noise and beam hardening artefacts, while copper helped to reduce the characteristic radiation generated by Tin. The grey value profile across the longest X-ray path is reported in Figure 5.17. It can be seen that no beam hardening corrupts the data sets, so the double material physical filter may represent a good solution to avoid image artefacts at high energies. With respect to other CT measurements conducted in this thesis, binning mode was used, so the voxel size is larger than in other investigations. The small integration time was set to cope with the dark current affecting the detector. The short integration time was compensated by increasing the number of frames per projection. The smaller the integration times, the higher the number of images to be set for image averaging. Figure 5.18 shows the distribution of noise in the background of an X-ray projection. The distribution presents a standard deviation of 170 grey values. The value was quantified after having corrected the detector.

The correction of scale error was based on five spheres leading to 10 independent sphere-to-sphere distances. Since three scans were conducted an average scale error correction value was used for the correction. A standard deviation was furthermore quantified for each considered sphere-to-sphere distance.

Each scan required less than 51 minutes. The temperature in the cabinet during scanning was 24 ± 1°C. As a consequence, the measurement results were corrected for an enhanced temperature of 4 °C. The surface determination was based on a local thresholding method implemented in VG Studio Max 2.2.6. All measurands were quantified as plane-to-plane distances. All the primitive features were evaluated using least square fit. The evaluations were automatically performed using a measurement template allowing improved replication of the inspection software. The datum system for the step gauge is performed according to the procedure used during calibration which used a number of three least square fitted planes. The evaluation time was estimated to be 40 min, including the time for producing the measuring program in VG Studio Max.

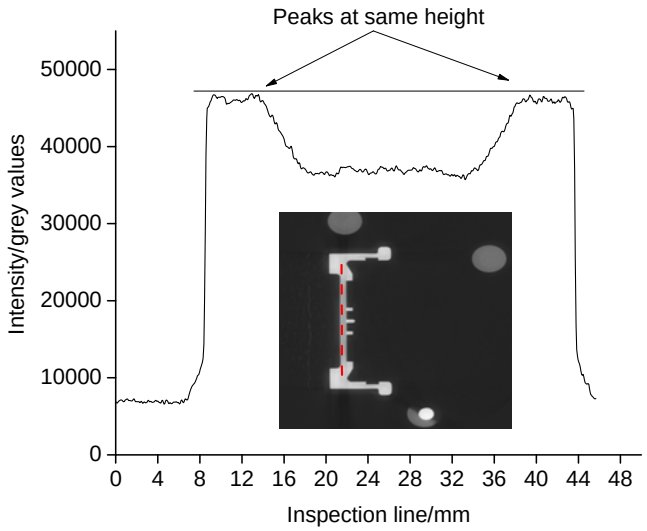

Figure 5.17. A grey value profile extracted along the longest X-ray travel of 45 mm (red dot line). The profile shows that the effect of beam hardening is negligible

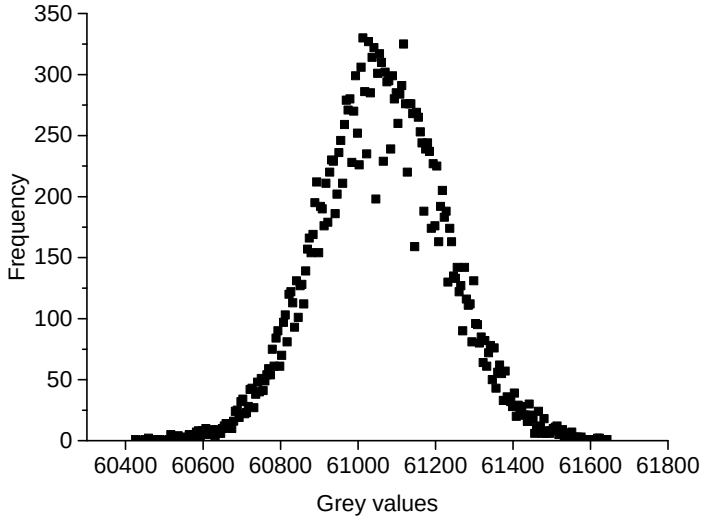

Figure 5.18. The distribution of noise in the background of an X-ray projection. The distribution presents a standard deviation of 170 grey values. The value was quantified after having corrected the detector

Measurement uncertainties for CT measurements, U, were estimated following ISO 14253-2 [114]. The formula for uncertainty estimation for CT measurements is given by equation 23

$$U = k \times \sqrt{u_r^2 + u_{tran}^2 + u_p^2 + u_T^2 + u_{noise}^2 + u_{datum}^2}. \quad (22)$$

Here, k is the coverage factor (k = 2, for a coverage interval of 95%), u_r is the standard uncertainty of the CT crown, stated in the calibration certificate, u_{tran} is the standard uncertainty due to the correction that was quantified as the maximum standard deviation of the sphere-to-sphere distances used for the correction. This uncertainty was quantified to be 0.5 µm, which is very high. Such high repeatability ensures that influence factors were constant in all CT measurements; u_p is the standard uncertainty from

measuring process based on the three CT measurements of the multi-feature workpiece. Note that correction and repeatability uncertainty were quantified using the same three data sets; u_T is the evaluation of standard uncertainty due to the temperature variability (± 1°C) by assuming a U-distribution [8]; u_{noise} is the standard uncertainty due to the noise based on the sphericity of two spheres of the CT crown. The deviation with respect to the reference values were assumed as the noise contribution. u_{datum} is the uncertainty contribution due to the repeatability of the datum system, based upon experience. With respect to previous measurement uncertainty, the datum uncertainty was reduced due to the low image noise. The uncertainty budget for each feature is shown in Table 5.13. It can be seen from the table that all measurands shows worse repeatability than the spheres of the CT crown, with the flatness measurements showing the worst repeatability. The different repeatability may be caused by the difference in X-ray absorption and surface texture between two objects.

Table 5.13. Uncertainty budget for all measurements of the multi-feature workpiece. All values are in µm

Uncertainty contribution	Symbol	Modelling	Measurands	
			F [µm]	L1 – L8 [µm]
Traceability	u_r	Type B	1.5	1.5
correction	u_{tran}	Type A	0.6	0.5
Repeatability	u_p	Type A	1.5	1.0
Temperature	u_T	Type B	0.2	0.2
Noise	u_{noise}	Type B	3.5	3.0
Datum	u_{datum}	Type A	-	2.6
Expanded uncertainty	U		8.7	9.5

Figure 5.19 reports the deviations of CT measurement with respect to CMM measurements. The measurement results are reported after having been corrected for the scale error and the enhanced temperature. It can be seen that no systematic trend can be observed as the size of measurand increases and that the magnitude of bias for measurements of all dimensional measurands is the same for most of the measurands. The measurement of *L3* showed the biggest bias, most probably due to the worse surface texture of the used features. The surface texture influenced the position of the centre of circle that was used for defining *L3* (see Figure 5.15). No effect of the fixture on the length measurements was observed although the plane used for defining all the measurands was covered by it.

The residual measurement deviations were also found to follow a Gaussian distribution closely, as quantified using an Anderson-Darling test at 95% confidence level (see Figure 5.20). The mean of the measurement deviations is very close to 0 (≈ - 0.001 mm).

The stated measurement uncertainties for CT measurements ensure a very good metrological compatibility with CMM measurements for all measurands, as confirmed using the E_n values (see Figure 5.21). As a consequence, CT and CMM measurements refer to the same measurand. The flatness measurement showed an E_n value as large as dimensional measurements. The similarity of E_n between geometrical and dimensional measurands is a result of low image noise, which was achieved using image averaging together with the short integration time. The E_n values show no correlation with the lengths, ensuring that the used uncertainty model does not require any adjustment as the length of feature increases. A recalculation of the expanded uncertainties was carried out in order to achieve $| E_n | = 0.99$. The aim of this step was to quantify the smallest measurement uncertainty that would still give a metrological agreement between CT and CMM measurements, representing the source of traceability in this investigation. The recalculated expanded uncertainties were found to be in the range of 2-5 µm depending on the measurand. The measurement uncertainties at $E_n = 0.99$ suggests that CT can deliver measurement results at same level of accuracy as a tactile CMM, when systematic errors are successfully corrected. The similarity of accuracy between CT and CMM measurements also highlights that CT can produce accurate results even when it runs in the fast scanning mode. It can be assumed that any effort spent in improving the imaging process reduces the measurement uncertainty and the associated costs (see Section 3.7).

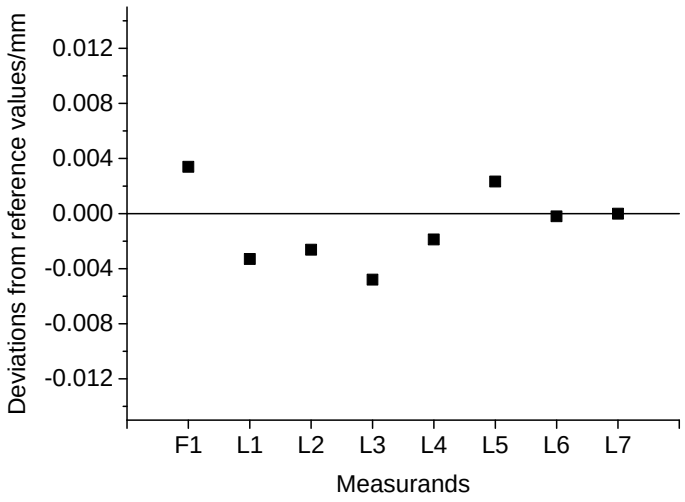

Figure 5.19. Deviations for all eight measurands of the multi-feature workpiece. All values in mm

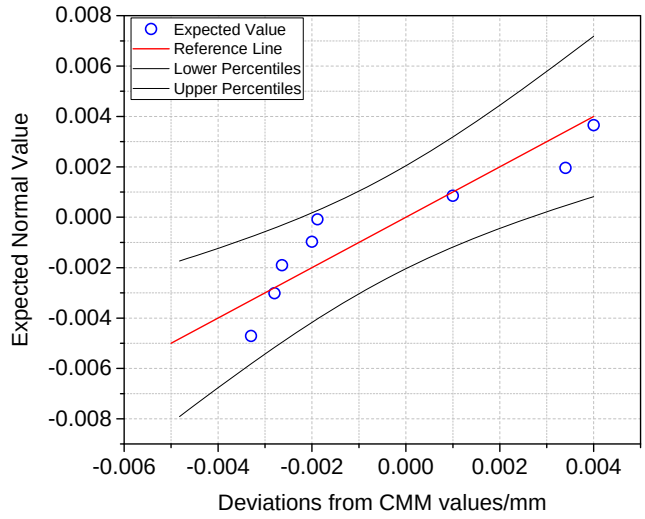

Figure 5.20. Anderson-Darling test conducted to prove that residual measurement deviations follow a normal distribution

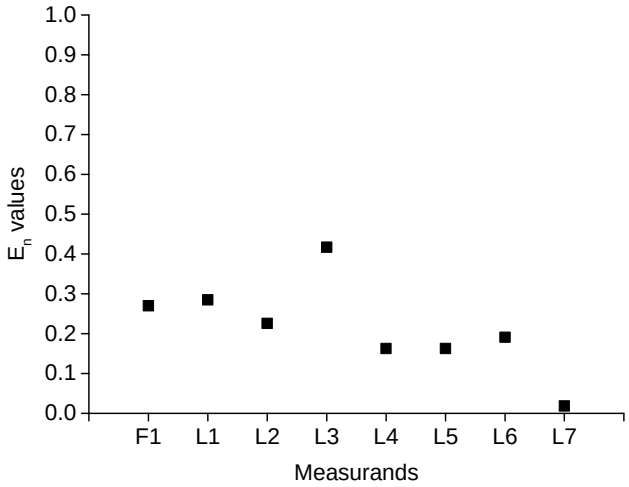

Figure 5.21. E_n values for all eight measurands of the multi-feature workpiece. The largest E_n value was found to be 0.49

It can be concluded that the CT crown yielded an appropriate correction but also that the CT crown was found to be thermally stable despite the enhanced temperature of 4 ºC.

5.5 Advantages of the developed reference artefacts

A clear advantage of the new reference artefacts is the possibility of using a datum system during the data set evaluation to correct scale errors in the measured volume, which is a big challenge in CT. By using the calibrated distances, measurements can be corrected within the entire volume of interest. The 3D artefact can be calibrated with the same uncertainty as reference artefacts commonly available for CT, presenting a calibration uncertainty below the CT repeatability and typical MPE values. The item allows high flexibility with respect to tube size and spatial distribution of spheres. These two parameters

can be modified almost freely to meet particular needs such as, small parts. By placing the online reference artefacts inside the CT volume, an ordinary CT scanner becomes a 3D coordinate measuring machine. This represents an affordable way to upgrade a CT system. It can be noticed that the artefacts can be used for scale correction both at image level and at reconstructed volume level, and even to assess probe error and volumetric anisotropies.

The artefacts allow a considerable reduction of time by compressing the full process of scanner calibration, scanning, measurement, and re-calibration, into a single process. As illustrated in in Table 5.14, a reduction of the total time of 50% or more can be achieved. A further advantage brought about by this new artefact is the possibility of minimising the data storage required, given that information regarding the workpiece and the reference artefact are stored within the same data set. Also in this case, a reduction in the order of 50% can be achieved, as illustrated in Table 5.14.

Such values can be increased further adopting an artefact dedicated specifically to the workpiece. This aspect is very important for industrial companies such as the pharmaceutical industry, where measurements must be stored for long periods of time.

Table 5.14. Comparison of time consumption and data file size between a conventional workflow with separate scanner calibration and a workflow involving the 3D artefact for scale correction concurrently with scanning

Typical workflow of CT measurement process	Workflow using the new 3D artefacts		
Step	Estimation of time per step	Step	Estimation of time per step
Scanning of reference artefact	2 h	Scanning of Workpiece + on-machine artefact	2 h
Scanning of workpiece	2 h		
Scanning of reference artefact (optional)	0 or 2 h		
Data analysis (2 or 3 data sets)	1.5 or 2.0 h	Data analysis (1 data set)	0.8 h
Overall time	5.5 – 8 h	Overall time	2.8 h
Data file size	4.3-6.3 GB	Data file size	2.5 GB

5.6 Conclusions

Two 3D artefacts for concurrent calibration of the scale in CT have been presented. The two prototypes were calibrated on a tactile CMM, and their applicability demonstrated using different workpieces having different sizes and materials. Lengths ranging from 2 mm to 45 mm and flatness were used as measurands.

- None of the investigations highlighted loss of image quality due to the presence of concurrent artefacts surrounding the workpiece. None of the investigations highlighted residual errors following a systematic pattern. All the investigations showed that the two artefacts appeared to be thermally stable even when the temperature within the CT cabinet increased.
- By using the new concurrent artefacts, the measurements uncertainties were quantified in the range of 7-10 μm for the majority of the investigated features. Smaller measurement uncertainties were furthermore achieved by accepting $| E_n | = 0.99$.
- Compared to existing artefacts, the new concurrent artefacts allow a considerable reduction of time (approx. 50%) and amount of data to be stored (approx. 50%) by compressing the full process of calibration, scanning, measurement, and re-calibration, into a single workflow.

Chapter 6

InteraqCT Comparison on CT of Assemblies

6.1 Interlaboratory comparisons in CT for metrology

Interlaboratory comparisons enable laboratories to assess their performance in conducting measurements by comparing their own results with others coming from other participants. International comparisons also give a snapshot of the maturity status of a new measuring technique. Any comparison requires three elements: comparison workpieces, fillable forms, and test instructions, known as technical protocol. Each comparison participant receives and measures the workpieces according to the technical protocol. Upon completing the task, each laboratory submits their test data to the comparison coordinator who is in charge of generating a final report. In the field of dimensional CT, several comparisons have been organized. The "CT Audit" intercomparison was the first international round-robin in the field of dimensional CT [77] . This intercomparison was organized and coordinated by the Laboratory of Industrial and Geometrical Metrology of the University of Padova, Italy. The circulation was carried out in the period from March 2010 to March 2011, and involved 15 participants. Four calibrated items were used in order to include a variety of dimensions, geometries and materials. A second comparison on industrial CT was organized by DTU Mechanical Engineering, Denmark, and carried out within the project "Centre for Industrial Application of CT scanning – CIA-CT" [58]. The main goals of this comparison were to test applicability of CT for measurement on small objects, commonly measured in industry, which are more representative than reference artefacts, to evaluate the impact of instrument settings and operator decisions on the measurement of items of two different materials and geometries. Different measurands are considered, encompassing diameters, roundness, and lengths. A number of 27 laboratories from 8 countries were involved. The parallel circulation of items took place in spring 2013 and the final report was available in September 2013.

6.2 InteraqCT comparison on CT of assemblies

The InteraqCT comparison represented a new activity that was organized with the aim of investigating the performance of CT with respect to dimensional measurements on assemblies. The comparison was designed to a) test applicability of CT for measurement on assemblies with features as well as materials commonly used in industry, b) evaluate the impact of the operator over the whole CT workflow, c) evaluate the impact of post-processing settings (such as noise reduction, BHC, volume segmentation, etc.) on the accuracy of CT measurements, d) collect and share knowledge on practical aspects related to the traceability of measurements using industrial CT, and e) support the development of CT metrology user community. In contrast to previous comparisons that only focused on physical workpieces, the InteraqCT comparison extends beyond the edge of physical items by introducing a voxel item. The voxel item is an item scanned by coordinator and electronically distributed to participants. The introduction of this new concept of comparison item brings the following advantages: (a) it enables determination of whether CT post-processing poses a problem for the accuracy of CT measurements by isolating CT post-processing from the whole CT measurements workflow; (b) it allows conducting a parallel circulation, based on the same item; (c) it does not require physical circulation, eliminating issues associated with the long-term stability; (d) it gives significant cost savings associated with manufacturing, calibration and shipping. A total number of 22 industrial CT scanners from Belgium (1 participant), Denmark (6 participants), Germany (8 participants), Italy (2 participants), Singapore (1 participant), and the UK (4 participants) took part in the comparison. National metrology institutes, manufacturers, universities, research centres, and CT end users are all represented within the comparison. The comparison has been concluded within a period of 12 months.

6.3 Items

A successful comparison is definitely based on an accurate selection of items and their materials, measurands and their measuring strategies as well as handling and transit strategies. The selection of the assemblies was conducted defining the following requirements: a) involving assemblies whose x-ray absorption ratios vary from 0.3 to 0.6, b) having items with and without well-defined geometries and low form errors, c) featuring multi-material measurands, d) having assemblies covering different measuring volumes to catch different classes of errors, e) being calibrated using a tactile CMM, f) involving materials with good dimensional stability, g) ease of manufacture and of positioning in a fixture to minimize the reproducibility uncertainty. While some specifications were relatively straightforward to be achieved, others (e.g. trade-off between number of assemblies and number of measurands or x-ray absorption ratios) required several iterations, during which the participants were actively involved. The process resulted in selecting two assemblies: *Assembly 1* and *Assembly 2*.

Assembly 1 (see Figure 6.1a) is a multi-material assembly comprising a cylindrical step gauge made of aluminium and a tube made of glass and two fastening caps. The assembly includes both mono-material measurands such as unidirectional and bidirectional lengths on the gauge and multi-material measurands, defined as the distances between the top of the teeth of the gauge and the tube. These measurands can be directly calibrated with tactile CMMs using off-the-shelf probes. The cylindrical step gauge is 56 mm long object with 6 grooves at 3.50 mm steps produced by milling from a 14 mm diameter extruded rod. Machining enabled a suitable surface finish (Ra = 0.40 ± 0.05 µm and Rz = 2.00 ± 0.05 µm), as quantified using a stylus instrument on a set of 5 gauges (λs = 2.5 µm and λc = 0.8 mm, sampling length of 4 mm, and 3 replications per gauge) [4]. The step gauges were made from aluminium alloy 2011 being a high mechanical strength alloy with excellent machining characteristics. This alloy unfortunately presents *Lead* and *Bismuth* that have very high x-ray absorption coefficients, resulting in changing the image quality locally. The effect of those two elements was investigated and found to be negligible at the magnification levels generally used for imaging the step gauge. Some local change in the image quality was however noted at very high magnifications (voxel sizes ≤ 8 µm). The glass was purchased as 1m long tubes and subsequently cut into smaller 55 mm long tubes in-house. The tubes have an outer diameter of 17.5 mm and a wall thickness of approximately 1.2 mm. This was assumed to be sufficient to prevent breakage caused by thermal expansion and contact pressure during handling. The aluminium caps and 10 nylon screws complete the assembly as the fastening system. 4 screws (M3 x 8 mm) constrain the relative displacements between the gauge and the tube, while 6 screws (M2 x 5 mm) constrain the relative rotations. The M2 x 5 screws push the glass against the step gauge, yielding a more stable connection over time.

Assembly 2 (see Figure 6.1b) is a CT scan of an industrial multi-material assembly provided by Novo Nordisk A/S. The inner component is made of polyoxymethylene. The outer component is made of acrylonitrile butadiene styrene-polycarbonate. Both components are produced via injection moulding. *Assembly 2* was distributed as 4 CT data sets having two different levels of noise. Noise in the data sets was tuned by changing the spot size, the detector calibration, and the number of images per projection. *Assembly 2* involves more complex shapes than *Assembly 1*.

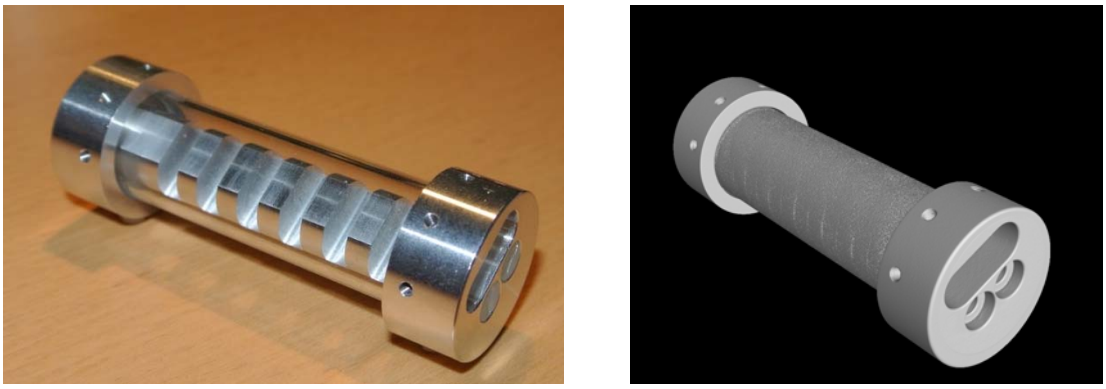

(a)

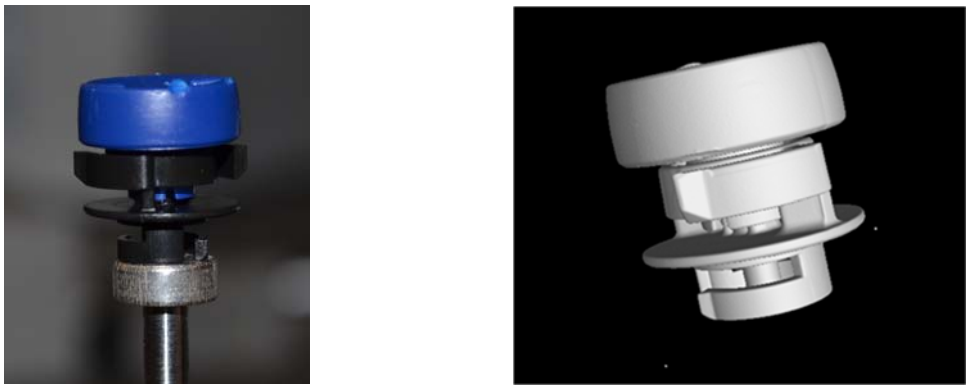

(b)

Figure 6.1. (a) Assembly 1 and its 3D representation, (b) Assembly 2 and its 3D representation

6.4 Measurands and measurement procedures

The measurands selected on Assembly 1 are the following: *L1*, *L2*, *L3*, *L4*, and T, which are shown in Figure 6.2. *L1*, *L2 L3*, and *L4* are mono-material lengths. *T* is a multi-material length. *L1* and *L4* are unidirectional lengths, while *L1*, *L2*, and *T* are bidirectional ones. *T* has a similar size to *L3*. The measurands were selected to compare the measurement accuracy and uncertainty strategy between mono-material and multi-material measurands as well as between unidirectional and bidirectional measurands.

Two different scanning approaches were considered within the comparison exercise for Assembly 1. The first approach, coded as "*Own Choice*", did not apply any scanning restrictions on any of the scanning parameters. The second one, coded as "*Fast Scan*", introduced a series of limitations, including the scanning time and the number of images per projection. The *Own Choice* strategy enabled the extraction of the best out of CT, as most of the influence factors, e.g. noise, undersampling, ring artefact and pixel delay, can be minimised. The *Fast Scan* approach attempted to put CT in a condition in which it is difficult to mitigate influencing factors due to the lack of time. By combining those approaches it would be possible to provide a good representation of the performance of CT. with special reference to fast scans. The latter is an important factor for successful adoption of CT in industry.

The measurands selected on *Assembly 2* are the following: *D1*, *D2*, *R1*, and *C1*, as shown in Figure 6.3. *D1* and *D2* are defined as two Gaussian diameters. *R1* is roundness of *D1* without filtering. *R1* is concentricity of *D2*. The measurands ensure different levels of difficulties of the measurement task for the participants. *D1* and *D2* are simpler measurands than *R1* and *C1*. *D1* and *D2* are moreover very robust because noise would only marginally affect them. *R1* is a more complex measurand because its estimation strongly depends on the method used for minimizing the noise. Ultimately, *C1* is the most complex measurand considered within the comparison as its assessment depends on how well the datum system is established.

Assembly 2 was provided as four data sets having different signal-to-noise ratios. 2 of the 4 data sets were provided with high signal-to-noise ratio. 2 of the 4 data sets were provided with low signal-to-noise ratio. No restriction on any of the inspection parameters, e.g. number of fitted points, was set. The different image quality among the data sets was introduced to investigate whether varying the image noise has any effect on the surface determination and thereby on measurement results.

No particular restrictions in connection with the number and location of alignment and inspection points were set. Participants only had two technical drawings and CAD files as the support material.

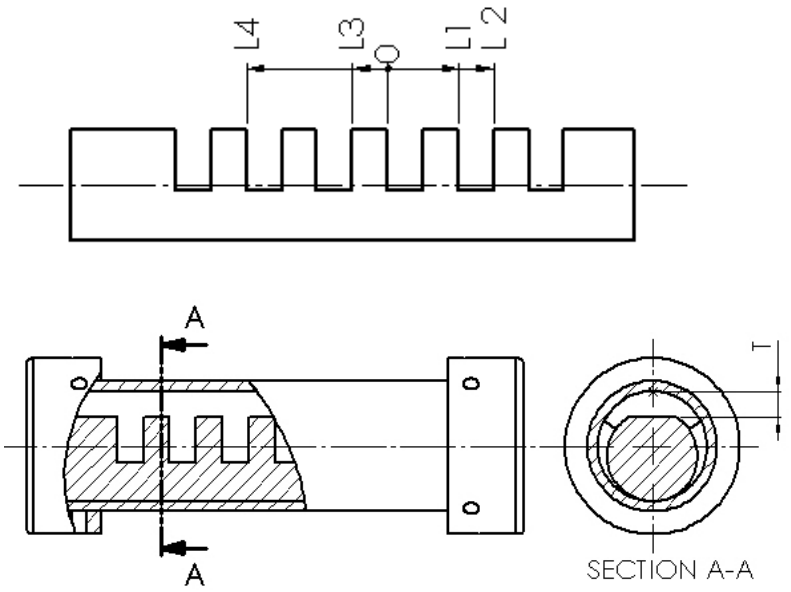

Figure 6.2. Overview of measurands of Assembly 1: L1, L2, L3, L4 and T

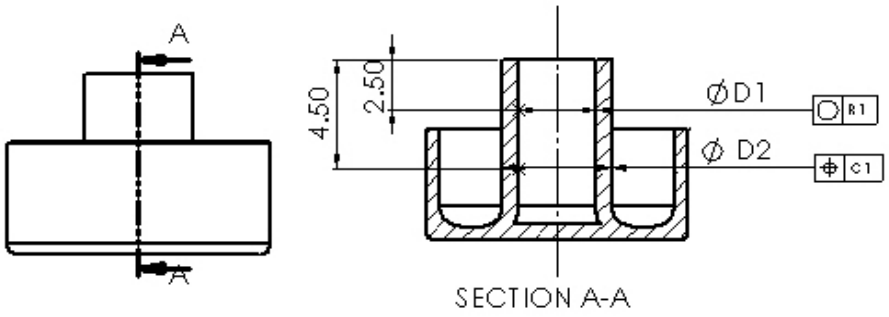

Figure 6.3. Overview of measurands of Assembly 2: D1, D2, R2, and C1

6.4 Reference values

The coordinate measuring machine used is a mechanical CMM equipped with a static probe. The CMM is of the type Zeiss UPMC 850 CARAT (see Figure 6.4), with some of its specifications shown in Table 6.1. The CMM is placed in a temperature controlled room (T = 20 °C ± 0.5 °C and a maximum RH of 60 %). The calibration equipment was calibrated during the comparison exercise and found to behave in agreement with the previous calibrations.

Figure 6.4. Zeiss UPMC 850 tactile CMM used as calibration equipment within the comparison

Table 6.1. Information on the Zeiss UPMC 850 CARAT used as calibration equipment

Measuring volume (x, y, z)	820 mm x 700 mm x 600 mm
MPE	One-dimensional length measuring uncertainty: u1 = (0.4 + L / 900) µm Three-dimensional length measuring uncertainty: u3 = (0.8 + L / 600) µm L expressed in mm.

The material standards used to generate traceability were a calibration sphere (see Figure 6.5) which was used to calibrate the probes, four gauge blocks (see Figure 6.6) and a ring gauge (see Figure 6.7), which were used as length references. The gauge blocks were assembled in such a way as to resemble the workpieces of *Assembly 1*. The ring gauge was used for multi-material measurand of Assembly 1 and for all measurands of *Assembly 2*.

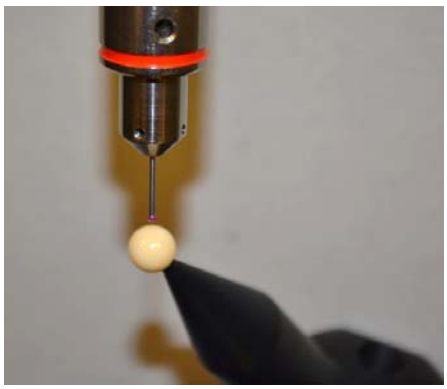

Figure 6.5. Calibration sphere, Ø8 mm. The sphere was used for calibrating all probes used in this work

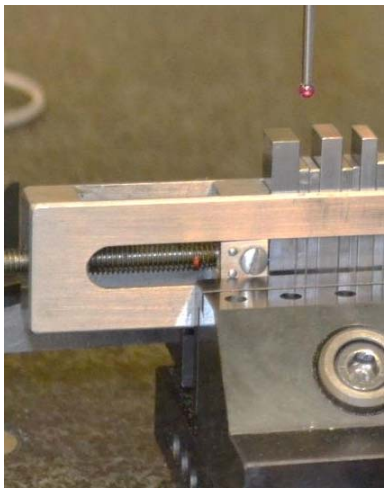

Figure 6.6. Step gauge created assembling single gauge blocks. The item was used for establishing traceability of L1, L2, L3, and L4 (Assembly 1)

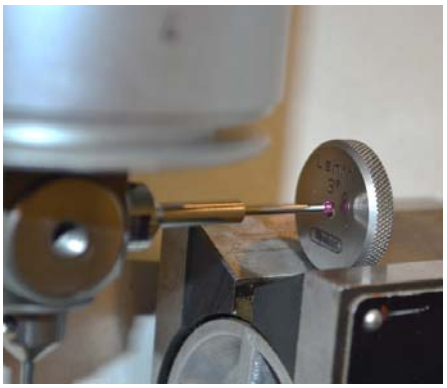

Figure 6.7. Ring gauge, Ø3 mm. The item was used for establishing traceability of T (Assembly 1) and D1, D2, R1, and C1 (Assembly 2)

The selected mono-material lengths of Assembly 1, *L1*, *L2*, *L3*, and *L4*, were measured as a point-to-point distance between flanks. Each point represents the centre of mass of 20 points distributed over 4 lines. In order to minimise the impact of flatness and parallelism errors on the measurements, a small area of each flank was used. The datum system for gauge measurements (see Figure 6.2) was created as follows: *Datum A* was based on two diameters of 30 equally distributed points each. *Datum B* was defined as a plane of 20 equally distributed points. Note that *Datum B* represents a common zone datum

(*CZ*). Ultimately, *Datum C* was based on a plane of 15 points. All features were least square fitted without removing outliers.

The selected multi-material length of *Assembly 1*, *T*, was measured as an average of 20 point-to-point distances. The average construction of the measurand was necessary to cope with the large form errors of the glass tube (≈ 200 µm). The datum system (see Figure 6.2) for gauge measurements was constructed using two 30-point diameters for Datum A, a 20-point plane for *Datum B*, and ultimately a 20-point plane for *Datum C*. Note that *Datum B* represents a common zone datum (*CZ*). All features were constructed using the least square fitting method.

The measurement set-up is illustrated in Figure 6.8. The fixture was placed in a part of the available measuring volume of the CMM being less affected by geometrical errors. The fixture position was used as a rough alignment throughout the course of the calibration task.

The probe configuration includes a probe of diameter Ø3 mm (hereafter "*Probe 1*") and a second probe of diameter Ø1 mm (hereafter "*Probe 2*"). The measurements of *L1*, *L2*, *L3*, and *L4* were conducted using Probe 1, while the measurements of *T* were carried out using both Probe 1 and Probe 2. The probes were re-qualified every 5 workpieces in order to monitor the extent of adhesive wear taking place between aluminium and ruby. Probe 1 and Probe 2 were corrected in order to have the same X- and Y-coordinates. Probing force was set at 0.10 N for measurements of *L1*, *L2*, *L3*, and *L4* and at 0.05 N for *L1*, *L2*, *L3*, and *L4*. All 22 workpieces were acclimatised for one week. The temperature of each workpiece was additionally checked using a laser thermometer before being measured. The variability of the temperature during calibration was assumed to be ± 0.5 °C, which takes into account the temperature sensor error and the variability of temperature within the workpiece. The items of *Assembly 1* were handled using gloves and cleaned gently using a soft brush. The workpieces were placed within a v-block and clamped using a vice fixture. The fixturing force was kept constant by marking the screw travel. A number of 5 repeated measurements were conducted on each item. Additional measurements were conducted after having repositioned the workpiece in the fixture. Those measurements were used to quantify an estimate of uncertainty contribution due to fixturing.

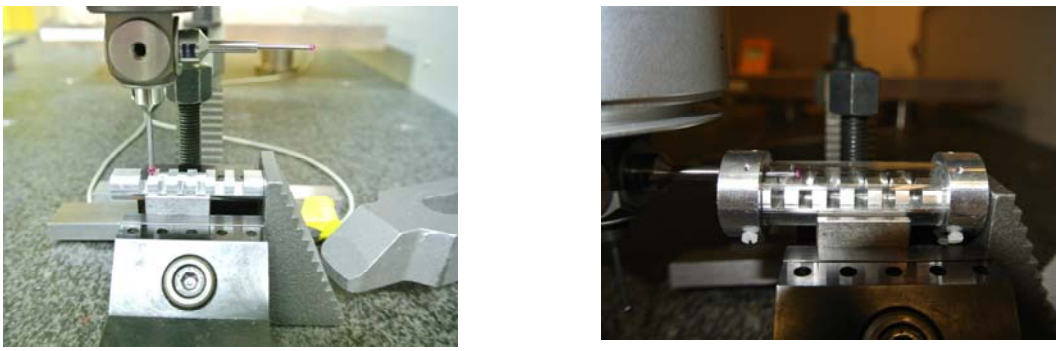

(a) (b)

Figure 6.8. Measurement setup for calibration of (a) L1, L2, L3, and L4 and (b) T

The selected features of *Assembly 2*, *D1*, *D2*, *R1*, and *C1*, were calibrated as follows. *D1* and *D2* were based on 100 equally distributed points. *R1* was measured using the continuous scanning mode approach. *C1* was measured using three circles of 40 points each distributed at three different inspection levels, namely at -4.4950 mm, -4.5000 mm and -4.5050 mm, with respect to the datum system given in Figure 6.3. The concentricity measurement was finally estimated as the average value of all measurements.

The datum system for Assembly 2 (see Figure 6.3) was based on two diameters of 25 equally distributed points each for *Datum A*, and 20 equally distributed points for *Datum B*. The measurement set-up is illustrated in Figure 6.9. The fixture was placed in a part of the CMM measuring volume less affected by geometrical errors. The workpiece was measured using a probe with Ø 1.0 x 15 mm and a probing force of 0.05 N. The workpiece was acclimatised for two weeks. The temperature of the workpiece was also checked using a laser thermometer before being measured. The temperature difference between measuring equipment and workpiece was assumed to be the same because of acclimatisation. The variability of the temperature during calibration was quantified to be 0.5 °C. This variability includes the temperature sensor error and the variability of temperature within the workpiece. The temperature was registered before each measurement.

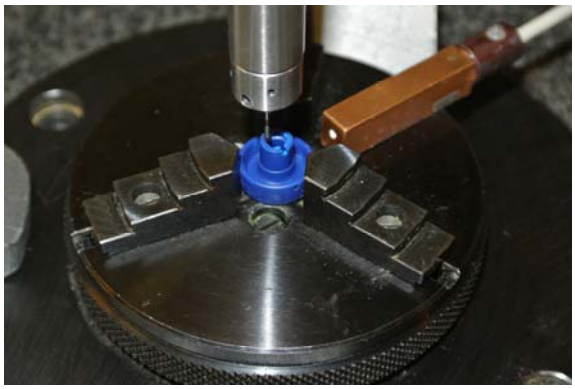

Figure 6.9. Measurement setup for calibration of selected measurands of Assembly 2, D1, D2, R1, and C1

6.5 Measurement Uncertainty

Measurement uncertainties were quantified for measurands of *Assembly 1* and *Assembly 2* using the PUMA approach [114] and Equations 24.

$$U = 2 \times \sqrt{\sum_{i=1}^{n} u_i^2}. \tag{23}$$

The uncertainty components of Equation 24 are described in Table 6.2 and Table 6.3 for Assembly 1 and Assembly 2, respectively. The two tables show the uncertainty components taken into account per measurand.

Table 6.2. List of the uncertainty contributors for the measuring uncertainty budget of the reference measurements of Assembly 1

Symbol	Description	Type	Measurand				
			L1	L2	L3	L4	T
$u_{r(1)}$	Uncertainty component from calibration sphere, Ø8 mm	B (rectangular)	X	X	X	X	X
$u_{r(2)}$	Uncertainty component from a gauge block, 4 mm	B (rectangular)			X		
$u_{r(3)}$	Uncertainty component from a gauge block, 7 mm	B (rectangular)	X				
$u_{r(4)}$	Uncertainty component from a gauge block, 10 mm	B (rectangular)		X			
$u_{r(5)}$	Uncertainty component from a gauge block, 14 mm	B (rectangular)				X	
$u_{r(6)}$	Uncertainty component from a calibration ring, Ø3 mm	B (rectangular)					X
$u_{rep(1,1)}$	Uncertainty component from repeatability on calibration sphere, Ø8 mm, measured using Probe 1	A	X	X	X	X	X
$u_{rep(1,2)}$	Uncertainty component from repeatability on calibration sphere, Ø8 mm, measured using Probe 2	A					X
$u_{rep(2)}$	Uncertainty component from repeatability on gauge block, 4 mm	A			X		
$u_{rep(3)}$	Uncertainty component from repeatability on gauge block, 7 mm	A	X				
$u_{rep(4)}$	Uncertainty component from repeatability on gauge block, 10 mm	A		X			
$u_{rep(5)}$	Uncertainty component from repeatability on gauge block, 14 mm	A				X	
$u_{rep(6,1)}$	Uncertainty component from repeatability on calibration ring, Ø3 mm, measured using Probe 1	A					X
$u_{rep(6,2)}$	Uncertainty component from repeatability on calibration ring, Ø3 mm, measured using Probe 2	A					X
u_{drift}	Uncertainty component due to CMM geometrical errors along the measuring axes	B (rectangular)	X				
$u_{e(1)}$	Uncertainty component from temperature deviation between standard reference temperature and calibration equipment	B (U-shape)					
$u_{e(2)}$	Uncertainty component from temperature deviation standard uncertainty arising from temperature deviation between standard reference temperature and workpieces	B (U-shape)					
$u_{e(3)}$	Uncertainty component from workpiece expansion coefficient uncertainty	B (U-shape)					
u_p	Uncertainty component from measurement process	A					
u_{fix}	Uncertainty component from fixturing process	A					

Table 6.3. List of the uncertainty contributors for the measuring uncertainty budget of the reference measurements of Assembly 2

Symbol	Description	Type	Measurand			
			D1	D2	C1	R1
$u_{r(1)}$	Uncertainty component from a calibration sphere, Ø8 mm	B (rectangular)	X	X		
$u_{r(2)}$	Uncertainty component from a calibration ring, Ø3 mm	B (rectangular)	X			
$u_{rep(1)}$	Uncertainty component from repeatability on calibration ring, Ø8 mm	A				
$u_{e(1)}$	Uncertainty component from temperature deviation between standard reference temperature and calibration equipment	B (U-shape)	X	X		
$u_{e(2)}$	Uncertainty component from temperature deviation standard uncertainty arising from temperature deviation between standard reference temperature and workpieces	B (U-shape)	X	X		
$u_{e(3)}$	Uncertainty component from workpiece expansion coefficient uncertainty	B (U-shape)	X	X		
u_p	Uncertainty component from measurement process	A	X			
u_{fix}	Uncertainty component from fixturing process	A				

The average reference expanded measurement uncertainties (k = 2) were estimated in the range of 1.1-2.6 µm, depending on the sample and measurand. The range of variation of the measurement uncertainties for the samples of Physical Assembly was found to be smaller than 0.5 µm, documenting that the samples are adequately homogeneous for use in the comparison [7]. The maximum deviation of each measurement with respect to its average value did not exceed 1.7 µm for all measurands, documenting the consistency of measurement process.

6.6 Stability of item

The status of the workpieces of *Assembly 1* was monitored at different times before circulation and after circulation as indicated in Table 6.4. From the table it can be seen that checks covered eight months. Due to some circulation delay, not all the workpieces were inspected at each inspection interval. The gauge measurands were checked before circulation (December 2015) and after circulation (June and July 2016). Preliminary tests were also conducted on five step gauges and on five glass tubes in November 2015. The gauge-tube measurand of each workpiece was monitored for four months, namely before circulation (December 2015) and after circulation (March, May and June 2016). A parallel monitoring of all selected measurands was not possible due to the design of *Assembly 1* which requires taking work-

pieces apart, resulting in permanently modifying the gauge-tube measurand. Disassembling of workpieces was done just after having proved the stability of workpieces of *Assembly 1*. Since the calibration equipment was not intensively used and no technical problems occurred during the comparison exercise, any systematic bias that may be present in the calibrations should be at the same extent as for all the conducted calibrations. Moreover, the environment temperature ranged from 19.89 ºC to 20.24 ºC during the comparison exercise, which fully complies with the laboratory requirements. Assuming the stability of calibration system and of the laboratory environment, the results should provide the required information regarding the workpiece stability.

Table 6.4. Dates of calibrations conducted to monitor the status of all workpiece of Assembly 1

		Measurand					Number of inspected workpieces
Month	Year	L1	L2	L3	L4	T	
December	2015	X	X	X	X	X	22 out of 22
March	2016					X	10 out of 22
May	2016					X	19 out of 22
June	2016	X	X	X	X		20 out of 22
July	2016	X	X	X	X		20 out of 22
August	2016	X	X	X	X	X	22 out of 22

In order to judge the agreement between measurements through time, the E_n value normalised with respect to the stated uncertainty was used. Table 6.5 shows that none of the workpieces exceeded the critical E_n value (E_n >1) as all measurands show deviations within the stated uncertainties. E_n values for the gauge measurands were found all to be below 0.85. The E_n values are larger *L2* and *L3* (bidirectional measurands) than for *L1* and *L4* (unidirectional measurands). The E_n values of *T* have same size as those ones of the gauge measurements.

Based on the results collected, we concluded that all the workpieces of *Assembly 1* are stable over the comparison exercise.

Table 6.5. Distribution of E_n values for all measurands of Assembly 1. None of the workpieces exceeded the critical E_n value (E_n >1).

	L1	L2	L3	L4	T
	E_n	E_n	E_n	E_n	E_n
AVG	0.40	0.58	0.57	0.41	0.36
MAX	0.80	0.84	0.85	0.75	0.60
MIN	0.00	0.01	0.11	0.06	0.04

The status of *Assembly 2* was not monitored due to the absence of a physical circulation. Reference measurements were conducted in December 2015 and in June 2016 for all measurands.

6.7 Results for Assembly 1 scanned using Own Choice approach

20 participants measured Assembly 1 and the results are shown in Figure 6.10, Figure 6.11, Figure 6.12, Figure 6.13, and Figure 6.14 for *L1*, *L2*, *L3*, *L4*, and *T*, respectively. Figure 6.10 shows that most of the participants are in good agreement with the reference measurements for *L1*. Some participants provided measurement results with deviations smaller than calibration uncertainties. 2 out of the 22 participants are not in agreement with the reference values, which could be due to threshold determination and non-corrected voxel and temperature corrections. The participants stated average expanded uncertainties in the range of 0.002 mm to 0.119 mm, with an average uncertainty of 0.008 mm for *L1*.

Figure 6.11 shows that 12 of the 22 participants are in good agreement with reference measurements for *L2*, with deviations ranging from -0.006 mm to 0.009 mm. As for *L1*, some participants were able to measure with deviations in the order of the calibration uncertainty of workpieces. 6 out of the 22 participants showed large deviations from the reference values, with deviations up to 0.140 mm. Apart from the possible influence of the factors already described above, an improper qualification of the centre of rotation and wider cone angle factors can also be factors that led to the larger deviations found for measurand *L2*. The stability of the datum system may also have contributed to the large deviations because second order errors are of increased importance to this measurand. The participants stated expanded uncertainties in the range of 0.003 mm to 0.080 mm, with an average uncertainty of 0.016 mm, for *L2* Figure 6.12 shows that 12 of the 22 participants are in good agreement with reference measurements for *L3*, with deviations falling within the stated measurement uncertainties. 7 out of the 22 participants provided measurements that are not in agreement with the reference values. The non-conforming participants showed systematic deviations varying from 0.050 mm to 0.126 mm. The measurement

results appeared to be both overestimated and underestimated with respect to the reference values. Such large differences can be due to a post-processing beam hardening correction, which corrupted the real distribution of the grey values, and due to an improper correction of scale errors. The participants stated expanded uncertainties in the range of 0.001 mm to 0.080 mm, with an average uncertainty of 0.014 mm, for *L3*.

Figure 6.13 shows that 20 out of the 22 participants are in good agreement with reference measurements for *L4*, with deviations below 0.010 mm. Some participants provided measurement results with deviation in the order of the calibration uncertainty of workpieces. 2 out of the 22 participants showed deviation up to 20 µm. Such large differences can be due to a post-processing beam hardening correction, which corrupted the real distribution of grey values, and due to an improper correction of scale errors. The stability of datum system may also have had an effect on the big deviations because second order errors gain in importance. The participants declared expanded uncertainties in the range of 0.002 mm to 0.080 mm, with an average uncertainty of 0.014 µm, for *L4*.

Figure 6.14 highlights that 11 participants are in good agreement with reference measurements for *T*, with deviations lying within the stated measurement uncertainties. It is interesting to note that although *T* and the length L3 are similar, both being bidirectional lengths of similar size, the deviations registered for *T* are larger than those observed for *L3*. This result confirms the greater difficulty in defining a multi-material surface determination and a stable datum system for measurements of *T* compared to *L3*. 4 out of the 22 participants showed measurement results that are not in agreement with reference measurements, with an average deviation of 0.057 mm. The participants declared expanded uncertainties for *T* in the range of 0.002 mm to 0.080 mm, with an average uncertainty of 0.014 mm. The uncertainty measurements stated for *T* are equal to the ones stated for *L3*.

Table 6.6 reports the deviation-to-voxel-size ratios for all measurands to demonstrate better the extent of the measurement errors. The length measurements *L1* show an average ratio of 11 % with a maximum value of 124 % and a minimum value of 0.2 %. The length measurements of *L2* show a mean ratio of 36 % with a maximum value of 245 % and a minimum value of 0.1 %. The length measurements for *L3* present an average ratio of 29 % with a maximum value of 195 % and a lowest value of 0.2 %. The length measurements of *L4* show a ratio of 20 % with a maximum value of 183 % and a minimum value of 0.1%. The length measurements of *T* have a ratio of 34 % with a maximum value of 115 % and a minimum value of 2 %. The majority of the participants obtained a sub-voxel accuracy. Larger deviation-to-voxel-size ratios refer to participants who did not correct systematic errors in a proper way.

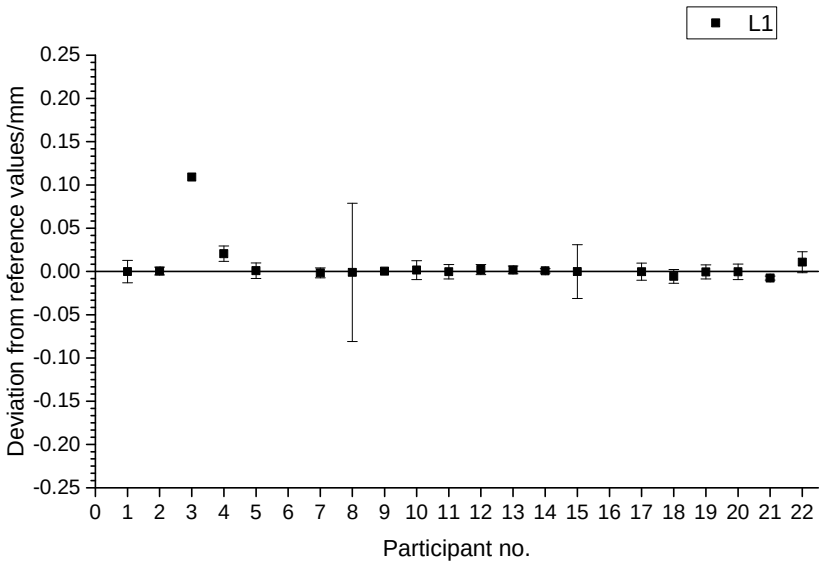

(a)

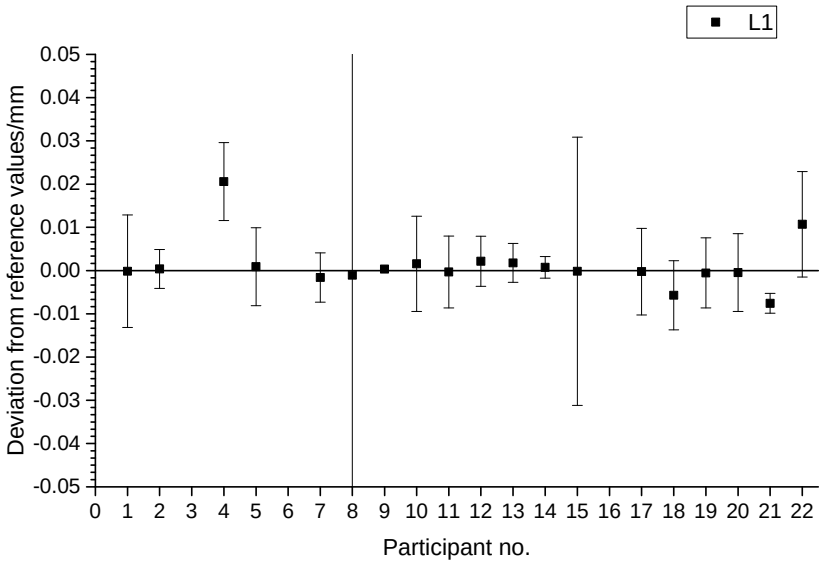

(b)

Figure 6.10. Results for Assembly 1. Length L1: (a) deviation range ± 0.25 mm, (b) deviation range ± 0.05 mm

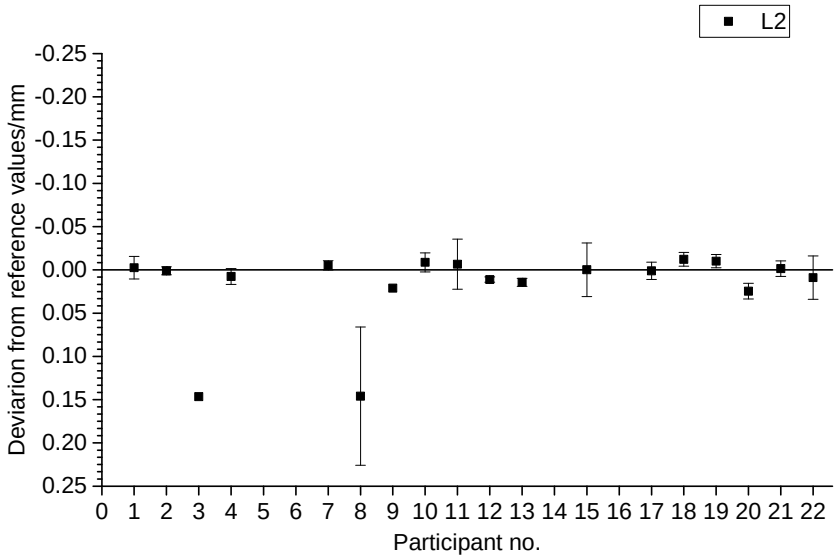

(a)

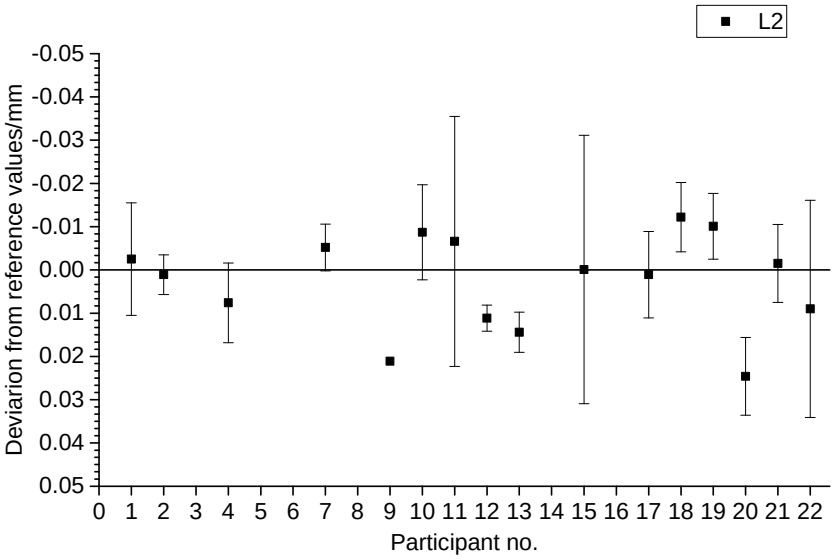

(b)

Figure 6.11. Results for Assembly 1. Length L2: (a) deviation range ± 0.25 mm, (b) deviation range ± 0.05 mm

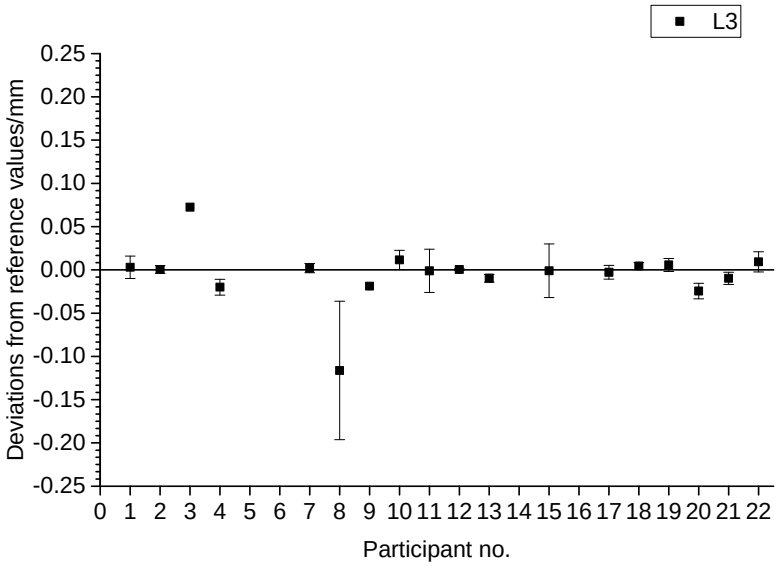

(a)

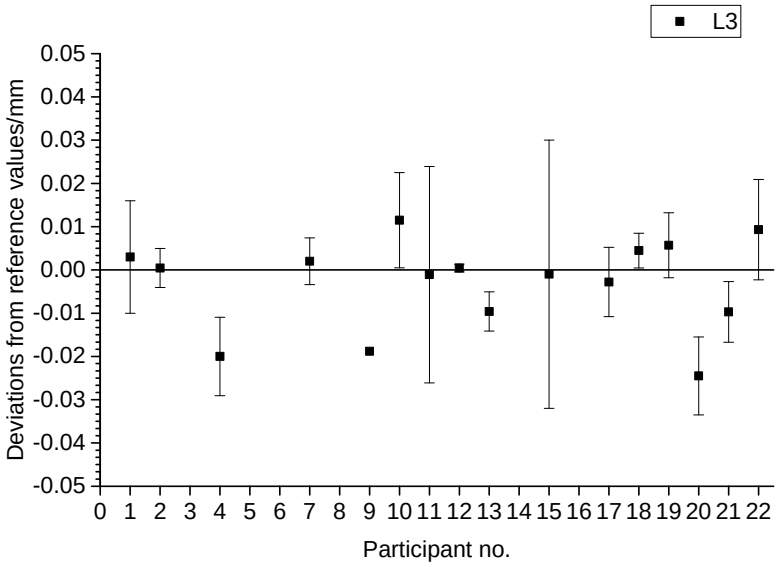

(b)

Figure 6.12. Results for Assembly 1. Length L3: (a) deviation range ± 0.25 mm, (b) deviation range ± 0.05 mm

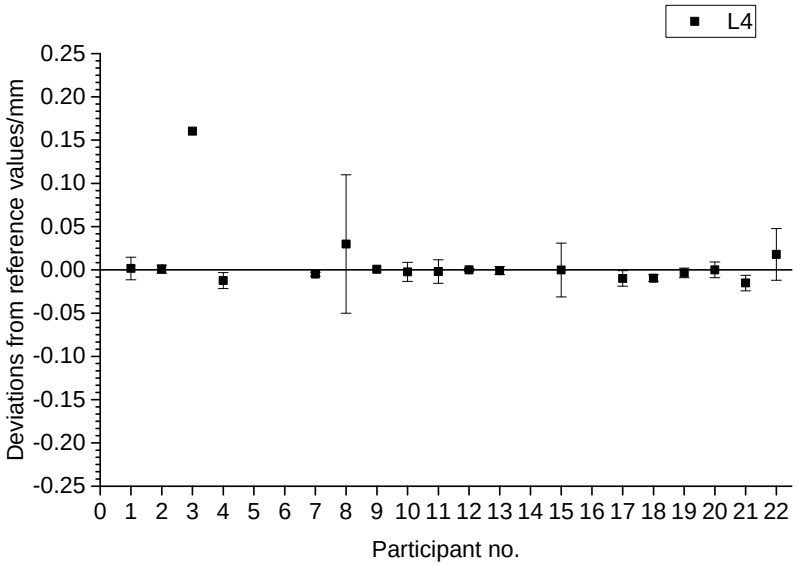

(a)

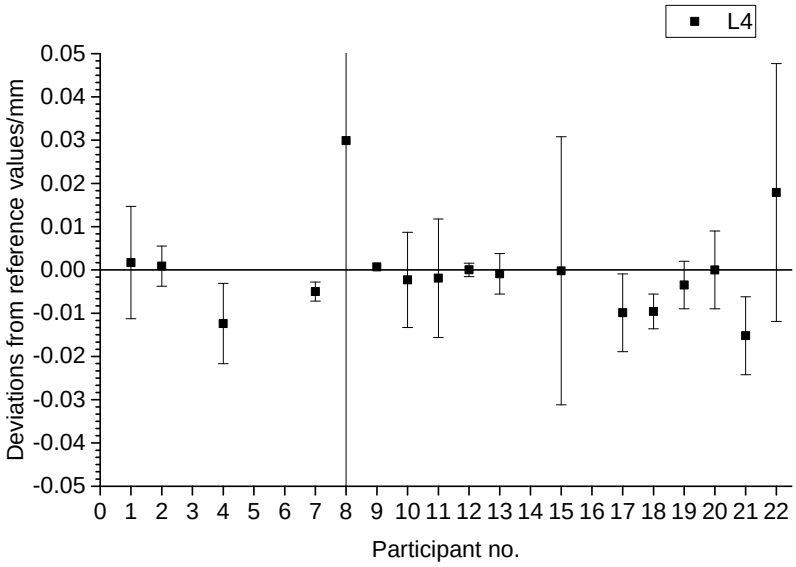

(b)

Figure 6.13. Results for Assembly 1. Length L4: (a) deviation range ± 0.25 mm, (b) deviation range ± 0.05 mm

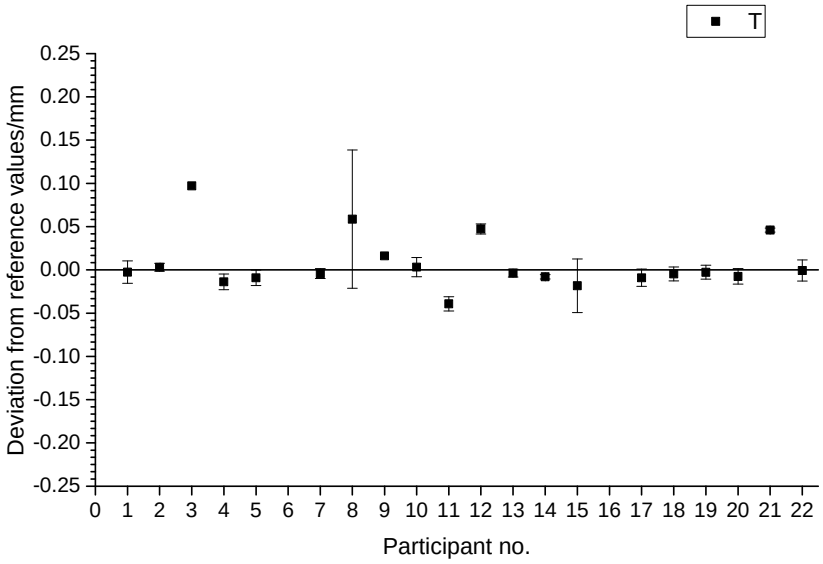

(a)

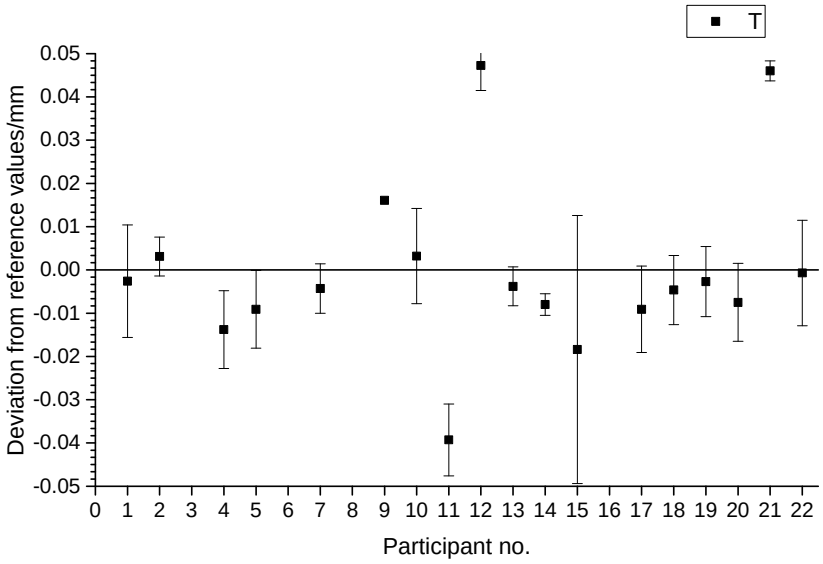

(b)

Figure 6.14. Results for Assembly 1. Length T: (a) deviation range ± 0.25 mm, (b) deviation range ± 0.05 mm

Table 6.6. Mean error-to-voxel size ratios (%) for Assembly 1 scanned using the Own Choice approach.

Participant no.	L1	L2	L3	L4	T
1	1	7	5	4	5
2	1	1	2	1	7
3	124	83	166	183	110
4	31	31	9	18	21
5	3	3	4	9	26
6					
7	5	8	18	10	13
8	2	195	245	52	99
9	1	28	29	1	25
10	4	31	27	7	8
11	1	3	19	7	111
12	5	0	24	3	113
13	2	9	13	0	4
14	2	31	33	1	17
15	0	1	1	0	21
16					
17	0	2	0	12	9
18	7	5	14	13	6
19	1	16	25	3	7
20	2	79	49	2	25
21	19	13	5	40	115
22	27	26	19	48	2

6.8 Results for Assembly 1 scanned using Fast Scan approach

The results are shown for *L1*, *L2*, *L3*, *L4*, and *T* Figure 6.15, Figure 6.16, Figure 6.17, Figure 6.18, and Figure 6.19, respectively. Figure 6.15 shows that 14 out of the 22 participants are in good agreement with the reference measurements for *L1*, with deviations below 0.097 mm. Some participants provided measurement results with deviations smaller than calibration uncertainty. 2 out of the 22 participants showed deviations up to 0.020 mm. The participants stated average expanded uncertainties in the range of 0.001 mm to 0.110 mm, with an average uncertainty of 0.022 mm, for *L1*. Figure 6.16 shows a good agreement among 13 participants and the calibration measurements for *L2*, with deviations ranging from –0.006 mm to 0.009 mm. Some of those participants were also able to measure with deviations within the calibration uncertainties. The participants stated average expanded uncertainties in the range of 0.002 mm to 0.110 mm, with an average uncertainty of 0.020 mm, for *L2*. Figure 6.17 shows that 13 out of the 22 participants are in good agreement with reference measurements for *L3*, with deviations ranging from –0.006 mm to 0.009 mm. Some participants were able to measure with deviations in the order of the calibration uncertainty of workpieces. The participants stated average expanded uncertainties in the range of 0.002 mm to 0.110 mm, with an average uncertainty of 0.020 mm, for *L3*.

Figure 6.18 depicts that 18 out of the 22 participants are in good agreement with the reference measurements for *L4*, with deviations below 0.01 mm. Some participants provided measurement results with deviations in the order of the calibration uncertainty of the workpieces. 2 out of the 22 participants showed deviations up to 0.020 mm. Such large differences can be due to a post-processing beam hardening correction, which corrupted the real distribution of the grey values, and due to an improper correction of scale errors. The participants stated average expanded uncertainties in the range of 0.001 mm to 0.110 mm, with an average uncertainty of 0.019 mm, for *L4*. Figure 6.19 highlights that participants are in good agreement with reference measurements for *T*, with deviations lying within the stated measurement uncertainties. 4 out of the 22 participants showed measurements results which are not in agreement with reference measurements, with an average deviation of 0.057 mm. These large deviations may be due to errors in defining the datum system and surface around both materials. The participants declared expanded uncertainties for *T* in the range of 0.002 mm to 0.110 mm, with an average uncertainty of 0.019 mm.

Table 6.7 lists the deviation-to-voxel-size ratios for all measurands. The length measurements *L1* show a ratio of 19% with a maximum value of 169% and a lowest value of 0.3%. The length measurements of *L2* show a ratio of 34% with a maximum value of 212% and a minimum value of 0.5%. The length measurements of *L3* show a ratio of 50% with a maximum value of 366% and a minimum value 1.2%. The length measurements of *L4* show a ratio of 26% with a maximum value of 252% and a minimum value of 0.5%. The length measurements of *T* show a ratio of 37% with a maximum value of 145% and a minimum value of 3%.

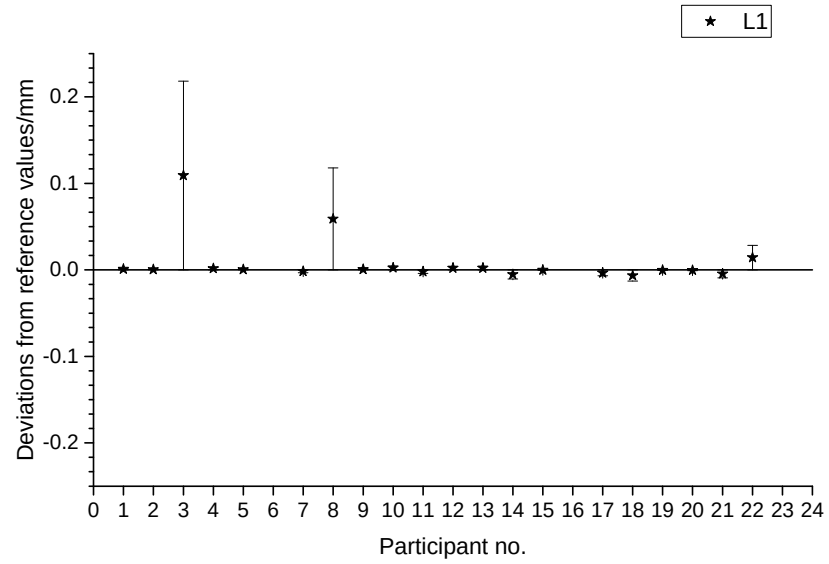

(a)

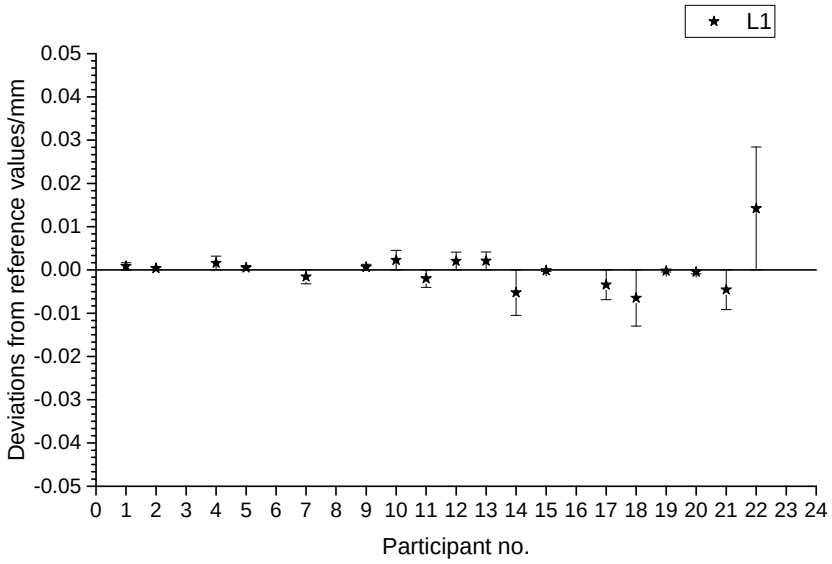

(b)

Figure 6.15. Results for Assembly 1. Length L1: (a) deviation range ± 0.25 mm, (b) deviation range ± 0.05 mm

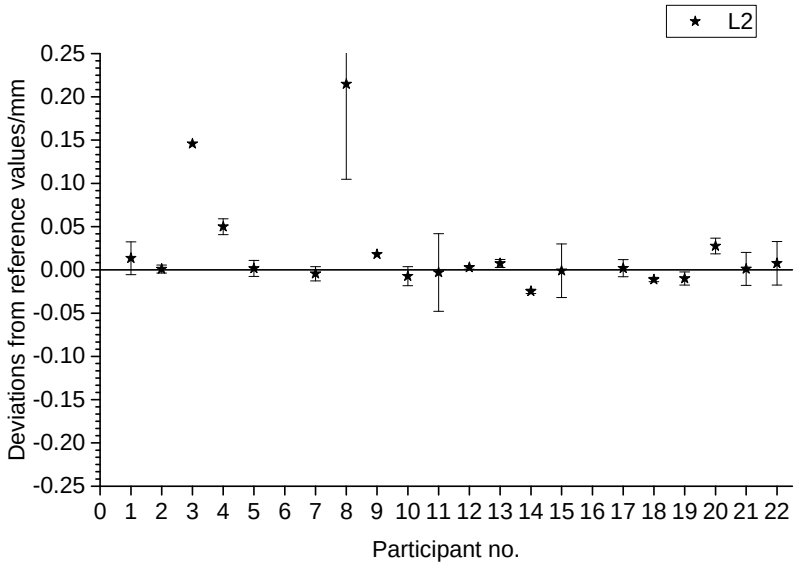

(a)

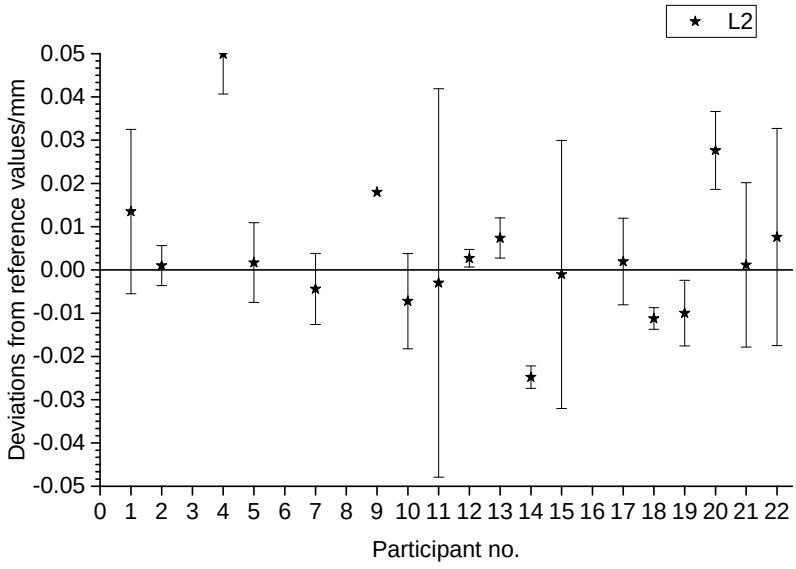

(b)

Figure 6.16. Results for Assembly 1. Length L2: (a) deviation range ± 0.25 mm, (b) deviation range ± 0.05 mm

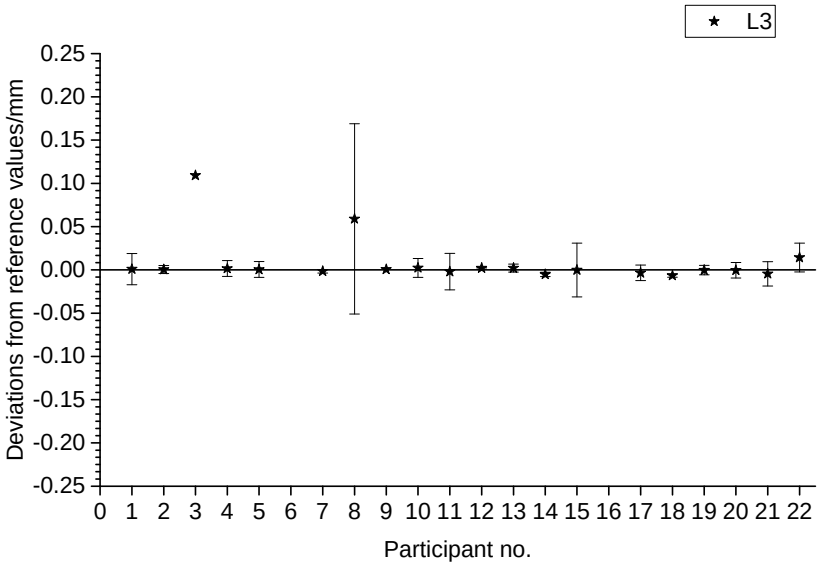

(a)

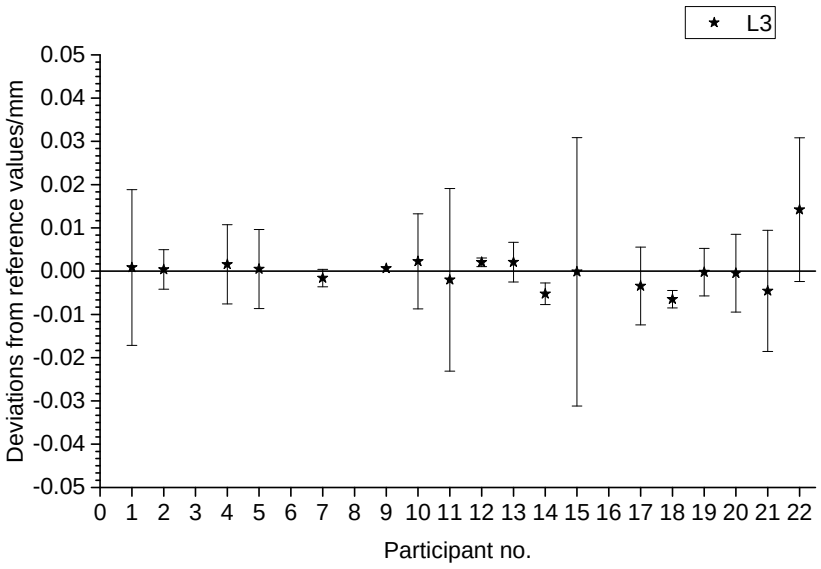

(b)

Figure 6.17. Results for Assembly 1. Length L3: (a) deviation range ± 0.25 mm, (b) deviation range ± 0.05 mm

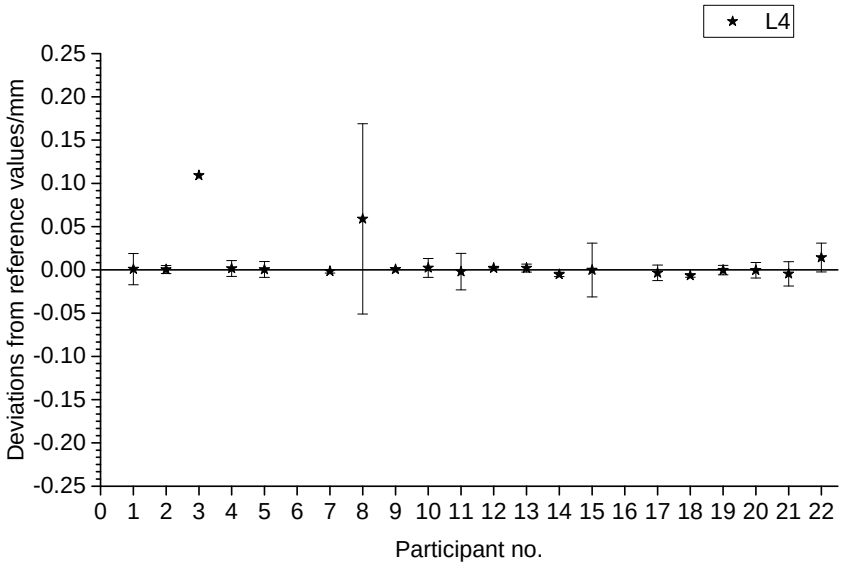

(a)

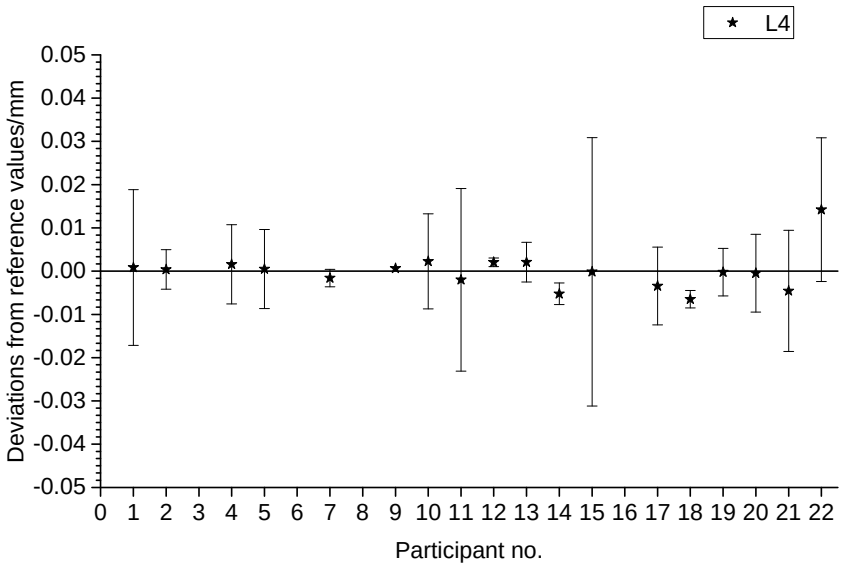

(b)

Figure 6.18. Results for Assembly 1. Length L4: (a) deviation range ± 0.25 mm, (b) deviation range ± 0.05 mm

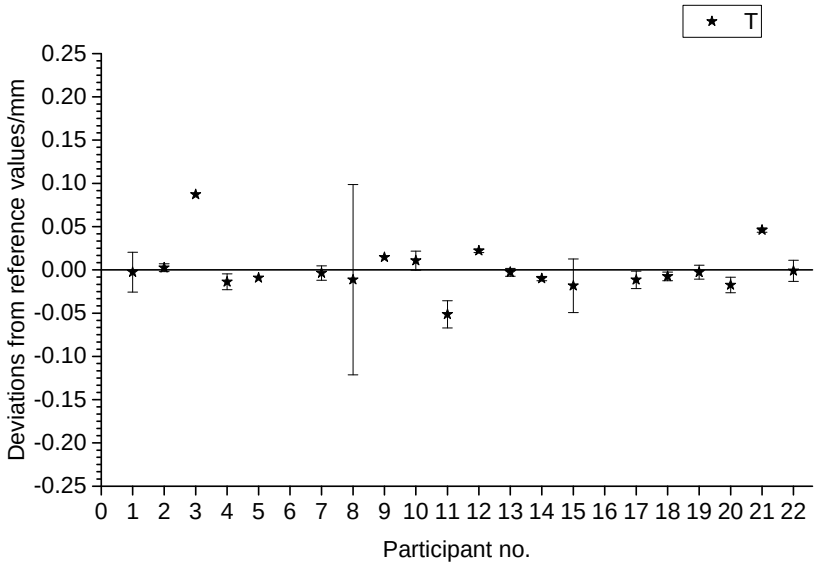

(a)

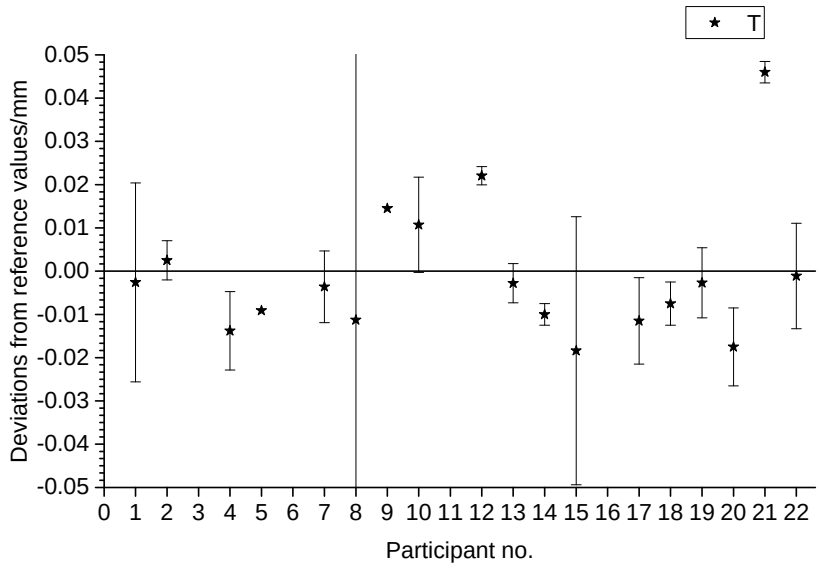

(b)

Figure 6.19. Results for Assembly 1. Length T: (a) deviation range ± 0.25 mm, (b) deviation range ± 0.05 mm

Table 6.7. Mean error-to-voxel size ratios (%) for Assembly 1 scanned using the Fast Scan approach.

Participant no.	L1	L2	L3	L4	T
1	2	23	27	4	5
2	1	1	2	1	5
3	170	130	228	251	136
4	2	7	74	18	21
5	1	4	5	10	26
6					
7	5	3	13	9	11
8	100	212	364	86	19
9	1	33	28	0	23
10	6	18	18	5	27
11	6	3	8	1	145
12	5	18	6	2	53
13	2	9	7	0	3
14	11	33	52	1	21
15	0	1	1	0	21
16					
17	8	4	4	29	25
18	8	6	14	12	10
19	1	17	27	3	7
20	2	122	92	1	58
21	11	8	3	22	115
22	36	35	19	59	3

6.9 Comparison between Own Choice and Fast Scan apprach

Figure 6.20 shows the deviations between two scanning approaches for all measurands. The deviation, δ, is defined for each measurement as follows:

$$\delta = X_{Fast\ scan} - X_{Own\ choice}, \tag{24}$$

here, $X_{Fast\ scan}$ is the measurement obtained using the Fast Scan approach and $X_{Own\ choice}$ is the measurement obtained using the Own Choice approach.

The measurements of *L1* show positive average deviations in the order of 0.002 mm, with a maximum deviation between the two approaches of 0.060 mm. The measurements of *L2* present positive average deviations in the order of 0.007 mm, with a maximum deviation between the two approaches of 0.070 mm. Participant no. 1, 3, and 8 show the biggest differences for this measurand. The results associated with *L3* show average deviations in the order of -0.001 mm, with a maximum deviation between the two approaches of 0.016 mm. The measurement results related to *L4* present average deviations in the order of 0.002 mm, with a maximum deviation between the two approaches smaller than 0.020 mm. Measurement deviations in the order of -0.005 mm, with a maximum deviation between the two approaches of -0.070 mm, are finally observed for *T*. The majority of the participants overestimated the measurement results of *L1*, *L2*, *L3*, and *L4*, and underestimated the measurement values of *T*. Statistical analysis conducted on measurement results highlighted that the number of outliers is larger in the Fast Scan approach than the Own Choice approach. Image analysis conducted on the data sets of the participants presenting large differences showed that the Fast Scan data sets are up to two times noisier than the data sets imaged using the Own Choice approach. Since noise influences bidirectional measurements, it can be explained the large difference between two scanning approaches for those participants.

13 out of the 22 participants declared similar measurement uncertainties for both scanning approaches, whereas 7 out of the 22 participants stated different uncertainty statements. Measurement uncertainties up to 111% larger were provided for Fast-Scan-based measurements compared to the measurements made using the Own Choice approach.

It can be concluded that the majority of the participants obtained similar measurement results and measurement uncertainties using both scanning approaches. The quantified deviations between the two scanning approaches are in the order of the repeatability of CT. Just a few participants achieved significantly different measurement results, most probably due to the impossibility of selecting suitable scanning parameters and preliminary corrections complying with the imposed scanning time.

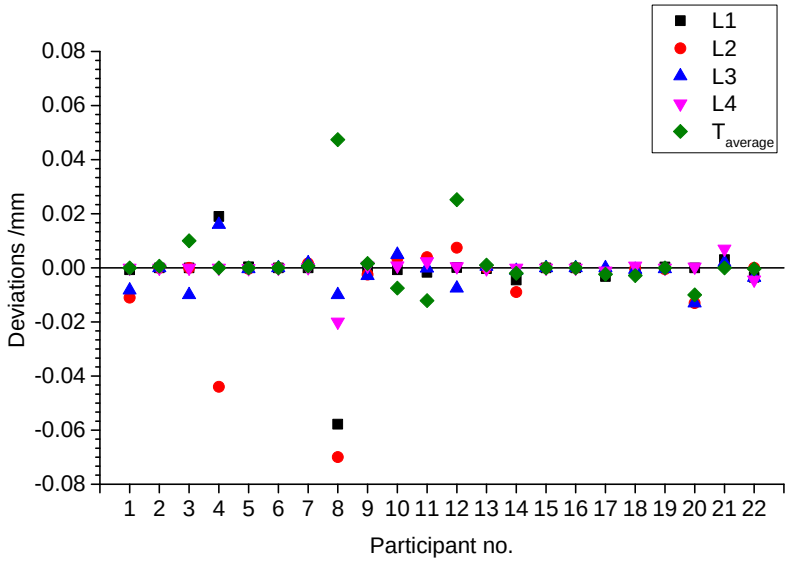

(a)

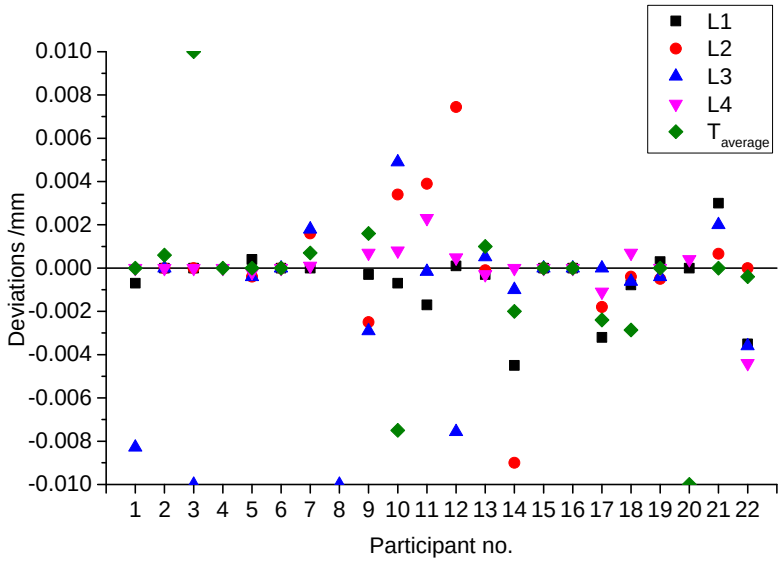

(b)

Figure 6.20. Deviations between two scanning approaches for all measurands: (a) deviation range ± 0.08 mm, (b) deviation range ± 0.01 mm

6.10 Agreement between participants and reference measurements

In order to ensure the agreement between reference measurements and participant measurements using the E_n, Figure 6.22, Figure 6.232, Figure 6.24, Figure 6.24 and Figure 6.25 show the distribution of E_n values calculated for Assembly 1.

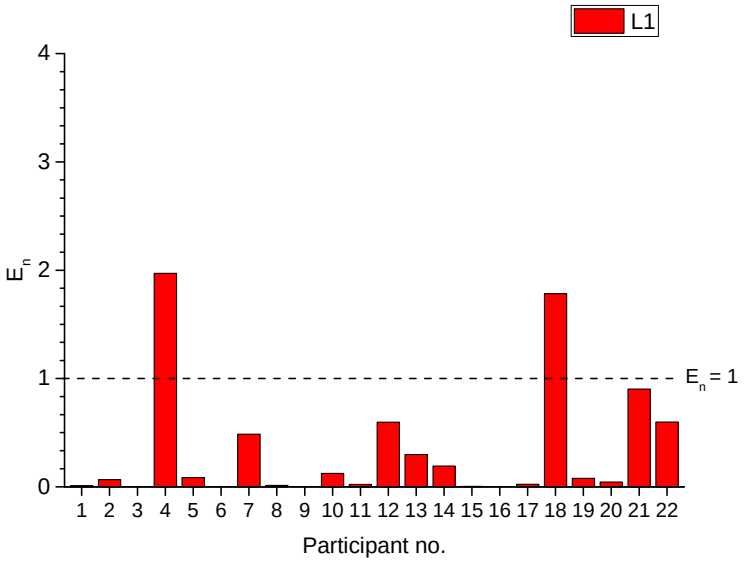

(a)

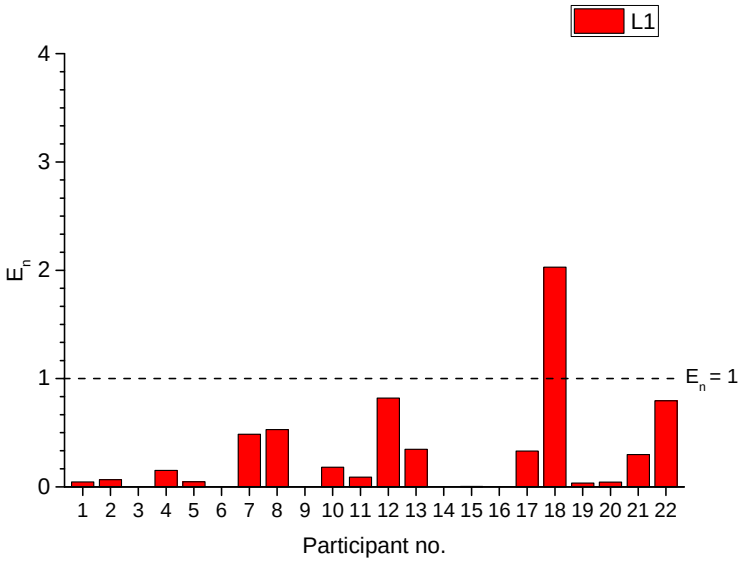

(b)

Figure 6.21. E_n values for the measurements of L1: (a) Own Choice approach (b) Fast Scan approach

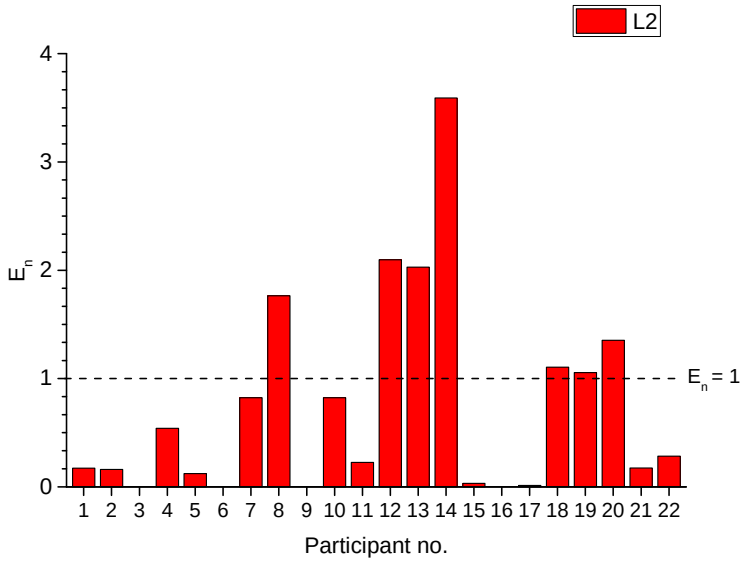

(a)

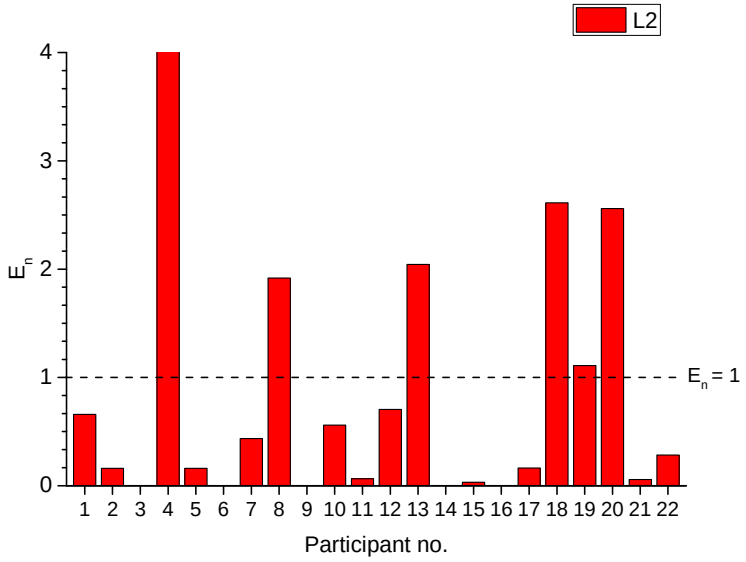

(b)

Figure 6.22. E_n values for the measurements of L2: (a) Own Choice approach (b) Fast Scan approach

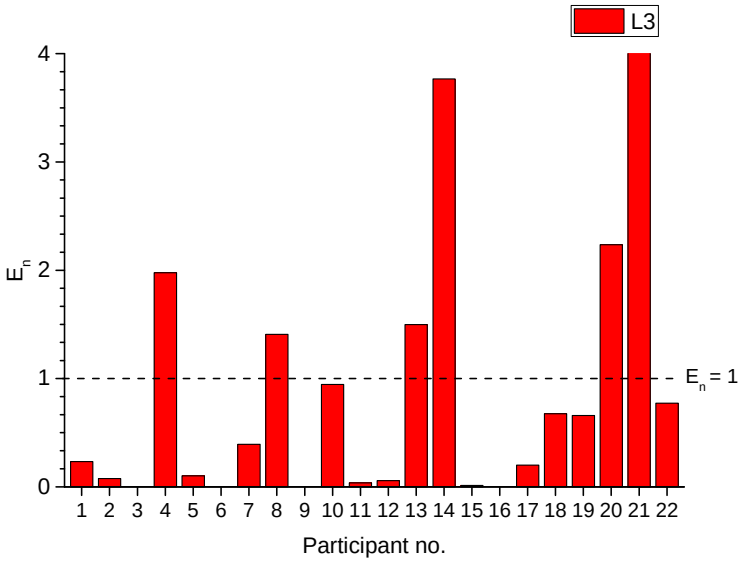

(a)

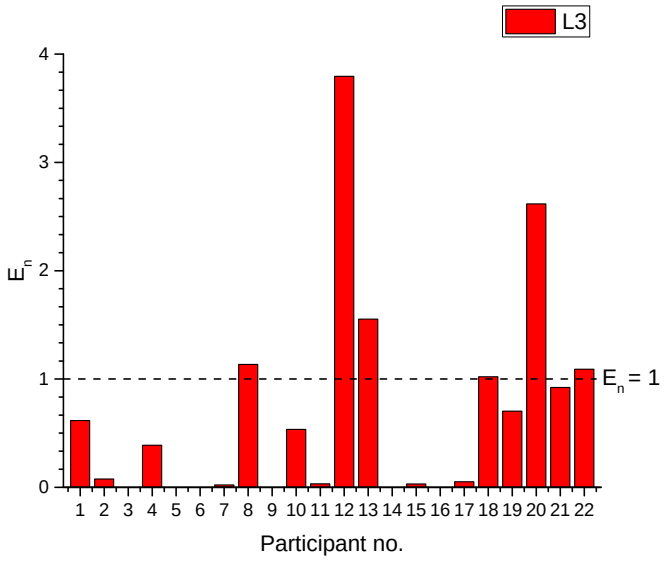

(b)

Figure 6.23. E_n values for the measurements of L3: (a) Own Choice approach (b) Fast Scan approach

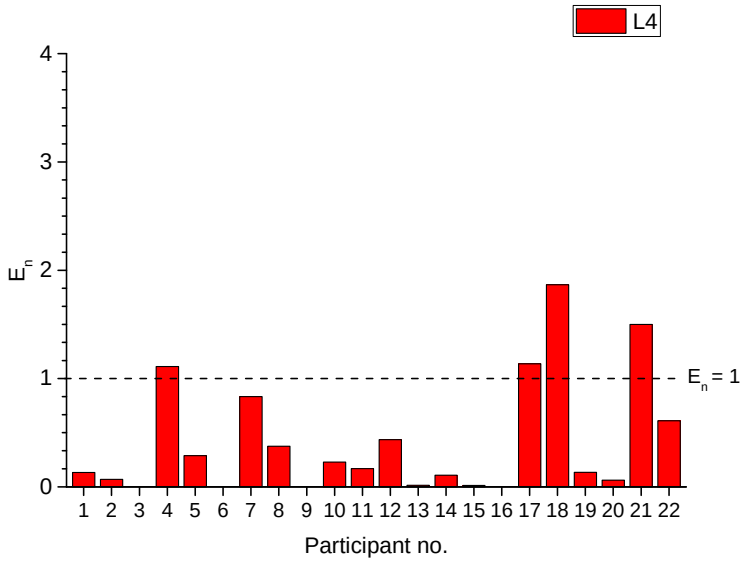

(a)

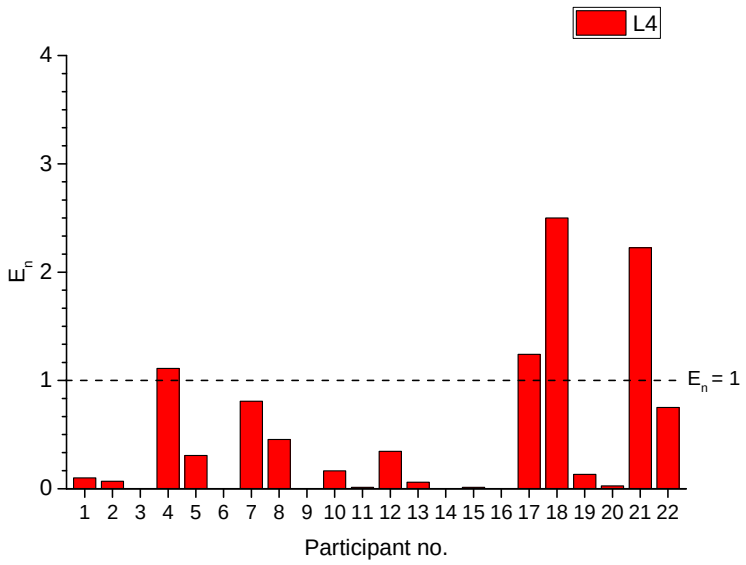

(b)

Figure 6.24. E_n values for the measurements of L4: (a) Own Choice approach (b) Fast Scan approach

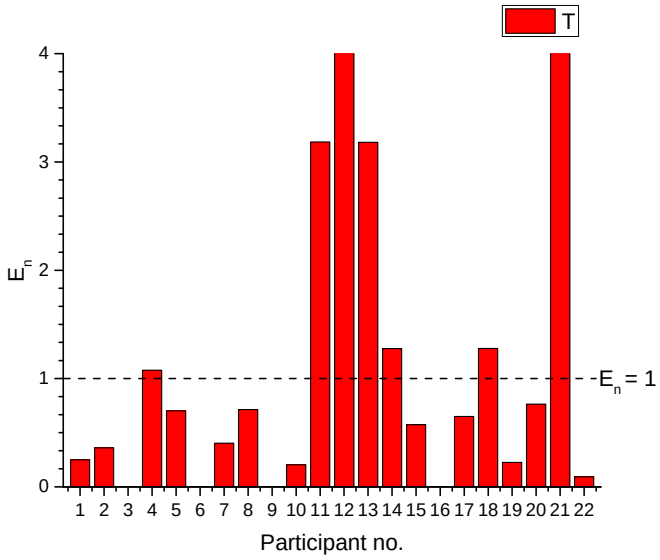

(a)

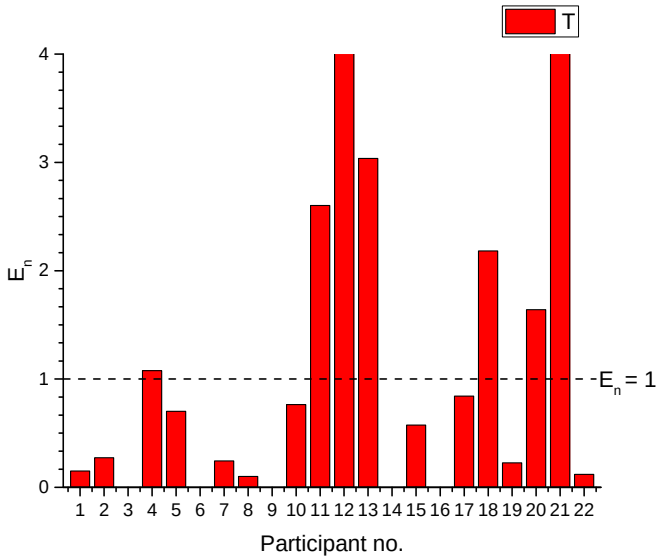

(b)

Figure 6.25. E_n values for the measurements of T: (a) Own Choice approach (b) Fast Scan approach

71% of the measurements conducted using the Own Choice approach are in agreement with the reference values. 59% of the measurement results carried out using the Fast Scan approach are in accordance with the reference values. The level of agreement strongly depends on the measurands. *L2* and *L3*, which are bidirectional measurands, show lower agreement than *L1* and *L4*, which are unidirectional lengths. The latter normally raise no problems due to their high robustness against noise and beam hardening artefacts. The measurements of *T* show a worse agreement than *L3* despite their similarities (both are bidirectional lengths of similar size). This result confirms the greater difficulty in defining a multi-material surface determination and a stable datum system for measurements of *T* compared to *L3*. The larger deviations registered for *T* may also be explained by the position of the measurand within the measured

volume. *T* does not lie in the centre of the beam as *L3* does, which may result in incrementing reconstruction errors. Measurements of *L2* are generally smaller than the calibration values, whereas *L3* are generally larger. This difference is due to the impact of noise and beam hardening on the surface determination and measurements. *L1* and *L4* present similar deviations despite the different size.

Figure 6.26 shows that the participants all present a similar trend of deviations but with different amplitude. The trends of deviations give evidence that X-ray systems suffer from geometrical errors. A few participants showed systematic errors due to either an inefficient correction of scale error or of temperature effects. Residual errors are also seen in systems corrected against the scale error by means of reference objects. Figure 6.27 and Figure 6.28 show the deviations of *L1*, *L2*, *L3*, *L4*, and T for the two scanning approaches. By using the scatter plots, it can be observed that *L1* shows that all participants are close to one another, whereas the remaining measurands show larger differences among the participants. The number of measurement outliers does not increase among the measurands, whereas the distribution spread does. Narrower distributions can be seen for *L1* and *L4* with respect to *L2*, *L3*, and *T*. The distributions of measurements of *L1* and *L4* present similar standard deviations values, suggesting that repeatability of inspections does not change as the size of a measurand increases. None of the distributions of deviations has zero mean, proving the presence of systematic errors in the measurement results.

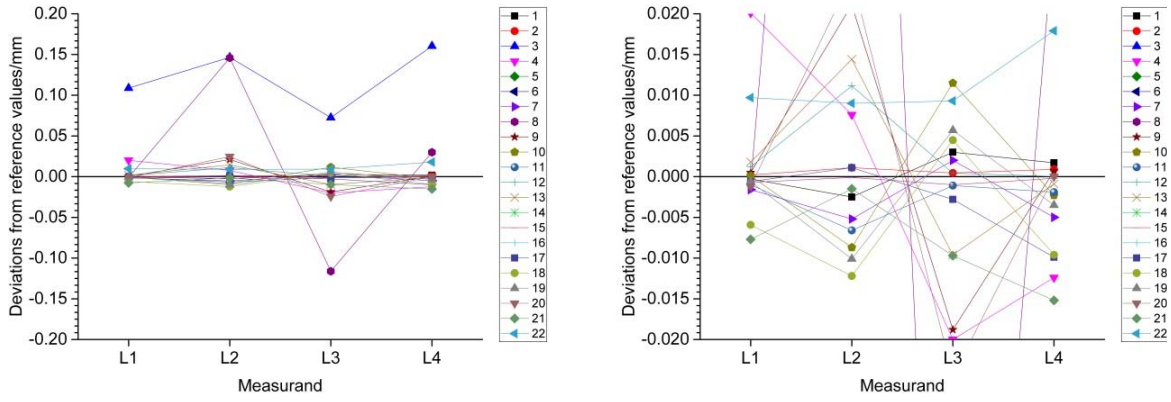

(a) (b)

Figure 6.26. Trends of deviations for the four measurands, L1, L2, L3, and L4: (a) deviation range ± 0.20 mm and (b) deviation range ± 0.020 mm

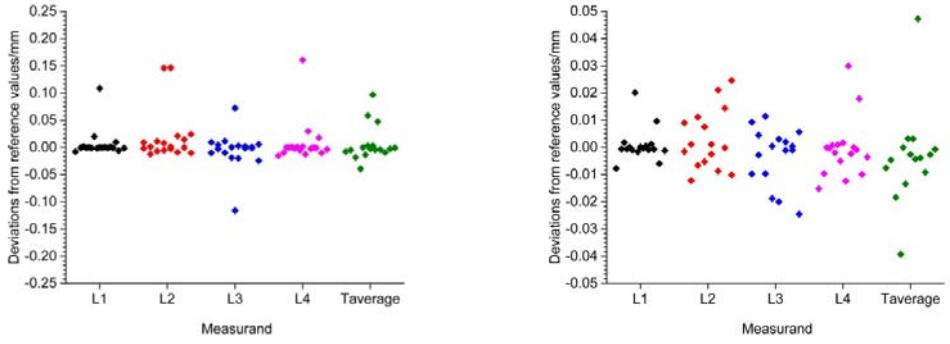

(a) (b)

Figure 6.27. Scatter plots for the four measurands scanned using the Own Choice approach, L1, L2, L3, and L4: (a) deviation range ± 0.25 mm and (b) deviation range ± 0.05 mm

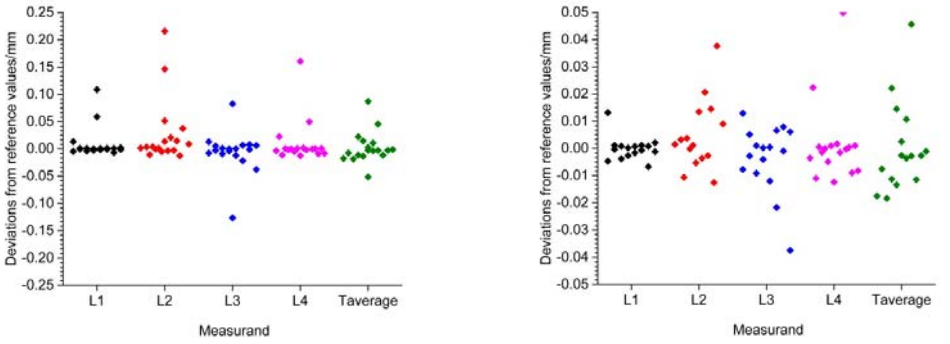

(a) (b)

Figure 6.28. Scatter plots for the four measurands scanned using the Fast Scan approach, L1, L2, L3, and L4: (a) deviation range ± 0.25 mm and (b) deviation range ± 0.05 mm

The spread of distributions varies with the scanning approaches. The Own Choice approach resulted in smaller distributions compared to the Fast Scan approach. The spread of distributions can be used for highlighting the impact of noise on the measurement results.

6.11 Industrial CT scanners used by the participants

The frequency of industrial CT scanners used is shown in Figure 6.29. The majority of the participants have access to CT systems for dimensional measurement while a very small number of the participants possess CT systems for general applications. Two main constructive differences between CT for dimensional measurement and CT for general applications are in the accuracy of the positioning system and in the stability of the cabinet temperature throughout the course of the inspection time. The frequency of MPE values is shown in Figure 6.30. The majority of the participants provided the MPE_{SD} values, while some others provided the MPE_E. The difference between the two MPE concepts is that in the MPE_E includes MPE_{SD} along with PF and PS values. PS is the error within which the range of radii of a calibrated sphere can be determined with a CT. PF is the error within which the form of a calibrated sphere can be determined using a CT.

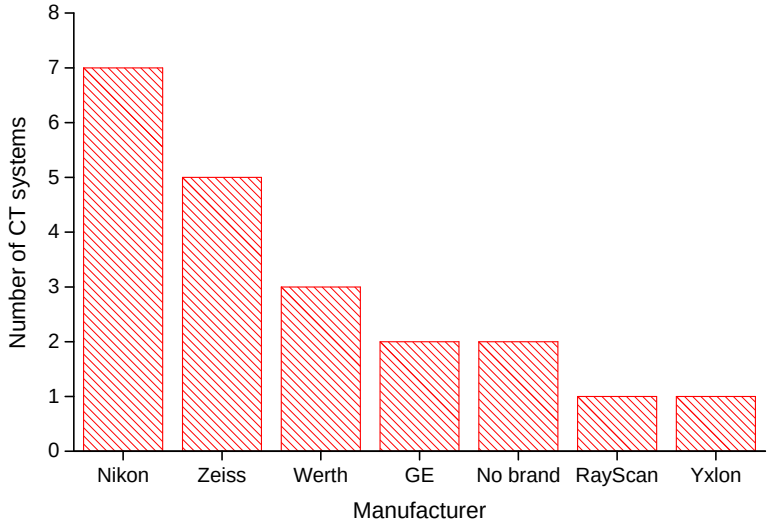

Figure 6.29. Brands of CT systems used within this comparison

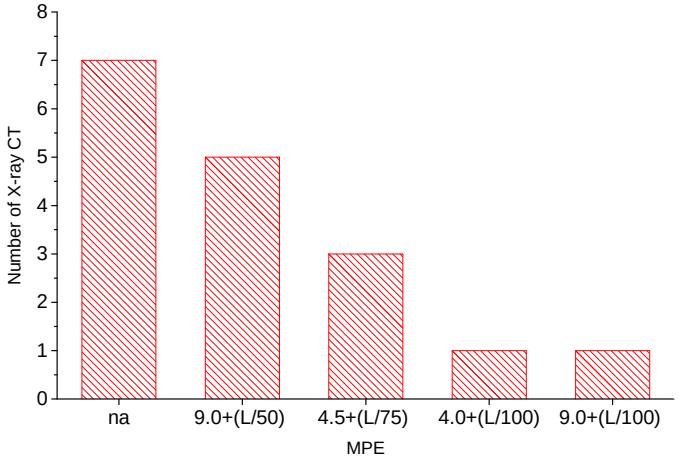

Figure 6.30. Frequency of MPE values

6.12 Assembly 1: impact of instrument settings and operator

18 out of the 22 participants oriented the workpieces in an inclined way in order to decrease the beam angle, which directly influences the Feldkamp artefacts. The workpiece could also have been measured upright without causing any differences as the measurands are far from the surface of the X-ray cone at any magnification.

14 out of the 22 participants applied a physical filter on the gun to re-shape the X-ray spectrum towards high energy (see Figure 6.31 and Figure 6.32), 10 of the 14 participants used copper (*Cu*), 2 out of the 22 participants used Tin (*Sn*), 1 out of 14 used Iron (*Fe*), and 1 of the 14 used Aluminium (*Al*). *Cu* has a higher photoelectric absorption than Compton scatter which makes it an efficient filter for industrial applications [131]. The photoelectric coefficient varies with energy and atomic number. The Compton coefficient is independent of energy and almost independent of atomic number. The K-shell binding energy of *Cu* is 9 keV, resulting in absorbing X-rays in the range of 9-30 keV. *Sn* has a K-shell binding energy of 29.2 keV, leading to absorbing photons of energies in the range of 30-70 keV through photo-electric interactions. This includes the characteristic radiation produced by X-ray target materials (e.g. Tungsten or Copper). 1 out of 20 participants used Sn together with *Cu* in order to compensate for the characteristic radiation generated by *Sn*. The K-shell binding energy of *Fe* resembles the one of *Cu*. The K-edge of *Al* is 1.56 keV, resulting in only absorbing low energy X-rays. *Al* can be used as filters for very soft materials, such as polymers, or for absorbing the X-ray fluorescence coming from filters with higher atomic number. X-ray fluorescence is the emission of secondary X-rays from a material that has been excited by high-energy X-rays. 12 of the 22 participants scanned the Assembly in good thermal conditions (T = 20 °C), while the remaining participants conducted their investigations in environments above 22 °C. The temperature values reported reflect the temperature within the X-ray CT cabinet. An overview of the temperature during scanning is given in Figure 6.33. Apart from the impact on the dimensional stability of the workpieces and the manipulator system, higher temperatures degrade the detector efficiency (DQE) and increase the dark current [132], which is a very important source of noise. 12 of the 22 participants scanned Assembly 1 once (see Figure 6.34.). 8 of the 22 participants scanned Assembly 1 more than once. A few participants repositioned the workpieces between two subsequent scans. 7 of the 22 participants performed a scale error correction using a reference artefact, as shown in Figure 6.35. Sphere-to-sphere distances or hole-to-hole distances were used for the correction. The scale error correction was conducted on CT scanners equipped with and without laser corrected linear guide-ways. The reference artefacts were also used for quantifying the measurement uncertainties. Other hard-ware corrections conducted by participants included detector calibration, which corrects for the non-uniform response of detector pixels, and axis qualification. Ring artefact corrections were conducted before scanning. Ring artefact corrections were based on either swimming of the workpiece across the detector by a few detector pixels or by post-processing the acquired projections.

The values of the current and voltage used for imaging the workpieces are shown in Figure 6.36. and Figure 6.37. It can be observed that higher voltage and current values were used for the Fast-Scan-based measurements compared to the Own-Choice-based measurements. An average voltage of 169 kV and of 173 was used for Own-Choice-based measurements and Fast-Scan-based measurements, respectively. As a general conclusion, the power varied between the two scanning. By conducting a statistical analysis, it was observed that the accuracy of length measurements would not depend upon the selected values of the current and voltage. It is therefore believed that the voltage is an important factor until a specific point ensuring that the workpiece is completely penetrated is reached. Likewise, the current is important until a certain value ensuring a minimum contrast between the background and the material is reached. By further increasing the voltage and current above those two points would not make any significant improvements.

The voxel sizes used by the participants are reported in Figure 6.38. The voxel sizes were calculated based on the detector pixel size p, the source-detector distance SDD, and the source-object distance SOD. Deviations from the reference values vs. voxel size are also given in Figure 6.39. for both scanning approaches. By performing a statistical analysis, it was observed that the accuracy of length measurements does not change with the voxel size. As a general conclusion the voxel size has no impact provided that the measurand is far larger than voxel size.

The prevalence of integration time is shown in Figure 6.40. The integration time strongly depends on the detector and on the power. When high X-ray powers are used the integration time can be reduced without affecting the image quality. It is however difficult to compare the integration time results because detectors and their integration time settings are tuned in connection with the X-ray power. It is known that a CT having a maximum X-ray voltage of 130kV has detector tuned differently from a CT having a maximum X-ray voltage of 200 kV. Longer integration times reduce the image quality due to dark current.

Most participants used image averaging to improve the image quality as shown in Figure 6.41. Most of the participants selected more than one image per projection. A few used 4 or more frames per projection. It should be noted that Participant 1, 2, 9, and 15 used more than one image per projection for scans conducted using the Fast Scan approach. Image averaging and integration can be synergistically used for improving image quality and reducing scanning time. For example, an integration time of 1 s and an image averaging of four frames produce the same image quality as an integration time of 4 s and no image averaging.

The scanning times used are shown in Figure 6.42. An average scanning time of 191 min was registered for Own-Choice-based measurements, with a maximum scanning time of 1120 min. An average scanning time of 40 min was used for Fast-Scan-based measurement, with a minimum scanning time of 9 min. Measurement deviations with respect to the scanning time are shown in Figure 6.43. It can be seen that even short scanning times lead to accurate measurements. This result confirms that the number

of projections has a minor impact on the accuracy of dimensional measurements. The number of projections can be therefore reduced when length measurements are made.

Most of the participants used an advanced thresholding method for segmenting the CT data sets. The surface determination was based on the average grey value intensity of the background and of the aluminium step gauge. Three participants used the region growing method starting from a seed point selected within the aluminium region of *Assembly 1*. Two participants used a Werth method whose features are not disclosed.

5 out of 18 participants applied a software beam hardening correction while reconstructing. 3 of these participants did not apply a physical filter on the X-ray source. Participants who used software correction of beam hardening are also the participants with large deviations from CMM values.

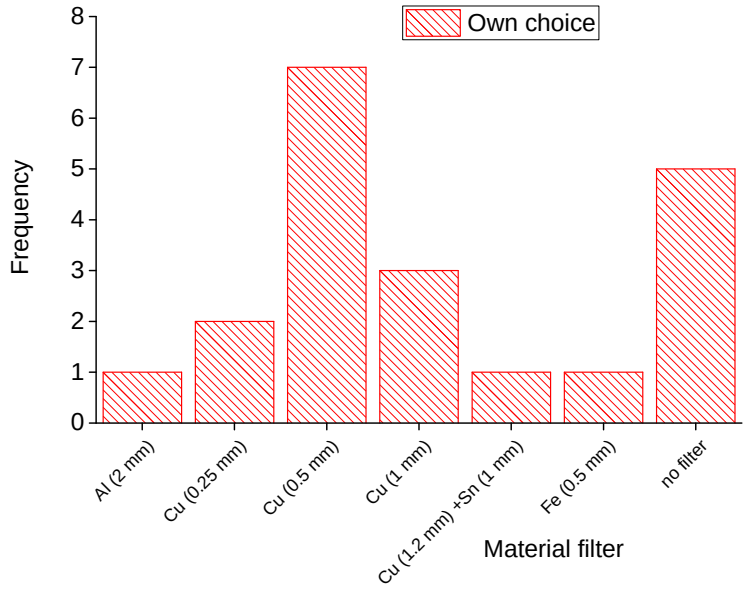

Figure 6.31. Pre-filter material and thickness in mm for Assembly 1 (Fast Scan approach)

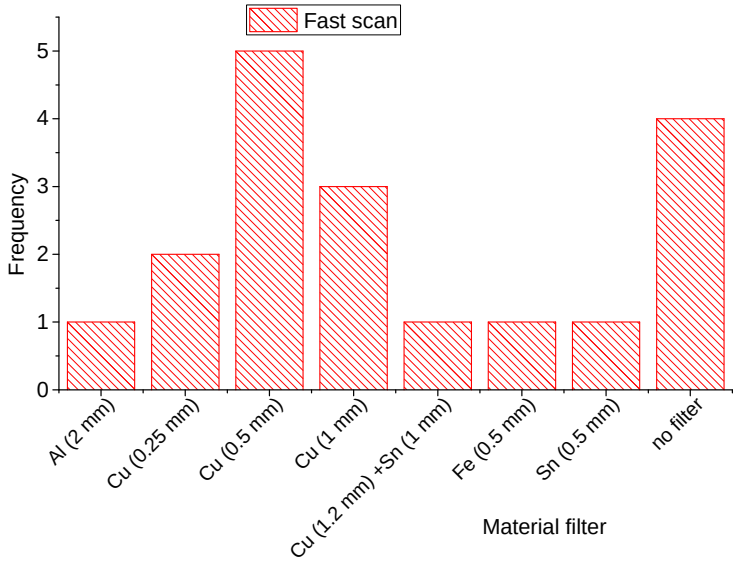

Figure 6.32. Pre-filter material and thickness in mm for Assembly 1 (Own Scan approach)

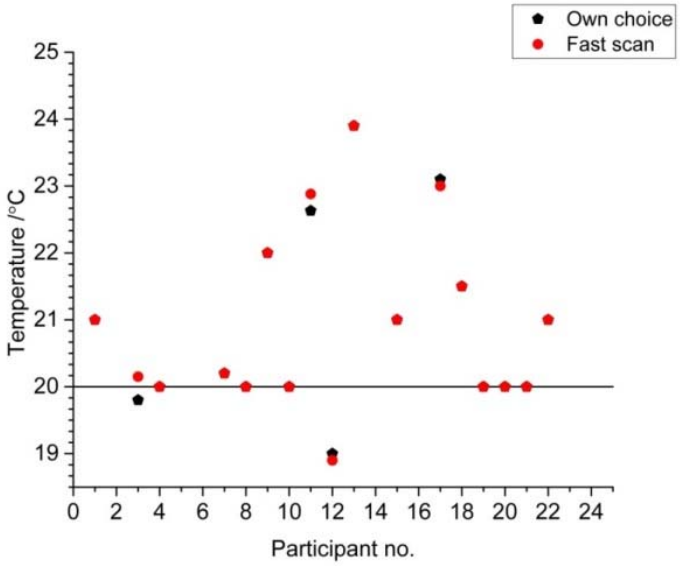

Figure 6.33. Temperature inside the CT scanner

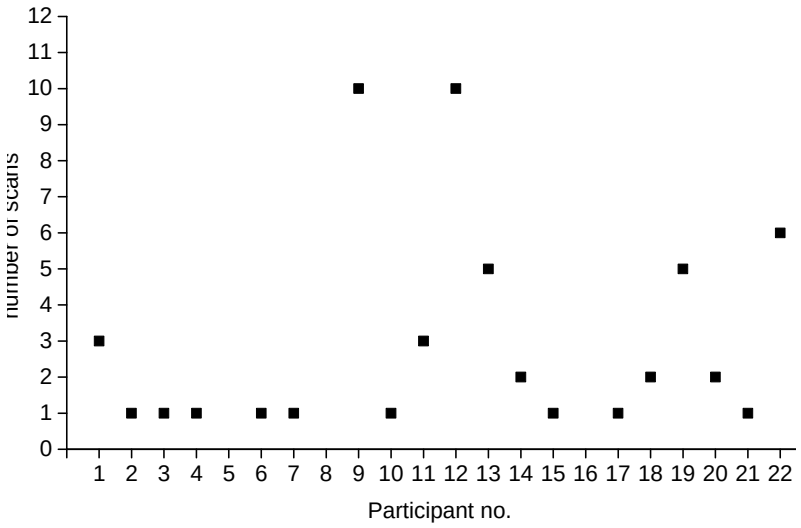

Figure 6.34. Number of scans per participant

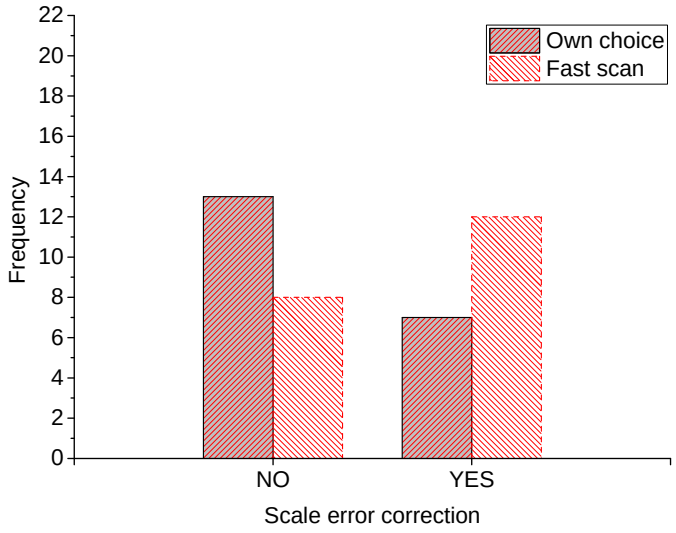

Figure 6.35. Scale error correction

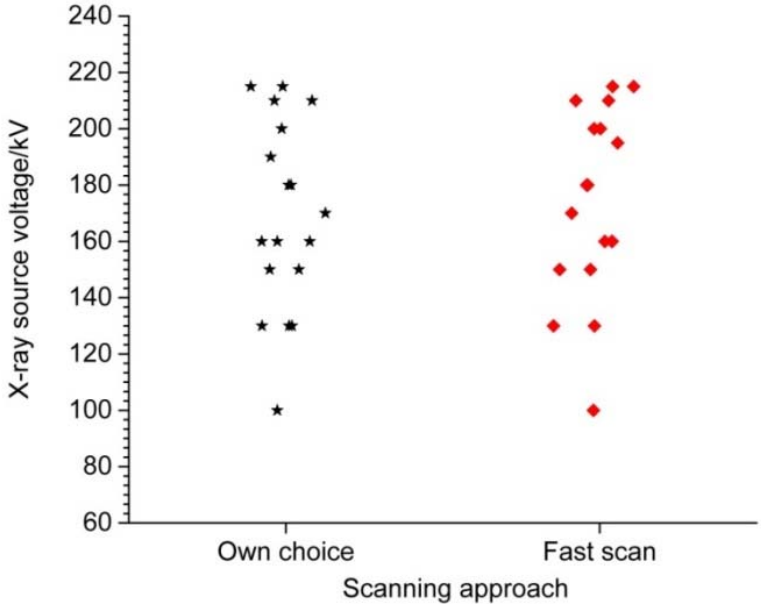

Figure 6.36. X-ray source voltage for both scanning approaches

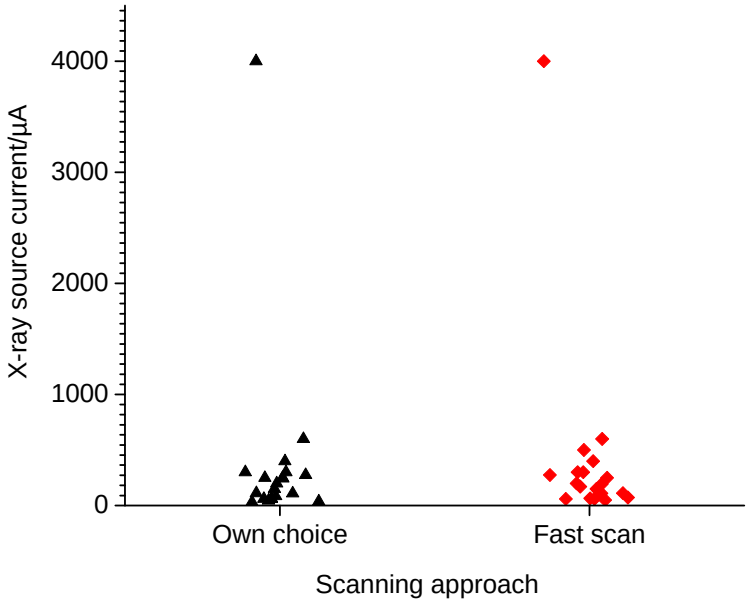

(a)

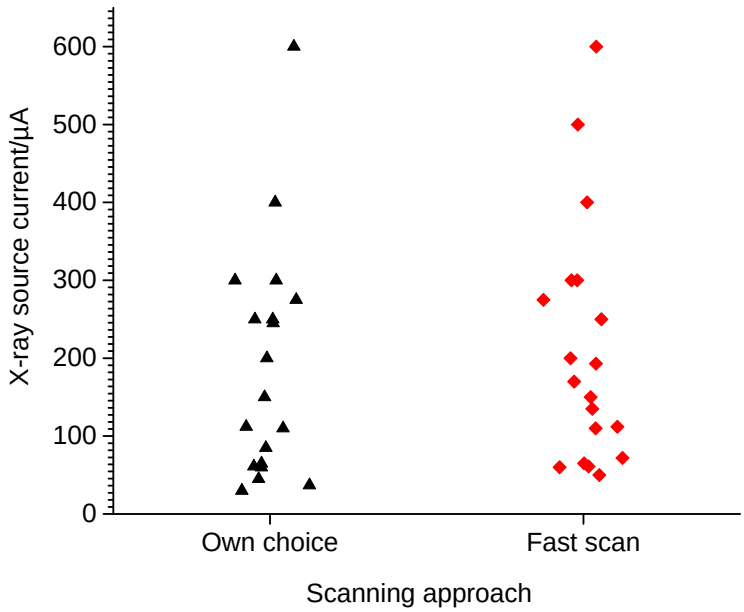

(b)

Figure 6.37. X-ray source voltage for both scanning approaches: (a) range up to 4500 µA and (b) range up to 600 µA

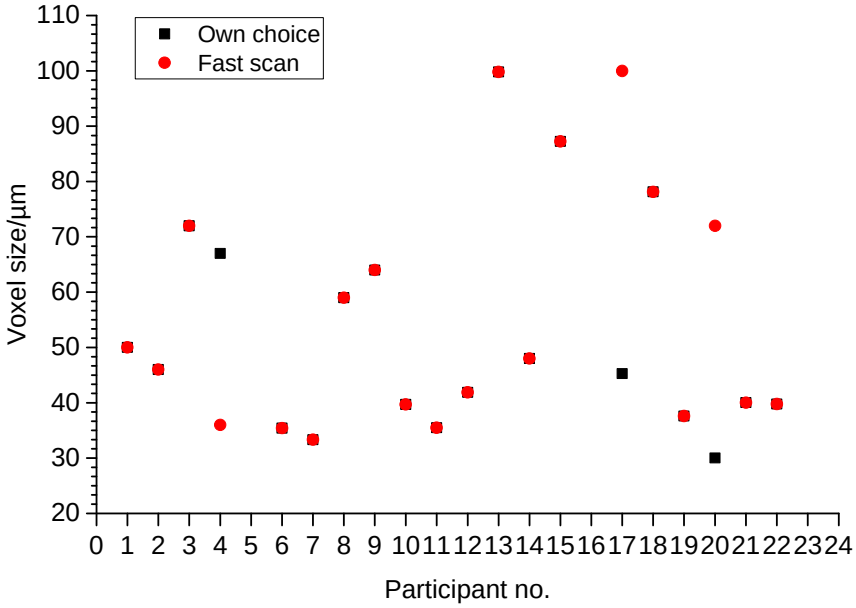

Figure 6.38. Voxel sizes used for both scanning approaches

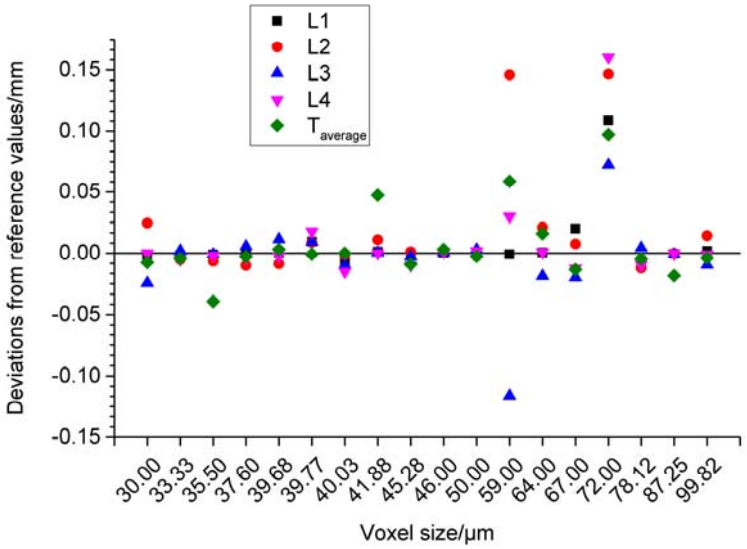

Figure 6.39. Deviation from reference values vs. voxel size for Item Assembly 1. Similar results for Own Choice and Fast Scan approach

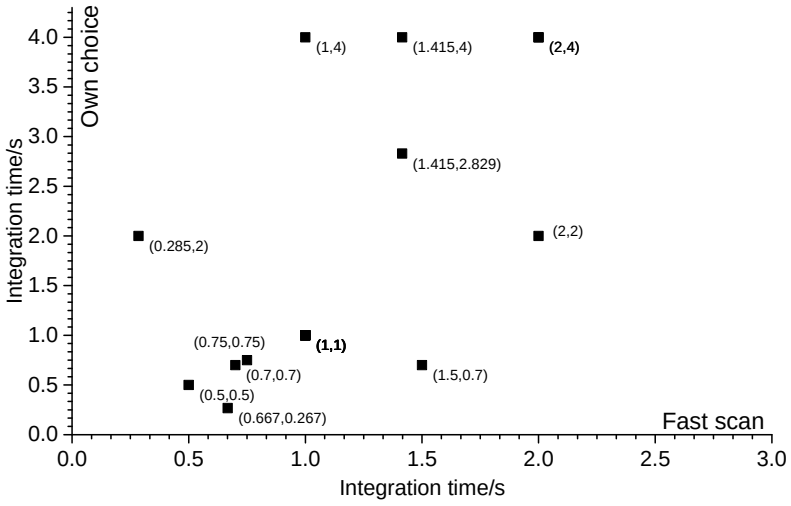

Figure 6.40. Frequency of integration time

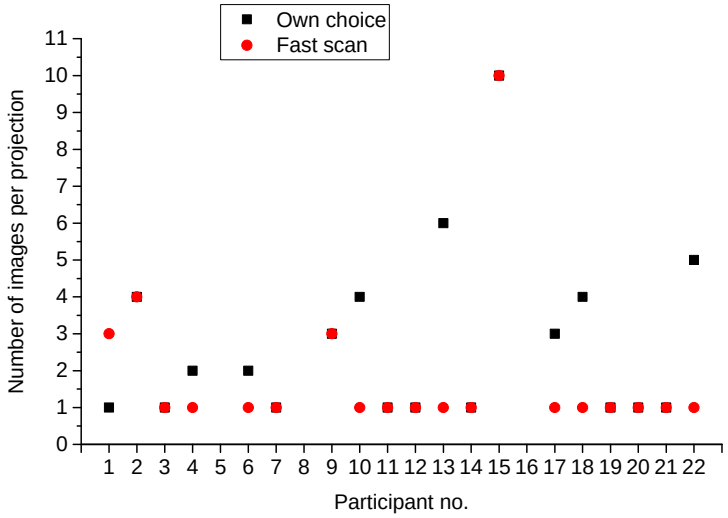

Figure 6.41. Number of image averaging for both scanning approaches

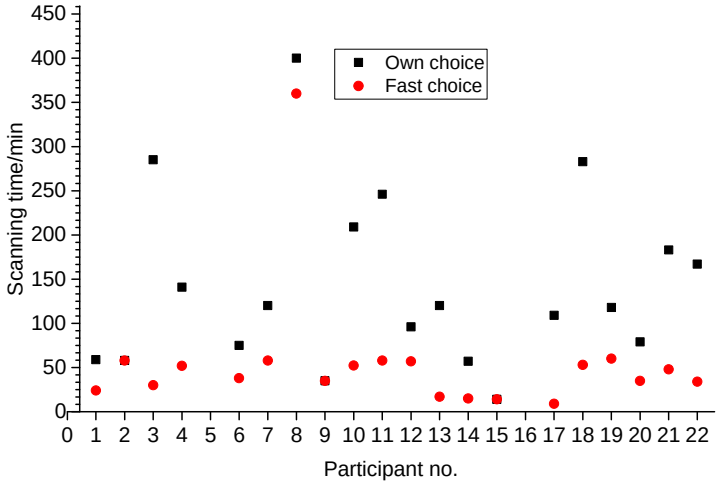

Figure 6.42. Scanning time for both scanning approaches

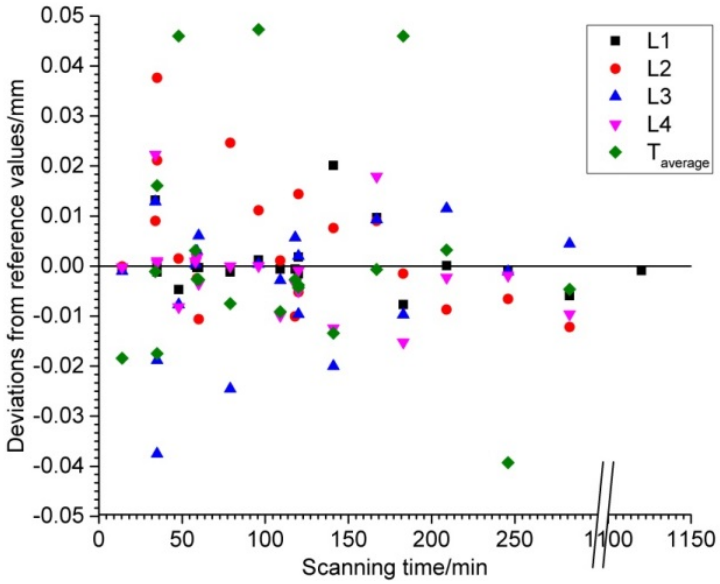

(a)

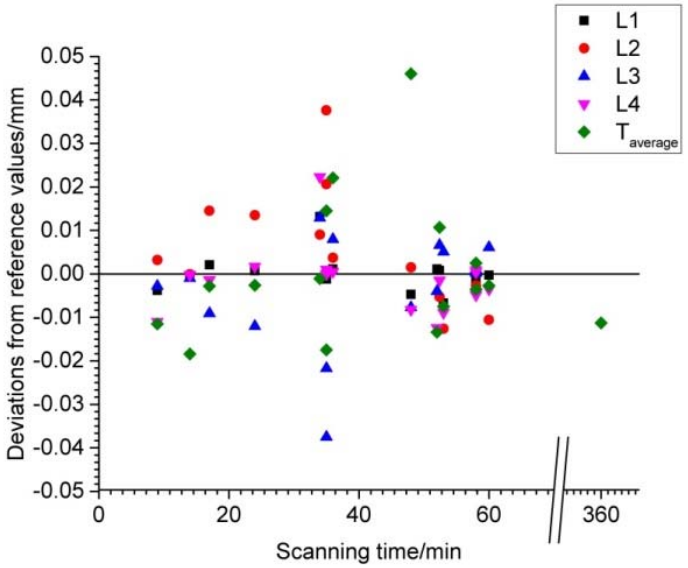

(b)

Figure 6.43. Deviation from reference values vs. scanning time for Assembly 1: (a) Own Choice and (b) Fast Scan. Range ± 0.05 mm.

6.13 Assembly 1: measurement uncertainty statements

The uncertainty methods applied by the participants are shown in Figure 6.44. 5 of the 22 participants used the MPE. 6 out of the 22 participants used more complex measurement uncertainty approaches which relied on reference objects scanned before or after the workpiece of Assembly 1. The environment temperature, the system repeatability, voxel size, probing error, detector errors, and rotary table errors represent the further considered contributions. It is important to report that participants who stated measurement uncertainties based on ISO 15530-3 (see Section 3.8 for an in-depth description) used reference objects which were not similar to Assembly 1. It is therefore believed that there exists some confusion among participants regarding the use of different methods to estimate the uncertainty in CT measurements. Finally, 3 of the 22 participants did not provide any measurement uncertainty statement, mainly due to the fact that those participants have recently started working in dimensional CT.

The frequency of uncertainty sizes for Assembly 1 is shown in Figure 6.45 and in Figure 6.46 for measurements conducted using the Own Choice approach and the Fast Scan approach, respectively. The presented uncertainty values comprise all the uncertainty provided by participants. Two main observations can be drawn from the figures. Firstly, the measurement uncertainties can be clustered in 5 groups having increasing magnitudes. The majority of the participants stated values below 10 µm (≈ MPE) for all measurands. 2 out of the 22 participants stated measurement uncertainties above 30 µm. The second observation is that larger measurement uncertainties were stated for Fast Scan´s measurements than for Own Choice´s ones. The increase of measurement uncertainties is mainly observed for the bidirectional measurements, which are more sensitive to surface noise. In contrast to the previous two pictures, Figure 6.47 and Figure 6.48 show the frequency of the values of measurement uncertainties ensuring E_n values < 0.99. This analysis was performed to investigate whether the participants underestimated or underestimated their uncertainty statements. From the two figures can be seen that the recalculated measurement uncertainties are generally smaller than those ones stated by participants for all measurands. This means that most of the participants measure better than they believe. From the figures it can also be seen that a few measurement uncertainties are found to be bigger at $E_n < 0.99$, indicating that some participants stated measurement uncertainties which were not large enough to include systematic errors affecting their CT measurements.

Based on the results it can be seen that most of the participants identified in the MPE value of their own CT systems an estimation of measurement uncertainty. Despite its simplicity, the use of MPE may present two potential limitations. Firstly, the MPE is quantified from scanning conditions which may not totally reflect the scans produced for the comparison. For example, the reference object used for quantifying the MPE may be different from Assembly 1 in terms of size, material and measurands. Secondly, the MPE, being defined as a range, needs to be converted into an uncertainty contribution using e.g. one of the probability distributions listed in the GUM. Most did not apply any distribution for converting the MPE into an uncertainty contribution. As a consequence, the MPE does not fully meet

the requirement of similarity between features that is necessary for establishing traceability in this comparison. It is also important to report that MPE is not a static parameter of a measuring equipment because it varies over time, especially when exceptional events occur. For example, a wrong replacement of filament can change the emission of X-rays modifying the MPE.

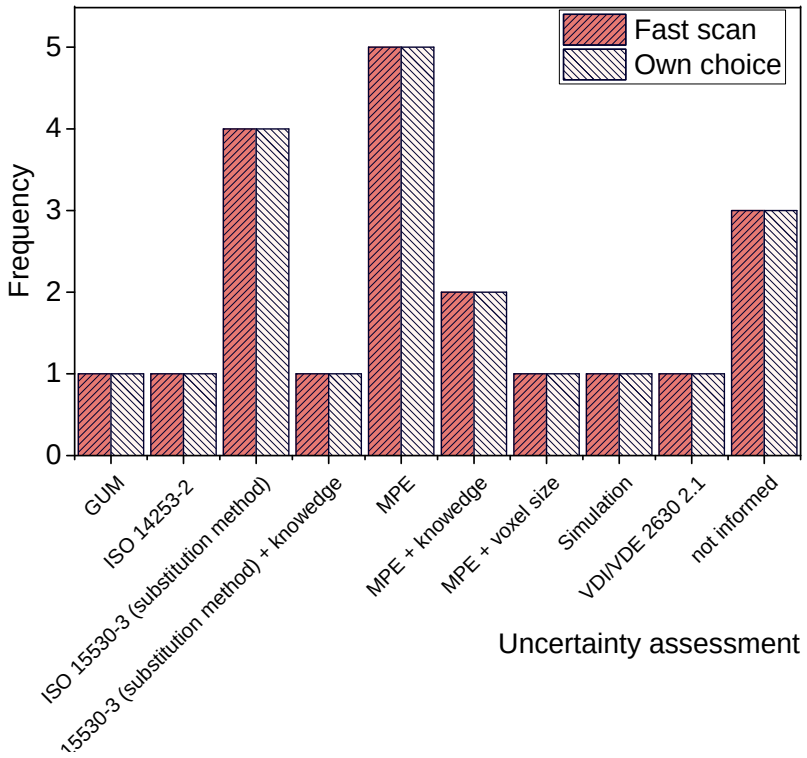

Figure 6.44. Frequency of uncertainty methods applied by the participants

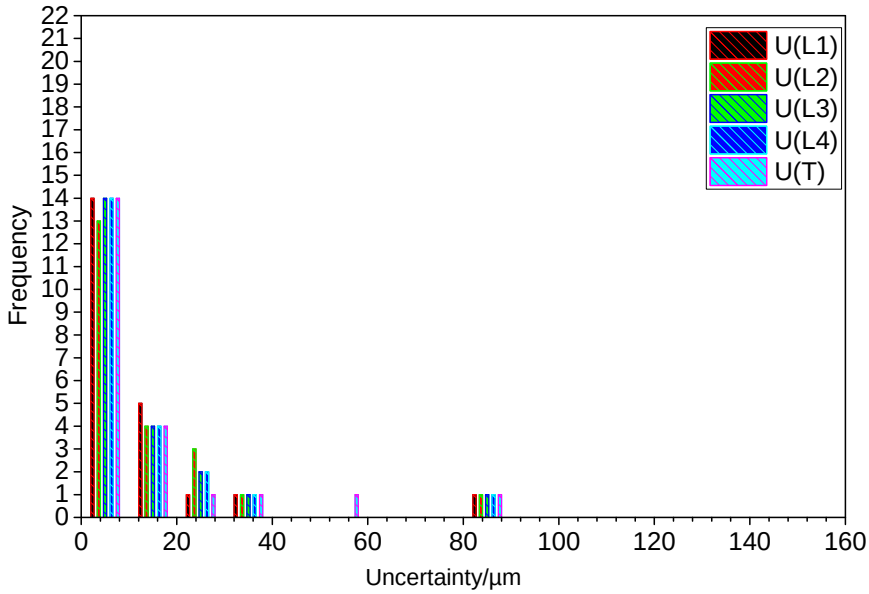

Figure 6.45. Histogram of uncertainty sizes for Assembly 1 scanned using the Own Choice approach

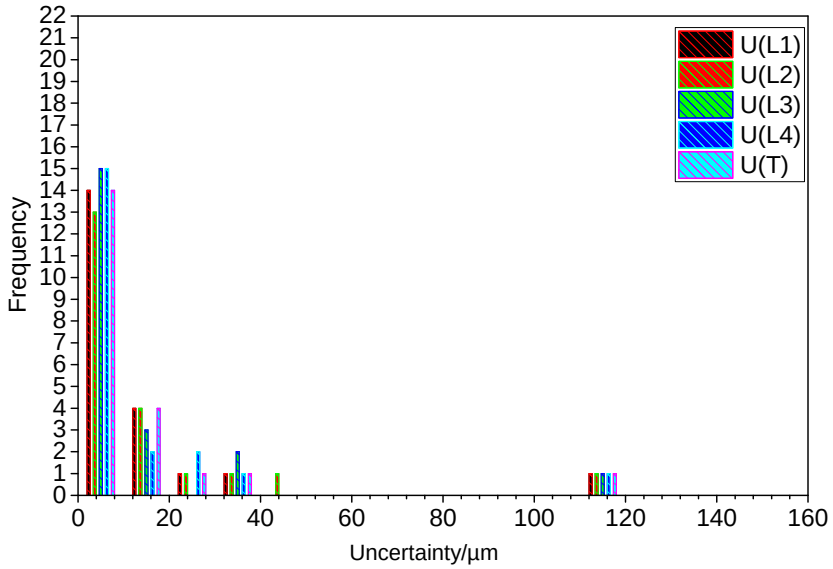

Figure 6.46. Histogram of uncertainty sizes for Assembly 1 scanned using the Fast Scan approach

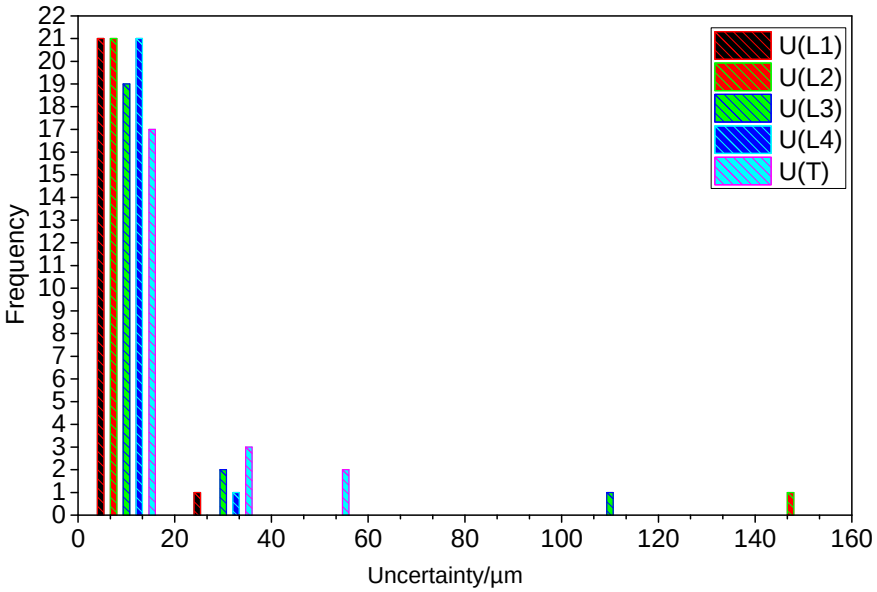

Figure 6.47. Histogram of uncertainty sizes for Assembly 1 ensuring E_n <0.99. The measurement uncertainties refer to the Own choice approach

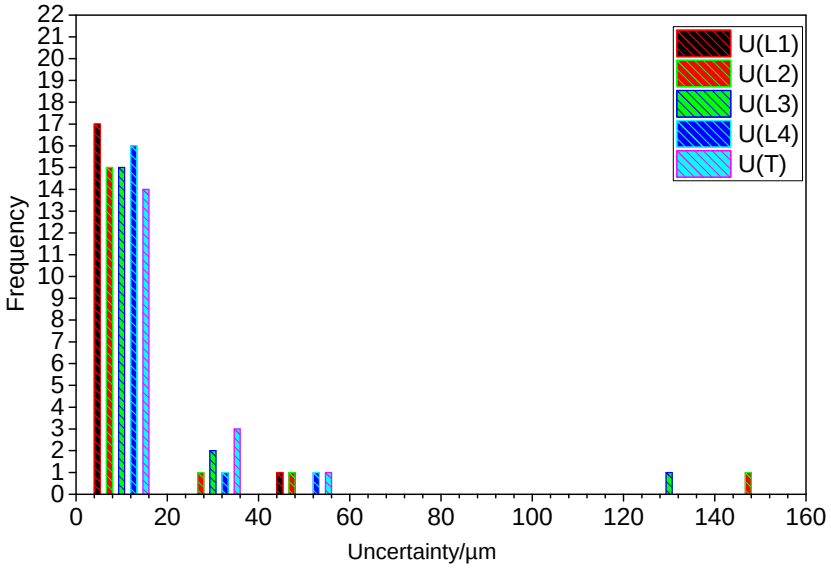

Figure 6.48. Histogram of uncertainty sizes for Assembly 1 ensuring E_n <0.99. The measurement uncertainties refer to the Fast Scan approach

6.14 Results for Assembly 2

16 participants of the comparison measured Assembly 2. Their results are shown in Figure 6.49 for the measurements conducted on the HR data sets and in Figure 6.50 for the measurements made on the *LR* data sets. From the measurements of the diameters *D1* and *D2*, it can be seen that those measurands were made without problems by all the participants. The standard deviation of the deviations among participants was found to be 1 µm for *D1* and *D2*. No difference in the standard deviation values was observed between *HR* and *LR* data sets, suggesting that noise has a minor impact on those measurands. It was also seen that different inspection software packages provided similar measurement results.

A good agreement among participants for measurements was observed for measurements of *R1*, although larger differences were observed among participants. The standard deviations were quantified to be approximately 1.5 µm and 2.5 µm for the measurements conducted on *HR* data sets and *LR* data sets, respectively. The increase in the standard deviation may be due to the image noise impairing the accuracy of the surface determination process. The increase in the standard deviation may also be due to the procedure used for quantifying the measurands, especially in connection with the removal of fitted points that deviate from the other fitted points. The statistical analysis of measurement results showed that the number of outliers, representing the participants which are far from the others, changed between the measurements conducted on the *HR* data sets and those ones made on the *LR* data sets. Four participants were found to be outliers for the *HR* data sets, while only 1 participant was found to be an outlier for the *LR* data sets. Fewer outliers were observed for *LR* data sets because the distribution of measurement results is wider, resulting in reducing the likelihood of outliers. The number of outliers was quantified using Grubbs' test [133].

The measurement results of *C1* show a worse agreement among participants. The standard deviations were found to be approximately 9 µm and 12 µm for the measurements conducted on HR data sets and *LR* data sets, respectively. As a result, the standard deviation of measurements of *C1* increased by approximately 34% for the *LR* data sets compared to the *HR* data sets. Concentricity is well known to be one of the most difficult tolerances to measure due to its difficulty in establishing the mid points of the feature. Therefore, the large variability can be due to errors in establishing a robust alignment system for quantifying concentricity.

It can be concluded that increasing the difficulty of the measurement task influences the results obtained by the participants. Simple measurands such as diameters yield no problems, while complex measurands such as roundness and concentricity affects the results. It can also be concluded that noise increases the measurement variability among participants by up to 34 % for complex measurands.

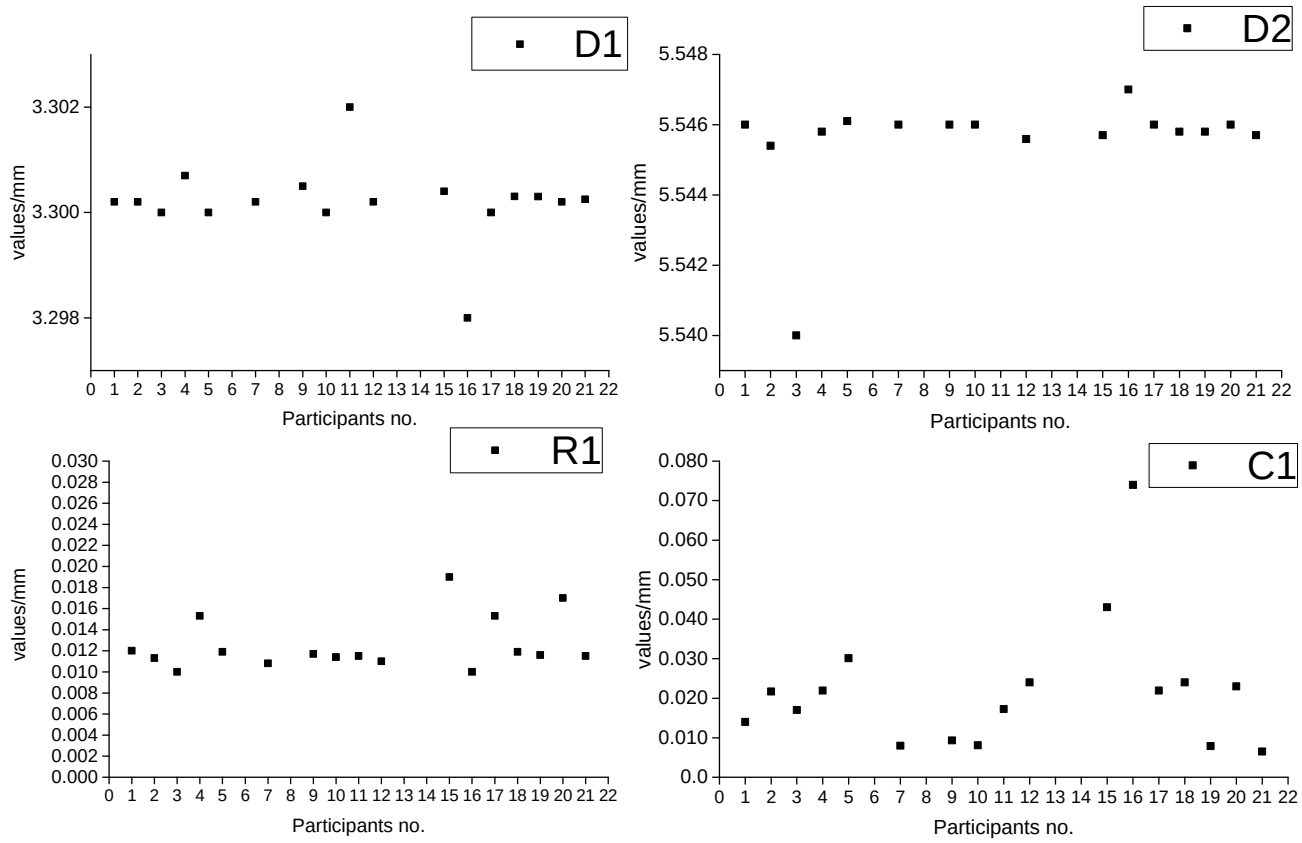

Figure 6.49. Results for Assembly 2 (HR data sets). The calibration value for D1 is 3.0012 ± 0.0010 mm, for D2 is 5.5432 ± 0.0010 mm, for R1 is 0.0074 ± 0.0015 and C1 is 0.0093 ± 0.0024 mm

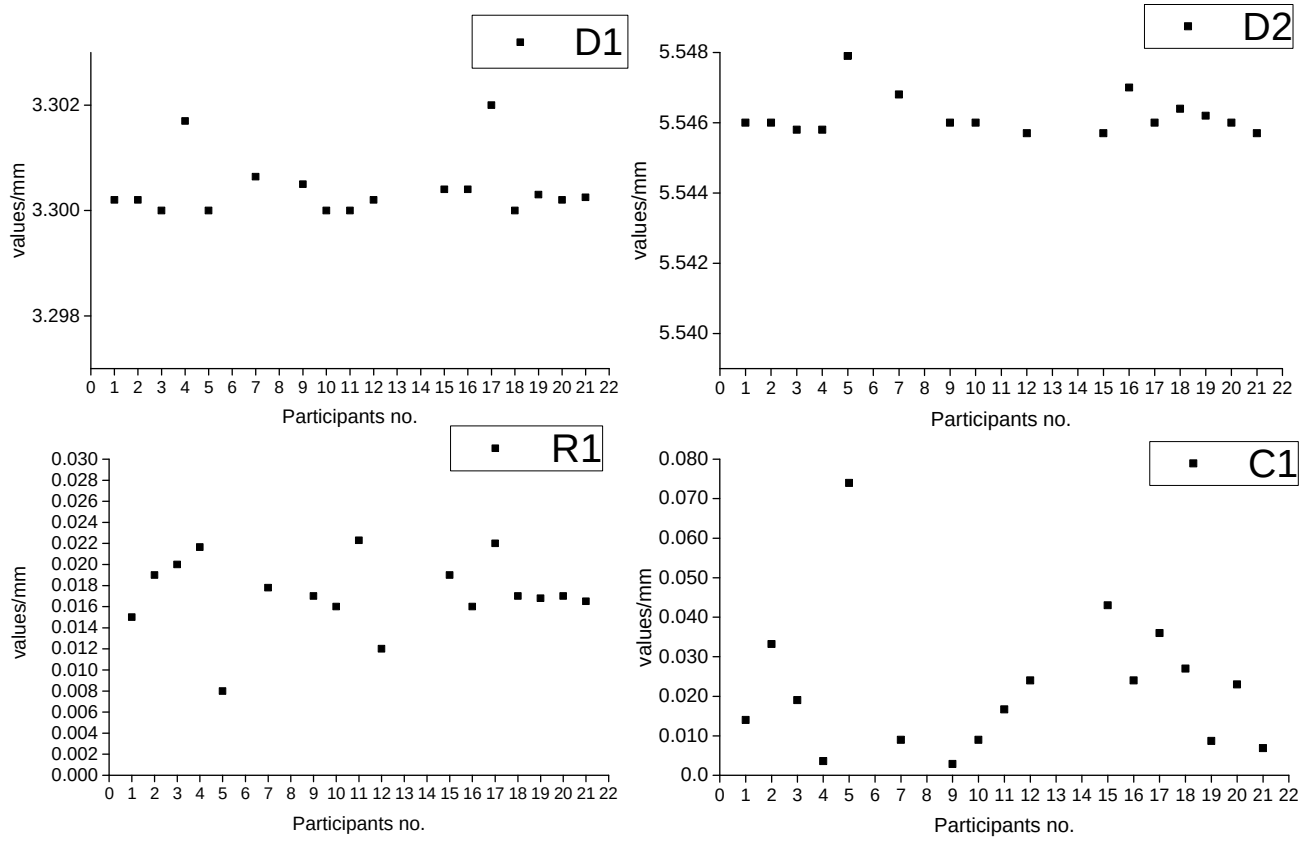

Figure 6.50. Results for Assembly 2 (LR data sets). The calibration value for D1 is 3.0012 ± 0.0010 mm, for D2 is 5.5432 ± 0.0010 mm, for R1 is 0.0074 ± 0.0015 and C1 is 0.0093 ± 0.0024 mm

6.15 Assembly 2: impact of operator

Regarding the inspection software, 16 out of 17 participants used VG StudioMAX inspection software, while only one participant used Zeiss Calypso. Different versions of VG StudioMAX were used by the participants, which may to some extent explain differences among the participants. Surface determination was based on advanced methods that all take into account the local behaviour of the grey values. Some participants applied morphological operators, such as opening and closing, before segmenting the data sets. Opening and closing in image processing serve as a noise removal technique. Opening removes small objects from the foreground of an image (usually taken as the dark pixels) and places them in the background, while closing removes small holes in the foreground, changing small areas of background into foreground. A typical use of opening and closing is for removing the noise created by the fixture around the workpiece. None of the participants filtered the volume using volumetric filters to minimise the effect of noise and of surface texture.

Although the data sets were distributed as voxel files, some participants decided to work on STL files. No substantial difference between measurements conducted using voxel files and STL files were observed due to the almost total absence of image artefacts within the data sets. STL files reduced the amount of data being handled by more than 90%. The majority of investigations were conducted in accordance with the technical protocol provided by the coordinator. Minor changes were, however, registered between the participants´ measuring strategies and the technical protocol. The recurring difference was the change of the primary datum, a cylinder, in order to cope with the taper of Assembly 2. Elementary feature such as cylinders, planes, and circles were used for defining the datum system and the five measurands. Most participants used the provided CAD model for alignment and evaluations. Some participants used the CAD model for more easily setting the measuring strategies. The CAD model was subsequently aligned with the voxel model using a best fit method and all features were moved from it to the voxel model.

Evaluations of the features were conducted in different ways, especially for the concentricity. The majority of the participants measured concentricity using the software script, while some others assessed the concentricity measuring the maximum distance between the median point of the cross section and the reference datum.

Depending on the measurand, the participants used a number of points ranging from 400 to 2000. By performing a One-way Anova analysis [134], no correlation between number of points and measurement results was observed.

6.16 Conclusions

The InteraqCT interlaboratory comparison represented a new activity that aimed at investigating the performance of CT with respect to dimensional measurements on assemblies. A total number of 22 industrial CT scanners from Belgium (1 participant), Denmark (6 participants), Germany (8 participants), Italy (2 participant), Singapore (1 participant), and the UK (4 participants) took part in the comparison. National metrology institutes, manufacturers, universities, research centres, and CT end users are all represented within the comparison. The comparison has been concluded within a period of 12 months using a parallel circulation of the comparison workpieces. In contrast to previous comparisons that only focused on physical items, the InteraqCT comparison extends beyond the edge of physical items by introducing a voxel item. The voxel item is an item scanned by coordinator and electronically distributed to participants. Two assemblies (*Assembly 1* and *Assembly 2*) with different materials and sizes were selected. *Assembly 1* is a physical item while *Assembly 2* is a voxel item of an industrial assembly. Various measurands are considered, encompassing lengths, diameters, roundness, and concentricity. A multi-material length is also included in the comparison. Two different scanning approaches were considered within the comparison exercise for Assembly 1. The first approach, coded as "Own Choice", does not apply any scanning restrictions on any of the parameters. The second one, coded as "Fast Scan", introduced a series of limitations, including the scanning time and the number of images per projection. The following conclusions can be drawn:

- All items have shown a good stability over the 8 months of the circulation. Depending on the item and measurand, the estimated reference expanded uncertainties (k=2) ranged approximately from 1.1 µm to 2.6 µm.
- The majority of the participants stated measurement uncertainties below 10 µm for all measurands of Assembly 1. 7 out of the 22 participants stated measurement uncertainties above 30 µm. The majority of the participants stated overestimated measurement uncertainties.
- 71% of the measurements conducted using the Own Choice approach are in agreement with the reference values while 59% of the measurement results based the Fast Scan approach are in accordance with the reference values. The majority of the participants obtained similar results in both scanning approaches. A few participants achieved significantly different measurement results, most probably due to the impossibility of selecting suitable scanning parameters. *L2* and *L3*, which are bidirectional measurands, show lower agreement than *L1* and *L4*, which are unidirectional lengths. T shows a worse agreement than *L3* despite their similarities (both are bidirectional length of similar size). This result confirms the greater difficulty in defining a multi-material surface determination.
- Regarding Assembly 2, a very good agreement was seen among most participants' results for *D1* and *D2*, with standard deviation values of approximately 1 µm regardless of the image quality of the used data sets. A good agreement was also seen among participants in connection

with *R1*, with standard deviation values of approximately 3 µm and of 5 µm for *HR* and *LR* data sets, respectively. A worse agreement was observed among participants for *C1*, with standard deviation values of approximately 9 µm and of 12 µm for *HR* and *LR* data sets, respectively.

Chapter 7

Conclusions

7.1 Summary

In this thesis, CT for metrology and its fundamental elements such as source, detector, positioning system and informatics infrastructure have been presented. It has been seen that a CT measurement for dimensional metrology requires a large number of hardware and software steps. Some of the steps are typically found in any imaging process based on X-rays, others are specifically required for dimensional metrology. Influence factors affecting any element of CT have been described and when possible quantified according to literature searches or own investigations. It has been seen that sizeable improvements in the accuracy of dimensional measurements can be obtained when the influence factors are reduced. A description of image artefacts commonly encountered in CT has been given.

The main elements of tolerance verification have been discussed within this work. It has been seen that there exists a standardized way of expressing the tolerances, which is known as Geometrical Product Specifications, ISO-GPS. With respect to traditional tolerancing methods, ISO-GPS avoids any specification ambiguities at inspection of a component by linking dimensional and geometrical information of a component. It has been seen that ISO-GPS, through ISO 14253-1, gives a rule for determining when a feature of a specific workpiece complies with a given tolerance, by taking into account the measurement uncertainty. Typical workflows for inspecting a workpiece using CMMs and CT have been presented and compared. It has been seen that CMMs ensure lower measurement uncertainty than CT that conversely ensures higher flexibility and lower cost of programming. It has also been recognized that CT suffers from the lack of international standards detailing the acceptance tests for verifying the performance of CT used for measuring linear dimensions compared CMMs. The estimation of measurement uncertainty in CT has also been presented as it is highly relevant to tolerance verification. It has been seen in the chapter that the measurement uncertainty in CT can be quantified using different approaches such as GUM, representing the most exhaustive method for estimation of uncertainty, PUMA which represents a simplification of GUM, and ultimately ISO 15530-3 and VDI/VDE 2630 part 2.1 which are two methods relying on calibrated workpieces. VDI/VDE 2630 part 2.1 is currently the only method specifically developed for CT.

An investigation regarding the opportunity of using the median filtering to improve the measurement accuracy has been conducted in this work. The Filtering stage and kernel size were selected as variables, while an industrial assembly was used as the workpiece. The results of investigation showed that the use of the medial filtering improved the accuracy of roundness and diameter measurements but not of length measurements, which showed larger deviations after f. The worsening of length measurements was investigated and found to be due to the smoothing of the asperities of component surfaces. Based on the obtained results, the median filter can represent a suitable tool for reducing noise arising from short scanning times. Median filtering can also be used to eliminate the contribution of the surface texture for data sets to measurement results.

A metrological comparison of surface determination methods available in a well-known inspection software package has been carried out in this work. Seven different surface determination methods were considered within the comparison. Three multi-material assemblies, each assembly included two components, having different x-ray absorption ratios were used as the workpieces. Apart from Global thresholding, all surface segmentation methods yielded a maximum measurement error of up to 40% of the used voxel size for bidirectional length measurements. None of the investigated surface determination methods allowed segmentation of the assemblies in a single step. All surface determination methods showed a similar repeatability regardless of the size of considered feature. The effect of the starting point on the accuracy of surface determination process was also investigated, leading to two main considerations. The first one is that better measurement results were achieved when the starting point was automatically defined for all surface determination methods. The second one is that the optimal thresholding value did not necessarily represent the minimum grey value between air and material distribution. This comparison demonstrated that multi-material surface determination methods are not currently available for end-users. Nevertheless mono-material surface determination methods appeared to be able to deliver accurate measurement results provided that the surface determination process is fine-tuned for each component in an assembly.

An investigation aiming at quantifying the extent to which the CT post-processing operations such as surface determination, feature fitting, and datum system contribute to the uncertainty of CT measurements has been carried out. Among the considered post-processing operations, the datum system was found to be the most prominent source of uncertainty in the investigation as large as the CT repeatability. This investigation also proved that the inspection of components which are fully assembled is feasible without any loss of accuracy provided that the components are not deformed after assembly. As a result, an increase in the throughput of a CT measurement of approximately 50% can be achieved.

A new type of concurrent reference objects for calibration of the scale error in CT has been presented in Chapter 5. A concurrent reference object is positioned and scanned together with the workpiece inside

the CT scanner producing a 3D reference system for the measurement. The two prototypes were calibrated on a tactile CMM, and their applicability demonstrated using different workpieces having different sizes and materials. None of the investigations highlighted loss of image quality due to the presence of a concurrent reference object surrounding a workpiece. None of the investigations highlighted residual errors presenting systematic trends due to inefficient corrections. Compared to existing artefacts, the new concurrent artefacts allow a considerable reduction of time (approx. 50%) and amount of data to be stored (approx. 50%) by compressing the process of calibration, scanning, and measurement into a single workflow.

An interlaboratory comparison on CT of assemblies has been carried out as a part of this work. A total number of 22 industrial CT scanners from Belgium (1 participant), Denmark (6 participants), Germany (8 participants), Italy (2 participant), Singapore (1 participant), and the UK (4 participants) took part in the comparison. National metrology institutes, manufacturers, universities, research centres, and end users were all represented within the comparison. In contrast to previous comparisons that only focused on physical items, the present comparison was based on the circulation of a physical, Assembly 1, and of a voxel, Assembly 2, assembly. The voxel assembly represented an imaging of an industrial item scanned by coordinator and distributed electronically to participants. The introduction of such new concept brought the following advantages: (a) it enabled determination of whether CT post-processing poses a problem for the accuracy of CT measurements by isolating CT post-processing from the whole CT measurements workflow; (b) it allowed a parallel circulation based on the same item; (b) it reduced the total economic cost of a comparison involving a large number of the participants. Assembly 1 represents a new kind of multi-material artefact including mono- and multi-material lengths. Various measurands are considered, encompassing lengths, diameters, roundness, and concentricity. A multi-material length was also included in a comparison for the first time. Two different scanning approaches were considered within the comparison exercise for Assembly 1. The first approach, coded as “Own Choice”, does not apply any scanning restrictions on any of the parameters. The second one, coded as “Fast Scan”, introduced a series of limitations, including the scanning time and the number of images per projection. The comparison has been concluded within a period of 12 months using a parallel circulation. All items have shown a good stability, within the measurement uncertainty, over the 8 months of circulation. From the length measurements on Assembly 1, it was concluded that length measurements were made without problems by the participants who corrected systematic errors efficiently. Many of the participants obtained similar results in both scanning approaches considered within the comparison, while a few participants achieved significantly different measurement results, most probably due to the impossibility of selecting suitable scanning parameters. From the measurements of Assembly 2, it was seen that increasing the level of difficulty from simple diameter measurements to more complex geometric quantities

gave severe difficulties for the participants. The majority of the participants stated measurement uncertainties for all measurands of Assembly 1 based on either manufacture specifications or uncertainty budgeting. The majority of the participants stated overestimated measurement uncertainties.

During this Ph.D.-project the author has investigated the use of CT for quality control of precision assemblies. In conclusion the main results from this project are in short:

- A quantification of several influence factors affecting CT measurements was carried out
- A new concept of reference artefact for concurrent calibration of scale error in CT has been developed
- A new multi-material artefact including mono- and multi-material lengths has been developed as the first of its kind in literature
- An international comparison of CT system based on a physical and a voxel assembly was carried out.

7.2 Outlook

The investigations and the achievements of the present work have contributed to the development of CT for dimensional metrology, with particular focus on tolerance verification of assemblies. Further research works will be undertaken with the following points.

- In this work, the research regarding CT for tolerance verification of assemblies has mainly focused on the materials with low capabilities of producing image artefacts and two-component assemblies. Further research will focus on the use of workpieces involving more than two components at a time, and materials with high absorption coefficients. Future research will also explore the opportunity to use CT for tolerance verification of objects having features close to the limit of the resolution (< 3µm). In this respect, a research work, involving high-resolution CT scans of the objects micro features, has been initiated during the present project with the collaboration of the author.
- Development of new concurrent calibration artefacts. The two concurrent calibration artefacts developed in this work have shown to be able to improve the performance of CT and its productivity. Further research will focus on the development of new artefacts for concurrent scale error correction based on multi-material elements. In this respect, a research work has been initiated during the present project with the collaboration of the author for looking into this opportunity.
- Implementation of an experimental database for increasingly accurate estimation of measurement uncertainty. During this work, different workpieces and CT have been used, so it will be possible to establish an early-stage database allowing quantification of the measurement uncertainty in CT by taking into account features, materials and scanning parameters.

- New research will focus on the possibility of combining CT and dimensional metrology with product design processes. The goal of this new research will be to help small and medium sized companies in develop products more efficiently by using CT and dimensional metrology to address design risks. This research will also be oriented to students in order to increase awareness about the benefits of metrology for product design process.
- Development of a model for quantifying the economic opportunities of using the CT as a tool for tolerance verification in productive environments. The research will be devoted to estimating the cost for a single feature measured using CT by taking into account the cost of consumable products, such as probes, fixture, the cost of programming in cases of changes in final products, the cost of maintenance, and cost of bad quality. The research will have the final aim of producing an exhaustive example of cost-benefit analysis for industries wishing to purchase a CT.

Chapter 8

References

[1] "Frost.com - Research, Growth Consulting, Events, Training." [Online]. Available: http://ww2.frost.com/. [Accessed: 10-Oct-2016].

[2] "Welcome to Novo Nordisk A/S." [Online]. Available: http://www.novonordisk.com/. [Accessed: 20-Oct-2016].

[3] "X-ray and CT Inspection | Products | Nikon Metrology." [Online]. Available: http://www.nikonmetrology.com/en_EU/Products/X-ray-and-CT-Inspection. [Accessed: 12-Oct-2016].

[4] "Micro to Nano European for all your supplies and consumables for electron microscopy, SEM, FIB, TEM, AFM, light microscopy, sample preparation tools and calibration standards." [Online]. Available: https://www.microtonano.com/index.php. [Accessed: 20-Oct-2016].

[5] A. Fleming, "On the history and development of the thermionic valve," *J. Sci. Instrum.*, vol. 11, no. 2, pp. 44–49, Feb. 1934.

[6] J. P. P. Kruth, M. Bartscher, S. Carmignato, R. Schmitt, L. De Chiffre, and A. Weckenmann, "Computed tomography for dimensional metrology," *CIRP Ann. - Manuf. Technol.*, vol. 60, no. 2, pp. 821–842, Jan. 2011.

[7] O. Hemberg, M. Otendal, and H. M. Hertz, "Liquid-metal-jet anode electron-impact x-ray source," *Appl. Phys. Lett.*, vol. 83, no. 7, p. 1483, 2003.

[8] R. A. Fosbinder and D. Orth, *Essentials of radiologic science*. Wolters Kluwer Health/Lippincott Williams & Wilkins, 2010.

[9] J. A. Seibert, "Flat-panel detectors: how much better are they?," *Pediatr. Radiol.*, vol. 36 Suppl 2, no. Suppl 2, pp. 173–81, Sep. 2006.

[10] T. T. Farman, R. H. Vandre, J. C. Pajak, S. R. Miller, A. Lempicki, and A. G. Farman, "Effects of scintillator on the detective quantum efficiency (DQE) of a digital imaging system.," *Oral Surg. Oral Med. Oral Pathol. Oral Radiol. Endod.*, vol. 101, no. 2, pp. 219–23, Feb. 2006.

[11] H. Mori, R. Kyuushima, K. Fujita, and M. Honda, "High resolution and high sensitivity CMOS panel sensors for X-ray imaging," in *2001 IEEE Nuclear Science Symposium Conference Record (Cat. No.01CH37310)*, 2002, vol. 1, pp. 29–33.

[12] E. M. G Prekas, M Breen, H Sabet, H Bhandari, G Derderian, F Robertson, CStapels, J Christian,

J Cool, S Nagarkar, V. V. Hamm and W. R. Hamm, “Direct deposition of microcolumnar scintillator on cMOS SSPM array: toward a photon counting detector for X-ray/gamma ray imaging,” in *AIP Conference Proceedings*, 2011, vol. 1412, no. 1, pp. 262–269.

[13] E. Wolf, *Progress in optics. Volume XXI*, vol. 21. North-Holland, 1984.

[14] I. M. Orlov, D. G. Morgan, and R. H. Cheng, “Efficient implementation of a filtered back-projection algorithm using a voxel-by-voxel approach,” *J. Struct. Biol.*, vol. 154, no. 3, pp. 287–296, 2006.

[15] G. T. Herman, “Image reconstruction from projections,” *Real-Time Imaging*, vol. 1, no. 1, pp. 3–18, 1995.

[16] F. Dennerlein, H. Kunze, and F. Noo, “Filtered backprojection reconstruction with depth-dependent filtering.,” *Tsinghua Sci. Technol.*, vol. 15, no. 1, pp. 17–24, Feb. 2010.

[17] M. Lyra, A. Ploussi, M. Lyra, and A. Ploussi, “Filtering in SPECT image reconstruction,” *Int. J. Biomed. Imaging*, vol. 2011, pp. 1–14, 2011.

[18] M. N. Salihin Yusoff and A. Zakaria, “Determination of the optimum filter for qualitative and quantitative 99mTc myocardial SPECT imaging,” *Int. J. Radiat. Res.*, vol. 6, no. 4, pp. 173–182, 2009.

[19] S. Horbelt, M. Liebling, and M. A. Unser, “Filter design for filtered back-projection guided by the interpolation model,” 2002, p. 806.

[20] L. A. Feldkamp, L. C. Davis, and J. W. Kress, “Practical cone-beam algorithm,” *J. Opt. Soc. Am. A*, vol. 1, no. 6, p. 612, Jun. 1984.

[21] I. A. Elbakri and J. A. Fessler, “Segmentation-free statistical image reconstruction for polyenergetic X-ray computed tomography,” in *Proceedings IEEE International Symposium on Biomedical Imaging*, pp. 828–831.

[22] M. Beister, D. Kolditz, and W. A. Kalender, “Iterative reconstruction methods in X-ray CT,” *Phys. Medica*, vol. 28, no. 2, pp. 94–108, 2012.

[23] C. Schmidgunst, D. Ritter, and E. Lang, “Calibration model of a dual gain flat panel detector for 2D and 3D x-ray imaging,” *Med. Phys.*, vol. 34, no. 9, p. 3649, 2007.

[24] B. R. Müller, A. Lange, M. P. Hentschel, and A. Kupsch, “A comfortable procedure for correcting X-ray detector backlight,” *J. Phys. Conf. Ser.*, vol. 425, no. 19, p. 192015, Mar. 2013.

[25] J. Starman, C. Tognina, L. Partain, and R. Fahrig, “A forward bias method for lag correction of an a-Si flat panel detector.,” *Med. Phys.*, vol. 39, no. 1, pp. 18–27, Jan. 2012.

[26] P. Müller, J. Hiller, A. Cantatore, G. Tosello, and L. De Chiffre, “New reference object for metrological performance testing of industrial CT systems,” in *Proceedings of the 12th euspen International Conference*, 2012.

[27] B. Sankur and B. Sankur, “Survey over image thresholding techniques and quantitative performance evaluation,” *J. Electron. Imaging*, vol. 13, no. 1, p. 146, Jan. 2004.

[28] N. Otsu, “A threshold selection method from gray-level histograms,” *IEEE Trans. Syst. Man.*

Cybern., vol. 9, no. 1, pp. 62–66, Jan. 1979.

[29] H. Yan, "Unified formulation of a class of image thresholding techniques," *Pattern Recognit.*, vol. 29, no. 12, pp. 2025–2032, 1996.

[30] S. Ontiveros, J. A. Yagüe, R. Jiménez, and F. Brosed, "Computer tomography 3D edge detection comparative for metrology applications," *Procedia Eng.*, vol. 63, pp. 710–719, 2013.

[31] R. Guo and S. M. Pandit, "Automatic threshold selection based on histogram modes and a discriminant criterion," *Mach. Vis. Appl.*, vol. 10, no. 5–6, pp. 331–338, Apr. 1998.

[32] A. Rosenfeld and P. De La Torre, "Histogram concavity analysis as an aid in threshold selection," *IEEE Trans. Syst. Man. Cybern.*, vol. SMC-13, no. 2, pp. 231–235, Mar. 1983.

[33] M. I. Sezan, "A peak detection algorithm and its application to histogram-based image data reduction," *Comput. Vision, Graph. Image Process.*, vol. 49, no. 1, pp. 36–51, 1990.

[34] J. Kittler and J. Illingworth, "Minimum error thresholding," *Pattern Recognit.*, vol. 19, no. 1, pp. 41–47, 1986.

[35] Verein Deutscher Ingenieure, "VDI/VDE 2630 Blatt 1.2: Computertomografie in der dimensionellen Messtechnik. Einflussgrößen auf das Messergebnis und Empfehlungen für dimensionelle Computertomografie-Messungen," pp. 1–15, 2008.

[36] J. Hiller, M. Maisl, and L. M. Reindl, "Physical characterization and performance evaluation of an x-ray micro-computed tomography system for dimensional metrology applications," *Meas. Sci. Technol.*, vol. 23, no. 8, p. 85404, Aug. 2012.

[37] Y. Tan, "Scanning and post-processing parameter optimization for CT dimensional metrology," KU Leuven, 2015.

[38] V. Lazurik, V. Moskvin, and T. Tabata, "Average depths of electron penetration: use as characteristic depths of exposure," *IEEE Trans. Nucl. Sci.*, vol. 45, no. 3, pp. 626–631, Jun. 1998.

[39] A. Ihsan, S. H. Heo, H. J. Kim, C. M. Kang, and S. O. Cho, "An optimal design of X-ray target for uniform X-ray emission from an electronic brachytherapy system," *Nucl. Instruments Methods Phys. Res. Sect. B Beam Interact. with Mater. Atoms*, vol. 269, no. 10, pp. 1053–1057, 2011.

[40] Z. H. Mehranian A, Ay MR, Alam NR, "Quantifying the effect of anode surface roughness on diagnostic x-ray spectra using Monte Carlo simulation," *Med. Phys.*, vol. 37, no. 2, p. 742, 2010.

[41] M. K. Simon and S. Dolinar, "Signal-to-Noise Ratio Estimation," in *Autonomous Software-Defined Radio Receivers for Deep Space Applications*, Hoboken, NJ, USA: John Wiley & Sons, Inc., 2006, pp. 121–192.

[42] A. Konstantinidis, "Evaluation of digital x-ray detectors for medical imaging applications," UCL (University College London), 2011.

[43] IEC, "IEC 62220-1 Medical electrical equipment – Characteristics of digital X-ray imaging devices – Part 1: Determination of the detective quantum efficiency," Geneva, Switzerland, 2003.

[44] D. Xi, G. Jianbao, J. Zou, R. Junyan, H. Zhanli, L. Xin, "The study of reconstruction image quality

resulting from geometric error in micro-CT system," *2010 4th Int. Conf. Bioinforma. Biomed. Eng.*, pp. 8–11, Jun. 2010.

[45] M. A. W. Jagadeesha Kumar, Alex Attridge, P K C Wood, "Analysis of the effect of cone-beam geometry and test object configuration on the measurement accuracy of a computed tomography scanner used for dimensional measurement," *Meas. Sci. Technol.*, vol. 22, no. 3, p. 35105, Mar. 2011.

[46] L. De Chiffre, S. Carmignato, J.-P. Kruth, R. Schmitt, and A. Weckenmann, "Industrial applications of computed tomography," *CIRP Ann. - Manuf. Technol.*, vol. 63, no. 2, pp. 655–677, 2014.

[47] V. Aloisi and S. Carmignato, "Influence of surface roughness on X-ray computed tomography dimensional measurements of additive manufactured parts," *Case Stud. Nondestruct. Test. Eval.*, vol. 6, pp. 104–110, 2016.

[48] A. B. G Stachowiak, *Engineering tribology*. Elsevier, 1993.

[49] P. Toft, "The Radon transform theory and implementation," Technical University of Denmark, 1996.

[50] S. E. Umbaugh and S. E. Umbaugh, *Digital image processing and analysis : human and computer vision applications with CVIPtools*. CRC Press, 2011.

[51] F. A. Arenhart, C. R. Baldo, T. L. Fernandes, and G. D. Donatelli, "Experimental investigation of the influencing factors on the structural resolution for dimensional measurements with CT systems," in *6th Conference on Industrial Computed Tomography,* 2016, p. 12.

[52] F. Borges de Oliveira, A. Stolfi, M. Bartscher, L. De Chiffre, and U. Neuschaefer-Rube, "Experimental investigation of surface determination process on multi-material components for dimensional computed tomography," *Case Stud. Nondestruct. Test. Eval.*, 2016.

[53] A. Stolfi, M. K. Thompson, L. Carli, and L. De Chiffre, "Quantifying the contribution of post-processing in computed tomography measurement uncertainty," *Procedia CIRP*, vol. 43, pp. 297–302, 2016.

[54] J. A. Yagüe-Fabra, S. Ontiveros, R. Jiménez, S. Chitchian, G. Tosello, and S. Carmignato, "A 3D edge detection technique for surface extraction in computed tomography for dimensional metrology applications," *CIRP Ann. - Manuf. Technol.*, vol. 62, no. 1, pp. 531–534, 2013.

[55] H. Villarraga, E. Morse, R. Hocken, S. Smith, E. Science, and O. Science, "a Study on material influences in dimensional computed tomography," *Aspe*, pp. 67–72, 2014.

[56] J. Angel, L. De Chiffre, J. P. Kruth, Y. Tan, and W. Dewulf, "Performance evaluation of CT measurements made on step gauges using statistical methodologies," *CIRP J. Manuf. Sci. Technol.*, vol. 11, pp. 68–72, Nov. 2015.

[57] J. Angel and L. De Chiffre, "Comparison on Computed Tomography using industrial items," *CIRP Ann. - Manuf. Technol.*, vol. 63, no. 1, pp. 473–476, 2014.

[58] P. Müller, J. Hiller, Y. Dai, J. L. Andreasen, H. N. Hansen, and L. De Chiffre, "Estimation of

measurement uncertainties in X-ray computed tomography metrology using the substitution method," *CIRP J. Manuf. Sci. Technol.*, vol. 7, no. 3, pp. 222–232, 2014.

[59] P Müller, J. Hiller, A. Cantatore, L. De Chiffre, "A study on evaluation strategies in dimensional X-ray computed tomography by estimation of measurement uncertainties," *Int. J. Metrol. Qual. Eng.*, vol. 3, no. 2, pp. 107–115, Nov. 2012.

[60] H. K. Tuy, "An inversion formula for cone-beam reconstruction," *SIAM J. Appl. Math.*, vol. 43, no. 3, pp. 546–552, Jun. 1983.

[61] M. Bartscher, O. Sato, F. Härtig, and U. Neuschaefer-Rube, "Current state of standardization in the field of dimensional computed tomography," *Meas. Sci. Technol.*, vol. 25, no. 6, p. 64013, Jun. 2014.

[62] "QRM GmbH - Quality assurance in radiology and medicine." [Online]. Available: http://www.qrm.de/.

[63] J. Kim, H. Guan, D. Gersten, and T. Zhang, "Evaluation of algebraic iterative image reconstruction methods for tetrahedron beam computed tomography systems.," *Int. J. Biomed. Imaging*, vol. 2013, p. 609704, 2013.

[64] R. A. Brooks and G. Di Chiro, "Beam hardening in X-ray reconstructive tomography," *Phys. Med. Biol.*, vol. 21, no. 3, p. 4, May 1976.

[65] H. Hall, "The Theory of Photoelectric Absorption for X-Rays and γ -Rays," *Rev. Mod. Phys.*, vol. 8, no. 4, pp. 358–397, Oct. 1936.

[66] J. F. Barrett and N. Keat, "Artifacts in CT: Recognition and Avoidance," *RadioGraphics*, vol. 24, no. 6, pp. 1679–1691, Nov. 2004.

[67] Y. Tan, K. Kiekens, F. Welkenhuyzen, J Angel, L De Chiffre, J.P. Kruth, "Simulation-aided investigation of beam hardening induced errors in CT dimensional metrology," *Meas. Sci. Technol.*, vol. 25, no. 6, p. 64014, Jun. 2014.

[68] E. Van de Casteele, D. Van Dyck, J. Sijbers, and E. Raman, "The effect of beam hardening on resolution in x-ray microtomography," in *roc. SPIE 5370, Medical Imaging 2004: Image Processing, 2089*, 2004, pp. 2089–2096.

[69] M. G Van Gompel, K Van Slambrouck, J. Defrise, K J Batenburg, J de Mey, and J. N. Sijbers, "Iterative correction of beam hardening artifacts in CT," *Med. Phys.*, vol. 38, no. S1, p. S36, 2011.

[70] "Trapet Precision Engineering." [Online]. Available: http://www.trapet.de/. [Accessed: 12-Oct-2016].

[71] S. Carmignato, D. Dreossi, L. Mancini, F. Marinello, G. Tromba, and E. Savio, "Testing of x-ray microtomography systems using a traceable geometrical standard," *Meas. Sci. Technol.*, vol. 20, no. 8, p. 84021, Aug. 2009.

[72] M. Bartscher, J. Illemann, and U. Neuschaefer-Rube, "ISO test survey on material influence in dimensional computed tomography," *Case Stud. Nondestruct. Test. Eval.*, 2016.

[73] P. Müller, D. Chiffre, L. ; Hansen, H. Nørgaard, and A. Cantatore, "Coordinate metrology by

traceable computed tomography," Technical University of Denmark, 2013.

[74] "ZERODUR® Extremely Low Expansion Glass Ceramic: SCHOTT Advanced Optics | SCHOTT AG," *SCHOTT AG*, 2016. [Online]. Available: http://www.schott.com/advanced_optics/english/products/optical-materials/zerodur-extremely-low-expansion-glass-ceramic/zerodur/index.html. [Accessed: 29-Oct-2016].

[75] U. Neuschaefer-Rube, M. Neugebauer, Ehrig, M. Bartscher, and U. Hilpert, "Tactile and optical microsensors: test procedures and standards," *Meas. Sci. Technol.*, vol. 19, no. 8, p. 84010, Aug. 2008.

[76] S. Carmignato, "Accuracy of industrial computed tomography measurements: Experimental results from an international comparison," *CIRP Ann. - Manuf. Technol.*, vol. 61, no. 1, pp. 491–494, 2012.

[77] J. J. Lifton, "The influence of scatter and beam hardening in X-ray computed tomography for dimensional metrology," 2015.

[78] G. Schick, "Metrology CT technology and its applications in the precision engineering industry" 2009, p. 75223S–75223S–8.

[79] R. Landauer, "Johnson-Nyquist noise derived from quantum mechanical transmission," *Phys. D Nonlinear Phenom.*, vol. 38, no. 1–3, pp. 226–229, Sep. 1989.

[80] S. M. Stigler, "Poisson on the poisson distribution," *Stat. Probab. Lett.*, vol. 1, no. 1, pp. 33–35, Jul. 1982.

[81] J. H. Siewerdsen, I. A. Cunningham, and D. A. Jaffray, "A framework for noise-power spectrum analysis of multidimensional images.," *Med. Phys.*, vol. 29, no. 11, pp. 2655–71, Nov. 2002.

[82] V. Van Nieuwenhove, J. De Beenhouwer, F. De Carlo, L. Mancini, F. Marone, and J. Sijbers, "Dynamic intensity normalization using eigen flat fields in X-ray imaging," *Opt. Express*, vol. 23, no. 21, p. 27975, Oct. 2015.

[83] K. Wärmefjord, J. S. Carlson, and R. Söderberg, "Controlling Geometrical Variation Caused by Assembly Fixtures," *J. Comput. Inf. Sci. Eng.*, vol. 16, no. 1, p. 11007, Feb. 2016.

[84] R. Söderberg, L. Lindkvist, and S. Dahlström, "Computer-aided robustness analysis for compliant assemblies," *J. Eng. Des.*, vol. 17, no. 5, pp. 411–428, Oct. 2006.

[85] "ISO - Technical committees - ISO/TC 213 - Dimensional and geometrical product specifications and verification." [Online]. Available: http://www.iso.org/iso/iso_technical_committee?commid=54924.

[86] Henrik S. Nielsen, *The ISO Geometrical Product Specifications Handbook - Find your way in GPS*, 1st ed. Denmark: ISO/Danish Standards, 2012.

[87] ISO 1101, "Geometrical product specifications (GPS) -- Geometrical tolerancing -- Tolerances of form, orientation, location and run-out," *Int. Organ. Stand.*, p. 103, 2012.

[88] S. D. Nigam and J. U. Turner, "Review of statistical approaches to tolerance analysis," *Comput. Des.*, vol. 27, no. 1, pp. 6–15, 1995.

[89] J. Y. Dantan and A. J. Qureshi, “Worst-case and statistical tolerance analysis based on quantified constraint satisfaction problems and Monte Carlo simulation,” *Comput. Des.*, vol. 41, no. 1, pp. 1–12, 2009.

[90] S.-S. Lin, H.-P. (Ben) Wang, and C. (Chuck) Zhang, “Statistical tolerance analysis based on beta distributions,” *J. Manuf. Syst.*, vol. 16, no. 2, pp. 150–158, 1997.

[91] M. Krumm, S. Kasperl, and M. Franz, “Reducing non-linear artifacts of multi-material objects in industrial 3D computed tomography,” *NDT E Int.*, vol. 41, no. 4, pp. 242–251, Jun. 2008.

[92] C. H. Kuo and J. C. Tsai, “An analytical computation method for statistical tolerance analysis of assemblies with truncated normal mean shift,” *Int. J. Prod. Res.*, vol. 49, no. 7, pp. 1937–1955, Apr. 2011.

[93] P. Varghese, R. N Braswell, B. Wang, and C. Zhang, “Statistical tolerance analysis using FRPDF and numerical convolution,” *Comput. Des.*, vol. 28, no. 9, pp. 723–732, 1996.

[94] F. Scholz, “Tolerance Stack Analysis Methods,” 1995.

[95] S. Khodaygan and M. R. Movahhedy, “Tolerance analysis of assemblies with asymmetric tolerances by unified uncertainty–accumulation model based on fuzzy logic,” *Int. J. Adv. Manuf. Technol.*, vol. 53, no. 5–8, pp. 777–788, Mar. 2011.

[96] H. Chen, S. Jin, Z. Li, and X. Lai, “A solution of partial parallel connections for the unified Jacobian–Torsor model,” *Mech. Mach. Theory*, vol. 91, pp. 39–49, 2015.

[97] W. Ghie, L. Laperrière, and A. Desrochers, “Statistical tolerance analysis using the unified Jacobian–Torsor model,” *Int. J. Prod. Res.*, vol. 48, no. 15, pp. 4609–4630, Aug. 2010.

[98] E. M. A. Anas, J. G. Kim, S. Y. Lee, and M. K. Hasan, “Comparison of ring artifact removal methods using flat panel detector based CT images.,” *Biomed. Eng. Online*, vol. 10, no. 1, p. 72, 2011.

[99] J. K. D. Zhengshu Shen, Gaurav Ameta, Jami J Shah, “A Comparative study of tolerance analysis methods,” *J. Comput. Inf. Sci. Eng.*, vol. 5, no. 3, p. 247, 2005.

[100] G. Ameta, S. Serge, and M. Giordano, “Comparison of spatial math models for tolerance analysis: tolerance-maps, deviation domain, and TTRS,” *J. Comput. Inf. Sci. Eng.*, vol. 11, no. 2, p. 21004, 2011.

[101] K. W. Chase, S. P. Magleby, and C. G. Glancy, “A Comprehensive dystem for computer-aided tolerance analysis of 2-D and 3-D mechanical assemblies,” in *Geometric Design Tolerancing: Theories, Standards and Applications*, Boston, MA: Springer US, 1998, pp. 294–307.

[102] R. J. Hocken and P. H. Pereira, *Coordinate measuring machines and systems*. CRC Press, 2012.

[103] Geometrical product specifications (GPS) -- Acceptance and reverification tests for coordinate measuring machines (CMM) -- Part 7:, “CMMs equipped with imaging probing systems,” *Int. Organ. Stand.*, p. 39, 2011.

[104] ISO 10360-6, “Geometrical Product Specifications (GPS) - Acceptance and reverification tests for coordinate measuring machines (CMM), Part 6: Estimation of errors in computing Gaussian

associated features," *Int. Organ. Stand.*, vol. 33, pp. 5–6, 2009.

[105] "ZEISS METROTOM - Industrial Computed tomography," *Carl Zeiss Industrielle Messtechnik GmbH*, 2016. [Online]. Available: http://www.zeiss.com/industrial-metrology/en_de/products/systems/computed-tomography/metrotom.html. [Accessed: 10-Oct-2016].

[106] VDI/VDE 2630 part 1.3, "Computed tomography in dimensional measurement - Guideline for the application of DIN EN ISO 10360 for coordinate measuring machines with CT-sensors," *VDI/VDE Soc. Metrol. Autom. Eng.*, 2011.

[107] ISO 14253-1, "Geometrical product specifications (GPS) -- Inspection by measurement of workpieces and measuring equipment -- Part 1: Decision rules for proving conformity or nonconformity with specifications," *Int. Organ. Stand.* , p. 15, 2013.

[108] J. A. Sładek, *Coordinate Metrology*. Berlin, Heidelberg: Springer Berlin Heidelberg, 2016.

[109] H. Kunzmann, T. Pfeifer, R. Schmitt, H. Schwenke, and A. Weckenmann, "Productive metrology - adding value to manufacture," *CIRP Ann. - Manuf. Technol.*, vol. 54, no. 2, pp. 155–168, 2005.

[110] A. Ihsan, S. H. Heo, and S. O. Cho, "Optimization of X-ray target parameters for a high-brightness microfocus X-ray tube," *Nucl. Instruments Methods Phys. Res. Sect. B Beam Interact. with Mater. Atoms*, vol. 264, no. 2, pp. 371–377, 2007.

[111] G. Beges, J. Drnovsek, and L. R. Pendrill, "Optimising calibration and measurement capabilities in terms of economics in conformity assessment," *Accredit. Qual. Assur.*, vol. 15, no. 3, pp. 147–154, Mar. 2010.

[112] ISO/IEC Guide 98-3, "Uncertainty of measurement – Part 3: Guide to the expression of uncertainty in measurement (GUM:1995)," *Int. Organ. Stand.*, p. 134, 2008.

[113] ISO 14253-2, "Geometrical product specifications (GPS) -- Inspection by measurement of workpieces and measuring equipment -- Part 2: Guidance for the estimation of uncertainty in GPS measurement, in calibration of measuring equipment and in product verification," *Int. Organ. Stand.* , p. 71, 2011.

[114] ISO 15530-3, "Geometrical product specifications (GPS) -- Coordinate measuring machines (CMM): Technique for determining the uncertainty of measurement -- Part 3: Use of calibrated workpieces or measurement standards," *Int. Organ. Stand.*, p. 18, 2011.

[115] VDI/VDE 2630 part 2.1, "Computed tomography in dimensional measurement - Determination of the uncertainty of measurement and the test process suitability of coordinate measurement systems with CT sensors," *VDI/VDE Soc. Metrol. Autom. Eng.*, p. 47, 2015.

[116] I. Farrance and R. Frenkel, "Uncertainty of Measurement: A Review of the Rules for Calculating Uncertainty Components through Functional Relationships.," *Clin. Biochem. Rev.*, vol. 33, no. 2, pp. 49–75, May 2012.

[117] S. D. Phillips, "Measurement Uncertainty and Traceability Issues: A Standards Activity Update | NIST," in *ASPE Spring Topical Meeting on Uncertainty Analysis in Measurement and Design*,

2004.

[118] R. Schmitt, C. Niggemann, and A, "Uncertainty in measurement for x-ray-computed tomography using calibrated work pieces," *Meas. Sci. Technol.*, vol. 21, no. 5, p. 54008, May 2010.

[119] K. Verma, B. K. Singh, and A. S. Thoke, "An enhancement in adaptive median filter for edge preservation," *Procedia Comput. Sci.*, vol. 48, pp. 29–36, 2015.

[120] F. A. Arenhart, V. C. Nardelli, and G. D. Donatelli, "Comparison of surface-based and image-based quality metrics for the analysis of dimensional computed tomography data," *Case Stud. Nondestruct. Test. Eval.*, 2016.

[121] V. Aurich and J. Weule, "Non-linear gaussian filters performing edge preserving diffusion," Springer Berlin Heidelberg, 1995, pp. 538–545.

[122] M. G. Cox, "The evaluation of key comparison data," *Metrologia*, vol. 39, no. 6, pp. 589–595, Dec. 2002.

[123] B. Muralikrishnan, *Computational Surface and Roundness Metrology*. London: Springer London, 2009.

[124] Chew Jian Chieh, "Making sense of the two-sample t-test." [Online]. Available: https://www.isixsigma.com/tools-templates/hypothesis-testing/making-sense-two-sample-t-test/. [Accessed: 29-Oct-2016].

[125] J. Angel, "Quality assurance of CT scanning for industrial applications," Technical University of Denmark, 2014.

[126] N. Mölders, M. Jankov, G. Kramm, N. Mölders, M. Jankov, and G. Kramm, "Application of gaussian error propagation principles for theoretical assessment of model uncertainty in simulated soil processes caused by thermal and hydraulic parameters," *J. Hydrometeorol.*, vol. 6, no. 6, pp. 1045–1062, Dec. 2005.

[127] M. G. Genton and A. Lucas, "Comprehensive definitions of breakdown points for independent and dependent observations," *J. R. Stat. Soc. Ser. B (Statistical Methodol.*, vol. 65, no. 1, pp. 81–94, Feb. 2003.

[128] "Why should I use a 2-sample t test?," *Minitab Inc.*, 2016. .

[129] ISO 4287, "Geometrical Product Specifications (GPS) -- Surface texture: Profile method -- Terms, definitions and surface texture parameters," *Int. Organ. Stand.*, p. 25, 1997.

[130] M. R. Ay, A. Mehranian, A. Maleki, H. Ghadiri, P. Ghafarian, and H. Zaidi, "Experimental assessment of the influence of beam hardening filters on image quality and patient dose in volumetric 64-slice X-ray CT scanners.," *Phys. Med.*, vol. 29, no. 3, pp. 249–60, May 2013.

[131] S. Maimon and G. W. Wicks, "nBn detector, an infrared detector with reduced dark current and higher operating temperature," *Appl. Phys. Lett.*, vol. 89, no. 15, p. 151109, 2006.

[132] K.K.L.B. Adikaram, M.A. Hussein, M. Effenberger, "Data transformation technique to improve the outlier detection power of Grubbs' test for data expected to follow linear relation," *J. Appl. Math.*, vol. 2015, pp. 1–9, 2015.

[133] B. L. Welch, “On the comparison of several mean values: an alternative approach,” *Biometrika*, vol. 38, no. 3/4, p. 330, Dec. 1951.

My references

[1] Stolfi, (2015). A predictive model for dimensional errors in fused deposition modeling. In Proceedings of the 15th International Conference of the European Society for Precision Engineering and Nanotechnology, Leuven, Belgium, pp. 97-98. ISBN: 978-0-9566790-7-9.

[2] Stolfi, J. Angel, & L. De Chiffre. (2015). Form measurements in an industrial CT scanner investigated using a polymer step gauge. In Proceedings of the 15th International Conference of the European Society for Precision Engineering and Nanotechnology. Leuven, Belgium, p. 203-204. ISBN: 978-0-9566790-7-9.

[3] Stolfi, & L. De Chiffre. (2015). CT Performance evaluation using Multi material assemblies. In Proceedings of International symposium on Digital Industrial Radiology and Computed Tomography. 2015. Ghent, Belgium, pp. 351-356.

[4] M. K. Thompson, A. Stolfi, & M. Mischkot. (2016). Process chain modeling and selection in an additive manufacturing context. C I R P - Journal of Manufacturing Science and Technology, 12, 25–34. DOI: 10.1016/j.cirpj.2015.09.005

[5] Stolfi, M. K. Thompson, L. Carli, & L. De Chiffre. (2016). Quantifying the contribution of post-processing in Computed Tomography measurement uncertainty. Procedia C I R P, 43, pp 297–302. DOI: 10.1016/j.procir.2016.02.123

[6] Stolfi, A., & De Chiffre, L. (2016). Selection of items for "InteraqCT Comparison on Assemblies". In Proceedings of the 6th Conference on Industrial Computed Tomography, Wels, Austria, p. 97-98.

[7] Stolfi, & L. De Chiffre, & F. Regi. (2016). Tolerance verification of an industrial assembly using Computed Tomography. In Proceedings of the 11th International Conference on Multi-Material Micro Manufacture (4M2016). Kgs. Lyngby, Denmark. pp. 261-264. ISBN 978-981-11-0749-8.

[8] Stolfi, M-H. Kallasse, L. Carli, & L. De Chiffre. (2016). Accuracy enhancement of CT measurements using data filtering. In Proceedings of the 6th Conference on Industrial Computed Tomography, Wels, Austria.

[9] Stolfi, & L. De Chiffre. (2016). CT crown for on-machine scale calibration in Computed Tomography. In Proceedings of the 16th International Conference of the European Society for Precision Engineering and Nanotechnology, Nottingham, United Kingdom, P1.34. ISSN 978-0-9566790-8-6.

[10] F. Borges de Oliveira, A. Stolfi, M. Bartscher, & L. De Chiffre. (2016). Experimental investigation of surface determination process on multi-material components for dimensional computed tomography. Case Studies in Nondestructive Testing and Evaluation. DOI: 10.1016/j.csndt.2016.04.003

[11] Stolfi, & L. De Chiffre. (2016). 3D artefact for concurrent scale calibration in Computed Tomography. Annals of the CIRP, 65(1), pp. 499-502. DOI: 10.1016/j.cirp.2016.04.069.

[12] Kraemer, A. Stolfi, T. Schneider, L. De Chiffre, G. Lanza, (2017). Traceability investigation in Computed Tomography using reference objects. In Proceedings of the 6th Conference on Industrial Computed Tomography, Leuven, Belgium, in press.

[13] P. Saxena, G. Bissacco, A. Stolfi, L. De Chiffre. (2017). Characterizing green fiber bottle prototypes using Computed Tomography. In Proceedings of the 7th Conference on Industrial Computed Tomography, Leuven, Belgium, in press.

[14] F. Borges de Oliveira, A. Stolfi,M. Bartscher, & N. Neugebauer, (2017). Proposal for multi-material probing error test for performance verification of Computed Tomography systems. In Proceedings of the 7th Conference on Industrial Computed Tomography, Leuven, Belgium, in press.

A. Stolfi, & L. De Chiffre. (2016). InteraqCT comparison on assemblies: Technical protocol. DTU Mechanical Engineering. pp 14. (report on DTU Orbit)

[15] Stolfi, & L. De Chiffre. (2016). InteraqCT comparison on assemblies: Reference measurements. DTU Mechanical Engineering. pp 134. (report on DTU Orbit)

[16] Stolfi, & L. De Chiffre. (2016). InteraqCT comparison on assemblies: Final report. DTU Mechanical Engineering. pp 64. pp 64. (report on DTU Orbit)

[17] Stolfi, L. De Chiffre, & S. Kasperl, Industrial X-ray Computed Tomography, book chapter in ” Error sources”, under review.

[18] M. Bartscher, U, Neuschaefer-Rube, J. Illemann, F. Borges de Oliveira, F. & A. Stolfi, A. Industrial X-ray Computed Tomography, book chapter in ”System Verification and Acceptance Testing”, under review.